Neoarchean (2.7 Ga) reworking of the Ungava craton by Fe-rich parental magmas

by

DEJAN MILIDRAGOVIC

Department of Earth and Planetary Sciences

McGill University, Montréal

December, 2013

A thesis submitted to

the Faculty of Graduate Studies and Research

in partial fulfilment of requirements of the degree of

Doctor of Philosophy

Abstract

The Neoarchean was a time of enhanced continental crust formation and wide-spread mafic magmatism related to global mantle melting. Mafic and ultramafic intrusions were emplaced across a large portion of the Ungava craton of the Northeast Superior Province, synchronous with the crystallization of large volumes of ca. 2.74-2.70 Ga intermediate to felsic plutonic rocks. The ca. 2.72-2.70 Ga mafic/ultramafic intrusions are locally known as the Qullinaaraaluk, Chateguay and Couture plutonic suites, and are herein referred to as the Q-suite. The Q-suite plutons have relatively unfractionated MREE/HREE ratios, variably elevated LREE/MREE ratios and strong depletions in HFSE, in particular Nb and Ta. The high Th/Yb ratios and chondritic to strongly radiogenic initial $^{143}Nd/^{144}Nd$ (2.72 Ga) ratios of the Q-suite intrusions suggest that their "calc-alkaline" trace element profiles may reflect the addition of significant tonalite-trondhjemite-granodiorite (TTG) component. The interaction between the Q-suite magmas and TTG crust is also evident in "hybrid" domains of intermediate-SiO_2 content (50-65 wt. %) that form along the margins of some intrusions. These "hybrid" domains strongly resemble the intermediate-SiO_2 members of the voluminous ca. 2.74-2.70 Ga pyroxene-bearing granitoids that make up more than 20% of the exposed surface of the Ungava craton. Mass-balance and thermodynamic modelling suggests that pyroxene-bearing granitoids with ~65 wt. % SiO_2 contain a significant juvenile (Q-suite) component modified by 40-50 % addition of trondhjemitic melt of the pre 2.74 Ga TTG crust.

Analyses of olivine ($Fo_{Max} \leq 0.84$) from peridotitic and dunitic cores of the Q-suite intrusions (Mg-number$\leq$ 0.82), suggest that their parental magmas were enriched in Fe

relative to present-day MORB, or hot-spot related magmas. The Q-suite intrusions of western and southern Ungava craton crystallized from magmas of subalkaline affinity, in contrast to the intrusions of the north-central Ungava craton which are mildly subalkaline to mildly alkaline (transitional). Parental liquid compositions of the subalkaline and transitional Q-suite intrusions estimated using the program alphaMELTS are Fe-rich high-Mg basalts (MgO = 10 wt. %, FeO^{TOT} = 13.5 wt.%, Al_2O_3 = 15 wt.%), and Al-poor ferropicrites (MgO ~14 wt. %, FeO^{TOT} = 17 wt.%, Al_2O_3 = 6.6 wt.%), respectively. These compositional differences may reflect melting of compositionally heterogeneous Fe-rich mantle sources under similar P-T conditions, or different degrees of melting of a common Fe-rich mantle source under different P-T conditions. The transitional parental magmas appear to represent high degree melts that last equilibrated with a harzburgitic residue, whereas the subalkaline parental magmas appear to represent lesser-degree partial melts that last equilibrated with a lherzolitic mantle residue.

The craton-wide distribution of Q-suite plutons and the large inferred Q-suite component in the ca. 2.74-2.70 Ga pyroxene-granitoids, suggests that ferropicritic underplating may have been a significant driving force in the reworking of the Ungava craton. Ferropicrites of similar age have also been emplaced into the southern and western Superior Province, as well as the Slave, W. Churchill, Kaapvaal, Yilgarn and Karelia cratons. The identification of ferropicritic rocks in at least five other Archean cratons suggests that melting of Fe-rich mantle domains may have had an important role in global cratonization ca. 2.7 Ga.

Résumé

Le Néoarchéen est caractérisé par un magmatisme mafique répandu relié à la fusion partielle du manteau à l'échelle globale et par une période intense de formation de croûte continentale. Des intrusions mafiques et ultramafiques sont mises en place dans l'ensemble du craton de l'Ungava, dans le secteur nord-est de la Province du Supérieur, simultanément à la cristallisation de grand volume de roches plutoniques de composition intermédiaire et felsique datées de ~ 2,74 à 2,70 Ga. Les intrusions mafiques et ultramafiques de ~ 2,72 à 2,70 Ga incluant les suites plutoniques Quillinaaraaluk, Chateguay et Couture forment une suite plutonique nommée ici la « suite-Q ». Les plutons de la suite-Q ont des ratios en terres rares intermédiaires versus terres rares lourdes relativement peu fractionnés, des ratios en terres rares légères versus terres rares intermédiaires variablement élevés et de fortes anomalies négatives en éléments à fort potentiel ionique (HFSE), en particulier en Nb et en Ta. Les ratios Th/Yb sont élevés et les ratios initiaux de $^{143}Nd/^{144}Nd$ de la suite-Q sont chondritiques à fortement radiogéniques, ce qui suggèrent que leurs signatures en éléments traces typiques des roches calco-alcalines reflètent l'addition d'un volume important de roches de type tonalite-trondhjémite-granodiorite (TTG). L'interaction entre les magmas de la suite-Q et la croûte composée de TTGs s'observe également le long des marges de certaines intrusions, marges qui sont caractérisées par des concentrations en SiO_2 plus élevées (50–65 % poids) et représentent des zones compositionnelles hybrides. Ces marges hybrides sont semblables aux unités à composition intermédiaire en SiO_2 appartenant aux granitoïdes à pyroxènes (~ 2,74 à 2,70 Ga) qui représentent plus de 20 % de la surface exposée du craton de l'Ungava. Des calculs d'équilibre de masse et une modélisation

thermodynamique indiquent que les granitoïdes à pyroxènes avec 65 % poids de SiO_2 contiennent une composante juvénile significative (suite-Q) modifiée par l'addition de 40 à 50 % d'un liquide trondhjémitique dérivé de la fusion partielle de la croûte de type TTG mise en place avant 2,74 Ga.

Les analyses d'olivine ($Fo_{Max} \leq 0.84$) des coeurs péridotitiques et dunitiques des intrusions de la suite-Q (Mg# $\leq$ 0.82) suggèrent que leurs magmas parents étaient enrichis en fer par rapport aux MORB ou aux magmas de points chauds modernes. Les intrusions de la suite-Q situées dans le secteur ouest et sud du craton de l'Ungava ont cristallisé à partir de magmas à affinité sub-alcaline contrairement à celles du centre-nord qui sont de compositions modérément sub-alcalines à légèrement alcalines (transitionnelles). Les liquides parentaux des intrusions sub-alcalines et transitionnelles de la suite-Q, modélisés à l'aide du logiciel alphaMELTS, sont des liquides basaltiques riches en fer et en magnésium (MgO = 10 % poids, FeO^{TOT} = 13,5 % poids, Al_2O_3 = 15 % poids) et des liquides ferropicritiques pauvres en aluminium (MgO ~14 % poids, FeO^{TOT} = 17 % poids, Al_2O_3 = 6,6 % poids), respectivement. Les différences compositionnelles peuvent être attribuées à la fusion de sources mantelliques riches en fer, à composition hétérogène, sous des conditions de pression et de température similaires, ou à différents degrés de fusion d'une source mantellique commune, riche en fer, sous des conditions de pression et de température différentes. Les magmas parents transitionnels semblent avoir été produits par des degrés de fusion partielle élevés et auraient par la suite été équilibrés avec un résidu harzburgitique du manteau. Au contraire, les magmas parents sub-alcalins pourraient représenter des magmas issus de degrés de fusion partielle plus faibles suivis de l'équilibrage de ces magmas avec un

résidu lherzolitique du manteau.

La grande distribution des plutons de la suite-Q dans le craton de l'Ungava et l'importante contribution d'une composante de la suite-Q dans les granitoïdes à pyroxènes âgés de ~2,74 à 2,70 Ga indiquent que l'accrétion par sous-placage de ferropicrite aurait joué un rôle moteur significatif dans le remaniement du craton. Des ferropicrites d'âges similaires ont également été mises en place dans le sud et l'ouest de la Province du Supérieur, ainsi que dans les cratons Slave, Churchill Ouest, Kaapvaal, Yilgarn et Karelia. L'identification de roches ferropicritiques dans au moins cinq autres cratons Archéens suggère que la fusion partielle de domaines mantelliques riches en fer aurait joué un rôle primordial dans la « cratonisation » globale à ~2,7 Ga.

Acknowledgements

I would like to thank Don Francis for his mentorship and patience and most importantly for opening my mind to the geological processes that transgress both the boundaries of time and our own planet.

I would like to thank Andrew Hynes and Bill Minarik for often letting me think aloud and helping me navigate through ideas. Both provided useful feedback on my research. The attempt to constrain nature of the Q-suite magmas through radiogenic isotopes was supported by Dominique Weis at the Pacific Centre for Isotopic and Geochemical Research (PCIGR) at the University of British Columbia. Finally, this project would not have been possible without the logistical support from the Pituvik Landholding Corporation and Johnny May's Air Charters, and the field assistance from Laila Chalati, Greg Dobbelsteyn, Nick Borque and Ian Carvalho-Campos.

I am very thankful to Lang Shi for assistance with microprobe work, and Glenna Keating for her dedicated work on the geochemical analyses of my samples. Statistical coaching by Vincent van Hinsberg was essential in the development of Chapter 3. Rich Friedman and Corey Wall analyzed the U-Pb isotopic compositions of zircons from Q-suite intrusions at PCIGR, while Bruno Keiffer, Jane Barling, Anaïs Fourny, and Vivian Lee offered crucial assistance with Nd and Hf- isotopic and trace element geochemical analyses. I benefited immeasurably from the real-life help of Anne Kosowski.

I am indebted to Keith Hodson for his assistance in setting up my own zircon-separation line, which included magnetic and gravity separation. I've had many office mates during my time at McGill, but Libby Sharman, Yumi Kitayama, and Ichiko Sugiyama deserve special mention. I thank Marc-Antoine Longpré and Anne-Aurélie

Sappin for taking the opportunity to have a laugh at the initial French translation of the abstract.

Scientific discussions with fellow graduate students, especially Michael Patterson, Nils Backeberg, Jason Coumans, and Grant Cox, were essential in keeping up with literature and developing new ideas. Making beer is the greatest non geological skill that I acquired during my stay. I thank my mentor Denis and my greatest protégé Ryan. I thank my friend Rebekah for providing me with a second home during my last semester at McGill.

Finally, I thank my mom Ines, my sister Darja, and Julia for all their love, patience and support. Darja and Ines' toughness and resilience during trying and tragic times were the greatest source of motivation.

Table of Contents

List of Tables

List of Figures

Contribution of Authors

In the summer of 2006, a reconnaissance mapping excursion by a team of McGill geologists identified a small, zoned ultramafic body, informally termed the DASH dyke, ~45 km southeast of the Village of Inukjuak on the Ungava Peninsula of northern Québec. The body belongs to a suite of Neoarchean mafic and ultramafic intrusions, termed the Q-suite, which were emplaced synchronously with an episode of near complete reworking of the Ungava craton. A preliminary study of the DASH dyke identified olivine of unusually Fe-rich composition (Fo_{80}) prompting Dr. Don Francis to initiate a project which would examine the role of Fe-rich magmas in the stabilization of the Ungava Craton. Following the completion of my M.Sc. degree in 2008, I took up the project as the topic of my PhD.

This study is the result of the collaboration with a number of coauthors, who co-signed the papers presented in this thesis. Each field season comprised detailed mapping of a number of mafic and ultramafic intrusions. These maps, included in Chapters 3 and 5 were produced by me with the assistance of my supervisor Don Francis, who also collected a large proportion of the ~400 sample set that forms the basis of this thesis. I separated and selected the zircon grains dated and reported in Chapter 3. The zircons were chemically abraded, dissolved, and dated at the PCIGR. The Nd and Hf isotopic and high precision trace element analyses included in chapter 2 were performed at PCIGR under the supervision of Dominique Weis. The isotopic data, including column separations and MC-ICP-MS analyses were entirely produced by me. Samples from the type Q-suite locality, which are presented in Chapter 2 were provided by Marc Constantin of Département de géologie et de genie géologique at Université Laval.

I am the main author of all chapters presented in this thesis. Papers 2, 3 and 4 were improved through scientific discussion and critical reviews from the coauthors. Don Francis is a coauthor on all three papers, and his scientific input was crucial in the development of ideas presented in the papers. Dominique Weis and Marc Constantin are coauthors for chapter 2. Dominique's help was crucial in interpretation of isotope data and evaluation of associated errors.

The current status of the material contained in this thesis is as follows:

Chapter 2: ACCEPTED WITH REVISIONS TO JOURNAL OF PETROLOGY– Milidragovic, D., Francis, D., Weis, D., and Constantin, M. Neoarchean (ca. 2.7 Ga) plutons of the Ungava craton, Québec, Canada: parental magma compositions and implications for Fe- rich mantle source regions.

Chapter 3: PUBLISHED – Milidragovic, D. and Francis, D., 2014. Ferropicrite-driven reworking of the Ungava craton and the genesis of the Neoarchean pyroxene-granitoids. Earth and Planetary Science Letters 386, 138-148,

doi: 10.1016/j.epsl.2013.10.051

Chapter 4: IN PREPARATION FOR LITHOS – Milidragovic, D. and Francis, D., Ca. 2.7 Ga ferropicritic magmatism: record of Fe-rich heterogeneities during Neoarchean global mantle melting.

CHAPTER 1. Introduction

The age and rate of growth of the continental crust, the buoyant outermost part of the Earth's lithosphere is a topic that has been debated for over 45 years since Hurley and Rand (1969) first generated a continental growth rate curve using the K-Ar and Rb-Sr isotopes. Since then, more than ten independently determined continental growth curves (Figure 1-1) have been constructed (Rino et al., 2004 and references therein; Belousova et al., 2010; Condie and Aster, 2010; Dhuime et al., 2012). There are two end-member models: one characterized by very early production of continental crust, followed by continuous recycling (Armstrong, 1981), and the other predicting steadily accelerating crustal growth (Hurley and Rand, 1969). Between these end-members, other models have argued for episodic crustal growth (Condie and Aster, 2010; Condie, 1998; McCulloch and Bennett, 1994; McLennan and Taylor, 1982), or continuous, but progressively decelerating crustal growth (Belousova et al., 2010; Dhuime et al., 2012). Of particular interest to this thesis are the models that argue for significant generation of continental crust during the period ca. 2.7 Ga (Condie and Aster, 2010; Condie, 1998; McLennan & Taylor, 1982).

Plots of zircon ages based on both continent-scale igneous populations, and detrital populations found in world's major sedimentary basins and river systems, display a pronounced peak at ~2.7 Ga (Belousova et al., 2010; Campbell and Allen, 2008; Condie et al., 2009; Condie, 1998; Lancaster et al., 2011; Rino et al., 2004). The ~2.7 Ga peak occurs on at least six widely separated cratons, indicating a period of globally-extensive granitic magmatism. The association of the zircon peak at ca. 2.7 Ga with a whole rock Nd-model age peak (Condie et al., 2009; McCulloch & Bennett, 1994) suggests that this period of global igneous activity involved the addition of significant mantle-derived

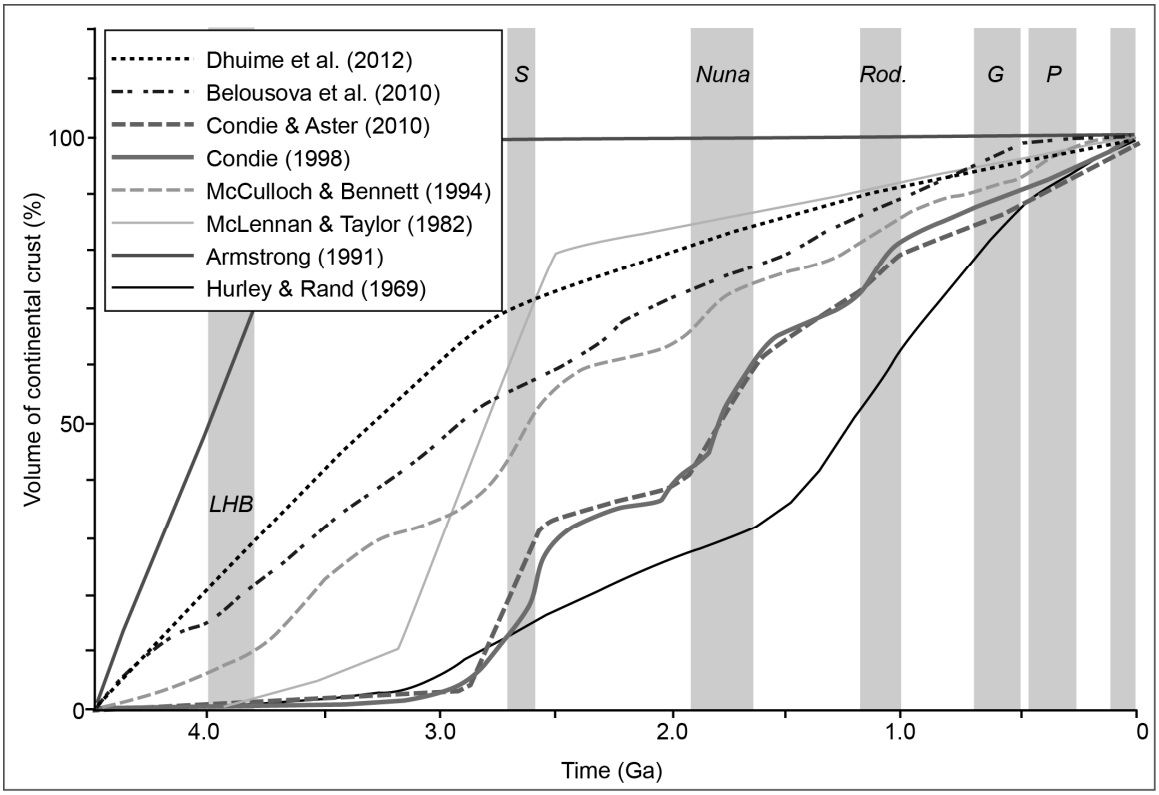

Figure 1-1: Select crustal growth curves.
The curves are adapted from Rino et al. (2004), Belousova et al. (2010), and Dhuime et al. (2012). The curve of Condie and Aster (2010) was integrated from their figure 9. The shaded columns indicate important periods in the Earth's history (LHB = Late Heavy Bombardment), S = Superia Supercontinent, Nuna = Nuna Supercontinent, R = Rodinia Supercontinent, G = Gondwana Supercontinent, P = Pangea Supercontinent.

material and accelerated formation of continental crust.

Recent Hafnium ± O-isotopic studies of ca. 2.7 Ga detrital zircons show that < 10 % of the analyzed grains have $\varepsilon_{Hf(2.7\ Ga)} > +4$ values that would be consistent with a juvenile origin (Belousova et al., 2010; Condie et al., 2011; Lancaster et al., 2011). These Hf data suggest that the majority of ca. 2.7 Ga zircons crystallized from anatectic melts, "recycled" from much older continental crust (Lancaster et al., 2011). Furthermore, the dramatic decrease in the frequency of mantle-like $\delta^{18}O$ values (+5.3 ± 0.6 ‰ VSMOW; Valley et al., 1998) in zircons younger than ~3 Ga has been interpreted to indicate a significant decrease in juvenile crust production in the Neoarchean (Dhuime et al., 2012). The most recent estimates of crustal growth rate have, therefore, argued for a relatively minor juvenile contribution during the global ca. 2.7 Ga cratonization event. Zircon isotopic studies are, however, inherently biased against juvenile (mafic) input because zircon saturation (Watson and Harrison, 1983) is typically not reached in magmas with less than 65 wt.% SiO_2 (Hoskin et al., 2000). The argument for the early development of continental crust, based on the Hf and O-isotopic compositions of zircon, is further complicated by the ineffectiveness of oxygen isotopic compositions in discriminating against recycled I-type granitoid components (5-7 ‰ VSMOW, Valley et al., 2005), which are characteristic of the majority of the Archean Tonalite-Trondhjemite-Granodiorite (TTG) suite. Mixing between the relatively unfractionated juvenile magmas and TTG melts that are characterized by relatively low Lu/Hf ratios may lead to spuriously old "hybrid" model ages (Figure 1-2) that lead to overestimates in the proportion of early (≤2.7 Ga) crustal addition. This summary demonstrates that there is a

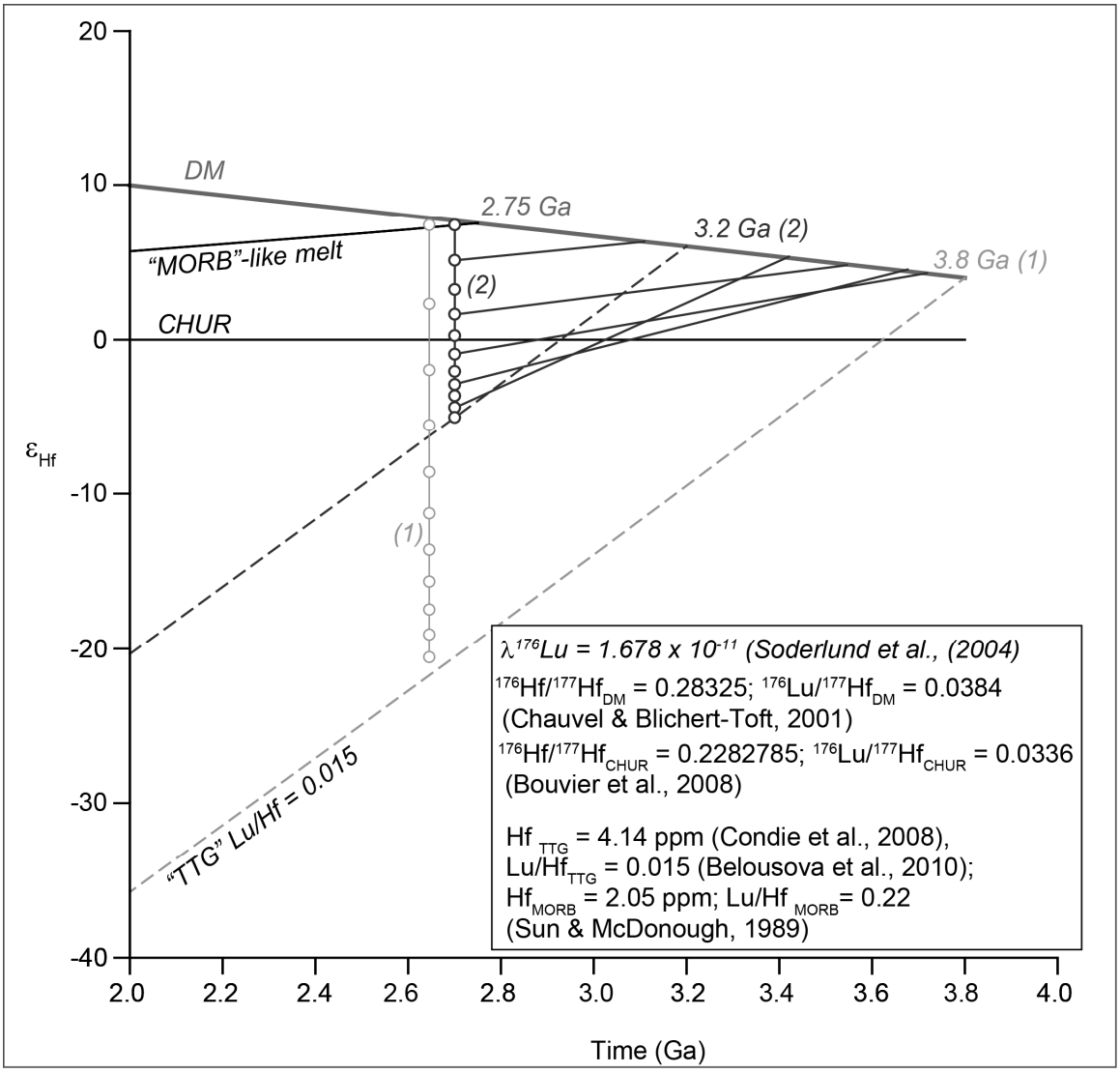
20
10
0
-10
-20
-30
-40
ε_{Hf}
DM
2.75 Ga
3.2 Ga (2)
3.8 Ga (1)
"MORB"-like melt
(2)
CHUR
(1)
"TTG" Lu/Hf = 0.015
$\lambda^{176}Lu$ = 1.678 x 10^{-11} (Soderlund et al., (2004)
$^{176}Hf/^{177}Hf_{DM}$ = 0.28325; $^{176}Lu/^{177}Hf_{DM}$ = 0.0384
(Chauvel & Blichert-Toft, 2001)
$^{176}Hf/^{177}Hf_{CHUR}$ = 0.2282785; $^{176}Lu/^{177}Hf_{CHUR}$ = 0.0336
(Bouvier et al., 2008)
Hf_{TTG} = 4.14 ppm (Condie et al., 2008),
Lu/Hf_{TTG} = 0.015 (Belousova et al., 2010);
Hf_{MORB} = 2.05 ppm; Lu/Hf_{MORB} = 0.22
(Sun & McDonough, 1989)
2.0
2.2
2.4
2.6
2.8
3.0
3.2
3.4
3.6
3.8
4.0
Time (Ga)

Figure 1-2: Conceptual εHf(T) evolution graph.

The figure illustrates the effect of contamination of juvenile magma separated from the depleted mantle (DM) reservoir ca. 2.75 Ga with evolved TTG crust, extracted from the mantle at 3.8 (1) and 3.2 (2) Ga. The Hf isotopic composition of the TTG evolves along lines originating at the composition of the DM, with slopes defined by initial Lu/Hf typical of the continental crust (Belousova et al., 2010). The Hf isotopic composition of the juvenile mafic melt evolves along a line defined by a MORB-like Lu/Hf. Mixing lines formed by mixing of the mafic magma and the TTG at 2.70 Ga are shown in 10% increments (the mixing line for scenario 1 is offset for clarity). Contamination of juvenile mafic magma by ~10 % TTG with a crustal residence of ~1 Ga, will yield zircon with near-chondritic, non-juvenile Hf-isotopic signatures. Also illustrated are the model ages calculated from the zircons crystallized from the hybrid magma formed by mixing of the juvenile mafic magma and TTG (T_{DM} = 3.2 Ga). A key observation is that mixing between relatively high Lu/Hf mafic melts and low Lu/Hf unradiogenic crust can yield spuriously old model ages that may be significantly "older" than either of the components. (All parameters used in calculations are shown in the figure).

large amount of uncertainty surrounding the evolution of continental crust and that the recent models, in particular, may significantly overestimate the amount of pre-2.7 Ga continental crust. The significance of the large modes in 2.7 Ga zircon and whole-rock Nd model ages remains a subject of debate, emphasizing the need for a better understanding of rocks that formed during the ca. 2.7 Ga global magmatic event. A better understanding of ca. 2.7 Ga rocks will help answer key questions about the proportion and character of the juvenile component in the newly formed continental crust, and the ultimate cause of this global igneous "bloom".

This thesis focuses on the first question by examining the link between the ca. 2.74-2.70 cratonization of the Northeastern Superior Province and the coeval mantle melting manifested by the widespread ultramafic plutons of the Qullinaaraaluk, Chateguay, and Couture suites (Simard, 2008), collectively referred to as the Q-suite. The Ungava craton of the Northeast Superior Province underwent a major episode of igneous activity and crustal reworking between ca. 2.74 and 2.70 Ga (Boily et al., 2009; Maurice et al., 2009). During this interval, the proto-cratonic crust, largely comprised of pre-2.74 Ga TTG suites, underwent large-scale melting, giving rise to voluminous granite-granodiorite-monzogranite (GGM) and pyroxene-bearing intermediate to felsic plutonic suites. Coeval with the crystallization of the ca. 2.74-2.70 Ga granitoid rocks, there was the emplacement of numerous and widespread mafic to ultramafic intrusions of the Q-suite. A preliminary study on a Q-suite intrusion situated approximately ~45 km SE of the Village of Inukjuak (Francis and Maurice, 2008) noted that the intrusion's peridotite core contained relict olivine crystals of unusually Fe-rich composition (Fo_{80}). The relatively high Fe-content of the peridotite and its constituent olivine provided the first clue that the

Neoarchean reworking of the Ungava craton may have been driven by ferropicrite underplating.

Ferropicritic magmas are relatively unusual in the geological record, requiring sources enriched in Fe relative to the standard pyrolitic (Ringwood, 1975) mantle. There is emerging evidence that ferropicritic magmas of ca. 2.7 Ga age were emplaced across the Superior Province (Goldstein and Francis, 2008; Green and Schulz, 1977; Kitayama and Francis, *in review;* Stone et al., 1987; Stone et al., 1995). Furthermore, a detailed survey of published literature (Francis et al., 1999; McIver et al., 1982; Papunen et al., 2009; Said and Kerrich, 2010; Sandeman et al., 2004; Schweitzer and Kröner, 1985; Van der Westhuizen et al., 1991) demonstrates that ca. 2.7 Ga ferropicritic magmas were emplaced into five other Archean cratons (Slave, W. Churchill, Yilgarn, Kaapvaal, Karelia). The globally widespread occurrence of ca. 2.7 Ga ferropicrites suggests that Fe-rich magmas may have had an important role in the ca. 2.7 Ga accelerated development of continental crust.

The main goals of this thesis are to:

1) Characterize the nature of the magmas parental to the ca. 2.72-2.70 Q-suite intrusions,

2) Assess the role of the Q-suite magmas in the ca. 2.74-2.70 Ga reworking of the Ungava craton, and

3) Assess the global extent of ca. 2.7 Ga ferropicritic magmatism, and to evaluate its importance to Neoarchean continental crustal growth.

Chapter 2 entitled “Neoarchean (ca. 2.7 Ga) plutons of the Ungava craton, Québec,

Canada: reconstructed parental magma compositions and implications for Fe- rich mantle source regions", was submitted to the "Journal of Petrology" and it constitutes a detailed petrological study of the Q-suite intrusions. It demonstrates two distinct types of Q-suite magmas; one of a subalkaline affinity, and the second characterized by a mildly alkaline to mildly-subalkaline affinity, straddling the plane of critical silica saturation. This paper develops a petrogenetic model for the generation of Q-suite parental liquids from sources, slightly less Fe-rich than L-type ordinary chondrites.

Chapter 3 entitled "Ferropicrite-driven reworking of the Ungava craton and the genesis of the Neoarchean pyroxene-granitoids" has been published in the journal "Earth and Planetary Science Letters" and demonstrates a genetic link between Q-suite parental magmas and the pyroxene-granitoid plutonic suite, which constitutes ~ 20% of the exposed Ungava craton. Mass-balance and thermodynamic modelling is consistent with a ~40-50% Q-suite component in the pyroxene-granodiorites containing ~65 % SiO_2. This discovery demonstrates the important role the juvenile Q-suite magmas had in the reworking of the Northeast Superior Province ca. 2.74-2.70 Ga.

Chapter 4 "Neoarchean (ca. 2.7 Ga) ferropicritic magmatism: a case for melting of Fe-rich mantle during growth and stabilization of the Superior Craton", provides a synthesis of global ca. 2.7 Ga ferropicritic magmatism, and establishes the Neoarchean as a time of melting of Fe-rich "plums" within a dominantly "pyrolitic" mantle. The manuscript is in preparation for the journal "Lithos".

The results presented in this thesis provide new insights into the generation of unusual Fe-rich magmas that accompanied the globally widespread ca. 2.7 Ga magmatic episode that resulted in significant production of new continental crust.

References

Armstrong, R.L., 1981. Radiogenic isotopes. The case for crustal recycling on a near-steady state no-continental Earth. Phil. Trans. R. Soc. Lond. A301, 443–472.

Belousova, E.A., Kostitsyn, Y.A., Griffin, W.L., Begg, G.C., O'Reilly, S.Y., Pearson, N.J., 2010. The growth of the continental crust: Constraints from zircon Hf-isotope data. Lithos 119, 457–466.

Boily, M., Leclair, A., Maurice, C., Bédard, J.H., David, J., 2009. Paleo- to Mesoarchean basement recycling and terrane definition in the Northeastern Superior Province, Québec, Canada. Precambrian Res. 168, 23–44.

Campbell, I.H., Allen, C.M., 2008. Formation of supercontinents linked to increases in atmospheric oxygen. Nat. Geosci. 1, 554–558.

Condie, K.C., 1998. Episodic continental growth and supercontinents: a mantle avalanche connection? Earth Planet. Sci. Lett. 163, 97–108.

Condie, K.C., Aster, R.C., 2010. Episodic zircon age spectra of orogenic granitoids: The supercontinent connection and continental growth. Precambrian Res. 180, 227–236.

Condie, K.C., Belousova, E., Griffin, W.L., Sircombe, K.N., 2009. Granitoid events in space and time: Constraints from igneous and detrital zircon age spectra. Gondwana Res. 15, 228–242.

Condie, K.C., Bickford, M.E., Aster, R.C., Belousova, E., Scholl, D.W., 2011. Episodic zircon ages, Hf isotopic composition, and the preservation rate of continental crust. Geol. Soc. Am. Bull. 123, 951–957.

Dhuime, B., Hawkesworth, C.J., Cawood, P.A, Storey, C.D., 2012. A change in the geodynamics of continental growth 3 billion years ago. Science 335, 1334–1336.

Francis, D., Ludden, J., Johnstone, R., Davis, W., 1999. Picrite evidence for more Fe in Archean mantle reservoirs. Earth Planet. Sci. Lett. 167, 197–213.

Francis, D., Maurice, C., 2008. Ferropicrites and Archean crustal reworking in the Northeastern Superior Province of Québec, Geochim. Cosmochim. Acta 72, S281.

Goldstein, S.B., Francis, D., 2008. The Petrogenesis and Mantle Source of Archaean Ferropicrites from the Western Superior Province, Ontario, Canada. J. Petrol. 49, 1729–1753.

Green, J.C., Schulz, K.J., 1977. Iron-rich basaltic komatiites in the early Precambrian Vermillion District, Minnesota. Can. J. Earth Sci. 14, 2181–2192.

Hoskin, P.W.O., Kinny, P.D., Wyborn, D., Chappell, B.W., 2000. Identifying accessory mineral saturation during differentiation in granitoid magmas: an integrated approach. J. Petrol. 41, 1365–1396.

Hurley, P.M., Rand, J.R., 1969. Pre-Drift Continental Nuclei. Science 164, 1229–1242.

Kitayama, Y., Francis, D., Fe-rich alkaline magmatism in the Archean Wawa greenstone belt (Ontario, Canada). *Submitted to Precambrian Res.*

Lancaster, P.J., Storey, C.D., Hawkesworth, C.J., Dhuime, B., 2011. Understanding the roles of crustal growth and preservation in the detrital zircon record. Earth Planet. Sci. Lett. 305, 405–412.

Maurice, C., David, J., Bédard, J.H., Francis, D., 2009. Evidence for a widespread mafic cover sequence and its implications for continental growth in the Northeastern Superior Province. Precambrian Res. 168, 45–65.

McCulloch, M.T., Bennett, V.C., 1994. Progressive growth of the Earth' s continental crust and depleted mantle: Geochemical constraints. Geochim. Cosmochim. Acta 58, 4717–4738.

McIver, J.R., Cawthorn, R.G., Wyatt, B.A., 1982. The Ventersdorp Supergroup - the youngest komatiitic sequence in southern Africa, *in:* Arndt, N.T., Nisbet, E.G. (Eds.), Komatiites. Allen and Unwin, Boston, pp. 81–90.

McLennan, S.M., Taylor, S.R., 1982. Geochemical constraints on the growth of the continental crust. J. Geol. 90, 347–361.

Papunen, H., Halkoaho, T., Luukkonen, E., 2009. Archaean Evolution of the Tipasjärvi-Kuhmo-Suomussalmi Greenstone Complex, Finland. Geol. Surv. Finl. Bulletin 4, 84 p.

Ringwood, A.E., 1975. Composition and Petrology of the Earth's Mantle. McGraw and Hill, New York.

Rino, S., Komiya, T., Windley, B.F., Katayama, I., Motoki, A., Hirata, T., 2004. Major episodic increases of continental crustal growth determined from zircon ages of river sands; implications for mantle overturns in the Early Precambrian. Phys. Earth Planet. Inter. 146, 369–394.

Said, N., Kerrich, R., 2010. Magnesian dyke suites of the 2.7 Ga Kambalda Sequence, Western Australia: Evidence for coeval melting of plume asthenosphere and metasomatised lithospheric mantle. Precambrian Res. 180, 183–203.

Sandeman, H., Hanmer, S., Davis, W., Ryan, J., Peterson, T., 2004. Neoarchaean volcanic rocks, Central Hearne supracrustal belt, Western Churchill Province, Canada: geochemical and isotopic evidence supporting intra-oceanic, supra-subduction zone extension. Precambrian Res. 134, 113–141.

Schweitzer, J., Kröner, A., 1985. Geochemistry and petrogenesis of Early Proterozoic intracrartonic volcanic rocks of the Ventersdorp Supergroup, South Africa. Chem. Geol. 51, 265–288.

Simard, M., 2008. Stratigraphie et géochronologie du nord-est de la Province du Supérieur, *in:* Simard, M. (Ed.), Synthèse Du Nord-Est de La Province Du Supérieur. Ministère de Ressources Naturelles et de la Faune, Québec, MM2008-2, pp. 23–86.

Stone, W.E., Crocket, J.H., Dickin, A.P., Fleet, M.E., 1995. Origin of Archean ferropicrites: geochemical constraints from the Boston Creek Flow, Abitibi greenstone belt, Ontario, Canada. Chem. Geol. 121, 51–71.

Stone, W.E., Jensen, L.S., Church, W.R., 1987. Petrography and geochemistry of an unusual Fe-rich basaltic komatiite from Boston Township, northeastern Ontario. Can. J. Earth Sci. 24, 2537–2550.

Valley, J.W., Kinny, P.D., Schulze, D.J., Spicuzza, M.J., 1998. Zircon megacrysts from kimberlite: oxygen isotope variability among mantle melts. Contrib. to Mineral. Petrol. 133, 1–11.

Valley, J.W., Lackey, J.S., Cavosie, A.J., Clechenko, C.C., Spicuzza, M.J., Basei, M.A.S., Bindeman, I.N., Ferreira, V.P., Sial, A.N., King, E.M., Peck, W.H., Sinha, A.K., Wei, C.S., 2005. 4.4 Billion years of crustal maturation: Oxygen isotope ratios of magmatic zircon. Contrib. to Mineral. Petrol. 150, 561–580.

Van der Westhuizen, W.A., de Brutyn, H., Meintjes, P.G., 1991. The Ventersdorp Supergroup: an overview. J. African Earth Sci. 13, 83–105.

Watson, E.B., Harrison, T.M., 1983. Zircon saturation revisited: temperature and composition effects in a variety of crustal magma types. Earth Planet. Sci. Lett. 64, 295–304.

CHAPTER 2. Neoarchean (ca. 2.7 Ga) plutons of the Ungava craton, Québec, Canada: parental magma compositions and implications for Fe-rich mantle source regions

Chapter 2 describes the petrology of a suite of ca. 2.72-2.70 Ga mafic to ultramafic plutonic rocks, collectively referred to as the Q-suite, which were emplaced during a major magmatic episode that led to near complete reworking of the Ungava craton. The chapter presents a new method of estimating parental magma compositions from ultramafic cumulate rocks using the program alphaMELTS, and establishes the unusually Fe-rich character of Q-suite parental magmas.

Abstract

Mafic to ultramafic intrusions of the Qullinaaraaluk suite (Q-suite) were emplaced into the Ungava craton of the Northeastern Superior Province during an episode of intense igneous activity and crustal reworking ca. 2.74-2.70 Ga. Orthopyroxene-rich Q-suite intrusions from the Hudson Bay Terrane and southwestern Rivière Arnaud Terrane, and orthopyroxene-poor Q-suite intrusions from the north-central Rivière Arnaud Terrane indicate the existence of at least two Q-suite magma types: a subalkaline magma parental to the orthopyroxene-rich intrusions and a transitional magma parental to the orthopyroxene-poor intrusions. Both types of intrusions are characterized by LREE-enriched, HFSE-depleted trace-element profiles that reflect, in large part, contamination by the TTG-dominated crust. Near chondritic to strongly sub-chondritic initial ε_{Nd} (2.72 Ga) values (+2 to -10) of the Q-suite intrusions reflect the combined effects of both the amount of crustal contamination and the age-dependant isotopic composition of the contaminant. The inferred trace element profiles of the uncontaminated Q-suite magmas were likely flat to LREE-depleted.

The transitional magmas that produced the least evolved dunitic cumulates of the Q-suite were ferropicrites (MgO ~14 wt. %, FeO^{TOT} ~17 wt. %). In contrast, the magmas parental to the primitive Q-suite harzburgites were Fe-rich high-Mg basalts (MgO ~11 wt. %; FeO ~14 wt. %). The high Fe contents of the Q-suite magmas are incompatible with derivation from a pyrolitic mantle (Mg-number ~0.90) and require sources significantly enriched in iron. Both magma types are also characterized by relatively low Ni contents, suggesting derivation from source regions depleted in Ni relative to pyrolitic mantle peridotite. Differences in major element compositions of the subalkaline and

transitional parental magmas may reflect compositional diversity among the Fe-rich mantle sources. Comparisons with melting experiments on compositions analogous to the Martian mantle suggest that the Q-suite magmas may also be generated by different degrees of melting of a common source with an Fe content slightly lower than that of the Homestead L5 ordinary chondrite (Mg-number = 0.77). The Fe-rich picritic to high-Mg basaltic magmas last equilibrated with a garnet-free harzburgitic to lherzolitic residues, at upper mantle pressures (≤5 GPa). The craton-wide occurrence of ca. 2.72-2.70 Ga Q-suite mafic to ultramafic plutons suggests that underplating by Fe-rich mantle melts may have had a key role in the ca. 2.74-2.70 Ga cratonization of the Northeastern Superior Province.

Keywords: cumulate; Fe-rich; ferropicrite; mantle; Neoarchean

1. Introduction

Numerous greenstone belts and intracratonic volcanic and plutonic rocks were emplaced during a globally widespread episode of mafic igneous activity ca. 2.7 Ga (Armstrong *et al.*, 1991; Arndt *et al.,* 1991; Polat, 2009; Duuring *et al.,* 2012; Wall *et al.*, 2012). The timing of this activity was synchronous with the worldwide crystallization of large volumes of granitic crust (Condie *et al.,* 2009, 2011; Van Kranendonk *et al*., 2012). The Ungava craton of Northeastern Superior Province in Canada also underwent a major episode of igneous activity and crustal reworking during this period (ca. 2.74-2.70 Ga; Boily *et al.*, 2009; Maurice *et al.*, 2009). At this time, the proto-cratonic crust, largely composed of tonalite-trondhjemite-granodiorite (TTG) plutonic suites, underwent large scale melting giving rise to voluminous granite-granodiorite-monzogranite (GGM) and pyroxene-bearing intermediate to felsic plutonic rocks. The reworking of the Ungava craton coincided with the widespread emplacement of small mafic-ultramafic intrusions, locally termed the Qullinaaraaluk, Chateguay, and Couture suites, and herein collectively referred to as the Q-suite. This temporal relationship, combined with evidence that the intermediate-SiO_2 (50-65 wt. %) pyroxene-granitoids of the Ungava craton were formed by simultaneous fractional crystallization and assimilation of TTG crust by the Q-suite magmas (Milidragovic and Francis, 2014), suggests a link between the cratonization of Ungava and regional crustal underplating by mantle melts.

In this paper, we present geochemical and isotopic data for Q-suite mafic to ultramafic intrusions from widely-spaced localities across the Ungava craton (Fig. 2-1) in order to constrain the nature of their parental magmas and mantle sources. Our results

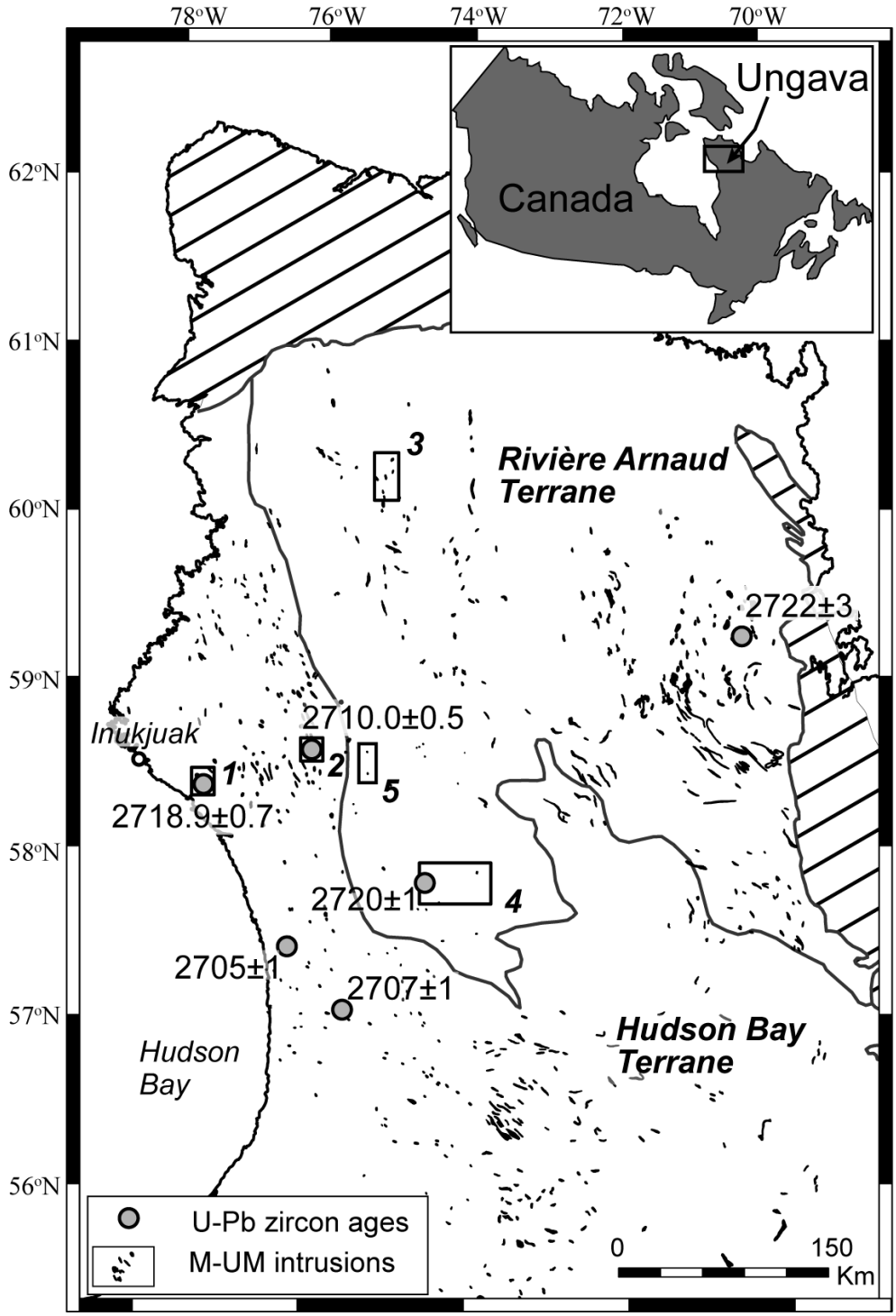

Figure 2-1: Neoarchean mafic/ultramafic plutons of the Ungava Peninsula.
The isotopically defined Hudson Bay (T_{DM} = 2.9-3.9 Ga) and Rivière Arnaud (T_{DM} = 2.8 -3.0 Ga) terranes, shown for reference, are after Boily *et al.* (2009). The numbered rectangles show the study areas discussed in the text. Locations of U-Pb dating sites (Simard, 2008; Milidragovic & Francis, 2014) are shown.

indicate that regional crustal underplating by Fe-rich picritic to high-Mg basaltic magmas was the terminal event that resulted in the reworking and cratonization of Northeastern Superior Province ca. 2.7 Ga.

2. Geological setting

The Ungava craton is a 600 x 500 km domain of the Canadian Shield, characterized by a strong north-northwest structural grain (Percival *et al.*, 2001; Leclair, 2008). It is dominated by Neoarchean plutonic rocks and interleaved complexes of high-grade, metavolcanic and metasedimentary rocks (Leclair, 2008; Maurice *et al.*, 2009); all built on an older Meso- to Eoarchean basement (Boily *et al.*, 2009) with an inferred Hadean component (O'Neil *et al.*, 2008) that is seldom preserved. The Neoarchean intrusive rocks of the Ungava craton comprise older (≥2.75 Ga), relatively sodic TTG suites (K/(K+Na) ~0.2) and younger (≤2.75 Ga), high-K GGM (K/(K+Na) ~ 0.4) and low-K (K/(K+Na) =0.2) pyroxene-bearing granitoid suites (Percival & Mortensen, 2002; Bédard, 2003), along with numerous, coeval mafic to ultramafic bodies (Simard, 2008; Milidragovic & Francis, 2014), herein collectively referred to as the Q-suite. Geobarometric data from felsic plutonic rocks indicate equilibration at mid-crustal levels (4-6.5 kbar), with a uniform depth of erosion across most of the Ungava craton (Bédard, 2003). Neodymium isotopic data indicate that two discrete terranes comprise the Ungava craton (Fig. 1; Boily *et al.*, 2009). The northeast-lying Rivière Arnaud terrane is characterized by juvenile Nd-isotopic compositions ($\varepsilon_{Nd(t)}$ = -0.7 - +2.3), in contrast to the isotopically more enriched Hudson Bay terrane ($\varepsilon_{Nd(t)}$ = -5.0 - +0.5) to the west.

A compilation of zircon U-Pb crystallization ages from the Ungava craton (n = 185; Maurice *et al.* (2009)) shows a strong mode centered at ~2.72 Ga, defined by the majority

of the GGM and pyroxene-granitoid crystallization ages. Early tectonic models for the Ungava craton involved a number of simultaneously active subduction zones in order to explain the craton-wide abundance of 2.74-2.70 Ga zircon ages, and the NNW structural grain of the craton (Stern *et al.*, 1994; Percival *et al.*, 2001; Percival & Mortensen, 2002). The abundance of inherited zircons (>2.75 Ga), coupled with the existence of isotopically (Boily *et al.*, 2009) and seismically distinct (Faure *et al.*, 2008) terranes that transgress the proposed arcs, however, argue against a plate tectonic accretionary model for the Ungava craton. More recent tectonic models favour an earlier assembly of the Rivière Arnaud and Hudson Bay terranes (ca. 2.76-2.74 Ga), with subsequent large scale melting (Maurice *et al.*, 2009) synchronous with the emplacement of the mafic-ultramafic plutons of the ca. 2.72-2.70 Ga Q-suite (Milidragovic and Francis, 2014).

Recent studies of the greenstone belts scattered across the Ungava craton have concluded that mafic volcanism occurred in seven distinct pulses 20-40 M.y. apart, between 2.88 and 2.72 Ga (Maurice *et al.*, 2009). The volcanic rocks that comprise the greenstone belts can be assigned to one of three geochemical suites: 1) an Mg-tholeiite suite, 2) an Fe-tholeiite suite characterized by elevated Fe and Ti contents, and 3) a Light Rare Earth Element (LREE)-enriched suite. The recognition that isolated Fe-rich tholeiites once formed a laterally continuous ca. 2.78 Ga cover sequence (Maurice *et al.*, 2009) provides the strongest argument against a ca. 2.74-2.70 Ga arc assembly of the Ungava craton. The two tholeiitic suites are characterized by positive initial ε_{Nd} values (+1 to +3.8), relatively unfractionated REE patterns, and an absence of negative Nb-Ta anomalies. In contrast, the younger LREE-enriched suite has a “calc-alkaline“ trace-element signature, with negative High Field Strength Element (HFSE) anomalies and

initial ε_{Nd} values that decrease with time (+3.1 to +0.5). Maurice at al. (2009) concluded that the "calc-alkaline" character of LREE-enriched suite reflects coupled fractional crystallization and crustal contamination of tholeiitic magmas in shallow to mid-crustal chambers, and attributed the secular decrease in initial ε_{Nd} values at ~2.75 Ga to the combined effects of increasing crustal contamination and a change from a TTG- to a GGM-dominated contaminant.

3. The Neoarchean Q-suite intrusions

The Qullinaaraaluk suite (Q-suite, *sensu lato*) intrusions are a volumetrically minor, but regionally widespread component of the Ungava craton (Simard, 2008). These intrusions have been previously assigned to the Qullinaaraaluk (*sensu stricto*), Couture, and Chateguay suites (Simard, 2008), primarily based on their geographic location. The intrusions appear to have been emplaced continuously ca. 2.72-2.70 Ga, as suggested by direct U-Pb zircon dating of Qullinaaraaluk suite (*sensu stricto*) gabbronorites (2707 ± 1, 2705 ± 1, 2718.9 ± 0.7, 2710.0 ± 0.5 Ma; Simard (2008); Milidragovic & Francis (2014)) and the age of one cross-cutting pegmatite (2720 ± 2; Simard (2008)). In addition, a gabbronorite situated in the easternmost Ungava craton has a U-Pb zircon crystallization age of 2722 ± 3 Ma (Simard, 2008) that is indistinguishable from the Q-suite ages from the western Ungava craton.

Although no absolute ages for the Couture Suite of the north-central Ungava craton exist, field relationships suggest that the mafic-ultramafic intrusions postdate the foliated tonalitic gneisses of the Suite de Rochefort (2789-2755 Ma) and are pre- to co-magmatic with the massive granites of the Suite de La Chevrotière (2734-2719 Ma; Simard, 2008). Based on these constraints and their unusual Fe-rich character, the intrusions of the

Couture Suite are considered to be part of the intrusive Q-suite.

3.1 Petrology and geochemistry of the Q-suite intrusions

We studied the Q-suite intrusions in three localities across the Ungava craton (Fig. 2-1). The first two are located within the Hudson Bay Terrane, ~45 km SE and 120 km E of the town of Inukjuak, respectively. The third one is located within the Rivière Arnaud Terrane, in the Lac Couture region of north-central Ungava. In addition, we examined samples collected in the southwestern Rivière Arnaud Terrane (Labbé *et al.*, 2001; Baker, 2005) and three samples collected by Majescor Resources in the Rivière Arnaud Terrane just east of the inferred boundary with the Hudson Bay Terrane (Boily *et al.*, 2009).

The Q-suite plutons are small (<10 km^2), irregularly zoned bodies whose forms range from dish-shaped sills to dykes and discontinuous "boudins" that follow local tectonic fabric. The intrusions are composed of cumulate rocks comprising a range of lithologies from olivine-dominated dunite and peridotite through pyroxene-dominated websterite and wehrlite to feldspar-rich gabbronorite and hornblendite. Overall, the intrusions are remarkably fresh, retaining much of the primary igneous mineralogy and textures. Despite incipient serpentinization, the peridotite cores commonly contain relict olivine crystals. The ultramafic lithologies of the Q-suite are commonly brecciated by decimetre-scale, pegmatitic felsic veins and dykes. Two of the mapped intrusions are flanked by intermediate-SiO_2 (50-65 wt. %), pyroxene-bearing plutonic rocks that are interpreted to be hybrids formed by simultaneous fractional crystallization and extensive assimilation of TTG crust by the Q-suite parental magmas (Milidragovic & Francis, 2014).

The intrusions of the Hudson Bay Terrane and the southwestern Rivière Arnaud

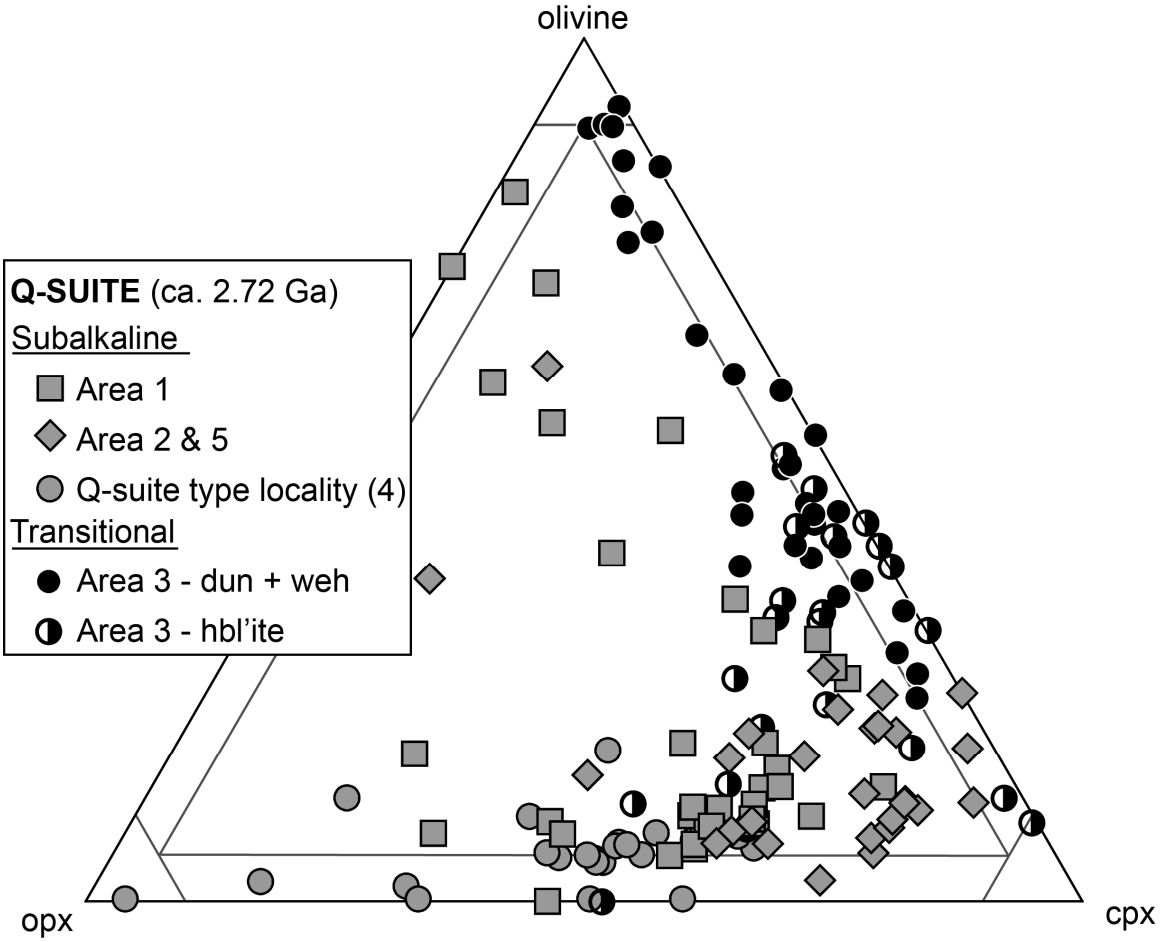

Figure 2-2: Normative olivine-diopside-hypersthene ternary diagram.
The diagram highlights the geochemically-distinct subalkaline, orthopyroxene-rich intrusions (grey symbols), and the transitional subalkaline-alkaline intrusions (black symbols) of the Q-suite. Only ultramafic lithologies (normative an+ab+or < 40 cat. %) are plotted. See Fig. 1 for area locations.

Terrane contain ubiquitous cumulate orthopyroxene and are strongly orthopyroxene-normative, whereas the Q-suite plutons from the Lac Couture region of the Rivière Arnaud Terrane lack cumulate orthopyroxene and plot along the Ol-Cpx join of the normative Ol-Opx-Cpx ternary diagram (Fig. 2-2). These two types of Q-suite intrusions are described separately, as their mineralogy indicates that they represent fundamentally different magma types.

3.1.1 Subalkaline Q-suite plutons

The orthopyroxene-rich Q-suite intrusions range from peridotite through websterite to gabbronorite. Although the CIPW normative compositions of peridotites and websterites show significant scatter, they all plot on the orthopyroxene side of the Ol-Cpx join in the Ol-Opx-Cpx ternary diagram (Fig. 2-2), indicating derivation from subalkaline magmas. The calculated normative mineralogies are in good overall agreement with the observed modal mineralogies, suggesting that the subalkaline Q-suite intrusions did not experience significant addition or removal of major elements following emplacement.

Peridotites are relatively rare, occurring as mesocumulate cores in zoned Q-suite bodies. The most magnesian (MgO $\geq$36 wt. % LOI-free) peridotites are harzburgites characterized by a complete absence of clinopyroxene and correspondingly low CaO concentrations (<2 wt. %). They are composed of centimetre-sized magnesio-hastingsite oikocrysts that enclose partially serpentinized olivine grains and macrocrysts of orthopyroxene with olivine inclusions (Fig. 2-3a). Euhedral to subhedral clinopyroxene is present in less magnesian peridotites and more evolved cumulate rocks of the subalkaline Q-suite intrusions. Clinopyroxene often contains cleavage-parallel exsolution of Cr-rich spinel and magnetite as well as irregular-shaped amphibole, all interpreted to be features

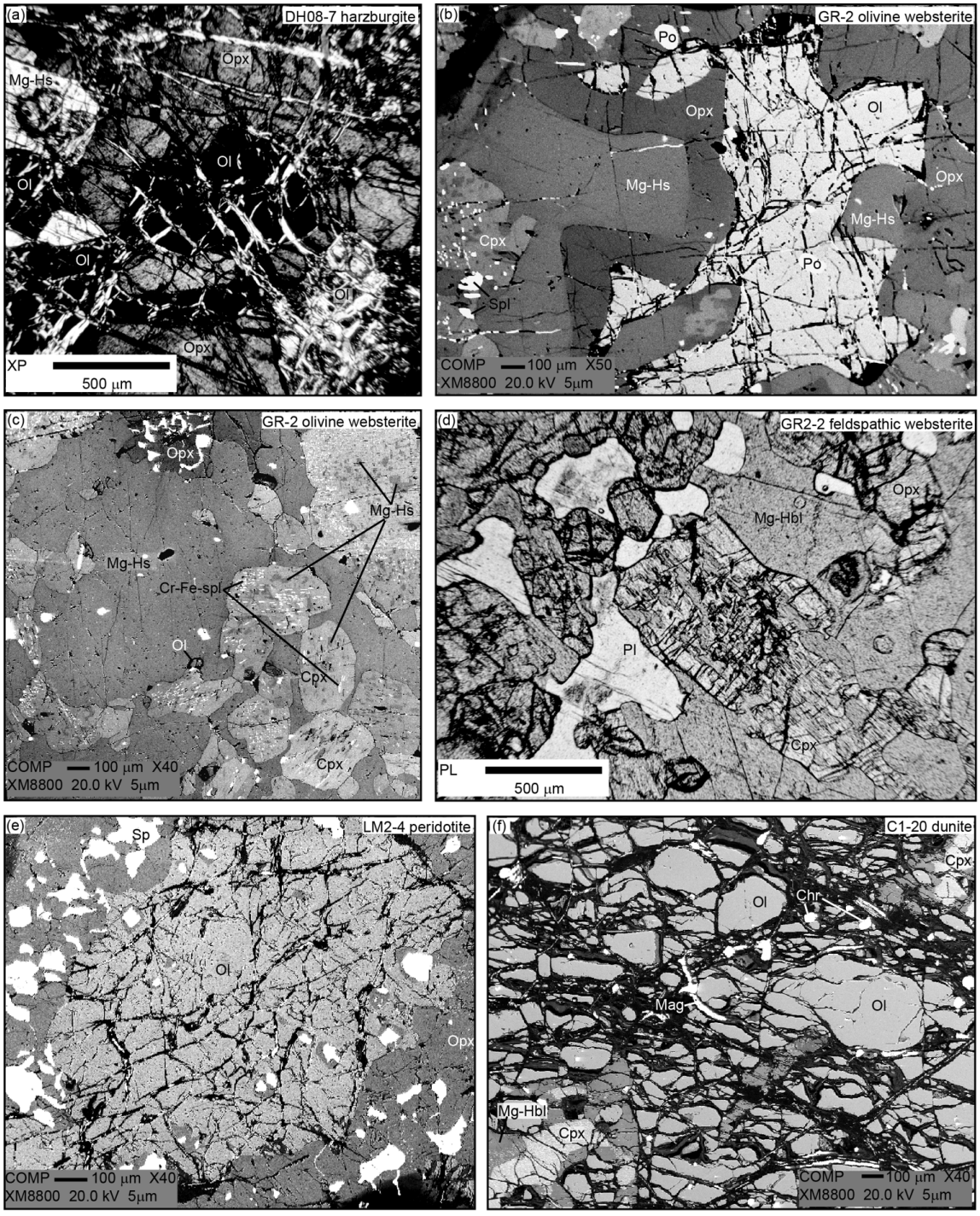
(a)
DH08-7 harzburgite
Opx
Mg-Hs
Ol
Ol
Ol
Ol
Opx
XP
500 μm
(b)
GR-2 olivine websterite
Po
Opx
Ol
Mg-Hs
Opx
Mg-Hs
Cpx
Po
Spl
COMP 100 μm X50
XM8800 20.0 kV 5μm
(c)
GR-2 olivine websterite
Opx
Mg-Hs
Mg-Hs
Cr-Fe-spl
Ol
Cpx
Cpx
COMP 100 μm X40
XM8800 20.0 kV 5μm
(d)
GR2-2 feldspathic websterite
Opx
Mg-Hbl
Pl
Cpx
PL
500 μm
(e)
LM2-4 peridotite
Sp
Ol
Opx
COMP 100 μm X40
XM8800 20.0 kV 5μm
(f)
C1-20 dunite
Cpx
Ol
Chr
Mag
Ol
Mg-Hbl
Cpx
COMP 100 μm X40
XM8800 20.0 kV 5μm

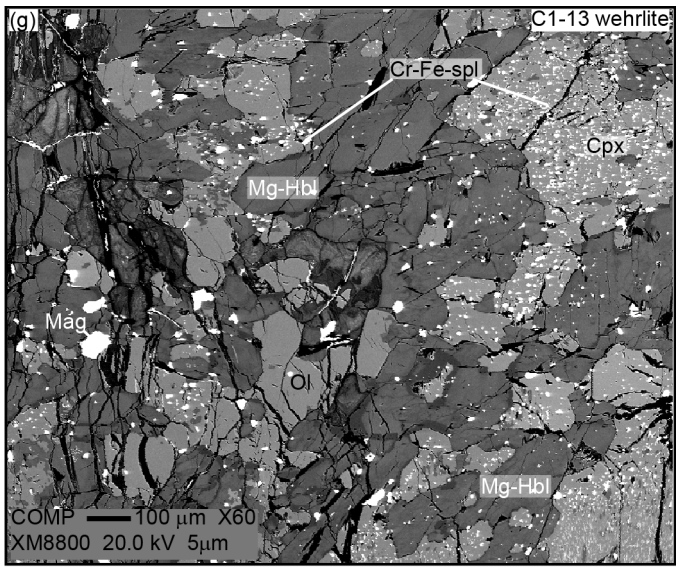

Figure 2-3: Representative petrographic images Q-suite ultramafic rocks.
Photomicrographs labeled a-e (Areas 1 and 2) are representative of the subalkaline intrusions. Images f and g are from the transitional subalkaline-alkaline intrusions of the Lac Couture region (Area 3). **(a)** Greyscale crossed-polars micrograph of harzburgite DH08-7 from the western Hudson Bay Terrane The figure shows a composite macrocryst of irregularly shaped, optically-continuous olivine (Ol; in extinction position) enclosed by orthopyroxene (Opx). The partially-serpentinized olivine grain in bottom right is also a part of the macrocryst. A part of an interstitial amphibole (Mg-Hs) crystal, showing pronounced cleavage is visible in the upper left corner of the image. **(b)** Back-scatter electron (BSE) image of olivine websterite GR-2 showing an irregularly shaped olivine, with embayed grain boundaries, armoured by orthopyroxene. Note the partial replacement of clinopyroxene (Cpx) by amphibole (dark patches) and exsolution of oxide (bright phase). Mg-Hs = magnesio-hastingsite, Po = pyrhottite. **(c)** BSE image of olivine websterite GR-2, showing the extensive exsolution of Cr-rich spinel (Cr, bright, acicular crystals) from clinopyroxene (light grey subhedral crystals). Sub-solidus growth of amphibole patches (medium grey) in the interior of clinopyroxene crystals is prominent. **(d)** Transmitted-light image of the feldspathic websterite GR2-2, showing the extensive sub-solidus replacement of clinopyroxene by magnesiohornblende (Mg-Hbl). Note the cuspate contacts between the interstitial plagioclase (Pl) and magnesiohornblende oikocrysts, interpreted to reflect the immiscible separation of the interstitial liquid according to magnesio-hastingsite (Na+Al-rich) = magnesiohornblende (Na+Al-poor) + plagioclase. **(e)** BSE image of an olivine from peridotite LM2-4. The olivine is mantled by orthopyroxene-spinel symplectite. Incipient orthopyroxene+spinel replacement of olivine is also evident in the interior of the grain. **(f)** BSE image of dunite C1-20 from the Lac Couture area, showing interstitial clinopyroxene (light grey) undergoing sub-microscopic exsolution of Fe-rich oxide (bright spots) and magnesiohornblende replacement (dark grey). **(g)** BSE image of wehrlite C1-13, showing clinopyroxene that has largely been replaced by magnesio-hornblende and undergone extensive exsolution of Cr-rich spinel

of subsolidus equilibration (Figs. 2-3b and 2-3c). Orthopyroxene is generally unaltered and only rarely shows thin lamellae of exsolved oxides or amphibole replacement.

The peridotites have high MgO (26-36 wt. %) and FeO^{TOT} (9.9-15.5 wt. %) contents (Table 2-1, Fig. 2-4a) that reflect their olivine-dominated primary mineralogy. The range in Al_2O_3 (2.3-4.6 wt. %), Ni (680-1680 ppm), and Cr (430-2260 ppm) reflects variable modal proportions of olivine, orthopyroxene and clinopyroxene versus interstitial amphibole. Low sulphur abundances (S <0.15 wt. %) and the absence of primary oxides indicate that the relatively low whole rock Mg-numbers ($Mg/(Mg+Fe^{TOT}$=0.75-0.82) do not reflect significant accumulation of Fe-rich sulphides or chromite. The subalkaline peridotites contain relict olivine cores (Table 2-2) that show a relatively small compositional variation (Fo_{80} – Fo_{82}; Ni = 1220-1550 ppm). The CaO contents of all analyzed olivines were below the detection limit (0.01 wt. %). In contrast to the majority of the Q-suite peridotites, a small (~50 m) body of fresh Ni-rich dunite, situated within a few meters of the Gladel River Q-suite intrusion (Milidragovic & Francis, 2014) and entirely enclosed by granite, contains highly magnesian olivine (Fo = 91.3 ± 0.02; Ni = 3420 ± 330 ppm).

Websterite is the predominant ultramafic lithology of the subalkaline Q-suite intrusions. When present, olivine is irregularly shaped and embayed, and typically armoured by orthopyroxene. The Ni abundances (600-2950 ppm) of these olivine grains commonly exceed those of olivines in the peridotites (Fig. 2-5). Orthopyroxene is relatively homogeneous within individual websterite samples and displays slightly elevated Mg-numbers relative to coexisting olivine, consistent with the olivine-orthopyroxene Fe-Mg partitioning experiments (Von Seckendorff & O'Neill, 1993).

Table 2-1: Representative geochemical analyses of the Q-suite intrusions

Sample	DH-08	DH08-7	DH08-9	DH-11	DH-03	PK09-17	LM2-4	LM2-10	LM3-5[2]	LM3-6	LM4-2	C1-16	C1-23
Area/zone[1]	1/18	1/18	1/18	1/18	1/18	1/18	2/18	2/18	2/18	2/18	2/18	3/18	3/18
Easting	359175	359177	359211	359143	359203	355746	434193	434116	439483	439573	439596	486034	486099
Northing	6460812	6460809	6460802	6460816	6460881	6469786	6492035	6492175	6490421	6490525	6497034	6674335	6674177
Lithology	harz.	harz.	perid.	web.	gabnor.	web.	perid.	gabnor.	web.	web.	perid.	dun.	dun.
Major elements (wt. %)													
SiO_2	39.24	38.38	41.27	51.58	56.86	48.56	47.00	47.66	49.61	49.55	42.42	37.87	36.39
TiO_2	0.09	0.1	0.17	0.23	0.22	0.27	0.21	0.81	0.35	0.29	0.16	0.08	0.09
Al_2O_3	2.53	2.78	2.90	4.80	11.56	3.39	3.72	18.89	4.79	4.71	4.33	0.92	0.84
MgO	32.60	32.82	28.51	18.66	9.03	22.27	25.60	6.25	17.68	17.58	27.11	37.68	34.87
FeO	13.48	13.42	13.34	9.96	6.80	10.34	15.21	9.87	9.50	9.44	13.29	14.5	15.99
MnO	0.16	0.17	0.20	0.18	0.12	0.19	0.23	0.12	0.20	0.2	0.21	0.28	0.27
CaO	1.09	1.64	3.52	9.67	8.29	12.91	5.09	10.20	16.38	16.22	4.97	2.19	2.02
Na_2O	0.18	0.25	0.37	1.07	2.86	0.47	0.33	2.74	0.53	0.54	0.47	0.1	0.04
K_2O	0.17	0.22	0.10	0.53	1.76	0.19	0.18	0.93	0.22	0.25	0.25	0.03	0.03
P_2O_5	0.03	0.03	0.03	0.11	0.03	0.04	0.04	0.27	0.03	0.03	0.05	0.02	0.02
LOI	9.15	8.76	8.04	1.87	1.76	0.69	1.45	1.52	0.25	0.34	5.38	4.67	7.67
Total	99.15	98.95	98.84	99.06	99.35	99.59	99.40	99.27	99.68	99.28	98.80	99.09	98.93
Trace elements (ppm)													
S	-	-	-	-	-	-	1475	-	-	-	-	440	<360
Th	0.73	0.76	0.90	2.88	0.80	0.62	0.21	0.80		0.96	0.90	-	<0.05
Nb	0.8	0.5	0.4	0.9	1.8	0.9	<0.3	5.1	0.6	0.8	0.7	<0.3	<0.2
Zr	11.1	16.0	9.9	37.1	39.6	24.1	11.7	60.0	22.8	23.8	18.6	<1	2
Y	1.4	2.2	3.8	6.0	13.7	6.5	4.5	16.4	9.8	8.9	4.1	<1.0	1
Cr	1626	1590	1670	1569	342.1	1435	1741	35.9	792.1	776.4	430.5	3908	3576
Ni	1572	1184	1164	1406	88	490	680	62	213	207	813	1460	1292
La	3.27	4.01	3.37	19.6	17.0	6.55	2.51	27.90	4.84	5.55	5.17	-	0.41
Ce	6.53	8.26	7.52	41.7	44.2	14.70	5.09	58.40	13.86	12.8	9.38	-	0.98
Pr	0.68	0.92	0.92	4.56	5.74	2.15	0.73	7.56	2.08	1.95	1.16	-	0.18
Nd	2.50	3.85	4.17	16.3	23.7	10.10	3.49	29.90	10.34	9.45	4.63	-	1.01
Sm	0.50	0.7	0.89	3.21	5.69	2.13	0.83	5.48	2.69	2.36	0.94	-	0.28
Eu	0.14	0.18	0.24	0.75	0.72	0.51	0.24	1.20	0.67	0.54	0.26	-	0.074
Gd	0.41	0.57	0.78	2.18	4.16	1.64	0.79	3.99	2.51	2.03	0.78	-	0.25
Tb	0.05	0.08	0.12	0.26	0.59	0.25	0.12	0.55	0.35	0.31	0.12	-	0.04
Dy	0.30	0.43	0.68	1.28	2.95	1.28	0.74	2.85	2.16	1.71	0.69	-	0.19
Ho	0.06	0.09	0.14	0.22	0.53	0.25	0.16	0.55	0.40	0.35	0.14	-	0.04
Er	0.18	0.24	0.38	0.61	1.40	0.69	0.50	1.73	1.13	1.01	0.45	-	0.12
Tm	0.027	0.041	0.051	0.087	0.19	0.099	0.080	0.26	0.17	0.15	0.070	-	0.017
Yb	0.19	0.25	0.37	0.54	1.17	0.62	0.55	1.58	1.05	0.91	0.45	-	0.11
Lu	0.033	0.024	0.038	0.081	0.18	0.11	0.091	0.26	0.15	0.14	0.076	-	0.020

Table 2-1: Representative analyses of the Q-suite intrusions (cont.)

Sample	C1-50	C1-48	C1-39[2]	D-22	D-24	D-16	C1-47	PT-9	UM03-08[2]
Area/zone[1]	3/18	3/18	3/18	3/18	3/18	3/18	3/18	1/18	5/18
Easting	486420	486252	486236	495060	494903	494548	486258	360083	468878
Northing	6674097	6674786	6673793	6699951	6700128	6698884	6674744	6470915	6446039
Lithology	dun.	weh.	weh.	bt. weh.	f. weh.	hblite.	gabbro	web.	web.
Major elements (wt. %)									
SiO_2	39.00	43.64	44.46	43.88	49.38	47.86	53.85	51.88	50.98
TiO_2	0.14	0.22	0.34	0.29	0.30	0.49	0.71	0.25	0.23
Al_2O_3	1.08	2.86	3.17	4.33	5.89	7.81	15.96	5.34	4.20
MgO	33.88	29.68	23.90	25.57	17.01	15.95	5.52	17.15	23.35
FeO	17.59	12.83	12.43	11.46	10.97	11.19	8.23	8.5	10.07
MnO	0.28	0.22	0.22	0.21	0.28	0.22	0.15	0.22	0.19
CaO	4.16	7.68	10.41	8.73	11.97	11.60	7.81	13.6	8.74
Na_2O	0.08	0.38	0.37	0.55	0.61	0.98	3.33	1.21	0.55
K_2O	0.02	0.15	0.14	0.56	0.25	1.23	2.40	0.38	0.40
P_2O_5	0.02	0.04	0.02	0.08	0.04	0.13	0.33	0.04	0.04
LOI	1.89	1.03	3.54	3.44	2.22	1.25	0.67	0.71	0.28
Total	98.75	99.19	99.18	99.31	99.13	98.85	98.99	99.49	99.50
Trace elements (ppm)									
S	<360	-	-	-				-	-
Th	0.08	0.25	0.13	1.10	0.38	2.11	3.07	1.47	1.57
Nb	<0.2	0.6	0.6	0.6	4.9	1.5	3.6	1.8	1.3
Zr	3	15.9	11.6	28.1	16.2	45.7	84.7	22.2	23.0
Y	2.1	5.5	7.2	7.5	8.6	12.3	16.2	16.1	6.1
Cr	3248	2477	957.5	996.5	1137	743.5	103	1226	2497
Ni	1055	723	308	580	328	214	32	284	805
La	0.48	3.31	1.99	7.55	4.05	16.70	29.10	11.7	4.74
Ce	1.73	8.69	8.11	16.30	11.80	37.50	60.40	30.5	11.61
Pr	0.32	1.44	1.53	2.43	1.98	4.39	7.28	4.07	1.53
Nd	1.75	7.30	8.86	11.70	10.00	19.80	30.80	18.1	6.87
Sm	0.57	1.750	2.54	2.60	2.60	4.32	6.09	4.48	1.53
Eu	0.15	0.44	0.61	0.66	0.74	1.10	1.56	0.69	0.35
Gd	0.5	1.45	2.17	2.08	2.28	3.50	4.51	3.86	1.34
Tb	0.08	0.20	0.28	0.28	0.32	0.48	0.58	0.61	0.21
Dy	0.39	1.01	1.62	1.39	1.62	2.48	2.93	3.22	1.22
Ho	0.07	0.20	0.33	0.27	0.31	0.48	0.56	0.64	0.23
Er	0.2	0.58	0.87	0.78	0.93	1.38	1.71	1.7	0.71
Tm	0.029	0.086	0.10	0.12	0.14	0.20	0.26	0.25	0.11
Yb	0.19	0.55	0.70	0.75	0.87	1.26	1.56	1.53	0.71
Lu	0.029	0.082	0.10	0.12	0.14	0.21	0.26	0.19	0.11

Representative whole rock major and trace element geochemical data from four study areas (complete data set is presented in the appendix table A1). The concentrations of major elements, Ba, Co, Cr, Ni, and V were determined by X-ray fluorescence (XRF) on fused 32 mm-diameter lithium borate beads at McGill University Geochemical Laboratories, using a Philips PW2440 4kW automated spectrometer system. The reported Ga, Nb, Pb, Sc, Rb, Sr, Y, and Zr were analyzed by XRF on 40 mm-diameter pressed powder pellets. An exception was made for the peridotite samples whose trace element abundances approach the detection limits of the XRF technique – the reported Nb, Zr, and Y concentrations in these samples were measured by inductively coupled - plasma mass spectrometry (ICP-MS). Uncertainty in SiO_2 (wt. %) measurements, based on four duplicate analyses of four samples is better than 0.6 % absolute. The uncertainty in major element determinations at a 95 % confidence interval is ~6 % relative when the concentration exceeds the element's quantification limit (defined as 3.3 x detection limit). The relative errors associated with the XRF-determined trace element concentrations are < 10 % for Cr, Ni, and 10-20% for the incompatible elements.

Table 2-2: Average olivine analyses from representative Q-suite intrusions

Sample:	GR-2	DH08-7	DH08-6	DH-07	DH-09	PK09-17	LM2-4	LM3-2	LM-3-3	LM3-5	C1-15
n	8	3	2	10	12	18	21	17	9	7	7
Area	1	1	1	1	1	1	2	2	2	2	3
Rock	web.	harz.	perid.	perid.	perid.	web.	web.	web.	web.	web.	dun.
WR Mg-	0.78	0.81	0.81	0.82	0.81	0.79	0.75	0.83	0.83	0.77	0.75
SiO_2	38.9 ± 0.3	39.2 ± 0.1	39.1 ± 0.0	39.4 ± 0.7	39.7 ± 0.4	38.8 ± 0.4	39.3 ± 0.4	38.9 ± 0.4	38.7 ± 0.5	38.5± 0.2	38.8 ± 0.1
TiO_2	<0.04.	<0.04	<0.04	<0.03	<0.03	<0.04	<0.04	<0.04	<0.04	<0.04	<0.04
Al_2O_3	<0.02	<0.02	<0.04	<0.02	<0.02	<0.04	<0.04	<0.04	<0.04	<0.04	<0.04
MgO	40.8 ± 0.4	44.1 ± 0.3	42.1 ± 0.5	43.0 ± 0.4	43.0 ± 0.3	40.2 ± 0.5	42.2 ± 0.8	40.5 ± 0.4	39.4 ± 0.5	38.1 ± 0.3	40.6 ± 0.6
FeO	20.5 ± 0.7	16.8 ± 0.7	18.9 ± 0.0	17.5 ± 0.3	17.1 ± 0.4	20.7 ± 0.8	18.2 ± 1.1	20.2 ± 0.7	21.2 ± 0.8	23.1 ± 0.7	20.8 ± 0.6
MnO	0.32 ± 0.04	0.23 ± 0.02	0.30 ± 0.03	0.28 ± 0.03	0.29 ± 0.03	0.29 ± 0.02	0.29 ± 0.04	0.33 ± 0.02	0.35 ± 0.01	0.36 ± 0.02	0.35 ± 0.03
CaO	<0.02	<0.02	0.01 ± 0.00	<0.01	<0.01	<0.01	<0.01	<0.01	<0.01	<0.01	<0.01
Na_2O	<0.02	<0.02	-	<0.04	<0.04	-	-	-	-	-	-
NiO	0.13 ± 0.02	0.19 ± 0.03	0.20 ± 0.01	0.16 ± 0.02	0.16 ± 0.02	0.10 ± 0.01	0.16 ± 0.01	0.15 ± 0.01	0.19 ± 0.01	0.06 ± 0.01	0.08 ± 0.01
Cr_2O_3	<0.05	<0.05	<0.07	<0.05	<0.05	<0.06	<0.06	<0.07	<0.07	<0.07	<0.07
P_2O_5	0.02 ± 0.01	0.01 ± 0.00	-	-	-	-	-	-	-	-	-
Total	100.7 ± 0.6	100.6 ± 0.5	100.6 ± 0.6	100.4 ± 0.8	100.3 ± 0.5	100.9 ± 1.0	100.1 ± 0.8	100.0 ± 0.9	99.9 ± 1.3	100.2 ± 0.9	100.6 ± 0.5
Fo	78.0 ± 0.6	82.4 ± 0.7	79.9 ± 0.2	81.4 ± 0.3	81.7 ± 0.4	77.6 ± 0.8	80.5 ± 1.2	78.2 ± 0.7	77.1 ± 0.4	74.6± 0.6	77.7 ± 0.7
Ni (ppm)	1036 ± 169	1454± 204	1536 ± 100	1256 ± 152	1223 ± 183	795 ± 83	1258 ± 68	1193 ± 50	1500 ± 118	509 ± 78	636 ± 74
Mg# liq	0.52	0.58	0.54	0.57	0.57	0.51	0.56	0.52	0.50	0.47	0.51

Sample:	C1-16	C1-18	C1-20	C1-23	C1-44	C1-50	C1-05	C1-39	D-22	UM03-08
n	7	5	6	6	5	5	7	8	6	7
Area	3	3	3	3	3	3	3	8	3	5
Rock	dun.	dun.	dun.	dun.	dun.	dun.	weh.	weh.	bt. weh.	web.
WR Mg#	0.82	0.81	0.81	0.80	0.77	0.77	0.78	0.77	0.80	0.81
SiO_2	39.6 ± 0.3	39.4 ± 0.3	39.5 ± 0.4	39.5 ± 0.3	38.9± 0.2	38.9 ± 0.3	38.4 ± 0.5	38.1 ± 0.2	38.5 ± 0.2	38.8 ± 0.3
TiO_2	<0.04.	<0.04	<0.04	<0.04	<0.04	<0.04	<0.04	<0.04	<0.04	<0.04
Al_2O_3	<0.04	<0.04	<0.04	<0.04	<0.04	<0.04	<0.04	<0.05	<0.05	<0.02
MgO	44.5 ± 0.3	44.0 ± 0.2	44.7 ± 0.4	43.2 ± 0.2	41.2 ± 0.4	41.2± 0.6	39.5 ± 1.8	38.0 ± 0.9	39.4 ± 1.1	41.4 ± 0.5
FeO	15.7± 0.3	16.2 ± 0.3	15.4 ± 0.2	17.2 ± 0.2	20.2 ± 0.3	20.0 ± 0.3	21.9 ± 2.1	24.0 ± 0.6	22.2 ± 1.2	19.9 ± 0.5
MnO	0.31 ± 0.02	0.31 ± 0.02	0.28 ± 0.02	0.29 ± 0.01	0.38 ± 0.02	0.33 ± 0.01	-	-	0.37 ± 0.04	0.25 ± 0.02
CaO	<0.01.	<0.01	0.01 ± 0.00	<0.01	<0.01	<0.01	<0.01	<0.01	<0.01	<0.01
Na_2O	-.	-	-	-	-	-	-	-	-	<0.03-
NiO	0.20 ± 0.01	0.15 ± 0.02	0.20 ± 0.02	0.18 ± 0.01	0.07 ± 0.01	0.14 ± 0.01	0.08 ± 0.02	0.07 ± 0.01	0.13 ± 0.06	0.38 ± 0.03
Cr_2O_3	<0.06.	<0.06	<0.06	<0.06	<0.07	<0.07	<0.07	<0.07	<0.06	<0.05
P_2O_5	-	-	-	-	-	-	-	-	-	-
Total	100.3 ± 0.7	100.1 ± 0.4	100.2 ± 0.8	100.4 ± 0.5	100.8 ± 0.3	100.5 ± 0.6	100.3 ± 0.3	100.6 ± 0.7	100.7 ± 0.4	100.7 ± 0.2
Fo	83.5 ± 0.2	82.9 ± 0.3	83.8 ± 0.2	81.7 ± 0.2	78.4 ± 0.4	78.6 ± 0.5	76.3 ± 2.6	73.9 ± 0.9	76.0 ± 1.5	78.8 ± 0.6
Ni (ppm)	1560 ± 77	1216± 150	1536 ± 154	1256 ± 152	578 ± 53	1124 ± 56	605 ± 125	523 ± 81	990 ± 526	2951 ± 262
Mg# liq	0.60	0.59	0.61	0.57	0.52	0.52	0.49	0.46	0.49	0.53

Olivine compositions were analyzed on a JEOL 8900 instrument at the McGill Electron Microprobe Microanalytical Facility under identical analytical conditions (20.0 kV accelerating voltage, 2.5 nA beam current, 5 μm beam diameter). Errors on individual oxides are ≤ 1% relative (2 s.d.)

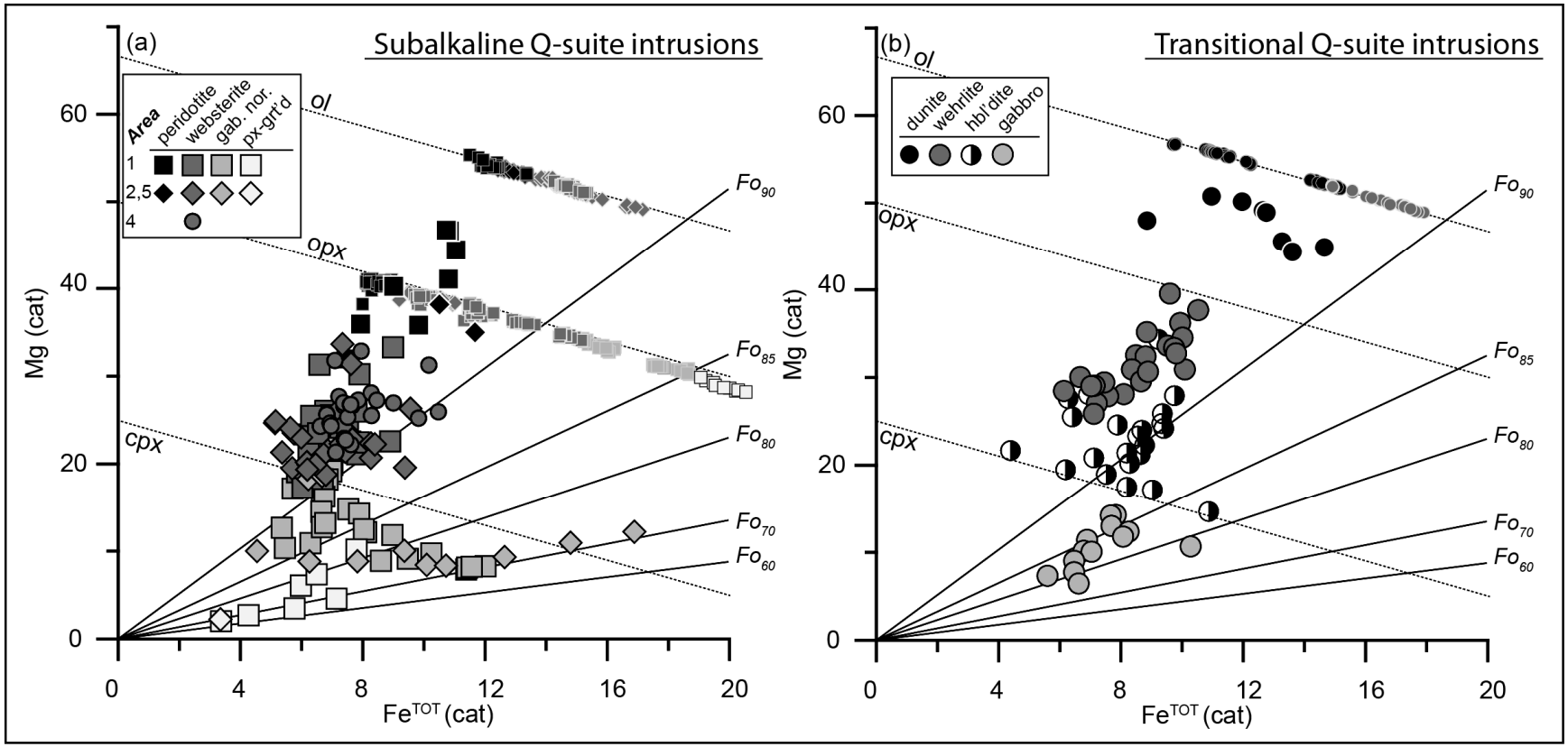

Figure 2-4: Mg vs. Fe^{TOT} cation plots of the Q-suite intrusions.
Lines radiating for the origin are isopleths for the Fo content of olivine coexisting with liquids whose Fe and Mg contents are specified by graph coordinates, adjusted to $Fe^{3+}/Fe^{TOT} = 0.05$. **(a)** Subalkaline Q-suite intrusions. **(b)** Transitional Q-suite intrusions. Analyses of olivine ± orthopyroxene, along with the lines of stoichiometric mineral compositions are also shown. Symbol shapes as in Fig. 2. Q-suite samples are colour-coded according to lithology.

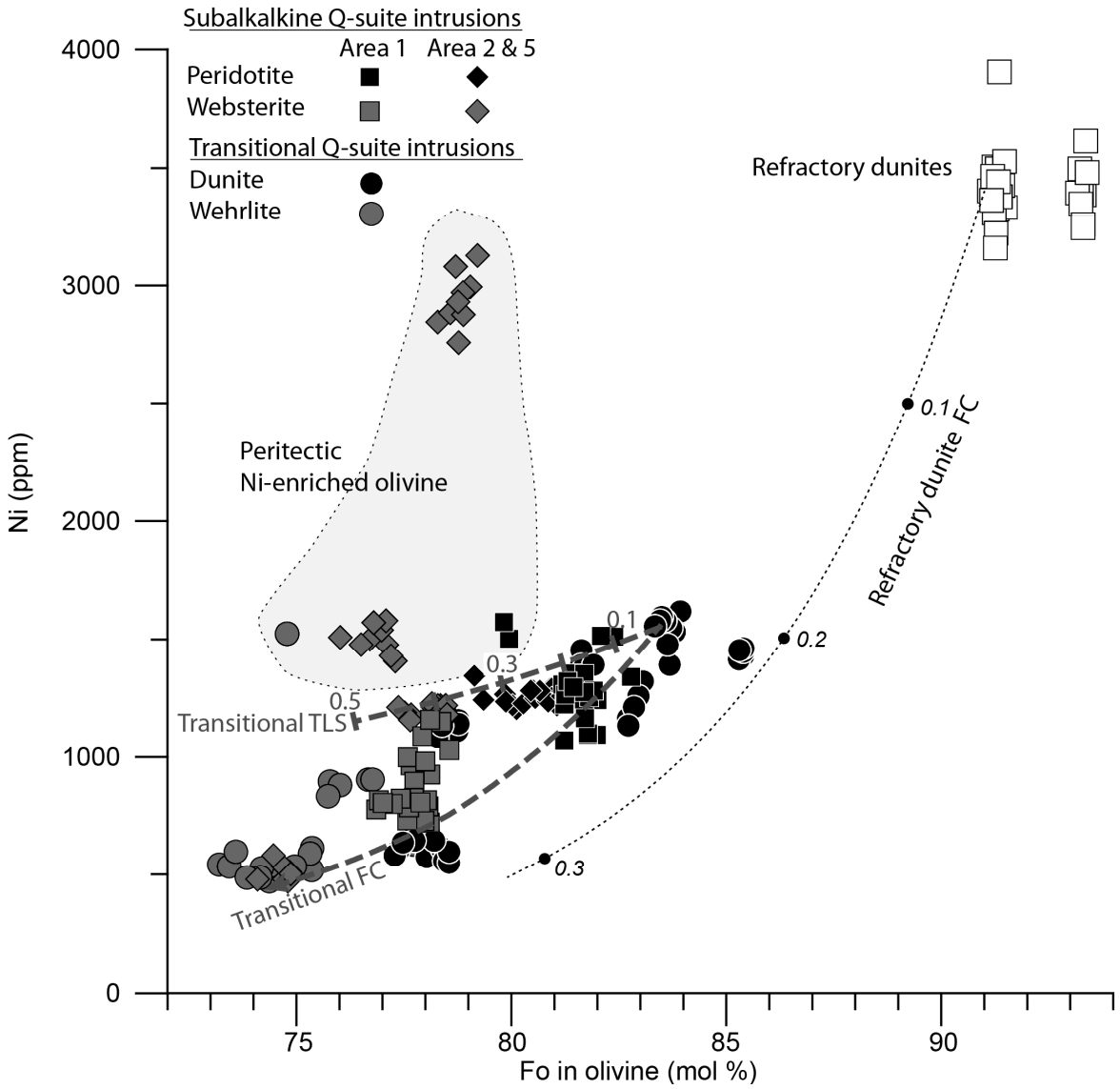

Figure 2-5: Ni (ppm) vs. Fo in olivine (mol %) plot of the Q-suite olivines.
Olivine grains, anomalously enriched in Ni, are shown in the shaded field, and may reflect post-crystallization Ni redistribution and gain, due to the peritectic reduction in olivine volume. Also shown are olivine compositions of the highly refractory dunite samples found in Area 1. The origin of the samples is uncertain, but fractional crystallization modelling suggests that they are not cumulates derived from more primitive Q-suite magmas. Thick grey lines: Evolution of olivine predicted by fractional crystallization (FC) modelling of the transitional parental liquid and the effect of trapped liquid shift on initial olivine ($Fo_{0.84}$, Ni = 1550 ppm) for trapped liquid fractions of 0.1-0.5.

In contrast, clinopyroxene within individual websterite samples has variable compositions with high Mg-numbers that are out of equilibrium with the coexisting olivine and orthopyroxene (Putirka, 2008). Magnesiohornblende, sometimes accompanied by biotite, is a volumetrically important phase in the websterite, occurring as large oikocrysts and forming irregular-shaped grains within clinopyroxene crystals (Fig. 2-3d). Accessory plagioclase is sometimes present as an interstitial phase in the websterite and is characterized by cuspate boundaries in contact with interstitial amphibole.

Hornblende-rich gabbroic rocks are found in all Q-suite intrusions. Hornblende replaces euhedral clinopyroxene grains and forms large oikocrysts that enclose both pyroxene and plagioclase. In some samples, nearly all of the pyroxene is consumed at the expense of amphibole, and plagioclase has been strongly altered. The most magnesian gabbronorites contain substantial orthopyroxene (≤32 normative wt. %), whose abundance decreases with increasing FeO^{TOT} and TiO_2. The evolved gabbronorites typically contain significant amounts of modal magnetite + ilmenite (≥3 wt %; calculated assuming $Fe_2O_3 = TiO_2 + 1.5$, c.f. Irvine & Baragar (1971)) and apatite (0.5-1 wt %). Magnetite-rich gabbroic rocks with (FeO^{TOT}+TiO_2) >13 wt. % are nepheline-normative (≤10 wt. %). The rare interstitial quartz grains indicate, however, that the "alkaline" normative composition of the magnetite-rich gabbros is a result of oxide accumulation which lowers the Si/O ratio relative to that of the parental magma.

Trace element spidergrams in which the subalkaline Q-suite samples are normalized to Mid-Ocean Ridge Basalt (MORB; Fig. 2-6a) are characterized by relatively unfractionated heavy REE (HREE), moderately to strongly fractionated LREE/ middle

REE (MREE), and strong relative depletions in the HFSE, all features characteristic of Phanerozoic "calc-alkaline" magmatic arcs (Pearce & Peate, 1995). The orthopyroxene-rich peridotites have the lowest trace element abundances, which increase with the modal abundance of clinopyroxene and interstitial component. The Q-suite websterites contain higher absolute trace element abundances than the peridotites and are slightly more LREE-enriched, but display similar relative depletions in HFSE. The gabbronorites contain the highest absolute trace-element abundances and have similar LREE/MREE ratios to those of websterites, but no systematic Eu-anomalies.

The subalkaline Q-suite intrusions of the Ungava craton exhibit the crystallization sequence: olivine, orthopyroxene, clinopyroxene, amphibole, plagioclase, ulvospinel, and apatite. The magma parental to the earliest-crystallized Q-suite cumulates was saturated in olivine, spinel and orthopyroxene. The composition of olivine in the most primitive harzburgite cumulates suggests that the parental magma had a lower Mg-number ($\geq$0.59) than most modern-day mantle-derived magmas. Except in a few websteritic samples affected by significant peritectic replacement of olivine by orthopyroxene, Ni concentrations in olivine are positively correlated with Fo (Fig. 2-5) and define a trend that is consistent with the combined effects of fractional crystallization of olivine and trapped liquid shift (Barnes, 1986). Fractional crystallization from MgO-rich magma cannot, however, explain the large difference in the Mg-number (8 mol %) and Ni contents (~2000 ppm) between the olivine of the most primitive Q-suite harzburgite and the olivine of the Ni-rich dunite found near the Gladel River intrusion (Fig. 2-5). Consequently, the dunite body appears to be a xenolith, genetically unrelated to the subalkaline Q-suite plutons.

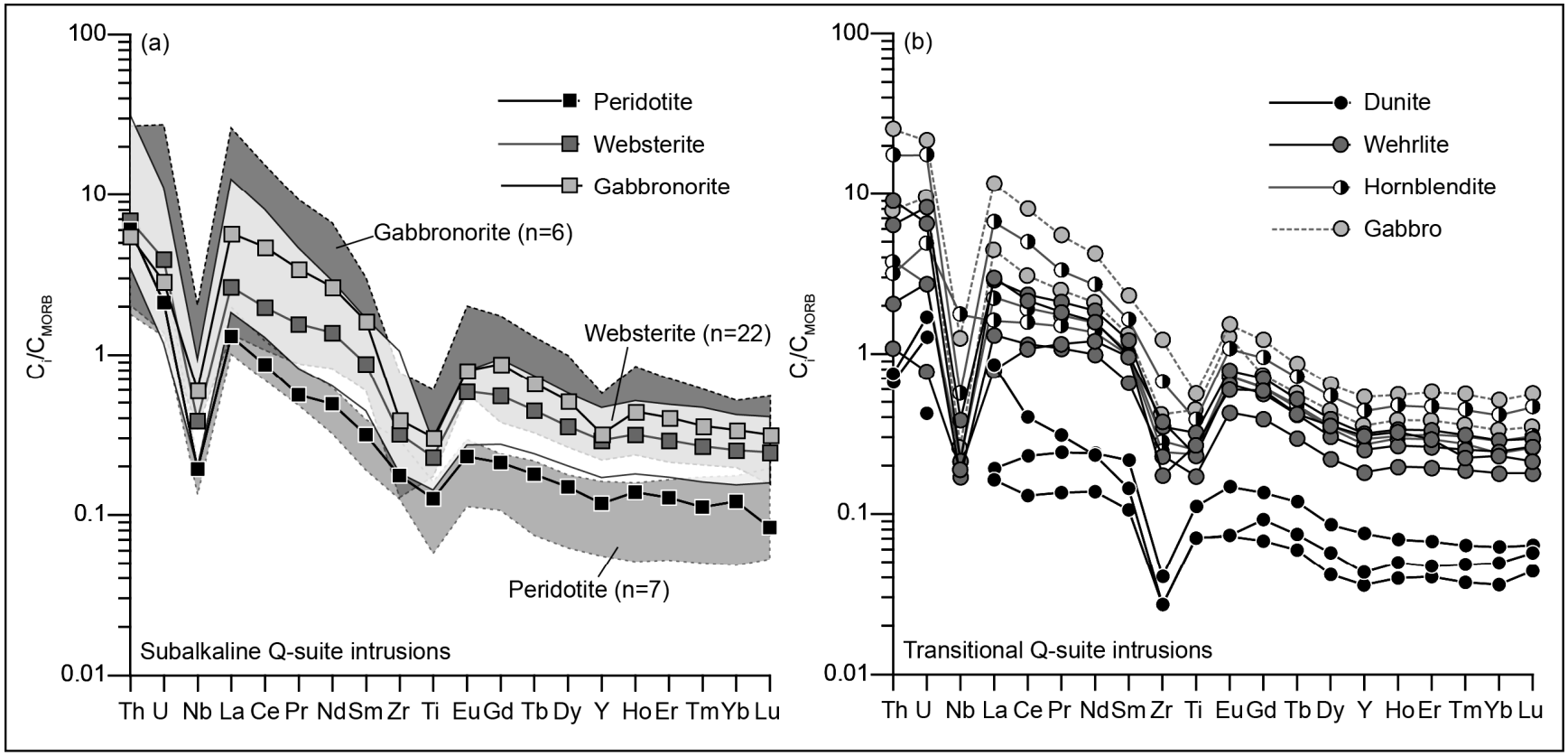

Figure 2-6: Q-suite trace element spidergrams.
MORB-normalized (Sun & McDonough, 1989) trace element spidergrams of the subalkaline **(a)** and transitional **(b)** Q-suite intrusions. For visual clarity only the calculated medians (lines) and the 95 percentile confidence intervals (shaded fields) are shown for the three main subalkaline lithologies in (a).

3.1.2 Transitional Q-suite plutons

In contrast to the orthopyroxene-rich ultramafic intrusives of the Hudson Bay Terrane and the southern Rivière Arnaud Terrane, the ultramafic rocks from the Lac Couture region (Fig. 2-1) of the north-central Rivière Arnaud Terrane contain no cumulus orthopyroxene and are only slightly (< 10 wt. %) hypersthene-normative, straddling the Ol-Cpx join of the Ol-Cpx-OPx normative diagram (Fig. 2-2). The margins of the Q-suite intrusives in this region are brecciated by leucocratic veins and dykes in a fashion similar to that observed in subalkaline plutons located elsewhere in the Ungava craton. In contrast to the latter, however, the transitional Q-suite plutons in the north-central Rivière Arnaud Terrane have experienced late, ductile deformation following the brecciation, which has disaggregated and transposed the breccia veins and created structurally complex, inhomogeneous domains that form the dominant lithology of the intrusions. Furthermore, the primary igneous mineralogy of the domains that have experienced ductile deformation is commonly obliterated, resulting in lithologies dominated by amphibole and variable amounts of feldspar.

The most magnesian cumulate rocks in the Lac Couture region are weakly to moderately serpentinized dunite mesocumulates composed of olivine, chromite, and interstitial clinopyroxene (Fig. 2-3f). The olivine is variably serpentinized and displays a large range in forsterite (Fo_{78} – Fo_{84}) and Ni contents (600 – 1600 ppm), but no detectable CaO (<0.01 wt. %). Interstitial clinopyroxene has been extensively to completely replaced by compositionally heterogeneous magnesiohornblende (Leake *et al.*, 1997). The dunites have high MgO (34-40 wt. %), FeO^{TOT} (12.4 - 20.0 wt. %), Ni (510-1560 ppm), and Cr (470-3910 ppm) contents, and low concentrations of Al_2O_3 (<1.5 wt. %)

and CaO (<5 wt. %), consistent with the relatively low abundances of interstitial minerals. The most primitive dunites of the transitional Q-suite are richer in MgO, CaO and Cr, have comparable FeO^{TOT} and Ni abundances, and are Al_2O_3-poor relative to the most magnesian subalkaline Q-suite harzburgites. The low sulphur contents (<0.05 wt. %) indicate that sulphide accumulation does not significantly contribute to the relatively high FeO^{TOT} concentrations and low whole-rock Mg-numbers (0.75-0.84) of the dunites. The dunites define a linear (Mg+Fe)/Ti vs. Si/Ti array, with a slope of 1.97 (R^2 =0.999), indicating that this compositional variation can be accounted for by olivine accumulation and that the dunites represent closed chemical systems (Russell & Nicholls, 1988). One pervasively-serpentinized dunite sample (C1-14) is anomalously FeO-poor (12.4 wt. %; Mg-number =0.84; Fo ~85) and plots below the (Mg+Fe)/Ti vs. Si/Ti array defined by the other dunites. The sample contains veins of magnetite that are both relatively wide (>0.2 mm) and continuous, suggesting local remobilization of Fe.

The wehrlites of the transitional plutons range from mesocumulates to orthocumulates and are substantially more altered than the associated dunites. The occurrence of orthopyroxene is limited to rare rims around olivine cores. The clinopyroxene of the wehrlites contains inclusions of Cr-rich spinel and is pervasively replaced by amphibole. The analyzed compositions of clinopyroxene are highly inhomogeneous and strongly depleted in Fe (($Mg/(Mg+Fe^{TOT})$= 0.86-0.92) relative to the coexisting olivine (Fo_{74}-Fo_{76}). The normative proportions of clinopyroxene and olivine in the wehrlites vary substantially (cpx:ol ~0.7-3.5), and these rocks define a linear array in Mg vs. Fe space (Fig. 2-4b). The wehrlitic samples that contain interstitial biotite crystals are characterized by higher contents of Al_2O_3 and K_2O.

A substantial proportion of rocks in the transitional Q-suite intrusions are largely composed of amphibole with interstitial feldspar. These hornblendites lack igneous textures and are interpreted to be metamorphic equivalents of the Q-suite wehrlites based on their close spatial association and indistinguishable trace element profiles. The hypersthene-normative hornblendites display a negative correlation between normative hypersthene contents and (Na+K)/Al ratios, suggesting that these anomalous samples may have experienced alkali losses.

Compared to the subalkaline Q-suite plutons, the transitional plutons contain a relatively minor gabbroic component. The gabbros of the transitional Q-suite plutons contain enclaves of wehrlite, suggesting relatively late emplacement. The gabbros have been metamorphosed to an assemblage composed entirely of plagioclase and hornblende, with minor biotite, titanite, and oxides. These rocks have distinct metamorphic textures characterized by polygonal grain boundaries and a pronounced mineral lineation defined by aggregates of hornblende porphyroblasts.

The overall trace element abundances of the transitional Q-suite cumulate rocks are low and comparable to the abundances of the subalkaline Q-suite intrusions (Fig. 2-6). The MORB-normalized trace element patterns of the transitional Q-suite are characterized by pronounced depletions in HFSE, including negative Zr-Hf anomalies, relatively unfractionated HREE, and mild enrichments in LREE relative to MREE. In contrast to the wehrlites and gabbros, which show similar depletions in Ti (Ti/Ti* = 0.3-0.45; Ti/Ti* = $Ti_{MORB}/(Sm_{MORB} \times Eu_{MORB})^{1/2}$) to the subalkaline Q-suite plutons, the dunites of the transitional Q-suite intrusions have smaller Ti depletions (Ti/Ti* =0.6-0.8). With the exception of Ti, however, the degree HFSE depletion is independent of the rock

type. Although some variation exists among different lithologies, there is a general increase in the LREE/MREE ratios from dunites to wehrlites to gabbros (Fig. 2-6). Some of the most magnesian dunites and wehrlites display relatively flat to convex upward LREE profiles (La/Sm_{MORB} = 0.8-2.0).

The transitional Q-suite intrusions of the north-central Ungava craton exhibit the crystallization sequence: olivine ± Cr-spinel, clinopyroxene, plagioclase, and ulvospinel. The extensive metamorphic overprinting of the transitional gabbros makes it difficult to assess whether the amphibole is magmatic. The whole rock (Mg-number ≤0.82) and analyzed olivine compositions (Fo ≤84) of the dunites suggest that they accumulated from a unusually Fe-rich picritic parental magma with an initial Mg-number of ~0.61 that was saturated only in olivine and Cr-rich spinel.

3.2 Isotope systematics of the Q-suite intrusions

The Q-suite intrusions were analyzed for Nd and Hf isotopes with the goals of gaining insight into the mantle source of their parental magmas and assessing the role of crustal contamination in their trace element chemistry (Tables 2-3 and 2-4). Neodymium isotopic ratios calculated at the time of emplacement of the Q-suite (~2.72 Ga) show a large scatter (Figs. 2-7a and 2-7b), with the majority of samples having initial $^{143}Nd/^{144}Nd$ ratios close to the bulk earth (i.e. Chondritic Uniform Reservoir (CHUR)). Initial $^{176}Hf/^{177}Hf$ ratios display a comparable scatter, ranging from near- Depleted Mantle (DM) values to significantly sub-chondritic values (Figs. 2-7c and 2-7d). There are no systematic differences between the calculated initial $^{143}Nd/^{144}Nd$ and $^{176}Hf/^{177}Hf$ ratios of the subalkaline and transitional Q-suite intrusions. There is, however a geographical dependence in the calculated initial $^{143}Nd/^{144}Nd$ ratios. Q-suite intrusions from the

Table 2-3: Nd isotopic determinations from Q-suite intrusions and surrounding granitoids

Sample	Lithology	Nd	Sm	Sm/Nd[c]	$^{143}Nd/^{144}Nd$	$^{147}Sm/^{144}Nd$[d]	$^{143}Nd/^{144}Nd$ (T)[e]	εNd (T)[f]	$f^{Sm/Nd}$ [g]	T_{CR}[h]
Hudson Bay Terrane										
GR-2[a]	ol. websterite	10.1	2.39	0.237 ± 8	0.511482 ± 7	0.1433 ± 49	0.508911 ± 95	-3.90 ± 1.87	-0.27	N/A
GR2-4[b]	mt. gabbronorite	8.73	2.07	0.237 ± 8	0.511504 ± 10	0.1433 ± 51	0.508932 ± 101	-3.48 ± 1.98	-0.27	N/A
GR2-8[a]	hybrid	20.84	4.13	0.198 ± 4	0.511148 ± 6	0.1198 ± 23	0.508997 ± 47	-2.20 ± 0.92	-0.39	3.25
GR2-9[a]	hybrid	22.31	3.98	0.179 ± 3	0.510956 ± 7	0.1079 ± 20	0.509020 ± 44	-1.76 ± 0.86	-0.45	3.16
GR2-10[a]	hybrid	24.14	4.07	0.169 ± 3	0.510850 ± 7	0.1019 ± 19	0.509022 ± 42	-1.71 ± 0.82	-0.48	3.13
GR2-11[a]	granite	17.38	2.31	0.133 ± 3	0.510301 ± 7	0.0803 ± 15	0.508859 ± 34	-4.93 ± 0.67	-0.59	3.25
GR2-11 rep.					*0.510306 ± 8*					
DH-02[b]	granite	13.5	2.50	0.185 ± 8	0.510577 ± 8	0.1119 ± 47	0.508569 ± 94	-10.62 ± 1.84	-0.43	3.84
DH-03[b]	gabbronorite	23.7	5.69	0.240 ± 8	0.511195 ± 7	0.1451 ± 51	0.508591 ± 98	-10.18 ± 1.93	-0.26	N/A
DH-10[b]	ol. websterite	4.69	1.26	0.269 ± 9	0.511676 ± 8	0.1624 ± 53	0.508761 ± 102	-6.84 ± 2.01	-0.17	N/A
DH-13[b]	f. websterite	15.3	3.08	0.201 ± 8	0.510927 ± 8	0.1217 ± 48	0.508743 ± 94	-7.20 ± 1.86	-0.38	3.67
DH08-7[b]	harzburgite	3.85	0.70	0.182 ± 8	0.511034 ± 10	0.1099 ± 47	0.509062 ± 95	-0.94 ± 1.87	-0.44	3.10
LM2-4[b]	peridotite	3.49	0.83	0.238 ± 8	0.511732 ± 6	0.1437 ± 51	0.509153 ± 97	0.85 ± 1.90	-0.27	N/A
LM3-5[a]	ol. websterite	10.34	2.69	0.260 ± 9	0.511839 ± 5	0.1572 ± 54	0.509017 ±102	-1.82 ± 2.01	-0.20	N/A
LM2-7[b]	granite	18.7	2.46	0.132 ± 7	0.510496 ± 7	0.0795 ± 44	0.509069 ± 87	-0.79 ± 1.70	-0.60	3.01
LM2-8[b]	hybrid	66.5	11.2	0.168 ± 8	0.510940 ± 6	0.1018 ± 46	0.509114 ± 89	0.08 ± 1.75	-0.48	3.01
LM2-8 rep.[b]					*0.510942 ± 6*					
LM2-10[b]	mt. gabbronorite	29.9	5.48	0.183 ± 8	0.511076 ± 6	0.1108 ± 47	0.509088 ± 91	-0.42 ± 1.79	-0.44	3.07
LM2-10 dup.[b]					*0.511081 ± 7*					
LM4-7[b]	pegmatite	38.8	6.41	0.165 ± 8	0.511188 ± 5	0.0998 ± 46	0.509396 ± 88	5.62 ± 1.74	-0.49	2.63
UM03-2008[a]	ol. websterite	6.87	1.53	0.223 ± 8	0.511615 ± 7	0.1348 ± 47	0.509196 ± 91	1.70 ± 1.78	-0.31	2.97
Riviere Arnaud Terrane - Lac Couture										
C1-20[b]	dunite	1.70	0.38	0.224 ± 8	0.512281 ± 6	0.1351 ± 50	0.509856 ± 95	14.67 ± 1.87	-0.31	1.71
C1-39[a]	wehrlite	8.86	2.54	0.287 ± 10	0.512244 ± 7	0.1735 ± 60	0.509129 ± 114	0.39 ± 2.24	-0.12	N/A
C1-39 dup.[a]					*0.512237 ± 7*					
D-22[b]	bt. wehrlite	11.7	2.60	0.222 ± 8	0.511584 ± 7	0.1343 ± 50	0.509174 ± 97	1.26 ± 1.90	-0.32	3.01
C1-47[b]	gabbro	30.8	6.10	0.198 ± 8	0.511256 ±6	0.1195 ± 48	0.509112 ± 93	0.04 ± 1.82	-0.39	3.06
C1-51[a]	tonalite	21.66	4.14	0.191 ± 4	0.511206 ± 8	0.1155 ± 22	0.509132 ± 47	0.45 ± 0.93	-0.41	3.02
C1-51 dup.[a]					*0.511195 ± 8*					
Riviere Arnaud Terrane - Lac Faribault										
1.13	harzburgite	14.26	3.12	0.219 ± 8	0.511498 ± 8	0.1324 ± 46	0.509120 ± 90	0.22 ± 1.77	-0.33	3.10
LF-9[a]	px-diorite	30.43	5.90	0.194 ± 4	0.511130 ± 6	0.1172 ± 22	0.509026 ± 46	-1.64 ± 0.90	-0.40	3.19
LF-9 rep.[a]					*0.511133 ± 6*					
LF-18[a]	granodiorite	4.98	0.57	0.115 ± 2	0.510257 ± 8	0.0697 ± 13	0.509006 ± 31	-2.03 ± 0.62	-0.65	3.06
LF-24[a]	f. websterite	17.71	3.67	0.207 ± 7	0.511196 ± 8	0.1252 ± 43	0.508948 ± 85	-3.17 ± 1.67	-0.36	3.36
LF-17[b]	gabbro	18.0	3.12	0.173 ± 8	0.510964 ± 6	0.1047 ± 47	0.509084 ± 90	-0.50 ± 1.76	-0.47	3.06
LF-22[b]	pegmatite	58.4	5.40	0.092 ± 7	0.510042 ± 7	0.0559 ± 42	0.509040 ± 82	-1.37 ± 1.61	-0.72	2.99
LF-29[b]	px-tonalite	22.0	4.45	0.202 ± 8	0.511164 ± 7	0.1222 ± 48	0.508970 ± 94	-2.75 ± 1.84	-0.38	3.31
Reference materials:										
BHVO-2					0.512984 ± 6					
BHVO-2 rep.					0.512998 ± 7					
G-2					0.512250 ± 10					

Nd isotopic data acquired at PCIGR, including a set of ≥ 2.82 Ga samples collected in the eastern Rivière Arnaud Terrane. The high pressure digestion technique (Pretorius *et al.,* 2006) was applied to the felsic samples, whereas the mafic samples were dissolved on a hotplate using the methodology described by Weis *et al.* (2006). Following dissolution, the Nd fractions were separated using ion exchange columns described by Weis *et al.* (2006). $^{143}Nd/^{144}Nd$ isotopic compositions of purified Nd solutions were calibrated against the Rennes (0.511973) standard, and measured on the PCIGR's Nu Plasma multi-collector ICP-MS. Analyses of USGS standard materials BHVO-2 and G-2, and blank, duplicate and replicate solutions were performed to ensure data quality.

[a] Trace element concentrations determined at the Pacific Centre for Isotopic and Geochemical Research, following the high-pressure dissolution technique of Pretorius et al. (2006).

[b]Trace element concentrations determined at Activation Laboratories.

[c] The 2σ uncertainty in Sm/Nd ratio of ultramafic samples analyzed at PCIGR, based on a replicate analyses of sample LM3-5 is 3.5%. The 2σ uncertainty in the Sm/Nd ratio of mafic to felsic samples, based on analyses of USGS reference materials BHVO-2 (duplicate) and BCR-2 is 1.9 %. The calculated 2σ uncertainty in Sm/Nd ratios of samples analyzed at ACTLABS, based on 13 duplicates analyzed in both laboratories is $2\sigma_{Sm/Nd} = 0.06 + 0.01(Sm/Nd)$

[d] Calculated $^{147}Sm/^{144}Nd$ ratio: $^{147}Sm/^{144}Nd = [0.149957 \times AwNd \times Sm\ (ppm)] / [(1/(3.69014 + (^{143}Nd/^{144}Nd)) \times AwSm \times Nd\ (ppm)]$ where:

AwNd = 144.2397, AwSm = 150.3656. The 2σ is calculated as: $$2\sigma_{(^{147}Sm/^{144}Nd)} = \frac{^{147}Sm}{^{144}Nd} \times \sqrt{\left(\frac{2\sigma_{Sm/Nd}}{Sm/Nd}\right)^2 + \left(\frac{2\sigma_{(^{143}Nd/^{144}Nd)}}{\left(3.69014 + \frac{^{143}Nd}{^{144}Nd}\right)}\right)^2}$$

[e]The $^{143}Nd/^{144}Nd$ ratio at the approximate time of emplacement of the Q-suite (2.72 Ga) was recalculated using $^{147}\lambda = 6.54 \times 10^{-12}$ (Lugmair & Marti, 1978) and the radioactive decay equation: $\left(\frac{^{143}Nd}{^{144}Nd}\right)_t = \left(\frac{^{143}Nd}{^{144}Nd}\right) - \left(\frac{^{147}Sm}{^{144}Nd}\right) \times \left(e^{\lambda t} - 1\right)$. The associated 2σ uncertainty is calculated as: $2\sigma_{(143/144)t} = 2\sigma_{(143/144)} + 2\sigma_{(147/144)} \times \left(e^{\lambda t} - 1\right)$.

[f] $\varepsilon_{Nd(2.72)}$ is the $^{143}Nd/^{144}Nd$ value normalized to the CHUR value at 2.72 Ga, assuming present day $(^{143}Nd/^{144}Nd)_{CHUR} = 0.512638$ and $(^{147}Sm/^{144}Nd)_{CHUR} = 0.1966$ (Hamilton *et al.,* 1983).

The $2\sigma_{(\varepsilon Nd)t}$ is $2\sigma_{(\varepsilon Nd)t} = \frac{10000 \times 2\sigma_{(143/144)_t}}{0.512638 - 0.1966 \times (e^{\lambda t} - 1)}$.

[g] $f^{Sm/Nd}$ is the sample $^{147}Sm/^{144}Nd$ relative to the present day CHUR value of 0.1966 and is given by: $f^{Sm/Nd} = \left(\frac{^{147}Sm}{^{144}Nd} - 0.1966\right) - 1$.

[h] The crustal residence age (T_{CR}) of Goldstein *et al* (1984) is calculated relative to the depleted mantle which evolved linearly over geological time from a chondritic $^{143}Nd/^{144}Nd$ ratio 4.5 Ga ago to a super-chondritic present-day ratio of 0.513163. The T_{CR} is thus a model age approximating the time that a sample has been isolated from its presumed depleted mantle (DM) source. The T_{CR} is calculated from:

$$T_{CR} = \frac{1}{\lambda} \ln\left(\frac{\frac{^{143}Nd}{^{144}Nd} - 0.513163}{\frac{^{147}Sm}{^{144}Nd} - 0.2137} + 1\right)$$

Table 2-4: Hf isotopic determinations from Q-suite intrusions and surrounding granitoids

Sample	Lithology	Hf	Lu	Lu/Hf[c]	$^{177}Hf/^{176}Hf$	$^{176}Lu/^{176}Hf$[d]	$^{176}Hf/^{177}Hf$ (T)[e]	εHf (T)[f]	T_{DM}[g]
Hudson Bay Terrane									
GR-2[a]	ol. websterite	0.60	0.11	0.186 ± 23	0.281788 ± 5	0.0265 ± 33	0.280408 ± 63	-22.29 ± 2.26	6.20
GR2-4[b]	mt. gabbronorite	0.7	0.095	0.136 ± 52	0.281972 ± 6	0.0193 ± 73	0.280968 ± 138	-2.37 ± 4.91	3.46
GR2-8[a]	hybrid	1.33	0.16	0.116 ± 11	0.281808 ± 6	0.0165 ± 15	0.280946 ± 34	-3.14 ± 1.21	3.42
GR2-9[a]	hybrid	3.00	0.17	0.055 ± 5	0.281350 ± 6	0.0079 ± 7	0.280939 ± 19	-3.39 ± 0.66	3.23
GR2-10[a]	hybrid	4.52	0.13	0.028 ± 3	0.281156 ± 5	0.0040 ± 4	0.280950 ± 12	-3.01 ± 0.42	3.16
GR2-11[a]	granite	3.27	0.04	0.013 ± 1	0.280955 ± 3	0.0018 ±2	0.280862 ± 6	-6.16 ± 0.23	3.26
GR2-11 rep.					*0.280957 ± 4*				
GR2-11 dup.					*0.280938 ± 5*				
GR3-7[b]	pegmatite	0.2	0.003	0.015 ± 32	0.281018 ± 12	0.0021 ± 46	0.280907 ± 95	-4.55 ± 3.38	3.20
DH-02[b]	granite	8.2	0.051	0.006 ± 31	0.281020 ± 5	0.0009 ± 44	0.280974 ± 84	-2.15 ±2.99	3.09
DH-03[b]	gabbronorite	2.1	0.18	0.084 ± 43	0.281818 ± 3	0.0119 ± 62	0.281198 ± 114	5.80 ± 4.06	2.82
DH-10[b]	ol. websterite	0.5	0.085	0.170 ± 57	0.282271 ± 3	0.0242 ± 81	0.281013 ± 149	-0.77 ± 5.30	3.56
DH-13[b]	f. websterite	2.2	0.096	0.044 ± 37	0.281440 ± 5	0.0062 ± 53	0.281117 ± 99	2.93 ± 3.53	2.93
LM2-4[b]	peridotite	0.3	0.091	0.303 ± 79	0.282621 ± 5	0.0431 ± 112	0.280376 ± 205	-23.43 ± 7.30	-7.70
LM3-5[a]	ol. websterite	0.91	0.15	0.165 ± 20	0.282197 ± 9	0.0234 ± 29	0.280977 ± 61	-2.06 ± 2.16	3.64
LM2-7[b]	granite	3.4	0.049	0.014 ± 32	0.281106 ± 5	0.0020 ± 46	0.280999 ± 88	-1.26 ± 3.12	3.07
LM2-8[b]	hybrid	6.2	0.30	0.048 ± 38	0.281254 ± 6	0.0069 ± 54	0.280896 ± 102	-4.95 ± 3.64	3.29
LM2-8 rep.[b]					*0.281263 ± 4*				
LM2-10[b]	mt. gabbronorite	2.0	0.26	0.130 ± 51	0.281781 ± 4	0.0185 ± 72	0.280819 ± 133	-7.66± 4.74	3.81
LM2-10 dup.[b]					*0.281894 ± 6*		0.280932 ± 135	-3.66 ± 4.81	3.53
LM2-10 dup.[b]					*0.281812 ± 5*		0.280850 ± 134	-6.57 ± 4.78	3.73
LM4-7[b]	pegmatite	3.6	0.15	0.042 ± 37	0.281266 ± 4	0.0059 ± 52	0.280958 ± 97	-2.73 ± 3.74	3.18
UM03-2008[a]	ol. websterite	0.78	0.11	0.144 ± 18	0.282090 ± 4	0.0205 ± 25	0.281021 ± 49	-0.49 ± 1.75	3.37
Riviere Arnaud Terrane - Lac Couture									
C1-39[a]	wehrlite	0.59	0.10	0.165 ± 20	0.282364 ± 3	0.0235 ± 29	0.281142 ± 55	3.81 ± 1.94	3.09
D-22[b]	bt. wehrlite	0.8	0.12	0.150 ± 54	0.281957 ± 4	0.0213 ± 77	0.280847 ± 142	-6.66 ± 5.05	3.90
C1-47[b]	gabbro	2.3	0.26	0.111 ± 48	0.281726 ± 12	0.0157 ± 68	0.280905 ± 133	-4.60± 4.75	3.49
C1-47 dup.[b]					*0.281722 ± 5*				
C1-49[b]	pegmatite	1.4	0.024	0.017 ± 33	0.281160 ± 4	0.0024± 47	0.281033 ± 88	-0.06 ± 3.12	3.03
C1-51[a]	tonalite	3.72	0.21	0.058 ± 5	0.281504 ± 3	0.0082 ± 8	0.281078 ± 17	1.53 ± 0.61	3.02
Riviere Arnaud Terrane - Lac Faribault									
LF-5[a]	harzburgite	1.13	0.11	0.097 ± 12	0.281788 ± 3	0.0138 ± 17	0.281071 ± 33	1.30 ± 1.19	3.09
LF-9[a]	px-diorite	2.55	0.28	0.109 ± 10	0.281705 ± 5	0.0155 ± 14	0.280899 ± 31	-4.84 ± 1.10	3.49
LF-18[a]	granodiorite	5.17	0.02	0.005 ± 0	0.281019 ± 6	0.0006 ± 1	0.280985 ± 7	-1.77 ± 0.26	3.08
LF-24[a]	f. websterite	2.23	0.17	0.078 ± 10	0.281601 ± 7	0.0111 ± 14	0.281022 ± 32	-0.44 ± 1.13	3.14
LF-17[b]	gabbro	1.2	0.14	0.113 ± 48	0.281848 ± 5	0.0160 ± 68	0.281015 ± 127	-0.68 ± 4.51	3.25
LF-22[b]	pegmatite	6.1	0.040	0.007 ± 31	0.281031 ± 6	0.0009 ± 44	0.280983 ± 85	-1.86 ± 3.04	3.08
LF-29[b]	px-tonalite	1.9	0.15	0.079 ± 43	0.281539 ± 5	0.0113 ± 61	0.280951 ± 114	-2.98 ± 4.07	3.28
Reference materials:									
BHVO-2					0.283103 ± 3				
G-2					0.282517 ± 2				

Hf isotopic data acquired at PCIGR, including a set of ≥ 2.82 Ga samples collected in the eastern Rivière Arnaud Terrane. The high pressure digestion technique (Pretorius *et al.,* 2006) was applied to the felsic samples, whereas the mafic samples were dissolved on a hotplate using the methodology described by Weis *et al.* (2006). Following dissolution, the Hf fractions were separated using ion exchange columns described by Weis *et al.* (2006, 2007). $^{176}Hf/^{177}Hf$ isotopic compositions of purified Hf solutions were calibrated against the Rennes JMC475 (0.282160) standard and measured on the PCIGR's Nu Plasma multi-collector ICP-MS. Analyses of USGS standard materials BHVO-2 and G-2, and blank, duplicate and replicate solutions were performed to ensure data quality.

[a] Trace element concentrations determined at the Pacific Centre for Isotopic and Geochemical Research, following the high-pressure dissolution technique of Pretorius *et al.* (2006).

[b]Trace element concentrations determined at Activation Laboratories. Based on 13 duplicate samples that were analyzed in both laboratories the 2σ uncertainties are: 1) $2\sigma_{Hf(ppm)}$ = 0.4 + 0.12[Hf] and 2) $2\sigma_{Lu(ppm)}$ = 0.008 + 0.07[Lu].

[c] The 2σ uncertainty in Lu/Hf ratio of ultramafic samples analyzed at PCIGR, based on replicate analyses of sample LM3-5 is 12 %. The 2σ uncertainty in the Lu/Hf ratio of mafic to felsic samples, based on analyses of USGS reference materials BHVO-2 (duplicate) and BCR-2 is 9 %. The calculated 2σ uncertainty in Lu/Hf ratios of samples analyzed at ACTLABS, based on 13 duplicates analyzed in both laboratories is $2\sigma_{Lu/Hf}$ = 0.03 + 0.16(Lu/Hf).

[d] Calculated $^{176}Lu/^{177}Hf$ ratio: $^{176}Lu/^{177}Hf$ = [0.0259 x AwLu x Lu (ppm)] / [(1/(5.094808 + ($^{176}Hf/^{177}Hf$)) x AwHf x Hf (ppm)] where:

AwLu = 174.966719, AwHf = 178.4864001. The 2σ is calculated as: $$2\sigma_{(176Lu/177Hf)} = \frac{^{176}Hf}{^{177}Hf} \times \sqrt{\left(\frac{2\sigma_{Lu/Hf}}{Lu/Hf}\right)^2 + \left(\frac{2\sigma_{(176Hf/177Hf)}}{\left(5.094808 + \frac{^{176}Hf}{^{177}Hf}\right)}\right)^2}$$

[e] The $^{176}Hf/^{177}Hf$ ratio at the approximate time of emplacement of the Q-suite (2.72 Ga) was recalculated using $^{176}\lambda$ = 1.867 x 10^{-11} Söderlund *et al.,* 2004) and the radioactive decay equation: $\left(\frac{^{176}Hf}{^{177}Hf}\right)_t = \left(\frac{^{176}Hf}{^{177}Hf}\right) - \left(\frac{^{176}Lu}{^{177}Hf}\right) \times \left(e^{\lambda t} - 1\right)$. The associated 2σ uncertainty is calculated as: $2\sigma_{(176Hf/177Hf)t} = 2\sigma_{(176Hf/177Hf)} + 2\sigma_{(176Lu/177Hf)} \times \left(e^{\lambda t} - 1\right)$.

[f] $\varepsilon_{Hf(2.72)}$ is the $^{176}Hf/^{177}Hf$ value normalized to the CHUR value at 2.72 Ga, assuming present day ($^{1476}Hf/^{177}Hf)_{CHUR}$ = 0.282785 and ($^{176}Lu/^{177}Hf)_{CHUR}$ = 0.0336 (Bouvier *et al.,* 2008). The $2\sigma_{(\varepsilon Hf)t}$ is $2\sigma_{(\varepsilon Hf)_t} = \frac{10000 \times 2\sigma_{(176Hf/177Hf)_t}}{0.282785 - 0.0336 \times (e^{lt} - 1)}$.

[g] The hafnium model age (T_{DM}) calculated relative to the depleted mantle which evolved linearly over geological time from a chondritic $^{176}Hf/^{177}Hf$ ratio 4.56 Ga ago to a super-chondritic present-day ratio of 0.28325 (Chauvel & Blichert-Toft, 2001). The T_{DM} is calculated from:

$$T_{DM} = \frac{1}{\lambda} \ln\left(\frac{\frac{^{176}Hf}{^{177}Hf} - 0.28325}{\frac{^{176}Lu}{^{177}Hf} - 0.0384} + 1\right)$$

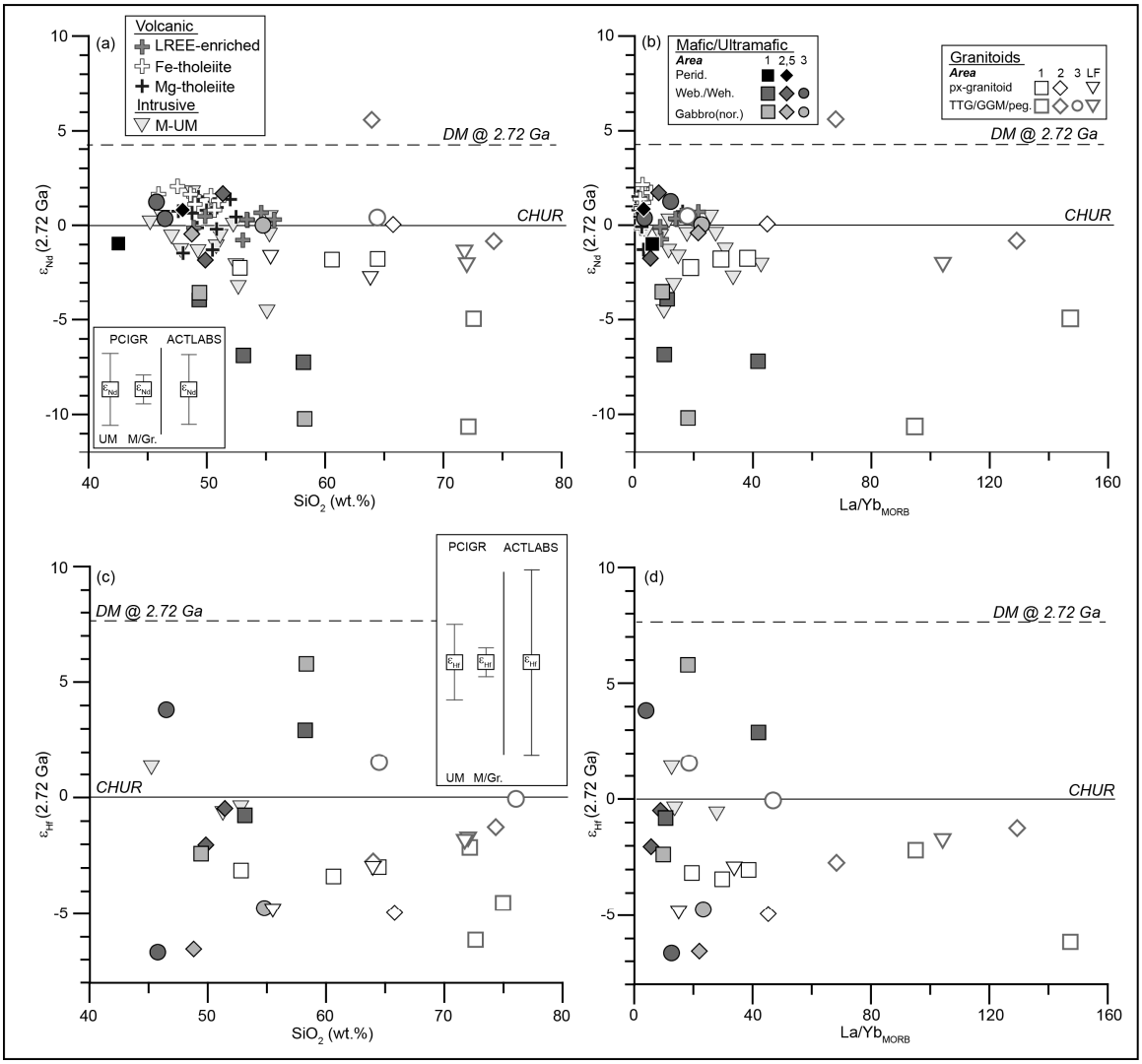

Figure 2-7: Isotopic (ε_{Nd} and ε_{Hf}) compositions of the Q-suite intrusions.

Isotopic (ε_{Nd} and ε_{Hf}) compositions of the Q-suite intrusions and the related granitoid rocks, calculated at 2.72 Ga. Isotopic compositions of the Bulk Silicate Earth, approximated by CHUR and the terrestrial upper mantle (DM) reservoirs are shown for reference. The average magnitude of ε_{Nd} and ε_{Hf} errors, calculated separately for samples whose trace-elements were analyzed at PCIGR and ACTLABS are shown as insets in (a) and (c). The errors associated with the PCIGR-analyzed samples are further subdivided by lithology (ultramafic vs. mafic-felsic). **(a)** ε_{Nd} vs. SiO_2 (wt. %) plot. Shown for comparison are the $\geq$ 2.82 Ga mafic intrusives from eastern Ungava craton (Tables 3 and 4), and the intrusive and metavolcanic data of Boily *et al.* (2009) and Maurice *et al.* (2009). **(b)** ε_{Nd} vs. $(La/Yb)_{MORB}$. **(c)** ε_{Hf} vs. SiO_2 (wt. %). **(d)** ε_{Hf} vs. $(La/Yb)_{MORB}$.

western Hudson Bay Terrane display lower initial $^{143}Nd/^{144}Nd$ ratios (ε_{Nd}(2.72 Ga) = +1 to -10) that decrease with increasing SiO_2 content and degree of REE fractionation, in contrast to the more restricted and more radiogenic $^{143}Nd/^{144}Nd$ ratios (ε_{Nd}(2.72 Ga) = +2 to -1) of the Q-suite intrusives of the eastern Hudson Bay and Rivière Arnaud terranes.

The initial $^{143}Nd/^{144}Nd$ ratios of Q-suite plutonic rocks extend to much lower values than those of the Neoarchean metavolcanic rocks emplaced in the Hudson Bay Terrane (Boily *et al.*, 2009; Maurice *et al.*, 2009). The analyzed granitic country rocks from the Hudson Bay Terrane have unradiogenic ε_{Nd} values at ~2.72 Ga (-1 to -10) that are significantly lower than those of the granitic rocks of the Rivière Arnaud Terrane (ε_{Nd}(2.72 Ga) = +0.5 to -3) to the east. As a result, the calculated crustal residence model ages (Goldstein *et al.*, 1984) of the TTG and GGM-series granitic rocks from the Hudson Bay Terrane (3.0-3.85 Ga) are older than the model ages of the granitoids from the Rivière Arnaud Terrane (3.0-3.3 Ga), consistent with the results of Boily *et al.* (2009). In contrast to the TTG and GGM-series rocks, the pyroxene-bearing granitoid rocks in the Hudson Bay Terrane have relatively high ε_{Nd} values (~ -2), precluding an origin through bulk remelting of an older TTG protolith and consistent with the evolution of a juvenile mantle-derived magma through assimilation-fractional crystallization (AFC; Milidragovic & Francis, 2014).

Although the initial $^{176}Hf/^{177}Hf$ ratios of the Q-suite intrusives seem independent of both their geographical location and degree of silica saturation (Fig. 2-7c), the initial $^{176}Hf/^{177}Hf$ ratios of the samples from the western Hudson Bay Terrane are negatively correlated with the initial $^{143}Nd/^{144}Nd$ ratios (Fig. 2-8). This trend, perpendicular to the Terrestrial Array (Vervoort *et al.,* 2011) extends to strongly radiogenic ε_{Hf}(2.72 Ga)

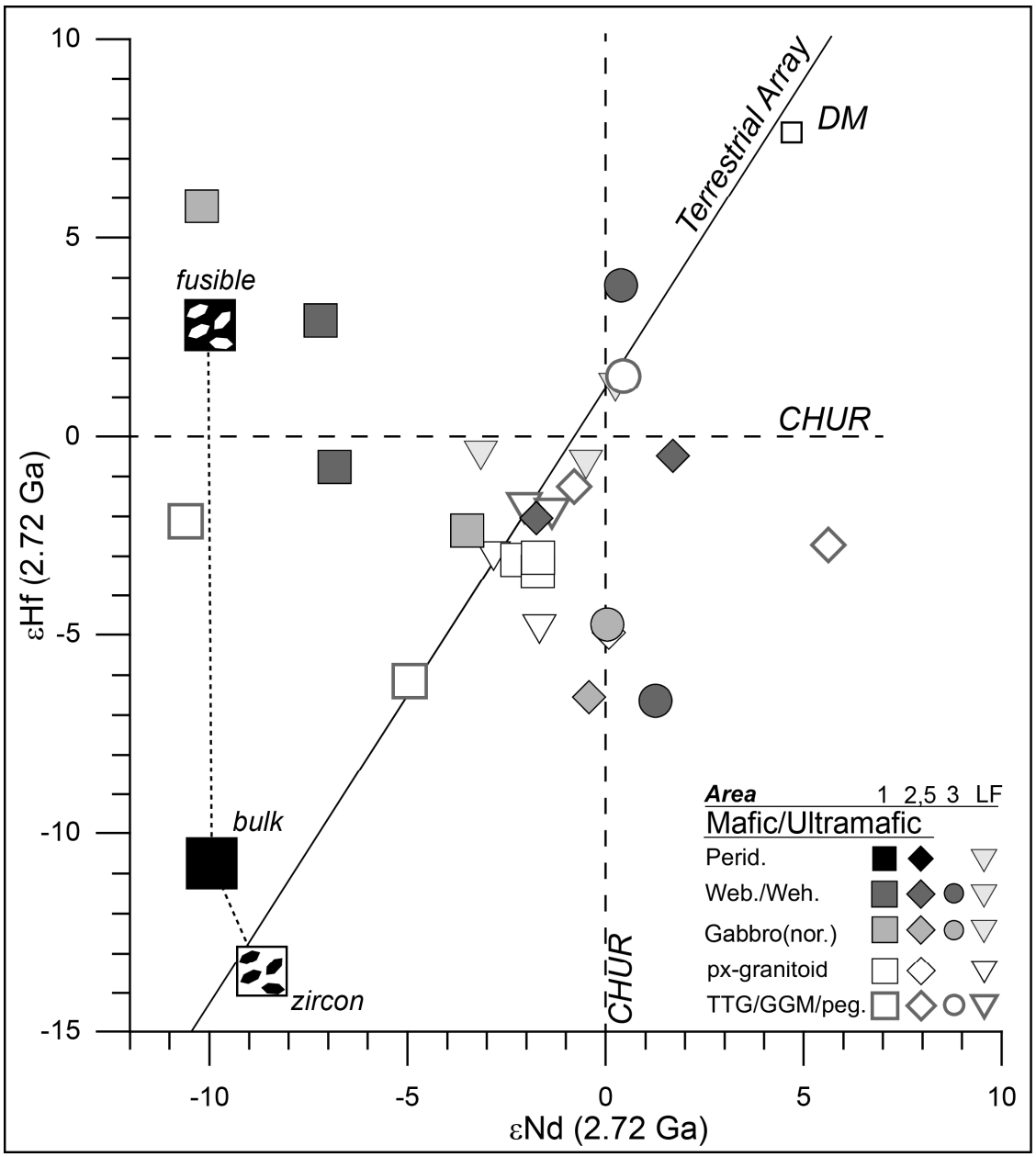

Figure 2-8: ε_{Hf} vs. ε_{Nd} (2.72 Ga) plot of the Q-suite intrusions.

. ε_{Hf} vs. ε_{Nd} (2.72 Ga) plot of the rocks analyzed in this study. Terrestrial Isotopic Array - $\varepsilon_{Hf} = 1.55 \times \varepsilon_{Nd} + 1.21$ (Vervoort *et al.,* 2011). Also shown are the isotopic compositions of a bulk granite (black box), its constituent zircon (white box with black pattern), and the zircon-free fraction (black box with white pattern), modelled calculated at 2.72 Ga, and assumed to have separated from the depleted mantle source at 3.8 Ga. The model bulk granite was assumed to have average continental crust abundances of Hf and Nd (5.3 ppm and 27 ppm; Rudnick & Gao, 2003), and $^{176}Lu/^{177}Hf$ (0.015; Griffin *et al.,* 2004) and Sm/Nd (0.115; Goldstein *et al.,* 1984) ratios. The crystallized granite was assumed to contain 0.5 wt % zircon. D_i^{Zir} values of 997, 333, 4.77, and 5.16 for used for Hf, Lu, Nd, and Sm, respectively (Fujimaki, 1986).

values (~ +7) and unradiogenic ε_{Nd}(2.72 Ga) values (~ -10). The fractionation of the two isotopic systems has previously been attributed to crustal anatexis in the presence of residual zircon and oxide minerals (Schmitz *et al.,* 2004).

4. Discussion

4.1 Major element composition of the Q-suite primary magmas

The Q-suite intrusions are cumulate bodies emplaced at middle crustal levels during the peak igneous activity of the Ungava craton. Their compositions therefore likely reflect a complex interplay between the physical sorting of liquidus phases, the amount of interstitial trapped liquid, and re-equilibration with evolving liquids. Furthermore, the low initial $^{143}Nd/^{144}Nd$ ratios of the samples from the Hudson Bay Terrane, approaching those of the surrounding granitoids, and the elevated Th/Yb_{MORB} ratios (5-210), indicate that the Q-suite intrusions have been contaminated by the felsic crust into which they were emplaced, further complicating the characterization their parental liquids.

We reconstructed the major element compositions of the subalkaline and transitional magmas (Table 2-5; Fig. 2-9) parental to the olivine-orthopyroxene cumulates form the western Hudson Bay Terrane and the dunites from the Lac Couture region, using the alphaMELTS software package (Smith & Asimow, 2005; Ghiorso & Sack, 1995). We modeled isobaric (500 MPa) melting of the most magnesian peridotites in increments of 1°C and calculated the major element compositions of melt and residual phases. The equilibrium melting calculations were performed from near-solidus temperatures until clinopyroxene was exhausted and the mode and composition of the residual minerals and the Mg-number of the liquid agreed with: 1) petrographic observations, 2) electron

Table 2-5: Reconstructed major element compositions of Q-suite magmas

	C1-16	C1-15	C1-15*	DH08-7	DH-08
SiO_2	46.5	46.6	45.4	47.9	48.05
TiO_2	0.6	0.9	0.8	0.6	0.8
Al_2O_3	6.6	6.7	5.7	14.8	16.5
Fe_2O_3	1.0	0.9	0.8	1.1	1.0
FeO	15.9	16.0	16.3	13.1	12.5
MgO	14.0	9.4	14.3	10.8	9.6
CaO	13.9	16.9	14.4	8.4	7.5
Na_2O	0.9	0.5	0.4	1.6	1.8
K_2O	0.2	0.2	0.2	1.4	1.8
P_2O_5	0.2	0.1	0.1	0.2	0.3
Cr_2O_3	0.2	1.8	1.6	0.11	0.1
NiO	0.02	0.01	0.03	0.02	0.02
Total	100.0	100	100.0	100.0	100.0
Fe^{3+}/Fe^{tot}	0.05	0.05	0.05	0.07	0.07
Fo (alphaMELTS)	0.84	-	-	83.1	82.0
Fo meas.	83.5	77.7	-	82.4	

*Primitive parental magma composition calculated by adding olivine to the C1-15 melt composition, using PRIMELT2.EXE (Herzberg & Asimow, 2008).

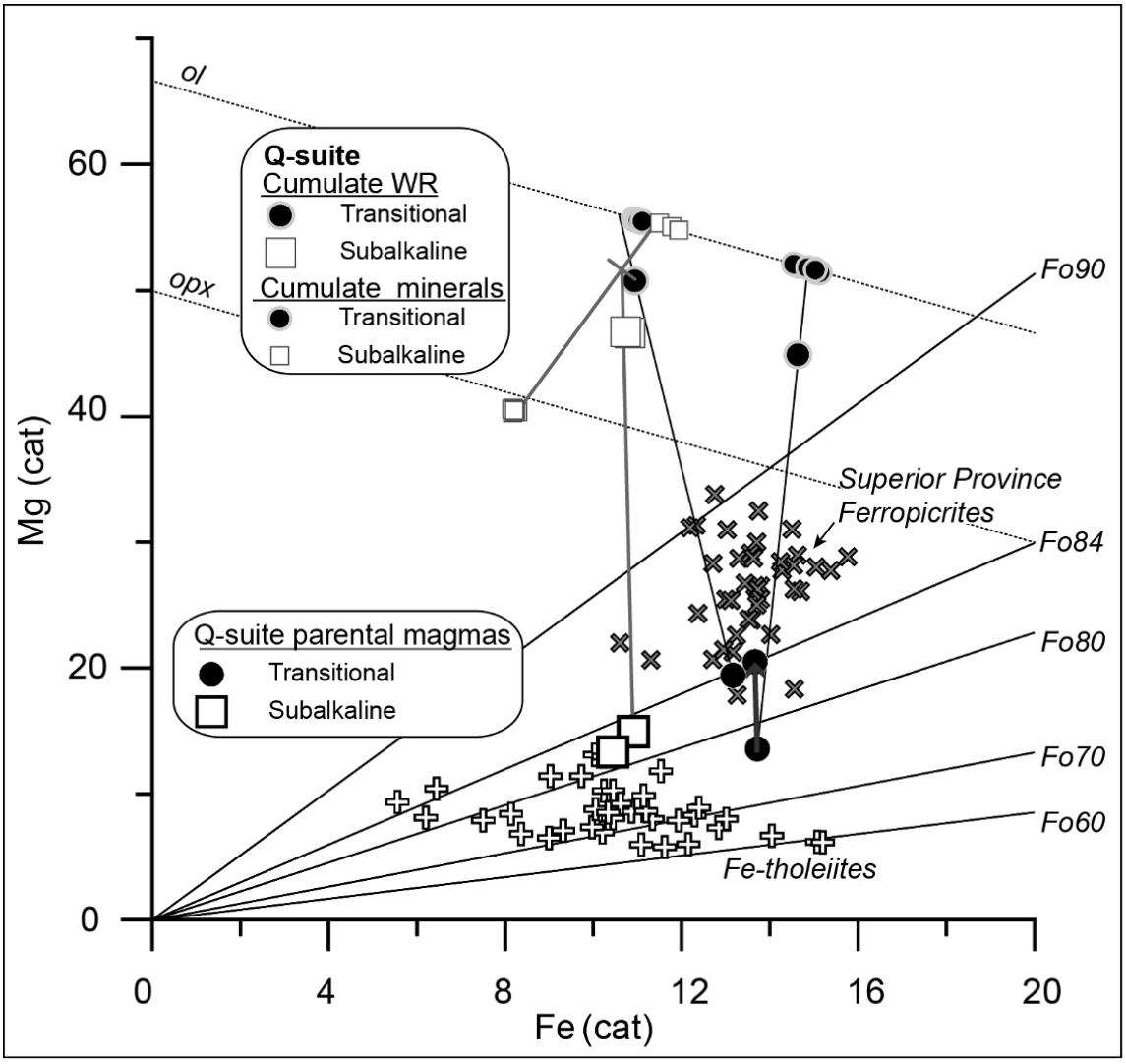

Figure 2-9: Mg vs. Fe^{TOT} cation plot of the Q-suite parental compositions.
Mg vs. Fe^{TOT} cation plot of the Q-suite olivine ± orthopyroxene cumulates, constituent cumulus minerals, calculated Q-suite parental liquids, and their and corresponding tie-lines. The tie-lines between the cumulus minerals of sample DH08-7 (ol_{60}:opx_{20}), the calculated liquid, and bulk harzburgite composition are light grey. The calculated transitional magma compositions are denoted by black circles, with the thick solid dark grey line connecting the calculated evolved liquid in equilibrium with Fo_{78} (C1-15) to a more primitive composition in equilibrium with Fo_{84} (C1-16), calculated using PRIMELT2 (Herzberg & Asimow, 2008). Shown for comparison are the Fe-tholeiite suite (white crosses; Maurice *et al,* 2009) and Archean ferropicrites of the Superior Province (Grey X's; Stone *et al.,* 1995; Goldstein & Francis, 2008; Kitayama & Francis, in preparation). Lines radiating from the origin are isopleths for the Fo content of olivine coexisting with liquids whose Fe and Mg contents are specified by graph coordinates, adjusted to $Fe^{3+}/Fe^{TOT} = 0.05$.

microprobe compositional data and 3) olivine-melt Fe-Mg partitioning (K_D = 0.3; Roeder & Emslie (1970)). The compositions of the calculated liquids at this point are taken to approximate the compositions of the magmas that produced the most primitive olivine cumulates of each pluton type.

4.1.1 Subalkaline Q-suite magmas

The calculated parental magmas for two harzburgitic samples (DH08-7 and DH-08), at a fO_2 = FMQ-1, are saturated in olivine (Fo =82.4 ±0.7), orthopyroxene, and Cr-rich spinel. The calculated magma is an MgO- and FeO-rich basalt (MgO ~ 11wt. %; FeO^{TOT} ~14 wt. %; SiO_2 = 48 wt. %), with a moderate Al_2O_3 content (15 wt. %), Mg-number of 0.60, and Fe^{3+}/Fe^{TOT} = 0.07, and comprises 17 % of the harzburgite cumulate (olivine:orthopyroxene ~ 6:1).

The Ni content of the calculated magma was estimated from the calculated MgO content and the observed olivine composition of sample DH08-7 using the empirical relationship D_{Ni} = (124.8/MgO) - 0.9 (Hart & Davis, 1978). The inferred Ni content of the liquid (140 ppm) is significantly lower than that of melts with a similar MgO content that have equilibrated with the pyrolitic mantle (~250 ppm; Herzberg, 2011). Inverse olivine fractionation (Fig. 10) using the program PRIMELT2.XLS (Herzberg & Asimow, 2008) demonstrates that the low Ni content of the subalkaline parental magma cannot be solely attributed to prior olivine fractionation from a primary liquid in equilibrium with a pyrolitic mantle. Thus, although some prior olivine fractionation may have occurred, the mantle source of the subalkaline Q-suite magma is inferred to be poor in Ni relative to model pyrolitic mantle.

The estimated major element composition of the subalkaline Q-suite parental

magma is similar to the ca. 2.78 Ga supracrustal Fe-tholeiitic basalts (Maurice *et al.*, 2009) in the Rivière Arnaud Terrane (Fig.9). The most primitive Fe-tholeiite lavas have ~10 wt. % MgO, ~15 wt. % Al_2O_3, and ~13.5 wt. % FeO^{TOT} and may be equivalent to the subalkaline Q-suite magmas. A genetic relationship between the Fe-tholeiitic metavolcanics and the Q-suite intrusive suite would suggest that Fe-rich magmas were emplaced in both the Hudson Bay and the Rivière Arnaud terranes over ≥ 80 M.y. period, consistent with the amalgamation of the two terranes prior to ~2.75 Ga (Boily *et al.*, 2009).

4.1.2 Transitional Q-suite magmas

In contrast to the parental magmas of the subalkaline plutons, the magmas of the most primitive transitional Q-suite intrusions were saturated only in olivine and Cr-rich spinel. AlphaMELTS equilibrium melting calculations at a fO_2 = FMQ-2 on the least altered, highest Mg-number dunite (sample C1-16) from the Lac Couture region yield a weakly hypersthene-normative picritic (MgO ~14 wt. %; SiO_2 ~46.5 wt. %) liquid that is Fe-rich (FeO^{TOT} ~17 wt. %; Fe^{3+}/Fe^{TOT} =0.05) and Al_2O_3-poor (~6.5 wt. %) compared to that calculated for the subalkaline intrusions. The calculated liquid is high in CaO (~14 wt. %) compared the calculated subalkaline parental magma (~8.5 wt. %). Calculations under more oxidizing conditions generated liquid compositions strongly enriched in FeO^{TOT} (≥18 wt. %), and in poor agreement (K_{Dcalc} ≤0.29) with the K_D value of Roeder & Emslie (1970). The observed olivine compositions (≤1600 ppm) suggest that the Ni content of the transitional parental magma was relatively low (~200 ppm). The model indicates the presence of 14 % trapped liquid in the dunite cumulate, consistent with the combined estimated proportions of interstitial clinopyroxene and amphibole determined

by least squares fitting the whole-rock composition with the measured mineral compositions.

The composition of the more evolved magma parental to the most Fe-rich dunite (sample C1-15; FeO^{TOT} = 19.95 wt. %; Mg-number = 0.75) was estimated by subtracting of the observed olivine composition (Fo = 77.7 ± 0.7) from the bulk dunite composition until the Mg-number of the remaining "liquid" was in equilibrium with the measured olivine. The resulting liquid composition is an Fe-rich high-MgO basalt (FeO^{TOT} ~17 wt. %; MgO ~ 9.5 wt. %) produced by ~18 % fractional crystallization of olivine from the parental ferropicrite.

The Ni contents (~200 ppm) of the calculated transitional Q-suite magmas are low in comparison to those expected of pyrolite-derived magmas with similar MgO contents (~350 ppm at 14 wt. % MgO; Herzberg, 2011). There is no evidence of early sulphide crystallization and prior high-pressure fractionation of olivine from primary pyrolite melts cannot account for the anomalously low Ni content of the estimated transitional parental liquid (Fig. 2-10). Consequently, the mantle source of the transitional Q-suite magma, like that of the subalkaline Q-suite magma, is interpreted to be Ni-poor relative to the pyrolitic mantle.

4.2 The origin of the "calc-alkaline" trace element signature of the Q-suite intrusions

The effects of crystal accumulation complicate the interpretation of the trace element systematics of the Q-suite magmas. Rocks that have accumulated mafic minerals display lower LREE/MREE ratios than the liquids from which they formed. Trace element compositions of the Q-suite parental liquids (Table 2-6) were estimated

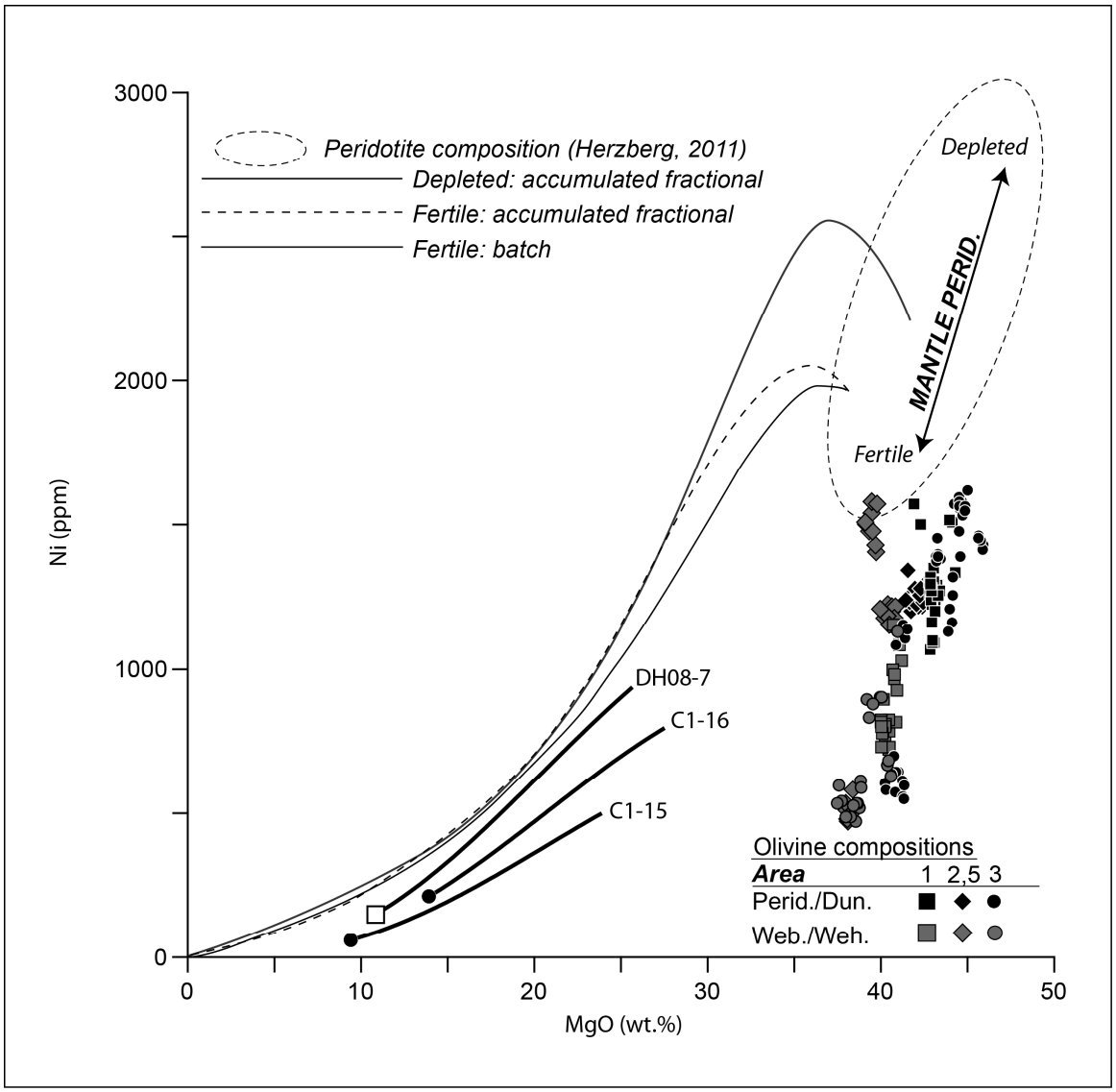

Figure 2-10: Ni (ppm) vs. MgO (wt. %).
Figure modified from Herzberg (2011) comparing the possible primary subalkaline (DH08-7) and transitional (C-15 and C-16) magmas with the primary melt compositions equilibrated with "pyrolitic" fertile and depleted mantle peridotite. Primary Q-suite magma compositions were calculated by fractional addition of olivine to the estimated parental melts using the program PRIMELT2.xls (Herzberg & Asimow, 2008). Measured olivine compositions from subalkaline (white squares) and transitional (white circles) Q-suite intrusions are shown for comparison.

from the most magnesian Q-suite cumulates using the method of Bédard, (1994), assuming trapped liquid fractions of 0.025, 0.05 and 0.10, and the liquid fractions calculated using alphaMELTS. Although the exact amount of trapped liquid is difficult to constrain, the overall trace-element patterns are not very sensitive to reasonable variations in the amount of trapped liquid (Fig. 2-11).

4.2.1 Subalkaline Q-suite magmas

The calculated trace element composition of the parental magma to two harzburgitic Q-suite samples (Fig. 2-11a) is strongly enriched in LREE relative to MREE (La/Gd_{MORB} = 10-40), has weakly fractionated MREE/HREE ratios (Gd/Yb_{MORB} = 2-3), and strongly depleted Nb, Ta and Ti contents (Nb/La_{MORB} = 0.1-0.2; Ti/Gd_{MORB} = 0.3-0.5; Ti/Ti* = 0.2-0.4; where $Ti/Ti^* = Ti_{MORB}/(Sm_{MORB} \times Eu_{MORB})^{1/2}$). Zirconium and Hf, in contrast, do not display significant depletions (Zr/Zr^* = 0.7-1.3; where $Zr/Zr^* = Zr_{MORB}/(Sm_{MORB} \times Eu_{MORB})^{1/2}$). The unradiogenic Nd ratios of the subalkaline Q-suite intrusions from the Hudson Bay Terrane (-1 to -10), the elevated Th/Yb ratios of both the subalkaline and transitional intrusions, and the arguments for an AFC origin of Ungava's intermediate-SiO_2 pyroxene-granitoids (Milidragovic & Francis, 2014), all imply that the incompatible trace-element patterns of the Q-suite intrusions reflect significant crustal addition. The negative correlation between the initial $^{143}Nd/^{144}Nd$ ratios and SiO_2 concentrations of the Q-suite rocks from the westernmost Hudson Bay Terrane suggests that the degree of contamination increased as crystallization proceeded (Fig. 2-7). In order to evaluate whether the "calc-alkaline" trace-element signature of the subalkaline Q-suite parental magmas is a primary magmatic feature, or the result of assimilation of the proto-cratonic granitic crust, we modeled the consequences of the assimilation of a low-K

Table 2-6: Reconstructed trace element compositions of Q-suite magmas

	C1-23			C1-50			C1-39			DH08-7			DH-09		
TMF	2.5	5	14	2.5	5	21	2.5	5	12	2.5	5	17	2.5	5	17
Th	-	-	-	3.1	1.6	0.4	4.9	2.5	1.1	28.4	14.8	4.4	15.4	8.0	2.4
U	0.8	0.4	0.1	2.3	1.2	0.3	1.4	0.7	0.3	6.8	3.5	1.1	2.6	1.4	0.4
Nb	-	-	-	-	-	-	5.7	4.6	3.0	14.7	10.6	4.0	14.4	10.5	4.0
La	13.1	7.5	2.9	14.1	8.2	2.3	30.4	22.8	13.4	109.	68.5	23.4	81.8	52.5	18.3
Ce	27.2	17.0	6.9	41.8	26.7	8.1	83.0	69.3	47.5	179.	126.	47.9	121.	87.6	34.2
Pr	4.3	2.9	1.3	6.3	4.4	1.5	10.3	10.2	9.85	15.6	12.3	5.3	9.7	7.8	3.5
Nd	20.8	15.2	7.0	29.1	21.4	8.0	48.4	45.4	38.7	53.7	46.0	22.0	29.0	25.2	12.4
Sm	5.0	3.9	1.9	8.2	6.3	1.6	11.1	10.8	10.0	7.8	7.3	3.9	5.1	4.7	2.6
Zr	35.3	25.8	13.2	40.2	31.5	13.2	70.3	62.9	48.5	255.	191.	87.7	117.	92.4	45.9
Hf	-	-	-	1.4	1.1	0.4	3.0	2.8	2.4	4.9	4.3	2.2	2.2	1.9	1.0
Ti	7025	6630	3278	13069	9725	3583	7497	8198	11105	3324	381	289	248	288	200
Eu	1.2	1.0	0.5	1.9	1.5	0.7	2.2	2.2	2.2	1.7	1.6	1.0	1.0	0.9	0.6
Gd	3.8	3.3	1.7	6.4	5.1	2.2	7.6	7.7	7.8	4.9	5.0	3.1	3.1	3.2	2.0
Tb	0.6	0.5	0.3	1.0	0.8	0.4	1.0	1.0	1.0	0.7	0.7	0.4	0.4	0.4	0.3
Dy	2.7	2.3	1.2	4.5	3.7	1.7	5.6	5.6	5.5	3.7	3.6	2.3	2.2	2.2	1.4
Y	14.2	12.1	6.5	24.5	20.0	9.0	31.5	31.3	30.8	21.4	21.0	13.1	13.4	13.3	8.3
Ho	0.6	0.5	0.3	0.8	0.7	0.3	1.2	1.2	1.1	0.8	0.8	0.5	0.4	0.4	0.2
Er	1.6	1.4	0.8	2.3	1.8	0.8	3.1	3.1	3.1	1.9	1.9	1.2	1.1	1.1	0.7
Tm	0.2	0.2	0.1	0.3	0.2	0.1	0.3	0.3	0.3	0.3	0.3	0.2	0.2	0.1	0.1
Yb	1.3	1.1	0.7	2.1	1.7	0.8	2.8	2.7	2.6	2.0	1.9	1.2	1.1	1.0	0.6
Lu	0.2	0.2	0.1	0.4	0.2	0.1	0.5	0.4	0.3	0.2	0.2	0.1	0.2	0.2	0.1

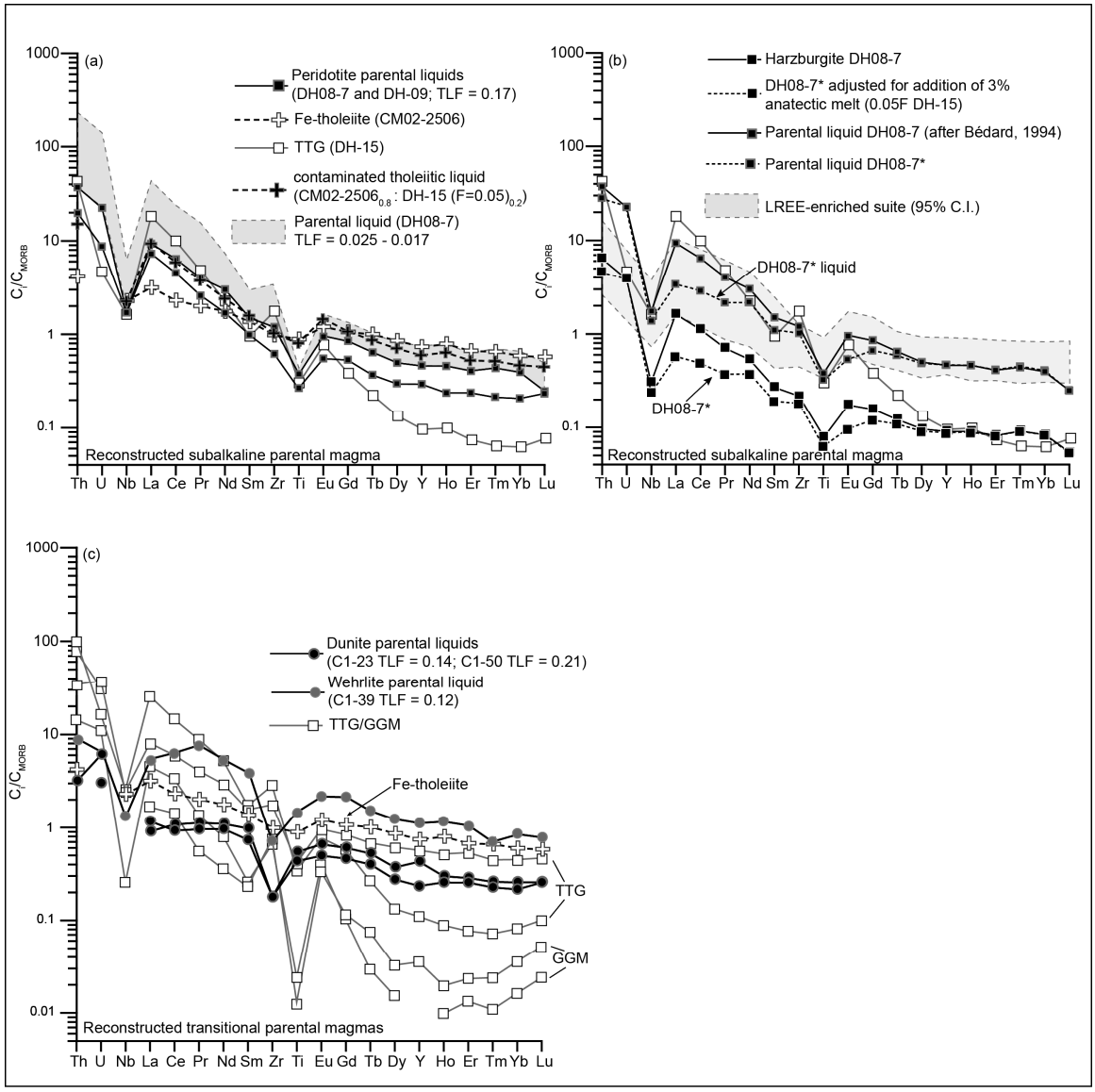
(a)
Peridotite parental liquids
(DH08-7 and DH-09; TLF = 0.17)
Fe-tholeiite (CM02-2506)
TTG (DH-15)
contaminated tholeiitic liquid
(CM02-2506$_{0.8}$: DH-15 (F=0.05)$_{0.2}$)
Parental liquid (DH08-7)
TLF = 0.025 - 0.017
Reconstructed subalkaline parental magma
(b)
Harzburgite DH08-7
DH08-7* adjusted for addition of 3%
anatectic melt (0.05F DH-15)
Parental liquid DH08-7 (after Bédard, 1994)
Parental liquid DH08-7*
LREE-enriched suite (95% C.I.)
DH08-7* liquid
DH08-7*
Reconstructed subalkaline parental magma
(c)
Dunite parental liquids
(C1-23 TLF = 0.14; C1-50 TLF = 0.21)
Wehrlite parental liquid
(C1-39 TLF = 0.12)
TTG/GGM
Fe-tholeiite
TTG
GGM
Reconstructed transitional parental magmas
C_i/C_{MORB}
1000
100
10
1
0.1
0.01
Th U Nb La Ce Pr Nd Sm Zr Ti Eu Gd Tb Dy Y Ho Er Tm Yb Lu

Figure 2-11: Parental liquid trace element spidergrams.
MORB-normalized spidergrams of the calculated trace element compositions (after Bédard (1994)) of the magmas parental to the subalkaline (a and b) and transitional (c) Q-suite intrusions. **(a)** Compositions calculated from a harzburgite and a peridotite from Area 1 (black lines with white squares represent parental compositions assuming 17% trapped interstitial melt, inferred from alphaMELTS calculations. The shaded field includes the range of concentrations included within the 2.5-17 % trapped liquid interval for sample DH08-7. Also shown is the composition of a TTG granodiorite (grey line with rectangles) proximal to the harzburgites, and the composition of a melt produced by 5 % modal batch melting (30 % quartz, 60 % plagioclase, 8% biotite, 1% magnetite, 1% zircon) of the TTG (thin black line). The model binary mixture consisting of 80% high-MgO Fe-tholeiite (dashed black line with crosses; Maurice et al., 2009) and 20% of the small degree TTG partial melt is shown as the grey line with grey crosses. **(b)** The effect of late-stage metasomatism by TTG anatectic melt (F=0.05). DH08-7 – bulk harzburgite composition; DH08-7* - harzburgite composition corrected for post-accumulation addition of 3% melt; DH08-7 liquid – melt composition calculated from uncorrected harzburgite at TLF = 0.17, calculated using the method of Bédard (1994); DH08-7* liquid- melt composition calculated from the corrected harzburgite composition. Shaded field = compositional range of LREE-enriched volcanic suite (Maurice *et al.,* 2009). **(c)** Black lines with black circles – calculated concentrations from two dunites and one wehrlite assuming 5% trapped liquid. Grey field – same as in 11B. Also shown are the compositions of nearby TTG (grey lines with grey rectangles) and GGM (black line with white rectangles) and their characteristic U-shaped MREE-HREE patterns.

granodiorite (sample DH-15) by an uncontaminated parental magma with a MORB-like trace element profile. A relatively primitive (MgO ~9 wt. %) tholeiitic basalt from the Duquet greenstone belt (CM02-2506; Maurice *et al.*, 2009) of north-central Ungava was chosen as a model parental liquid because of its relatively high FeO content, and the low degree of crustal contamination suggested by its weakly fractionated trace element profile and position within the MORB array (Pearce, 2008). Neither mixing calculations performed using a bulk granodiorite composition, nor partial melts of the granodiorite (F =0.05 to 0.30; Fig. 2-11a) are able to reproduce the negative HFSE anomalies and the degree of LREE/MREE fractionation of the calculated subalkaline Q-suite magmas, while remaining sufficiently mafic to crystallize olivine ± orthopyroxene only. The "calc-alkaline" signature of the subalkaline Q-suite intrusions is, thus, unlikely to reflect the simultaneous fractional crystallization and assimilation of continental crust by tholeiitic magmas with unfractionated trace element profiles.

Bédard's (1994) method assumes a closed system in which the cumulus phases crystallized in equilibrium with the trapped interstitial liquid. Significant departures from this idealized situation, such as infiltration of small volumes of trace element-enriched crustal melts following crystal accumulation will magnify the contamination signature. The ubiquitous presence of late pegmatitic veins and intrusions that is characteristic of the Q-suite plutons suggests that post-emplacement contamination by LREE-enriched, HFSE-depleted melts is likely. The significantly lower initial $^{143}Nd/^{144}Nd$ ratios of the mafic Q-suite samples from the western Hudson Bay Terrane (ε_{Nd}(2.72 Ga) ≥-10), compared to the spatially associated pyroxene-granitoid hybrids (ε_{Nd}(2.72 Ga) ~-2), provides strong evidence for open-system behaviour, in which crustal contaminant may

have been introduced following crystallization. Figure 2-11b demonstrates the effect of subtracting 3% of trace element-rich, zircon-saturated melt derived through 5 % anatexis of TTG (sample DH-15) from a bulk Q-suite harzburgite analysis. The calculated parental liquid for the harzburgitic composition, adjusted for the presence of 3% of crustal melt, shows less pronounced trace element fractionation (La/Gd_{MORB} =5, Nb/La_{MORB} =0.4) and is similar to the late LREE-enriched metavolcanics of the Ungava craton, which were interpreted by Maurice *et al.* (2009) to be crustally-contaminated Mg and Fe-tholeiites. Although, the addition of a 3% crustal component to the harzburgite could have produced the rims of orthopyroxene observed around olivine through peritectic reaction, its effect on the calculated major element composition of the parental liquid is relatively small.

The retention of zircon in the TTG residue may explain the negatively-correlated initial ε_{Nd}(2.72 Ga) and ε_{Hf}(2.72 Ga) values of the Q-suite intrusions from the Western Hudson Bay Terrane. Prolonged crustal residence (≤1 b.y.; Boily *et al.*, 2009; this study) would impart a strong fractionation between the Nd and Hf isotopes in the different mineral phases of the TTG (Fig. 2-8). Selective contamination by anatectic melts that have left residual zircon in their source may have given Q-suite plutons of the isotopically old Hudson Bay Terrane their unradiogenic $^{143}Nd/^{144}Nd$ and corresponding radiogenic $^{176}Hf/^{177}Hf$ ratios.

The preceding arguments indicate that the "arc-like" trace element signature of the calculated parental magmas of the subalkaline Q-suite plutons cannot be unequivocally interpreted as a source-enrichment feature, as many of the trace elements of the Q-suite cumulates are highly sensitive to contamination by low-degree anatectic melts. Our calculations suggest that the Q-suite harzburgites may have crystallized from relatively

unfractionated parental magmas that were modified by simultaneous fractional crystallization and assimilation of TTG crust as proposed by Maurice *et al.* (2009) for the genesis of the LREE-enriched metavolcanics. The TTG and their partial melts are, however, strongly depleted in HREE ($Yb_{MORB\ (TTG)}$ =0.15 +0.5/-0.13, based on 109 samples from the Québec government's E-sigéom database; Milidragovic & Francis, 2014) and ineffective in modifying the relatively unfractionated HREE profiles of the subalkaline Q-suite plutons (Fig. 2-11b). The calculated HREE concentrations of the subalkaline Q-suite parental magmas are, therefore, thought to be representative of their primary magmatic values. The subalkaline Q-suite parental magmas are depleted in HREE relative to MORB (Yb_{MORB} ~0.4). The relatively flat HREE-profiles (Gd/Yb_{MORB} ~2), however, indicate that the primary subalkaline Q-suite magmas did not equilibrate with a garnet-bearing residue, suggesting either derivation from relatively shallow mantle depths or complete exhaustion of garnet from the mantle source. Furthermore, the low absolute abundance of HREE in the subalkaline Q-suite magmas suggests derivation from either a source depleted in incompatible trace elements relative to the source of MORB or a source characterized by a higher pyroxene:olivine ratio and thus higher bulk partition coefficient values.

4.2.2 Transitional Q-suite magmas

The trace element composition of the ferropicritic magmas parental to the transitional Q-suite intrusions was determined from two dunite samples and one wehrlite. Although the low HREE abundances (Yb_{MORB} =0.30-0.85), weakly fractionated MREE/HREE (Gd/Yb_{MORB} =2-3), and strongly depleted Nb-Ta (Nb/La_{MORB} <0.3) are comparable to those calculated for the subalkaline parental magmas, the calculated

transitional parental magmas have flat to convex upward LREE (La/Gd_{MORB} =2-7) profiles (Fig 2-11c) that are not consistent with a primary "calc-alkaline" signature. As in the case of the subalkaline Q-suite plutons, the HREE contents of the transitional Q-suite magmas were relatively insensitive to contamination by the HREE-depleted anatectic melts. Consequently, the relatively flat HREE profiles (Gd/Yb_{MORB} ~2) of the calculated transitional parental liquids suggest that the ferropicritic Q-suite magmas last equilibrated with a garnet-free mantle residue. The absolute concentrations of HREE in the calculated transitional parental magmas are low with respect to MORB (Yb_{MORB} ~0.2) and similar to those estimated for the subalkaline parental magmas.

The calculated transitional parental magmas are characterized by stronger depletions of Zr and Hf (Zr/Sm_{MORB} =0.15-0.20; Zr/Zr* =0.15-0.30), but less pronounced Ti depletions (Ti/Gd_{MORB} =0.5-1.0; Ti/Ti* =0.4-0.7) compared to the calculated subalkaline parental magmas. The origin of the pronounced Zr-Hf anomalies in the transitional Q-suite intrusions (Fig. 2-6) is intriguing. The early TTG and the late GGM-series rocks sampled in the Lac Couture region (Fig. 2-11b) have U-shaped HREE patterns and positive Zr anomalies (Zr/Zr* =1.3-2.7), suggesting that they may represent zircon-bearing residues of crustal partial melting (Watson, 1979) or second-stage bulk melts of such residues. The widespread occurrence of inherited zircon cores in ca. 2.74-2.70 Ga granites across the craton suggests that incomplete zircon dissolution during the reworking of the Ungava craton was common. It is therefore possible that the Zr-Hf depletion of the transitional Q-suite intrusions reflects contamination by LREE-enriched crustal melts that have left residual zircon in the TTG source.

The foregoing considerations indicate that the primary Q-suite magmas had low

abundances of HREE and HFSE relative to MORB and were characterized by flat to LREE-depleted trace element profiles. The Q-suite magmas were modified, upon emplacement into the crust, by LREE-enriched anatectic melts.

4.3 Origin and source of the Q-suite magmas

Although Fe-rich picritic magmas (FeO^{TOT}>13.0 wt.%, MgO ≥ 12.0 wt. %) are uncommon, they have been identified in the southern/western Superior (Kitayama & Francis, in preparation; Green & Schulz, 1977; Stone *et al.,* 1995; Goldstein & Francis, 2008) and Slave (Francis *et al.,* 1999) provinces of North America, NW Russia (Hanski & Smolkin, 1995), Namibia (Gibson *et al.,* 2000), Japan (Ichiyama *et al.,* 2006), and Antarctica (Heinonen & Luttinen, 2008). The Neoarchean ferropicrites from the Boston Creek Flow (2720 ± 2 Ma, Corfu & Noble (1992); FeO^{TOT} ~ 17 wt. %, Al_2O_3 = 5.0 wt. %) and western Superior Province (FeO^{TOT} ~18 wt. %, Al_2O_3 = 5.5 wt. %), in particular, have high FeO^{TOT} and low Al_2O_3 contents, similar to the transitional Q-suite magma.

There is a general consensus that the high Fe contents of ferropicrite magmas cannot be produced by the melting of fertile lherzolitic mantle of pyrolitic composition (Hanski & Smolkin, 1995; Francis *et al.*, 1999; Gibson *et al.*, 2000; Tuff *et al.*, 2005; Goldstein & Francis, 2008). Furthermore, experimental data indicates that ferropicrite magmas can not coexist with a mantle residue containing both olivine and garnet (Hanski & Smolkin, 1995; Stone *et al.*, 1995; Tuff *et al.*, 2005). There are presently two classes of models for the petrogenesis of ferropicritic magmas. The first (Hanski & Smolkin, 1995; Stone *et al.*, 1995) argue that the low Al_2O_3 contents, the enrichment in the incompatible elements, and fractionated REE ratios of ferropicrites reflect a two-stage evolution. During the first stage the mantle source undergoes melting, enrichment in compatible

elements and depletion in Al_2O_3. A subsequent metasomatic enrichment event refertilizes the mantle and produces the observed incompatible element enrichment. A variant of this model, proposed by Goldstein & Francis (2008), begins with an olivine flotation cumulate crystallizing from a deep magma ocean that is also undergoing garnet fractionation, depleting the residual liquid in Al_2O_3 and HREE. The second class of models posits that ferropicritic magmas are generated by the melting of garnet-pyroxenite (e.g. HK-66; Kuno & Aoki (1970)) produced by hybridization of mantle peridotite and enriched subducted oceanic crust. The segregation of melt from an olivine-free source, composed of ~75% eclogite and ~25% peridotite, is proposed to provide an explanation for the high Ni (250-900 ppm), low Al_2O_3 (9 wt. %) contents, and fractionated REE patterns of ferropicrites in Namibia (Tuff *et al.*, 2005). Goldstein & Francis (2008) argued that the majority of the known garnet-pyroxenites have MgO and FeO contents that are too low to produce ferropicritic magmas and that no two-component mixture of fertile lherzolite and Fe-rich basalt is capable of producing the FeO contents of the Western Superior ferropicrites.

The magmas parental to the Q-suite plutons are enriched in Fe compared to most modern-day mantle-derived magmas and the estimated parental magmas of most of the world's ultramafic plutonic rocks. The Fe-rich character and coeval emplacement of subalkaline and transitional Q-suite intrusions suggest that their parental magmas may be genetically related. The two magmas, however, have markedly different CaO/Al_2O_3 ratios and FeO concentrations that preclude a relationship through olivine-dominated crystal fractionation. Although the abundance of peritectic orthopyroxene and greater relative enrichment in LREE (La/Sm_{MORB} =6-7) suggest that the most magnesian subalkaline

intrusions have experienced greater crustal contamination than the transitional dunites (La/Sm_{MORB} =1-6), the large difference in Al_2O_3 concentrations between the two parental magma types at relatively similar SiO_2 contents implies that the subalkaline Q-suite magma cannot be derived from the transitional Q-suite magma through coupled fractional crystallization and assimilation of continental crust.

4.3.1 Experimental constraints on the petrogenesis of the Q-suite magmas

Experimental melts of fertile Mg-rich peridotite (Takahashi & Kushiro, 1983; Baker & Stolper, 1994; Falloon *et al.*, 1999) have FeO contents that are significantly lower than those of the Q-suite magmas and other Superior Province ferropicrites (Figs. 2-9 and 2-12). Goldstein & Francis (2008) argued that an iron-rich peridotite representative of the Martian mantle composition yields melts that better match the Fe contents of the Superior Province ferropicrites. For example, isobaric melts of the ordinary chondrite Homestead L5 (Mg-number =0.77; Agee & Draper, 2004) at pressures of 4.7-5 GPa are strongly enriched in FeO (~20-30 wt. %) and MgO (~14-25 wt. %). Low pressure (1.5 GPa) melts of DW-Mars spinel lherzolite (Mg-number =0.75; Bertka & Holloway, 1994) have FeO (16-21 wt. %) and MgO (9-24 wt. %) contents comparable to those of the Q-suite parental magmas. The FeO concentrations of DW-Mars melting experiments at ~11 and 14 wt. % MgO, however, are ~2.5 wt. % higher than those of the Q-suite parental magmas, indicating that the mantle source regions of the Q-suite magmas were less Fe-enriched than DW-Mars.

Low-degree, near-solidus melts of DW-Mars, equilibrated with a lherzolitic assemblage have Al_2O_3 contents (11.5-13.0 wt. %) that are significantly higher than those of high-degree melts (4-7.5 wt. %) in equilibrium with a harzburgitic residue. The 9

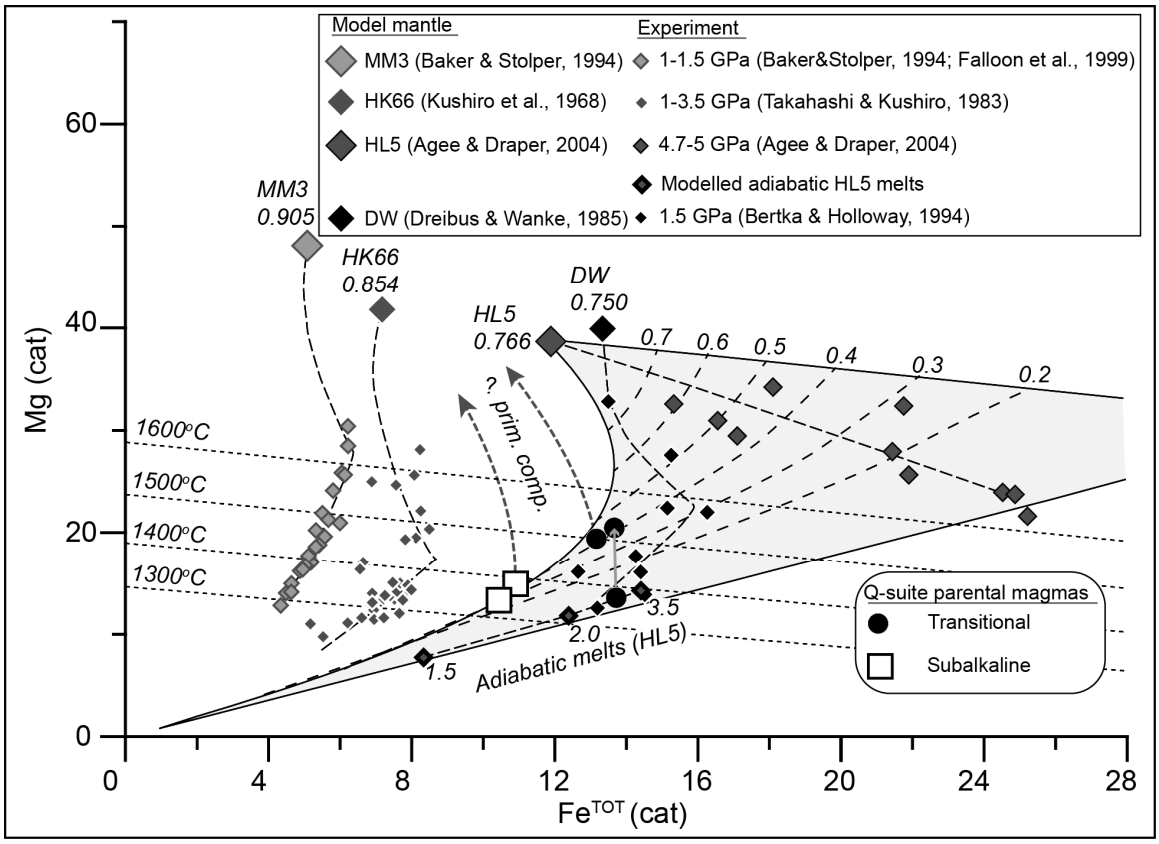

Figure 2-12: Experimental constraints on the genesis of Q-suite magmas.
Mg vs. Fe^{TOT} cation plot comparing the calculated compositions of the Q-suite parental magmas (symbols as in Fig. 2-9) to experimental melt compositions of fertile lherzolite MM3 at 1.0-1.5 GPa (Baker & Stolper, 1994; Falloon *et al.,* 1999), fertile lherzolite HK66 at 0.5-3.5 GPa (Takahashi & Kushiro, 1983), ordinary chondrite Homestead L5 at 4.7-5.0 GPa (Agee & Draper, 2004) and Fe-rich spinel lherzolite DW-Mars at 1.5 GPa (Bertka & Holloway, 1994). The gently sloping lines are isotherms calculated for P = 5 GPa (Putirka et al., 2007) using the anhydrous composition of the transitional Q-suite parental magma. The light grey "sail" - shaped field (calculated after Langmuir & Hanson (1980)) encloses liquid compositions that may coexist with a mantle having the composition of the ordinary chondrite HL5. Dashed contours indicate the melt compositions at fixed intervals of melting (F=0.2-0.7). Adiabatic (batch) melt compositions calculated using alphaMELTS for parcels of HL5 that begin melting at 3.5, 2.0 and 1.5 GPa and terminate at 1.0 Ga are also shown.

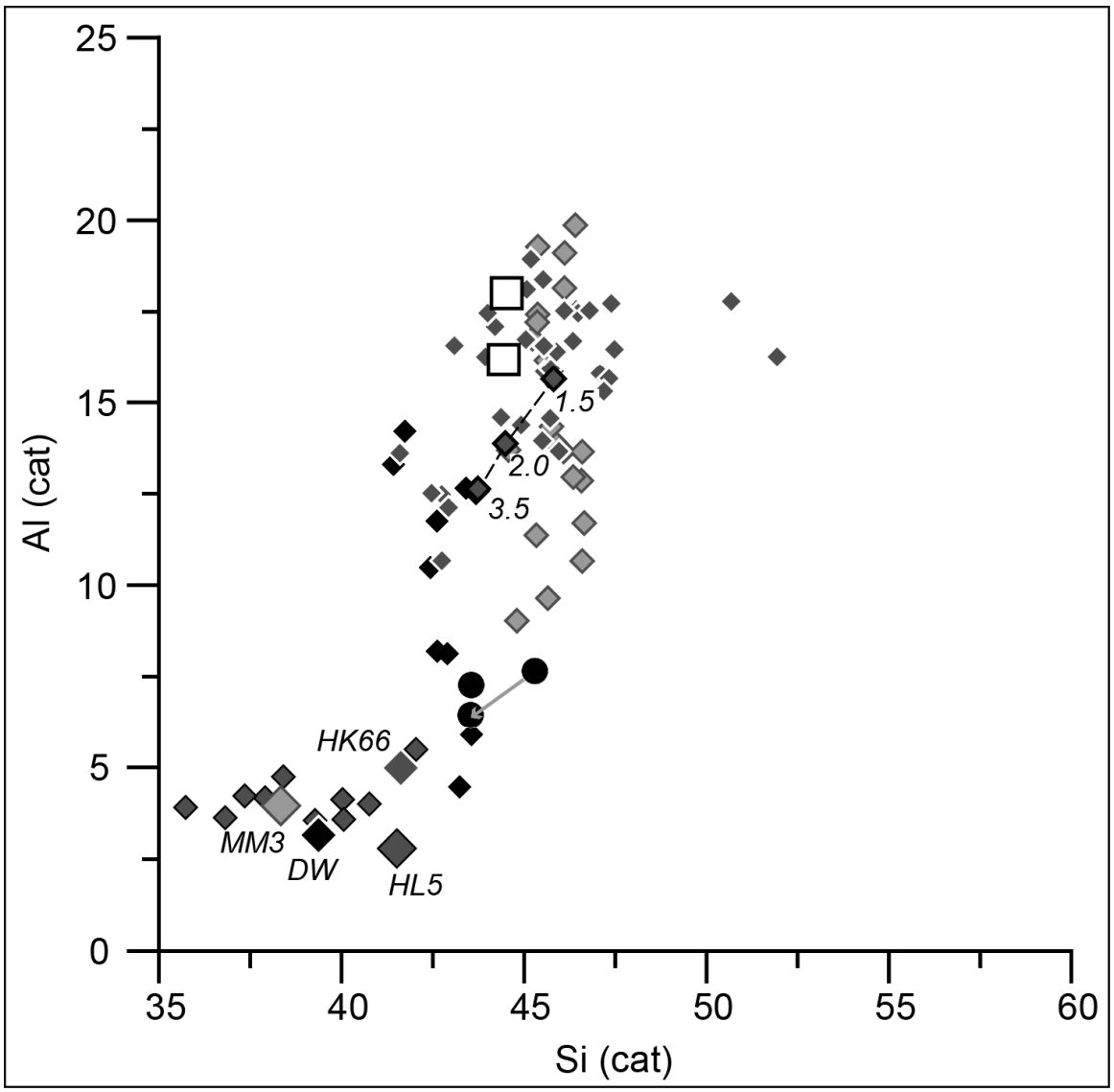

Figure 2-13: Al vs. Si cation plot of the Q-suite parental magmas.
The parental compositions are compared to the compositions of experimental melts of MM3, HK66, DW-Mars, and Homestead L5, as well as the adiabatic melts of HL5, calculated using alphaMELTS. Symbols as in Fig. 2-12.

wt. % difference in Al_2O_3 content between the DW-Mars melts formed by different degrees of partial melting of the same mantle source is within the range of the difference between the subalkaline and transitional Q-suite parental magmas (8-11 wt. %; Fig. 2-13). In contrast to the melts of DW-Mars that also display a decrease in CaO concentrations with increased degrees of melting, the CaO content (<14 wt. %) of the transitional Q-suite parental magma is higher than that of the subalkaline parental magma (~8.5 wt. %), however.

There are two plausible explanations for the high CaO content of the calculated transitional parental magmas. The high CaO concentration may be an artefact of our method for reconstructing parental liquid compositions from bulk chemical analyses of cumulate rocks, which assumes closed system behaviour with no metasomatic effects or movement of interstitial liquid. Alternatively, the high CaO content may reflect the mineralogy of the Fe-rich source. Bertka & Holloway (1994) noted that the solidus clinopyroxene phase in the DW-Mars mantle at 1.5 GPa is pigeonite, which buffers the CaO content of the melt at lower concentrations than Ca-rich clinopyroxene and yields melts that are progressively more depleted in CaO and Al_2O_3. In contrast, mantle sources in which high-Ca clinopyroxene is stable (e.g. Baker & Stolper, 1994) yield melts that get progressively richer in CaO and poorer in Al_2O_3, until the point of clinopyroxene exhaustion. Thus, the difference in CaO and Al_2O_3 concentrations of the subalkaline and transitional Q-suite magmas may reflect the different degrees of melting a mantle source containing high-Ca clinopyroxene.

4.4 The petrogenesis of the Q-suite magmas

The compositional differences between the subalkaline and transitional Q-suite

parental magmas may reflect: 1) melting of mantle domains with different compositions under similar P-T conditions, 2) mixing between ferropicritic and Mg-tholeiitic magmas to generate intermediate Fe contents of the subalkaline Q-suite magmas, or 3) variable degrees of melting of a common Fe-enriched mantle source under different P-T conditions.

If the Ungava's sub-cratonic mantle was characterized by relatively uniform geothermal gradients, the difference in the FeO contents between the subalkaline and transitional Q-suite magmas implies different Mg/Fe ratios and Al_2O_3 contents of their mantle source regions. Assuming that the transitional parental magma approaches a primary melt composition, the primary composition of the subalkaline Q-suite magma with an equivalent liquidus temperature (~1500 °C; Fig. 2-12), calculated by adding olivine, contains ~15 wt. % MgO ~13 wt., % Al_2O_3, and ~14 wt. % FeO^{TOT}. This primary subalkaline ferropicritic magma would have last equilibrated with a source having an Mg-number of ~0.86, slightly higher than the minimum Mg-number (~0.84) of the depleted residue in equilibrium with the primary transitional liquid.

Neoarchean ferropicritic rocks of the southern/western Superior Province are interlayered with komatiites, and tholeiitic and calc-alkaline basalts (Stone *et al.,* 1987; Goldstein & Francis, 2008), indicating near-synchronous emplacement of magmas derived from sources with fundamentally different Fe contents. Furthermore, Kitayama and Francis (in preparation) argued that the Fe-rich volcanics at the top of the Pulpwood-Playter Harbours assemblage are mixtures between tholeiitic and ferropicritic magmas. It is possible, therefore, that the transitional ferropicritic liquids mixed with subalkaline Fe-poor magmas during their emplacement. Such mixing is, however, inconsistent with the

relatively high Al_2O_3 contents of the subalkaline Q-suite parental magmas, which are indistinguishable from the Al_2O_3 contents of Ungava craton's Mg-tholeiites (Maurice *et al.,* 2009).

In a single source scenario, relatively low degree melting of an iron-rich mantle source would produce an Fe-rich, high-Mg basaltic liquid in equilibrium with a garnet-free lherzolitic assemblage. Larger degree melting of an Fe-enriched source to the point of clinopyroxene exhaustion would yield ferropicritic melts in equilibrium with a harzburgitic assemblage, which are rich in CaO, MgO and FeO^{TOT}. A mantle source with an initial Fe/Mg ratio intermediate between the ordinary chondrite Homestead L5 (Mg-number = 0.77) and garnet-pyroxenite HK-66 (Mg-number =0.85) is required to provide melts of comparable Mg and Fe contents to the Q-suite magmas (Fig. 2-12).

If the transitional and subalkaline Q-suite magmas were derived from a common source, then the differences in their compositions must reflect variable degrees of adiabatic decompression melting at upper mantle pressures. The larger degree of melting necessary for the genesis of the transitional magmas requires a longer interval of melting and suggests that melting initiated at a greater depth than that for the subalkaline magmas. Such a geodynamic scenario requires the existence of mantle domains with different potential temperatures. Alternatively, more extensive melting might have been attained underneath relatively thin lithosphere, which permits melting to continue to shallower levels.

Liquids generated through adiabatic decompression become progressively more depleted in FeO, while undergoing only a slight decrease in MgO (Langmuir & Hanson, 1980; Francis *et al.*, 1981), defining shallow positive slopes in MgO vs. FeO diagrams.

Consequently, the significantly higher MgO contents of the transitional Q-suite ferropicrites (Fig. 2-12) suggest that they originated at greater pressures than the Fe-rich basalts parental to the subalkaline Q-suite intrusions (Langmuir & Hanson, 1980). Near-solidus experimental melts of Homestead L5 at ~5 GPa contain ~14 wt. % MgO, comparable to that of the estimated transitional parental magma. Goldstein & Francis (2008) argued that at pressures greater than ~5 GPa ferropicritic liquids become negatively buoyant relative to the surrounding pyrolitic mantle, constraining the corresponding depth (~150 km) as the approximate maximum for the generation of ferropicritic liquids. The melting field calculated for the Homestead L5 composition using the method of Langmuir & Hanson (1980) suggests that a large degree of adiabatic melting (~40 %; Fig. 2-12), initiated at ~5 GPa, is required to generate the MgO and FeO contents of the transitional Q-suite parental magmas from an ordinary chondrite-like composition. Melting of a less Fe-enriched source would shift the melting field towards less Fe-rich compositions and consequently lower the required degree of melting. The ~150 °C temperature difference between the subalkaline and transitional parental liquids calculated at the same pressure (~5 GPa) corresponds to ~45 km difference in average melting depth, assuming a ~110 °C/GPa P-T gradient (Green & Liebermann, 1976) of the dry pyrolitic solidus. Consequently, lower degrees (10-20 %) of adiabatic melting of a mantle source similar in composition to that of the transitional parental magma, initiated at pressures of ~3.5 GPa, could generate MgO and FeO contents similar to those of the subalkaline magmas. The modal proportion of garnet in peridotite is dependant on the bulk pyroxene/ Al_2O_3 ratio, pressure and temperature (Green & Ringwood, 1967). The higher Archean geothermal gradients relative to present (Richter, 1988; Campbell *et al.,*

1989) and the inferred low Al_2O_3 contents of the ferropicrite mantle sources (Hanski & Smolkin, 1995; Stone *et al.,* 1995; Goldstein & Francis, 2008) may have limited garnet stability to pressures ≥3.5 GPa, thus accounting for the relatively undepleted Al_2O_3 contents and the unfractionated HREE of the subalkaline Q-suite magmas. The large-degree of melting suggested in the generation of the transitional parental liquids would have melted garnet out of the harzburgite residue.

High-pressure experimental melts of Homestead L5 (Al_2O_3 = 2.7 wt. %) have low Al_2O_3 contents (3-5 wt. %) regardless of the extent of melting. Melts generated in an adiabatically rising mantle will become progressively richer in both Al_2O_3 and SiO_2. The relatively high Al_2O_3 content of the subalkaline magmas is problematic, however. AlphaMELTS modeled Al_2O_3 contents of the melts of HL5 generated by adiabatic decompression between 3.5-1.0 GPa, contain only ~11.5 wt. % Al_2O_3, significantly lower than the estimated Al_2O_3 content of the subalkaline parental magma. The discrepancy between the modeling results and the higher Al_2O_3 content of the subalkaline Q-suite parental magma may reflect compositional heterogeneities within the Fe-rich mantle domains, the presence of hydrous phases such as amphibole in the upper mantle (<2.5 GPa) that are not well modelled by the pMELTS (Ghiorso *et al.,* 2002) algorithm, or errors associated with modeling of strongly Fe-enriched compositions with AlphaMELTS.

4.5 The significance of Fe-rich magmatism for Neoarchean crustal growth

The origin of the Fe-rich mantle domains in the Archean mantle that produced the predominantly Mg-rich greenstone belts is intriguing. Stone *et al.* (1995) suggested that the source of the Boston Creek flow ferropicrites attained its high Fe content through

metasomatism by small-degree melts rich in Fe and Ti that were derived from a garnet-bearing mantle. Metasomatic enrichment through recycling of subducted banded iron formation (BIF; Sleep, pers. comm.) might be an effective way of increasing the Fe/Mg ratio of pyrolitic mantle. However, the reaction of peridotite with the typically siliceous BIFs at upper mantle pressures would favour the generation of olivine-free pyroxenite (Herzberg, 2011) yielding hypersthene-normative melts incompatible with the transitional Q-suite intrusions. Goldstein & Francis (2008) argued that garnet fractionation from a Hadean magma-ocean would produce a residual, olivine-saturated liquid with a lower Mg-number than that of pyrolite. Alternatively, the Fe-rich domains may originate from the primordial lower mantle and be transported to the upper mantle by deep-seated plumes or catastrophic convective overturn as proposed by Condie (1998).

Finally, the Fe-rich mantle heterogeneities may originate from the infall of Fe-rich meteorites, such as ordinary chondrites. Following the early segregation of Fe into the core within ~100 Myr of the formation of the solar system (Kleine *et al.,* 2004), the Earth was bombarded by rocky planetisimals and meteorites over the ensuing ~0.5 Byr, ending with the intense Late Heavy Bombardment (LHB) ca. 3.85 Ga (Moorbath, 2005; Van Kranendonk *et al.,* 2012). The fate of this extraterrestrial material in the mantle is uncertain; it may have sunk into the lower mantle, homogenized with the predominant pyrolitic mantle, or remained as dispersed and isolated blobs.

Regardless of their origin, the craton-wide distribution of the Q-suite intrusions suggests that Fe-rich mantle melts may have underplated the Ungava proto-craton ca. 2.7 Ga, perhaps extending to other parts of the Superior Province, as much as 1500 km away. The temporal link between the increased production of global juvenile crust ca. 2.7 Ga

(e.g. Condie, 1998, 2000; Rino *et al.,* 2004; Hawkesworth *et al.,* 2009; Condie & Aster, 2010) and the important role of Q-suite magmas in the cratonization of Ungava (Milidragovic & Francis, 2014) suggests that melting of Fe-rich mantle, approaching the composition of the ordinary chondrite, may have had a significant part in Neoarchean crustal growth.

4.6 A geodynamic model for Neoarchean stabilization of the Ungava craton

The stabilization of the Ungava craton occurred during a period of intense ca. 2.78-2.63 Ga global magmatism that generated arguably the largest volume of continental crust in the Earth's history (Condie, 1998; Rino *et al.,* 2004; Condie *et al.,* 2009; Hawkesworth *et al.,* 2009; Condie & Aster, 2010; Van Kranendonk *et al.,* 2012). This event is widely attributed to catastrophic instability, which may have led to mantle overturn (Stein & Hofmann, 1994; Condie, 1998, 2000; Rino *et al.,* 2004). The ca. 2.74-2.70 Ga cratonization of the Northeastern Superior Province was preceded by episodic volcanism beginning ca. 2.88 Ga, with the earliest Fe-rich lavas postdating the Mg-tholeiitic suites by ~100 Myr (Maurice *et al.,* 2009). Calculations by Goldstein & Francis (2008) demonstrate that ferropicritic liquids are significantly more dense than Fe-poor komatiitic liquids. Consequently, at 150 km depth, the net upward-driving force on ferropicritic liquids is less than 20% that on Fe-poor liquids (assuming the density values of ρ_{PREM} = 3.36 g/cm^3, $\rho_{komatiite}$= 3.18 g/cm^3, and $\rho_{ferropicrite}$= 3.33 g/cm^3 of Goldstein & Francis (2008) and the relationship $\frac{\sum F_{ferropicrite}}{\sum F_{komatiite}} = \frac{\rho_{PREM} - \rho_{ferropicrite}}{\rho_{PREM} - \rho_{komatiite}}$, where PREM is the Preliminary Reference Earth Model of (Dziewonski & Anderson, 1981)). Dense, Fe-rich magmas would rise at lower rates relative to the less dense Mg-tholeiites, delaying

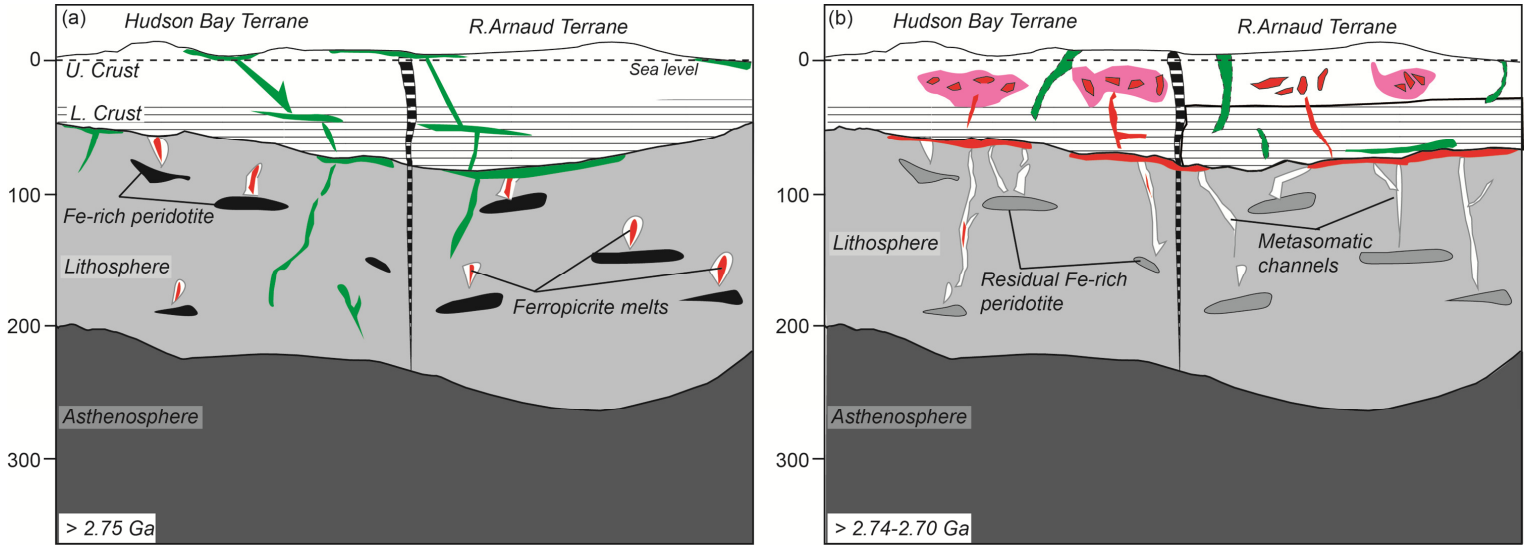

Figure 2-14: A schematic illustrating ca. 2.75-2.70 Ga evolution of the Ungava craton.
(a) ca. 2.75 Ga- Prior to and immediately after the assembly of Hudson Bay and Riviere Arnaud terranes (suture indicated by thick horizontal stripes), Ungava proto-craton was periodically intruded by Mg-rich komatiitic and tholeiitic magmas (green), generated by melting of the underlying lithospheric mantle. Fe-rich heterogeneities (black) within the lithospheric mantle also experienced melting during this time, but due to significantly higher density of ferropicrite magmas (red) their ascent was slowed. In addition, the ascent may have been slowed by the reaction between ferropicrite melts and the depleted harzburgitic mantle, which require the development of metasomatic channels before ferropicrite melt can propagate upward. Ca. 2.78 Ga Fe-rich tholeiites (Maurice et al., 2009) may be samples Fe-rich domains derived by melting at shallow depths. The relatively uncontaminated geochemical signatures of pre-2.75 Ga volcanics, suggest limited interaction between mantle melts and the Ungava proto-craton. **(b)** 2.74 2.70 Ga - By 2.72 Ga ferropicritic magmas, parental to the Q-suite, underplated the Ungava proto-craton, possibly leaving channels of metasomatized peridotite/pyroxenite in the lithopheric mantle. Q-suite magmas were emplaced at middle crustal depths, where they produced zoned plutons and mixed with partially molten proto-cratonic crust to generate the pyroxene-granitoid suite (pink). Some convective overturn in the "softened" proto-craton may have led to dismemberment of the once-continuous supracrustal successions that now form linear greenstone belts.

their emplacement in the crust. During their accent through the mantle, Fe-rich magmas may have carried fragments of highly refractory, melt-depleted mantle, similar to the Ni-rich dunites observed at the Gladel River intrusion. In this scenario, the komatiitic and Mg-tholeiitic volcanism (Maurice *et al.,* 2003, 2009) are the dominant manifestation of the Neoarchean mantle "overturn" event (Fig. 2-14). These magmas likely supplied large amounts of heat to the Ungava proto-craton, leading to its gradual "softening" (Maurice *et al.,* 2009; Milidragovic & Francis, 2014). Iron-rich magmas reached the Ungava proto-craton ca. 2.78 Ga, while it was still relatively cool and anatexis and contamination were minor (Maurice *et al.,* 2009). By 2.72 Ga, virtually all mantle melts at the base of the Ungava craton were Fe-rich. By this time, crustal rocks were partially molten and Fe-rich magmas were extensively contaminated, yielding the LREE-rich volcanic suites and "hybrid" pyroxene-granitoids (Maurice *et al.,* 2009; Milidragovic & Francis, 2014).

5. Conclusions

The intense igneous activity that led to the near-complete re-melting of the Ungava proto-craton ca. 2.74-2.72 Ga was accompanied by craton-wide emplacement of Fe-rich mafic to ultramafic plutons of the Q-suite. The Q-suite plutons are crystal cumulates produced by mantle-derived melts that ranged in composition from transitional ferropicrites to subalkaline, Fe-rich high-Mg basalts. The estimated major element composition of the Q-suite parental magmas indicates that they were derived by partial melting of Fe-rich sources at upper mantle pressures ($\leq$5 GPa). The composition of the mantle source may have been similar to, but slightly less Fe-enriched than, the ordinary chondrite Homestead L5. If the subalkaline and transitional Q-suite magmas were derived from geochemically similar sources, their compositions must reflect a difference in depth

and extent of melting. The smaller-degree subalkaline melts would have been derived at lower pressures by melting of a lherzolitic assemblage. In contrast, the transitional Q-suite magmas may represent harzburgite-equilibrated melts initiated at greater depths. The Q-suite intrusions are characterized by moderate to strong enrichments in LREE relative to HREE, relatively unfractionated HREE, and strong depletions in the HFSE, reflecting in part contamination by crustal anatectic melts. The primary Q-suite magmas, however, had low overall trace element abundances, and were characterized by flat to LREE-depleted profiles.

The synchronous emplacement of the Q-suite intrusions and reworking of the Ungava craton suggests that underplating by anomalously Fe-rich magmas may have been the terminal event in the cratonization of the Northeastern Superior Province. The presence of Fe-rich ultramafic rocks of similar age in the southern and western parts of the Superior Province suggests that melting of Fe-rich mantle domains may have had an important role during the 2.7 Ga peak in continental crust production and recycling.

Acknowledgments

We would like to acknowledge the invaluable assistance by the kind and generous people of the Pituvik Landholding Corporation and Johnny May's Air Charters. We wish to thank Bruno Kieffer, Jane Barling, Vivian Lai and Anaïs Fourny of PCIGR for assistance with sample processing and multi collector ICP-MS measurements. We also acknowledge Bill Minarik for overseeing the whole-rock XRF analyses, and for being a willing discussion participant. This work was supported by the Natural Science and Research Council of Canada grants to D.F and D.W.

Supplementary data

Supplementary data for this paper are available at Journal of Petrology online.

References

Agee, C.B. & Draper, D.S. (2004). Experimental constraints on the origin of Martian meteorites and the composition of the Martian mantle. *Earth and Planetary Science Letters* **224**, 415–429.

Armstrong, R.A., Compston, W., Retief, E.A., Williams, I.S. & Welke, H.J. (1991). Zircon ion microprobe studies bearing on the age and evolution og the Witwatersrand triad. *Precambrian Research* **53**, 243–266.

Arndt, N.T., Nelson, D.R., Compston, W., Trendall, A.F. & Thorne, A.M. (1991) The age of the Fortescue Group, Hammersley Basin, Western Australia, from ion microprobe zircon U-Pb results. *Australian Journal of Earth Sciences* **38**, 261–281.

Baker, M. (2005). Pétrologie et métallogénie de l'indice de Ni-Cu-Co de Qullinaaraaluk et d'intrusions mafiques-ultramafiques du domaine du Lac Minto, sous-province de Minto, Québec. *M.Sc. memoir, Université Laval*, 256 p.

Baker, M.B. & Stolper, E.M. (1994). Determining the compositions of high-pressure melts using diamond aggregates. *Geochimica et Cosmochimica Acta* **58**, 2811–2827.

Barnes, S.J. (1986). The effect of trapped liquid crystallization on cumulus mineral compositions in layered intrusions. *Contributions to Mineralogy and Petrology* **93**, 524–531.

Bédard, J.H. (1994) A procedure for calculating the equilibrium distribution of trace elements among the minerals of cumulate rocks, and the concentration of trace elements in the coexisting liquids. *Chemical Geology* **118**, 143–153.

Bédard, J.H. (2003). Metamorphism in the Archaean Minto Block, Northern Superior Province, Canada. *The Journal of Geology* **111**, 183–205.

Bédard, J.H. (2006). A catalytic delamination-driven model for coupled genesis of Archaean crust and sub-continental lithospheric mantle. *Geochimica et Cosmochimica Acta* **70**, 1188–1214.

Bertka, C.M. & Holloway, J.R. (1994). Anhydrous partial melting of an iron-rich mantle II: primary melt compositions at 15 kbar. *Contributions to Mineralogy and Petrology* **115**, 323–338.

Boily, M., Leclair, A., Maurice, C., Bédard, J.H. & David, J. (2009). Paleo- to Mesoarchean basement recycling and terrane definition in the Northeastern Superior Province, Québec, Canada. *Precambrian Research* **168**, 23–44.

Bouvier, A., Vervoort, J.D. & Patchett, P.J. (2008). The Lu-Hf and Sm-Nd isotopic composition of CHUR: Constraints from unequilibrated chondrites and implications for the bulk composition of terrestrial planets. *Earth and Planetary Science Letters* **273**, 48–57.

Campbell, I.H., Griffiths, R.W. & Hill, R.I. (1989). Melting in an Archean mantle plume: heads it's basalts, tails it's komatiites. *Nature* **339**, 697–699.

Chauvel, C. & Blichert-Toft, J. (2001) A hafnium isotope and trace element perspective on melting of the depleted mantle. *Earth and Planetary Science Letters* **190**, 137–151.

Condie, K.C. (1998). Episodic continental growth and supercontinents: a mantle avalanche connection? *Earth and Planetary Science Letters* **163**, 97–108.

Condie, K.C. (2000). Episodic continental growth models: afterthoughts and extensions. *Tectonophysics* **322**, 153–162.

Condie, K.C. & Aster, R.C. (2010). Episodic zircon age spectra of orogenic granitoids: The supercontinent connection and continental growth. *Precambrian Research* **180**, 227–236.

Condie, K.C., Belousova, E., Griffin, W.L. & Sircombe, K.N. (2009). Granitoid events in space and time: Constraints from igneous and detrital zircon age spectra. *Gondwana Research* **15**, 228–242.

Condie, K.C., Bickford, M.E., Aster, R.C., Belousova, E. & Scholl, D.W. (2011). Episodic zircon ages, Hf isotopic composition, and the preservation rate of continental crust. *Geological Society of America Bulletin* **123**, 951–957.

Corfu, F. & Noble, S.R. (1992). Genesis of the southern Abitibi greenstone belt, Superior Province, Canada: Evidence form zircon Hf-isotope analyses using a single fillament technique. *Geochimica et Cosmochimica Acta* **56**, 2527–2531.

Duuring, P., Bleeker, W., Beresford, S.W., Fiorentini, M.L. & Rosengren, N.M. (2012). Structural evolution of the Agnew-Wiluna greenstone belt, Eastern Yilgarn Craton and implications for komatiite-hosted Ni sulfide exploration. *Australian Journal of Earth Sciences* **59**, 765–791.

Dziewonski, A.M. & Anderson, D.L. (1981). Preliminary reference Earth model. *Physics and Chemistry of the Earth* **25**, 297–356.

Falloon, T.J., Green, D.H., Danyushevsky, L. V. & Faul, U.H. (1999). Peridotite melting at 1.0 and 1.5 GPa: an experimental evaluation of techniques using diamond aggregates and mineral mixes for determination of near-solidus melts. *Journal of Petrology* **40**, 1343–1375.

Faure, S., Daigneault, R. & Godey, S. (2008). Upper mantle architecture of the Archean Superior Province and the implication for the dimension, orientation, metamorphism, and mineralization of the greenstone belts. In: GAC-MAC Joint Annual Meeting, Program with Abstracts **33**, Québec City, Québec, Canada. May 26-28, 2008, p. 55.

Francis, D., Ludden, J., Johnstone, R. & Davis, W. (1999). Picrite evidence for more Fe in Archean mantle reservoirs. *Earth and Planetary Science Letters* **167**, 197–213.

Francis, D.M., Hynes, A.J., Ludden, J.N. & Bédard, J.H. (1981). Crystal fractionation and partial melting in the petrogenesis of a Proterozoic high-MgO volcanic suite, Ungava, Qubéc. *Contributions to Mineralogy and Petrology* **78**, 27–36.

Fujimaki, H. (1986). Partition-Coefficients of Hf, Zr, and REE between Zircon, Apatite, and Liquid. *Contributions to Mineralogy and Petrology* **94**, 42–45.

Ghiorso, M.S., Hirschmann, M.M., Reiners, P.W. & Kress, V.C. (2002). The pMELTS: A revision of MELTS for improved calculation of phase relations and major element partitioning related to partial melting of the mantle to 3 GPa. *Geochemistry, Geophysics, Geosystems* **3**, 1-35.

Ghiorso, M.S. & Sack, R.O. (1995). Chemical mass transfer in magmatic processes IV. A revised and internally consistent thermodynamic model for the interpolation and extrapolation of liquid-solid equilibria in magmatic systems at elevated temperatures and pressures. *Contributions to Mineralogy and Petrology* **119**, 197–212.

Gibson, S.A., Thompson, R.N. & Dickin, A.P. (2000). Ferropicrites: Geochemical evidence for Fe-rich streaks in upwelling mantle plumes. *Earth and Planetary Science Letters* **174**, 355–374.

Goldstein, S.B. & Francis, D. (2008). The Petrogenesis and Mantle Source of Archaean Ferropicrites from the Western Superior Province, Ontario, Canada. *Journal of Petrology* **49**, 1729–1753.

Goldstein, S.L., O'Nions, R.K. & Hamilton, P.J. (1984). A Sm-Nd isotopic study of atmospheric dusts and particulates from major river systems. *Earth and Planetary Science Letters* **70**, 221–236.

Green, D.H. & Liebermann, R.C. (1976). Phase equilibria and elastic properties of a pyrolite model for the oceanic upper mantle. *Tectonophysics* **32**, 61–92.

Green, D.H. & Ringwood, A.E. (1967). The stability fields of aluminous pyroxene peridotite and garnet peridotite and their relevance in upper mantle structure. *Earth and Planetary Science Letters* **3**, 151–160.

Green, J.C. & Schulz, K.J. (1977). Iron-rich basaltic komatiites in the early Precambrian Vermillion District, Minnesota. *Canadian Journal of Earth Sciences* **14**, 2181–2192.

Griffin, W.L., Belousova, E.A., Shee, S.R., Pearson, N.J. & O'Reilly, S.Y. (2004). Archean crustal evolution in the northern Yilgarn Craton: U–Pb and Hf-isotope evidence from detrital zircons. *Precambrian Research* **131**, 231–282.

Hamilton, P.J., O'Nions, R.K., Bridgwater, D. & Nutman, A. (1983). Sm–Nd studies of Archaean metasediments and metavolcanics from West Greenland and their implications for the Earth's early history. *Earth and Planetary Science Letters* **62**, 263–272.

Hanski, E.J. & Smolkin, V.F. (1995). Iron- and LREE-enriched mantle source for early Proterozoic intraplate magmatism as exemplified by the Pechenga ferropicrites, Kola Peninsula, Russia. *Lithos* **34**, 107–125.

Hart, S.R. & Davis, K.E. (1978). Nickel partitioning between olivine and silicate melt. *Earth and Planetary Science Letters* **40**, 203–219.

Hawkesworth, C., Cawood, P., Kemp, T., Storey, C. & Dhuime, B. (2009). A matter of preservation. *Science* **323**, 49–50.

Hawkesworth, C.J., Dhuime, B., Pietranik, A.B., Cawood, P.A., Kemp, A.I.S. & Storey, C.D. (2010). The generation and evolution of the continental crust. *Journal of the Geological* Society **167**, 229–248.

Heinonen, J.S. & Luttinen, A. V. (2008). Jurassic dikes of Vestfjella, western Dronning Maud Land, Antarctica: Geochemical tracing of ferropicrite sources. *Lithos* **105**, 347–364.

Herzberg, C. (2011). Identification of Source Lithology in the Hawaiian and Canary Islands: Implications for Origins. *Journal of Petrology* **52**, 113–146.

Herzberg, C. & Asimow, P.D. (2008). Petrology of some oceanic island basalts: PRIMELT2.XLS software for primary magma calculation. *Geochemistry, Geophysics, Geosystems* **9**, 1-25.

Ichiyama, Y., Ishiwatari, A., Hirahara, Y. & Shuto, K. (2006). Geochemical and isotopic constraints on the genesis of the Permian ferropicritic rocks from the Mino-Tamba belt, SW Japan. *Lithos* **89**, 47–65.

Irvine, T.N. & Baragar, W.R.A. (1971). A Guide to the Chemical Classification of the Common Volcanic Rocks. *Canadian Journal of Earth Sciences* **8**, 523–548.

Kleine, T., Mezger, K., Palme, H. & Münker, C. (2004). The W isotope evolution of the bulk silicate Earth: constraints on the timing and mechanisms of core formation and accretion. *Earth and Planetary Science Letters* **228**, 109–123.

Kuno, H. & Aoki, K. (1970). Chemistry of ultramafic nodules and their bearing on the origin of basaltic magmas. *Physics of the Earth and Planetary Interiors* **3**, 427–436.

Labbé, J., Lacoste, P., Leclair, A., Parent, M. & Davy, J. (2001). The Qullinaaraaluk Ni-Cu-Co showing: a new type of mineralization in the Archean rocks of the Far North. Géologie Quebéc PRO2001-05, 1–11.

Langmuir, C.H. & Hanson, G.N. (1980). An evaluation of major element heterogeneity in the mantle sources of basalts. *Philosophical Transactions of the Royal Society* **A297**, 383–407.

Leake, B.E., Wooley, A.R., Arps, C.E.S., Birch, W.D., Gilbert, M.C., Grice, J.D., Hawthorne, F.., Kato, A., Kisch, H.J., Krivovichev, V.G., Linthout, K., Laird, J., Mandarino, J.A., Maresch, W.V., Nickel, E.., Rock, N.M.S., Schumacher, J.S., Smith, D.C., Stephenson, N.C.N., Whittaker, E.J.W. & Youzhi, G. (1997). Nomenclature of amphiboles: report of the subcommittee on amphiboles of the International Mineralogical Association Commission on New Minerals and Mineral Names. *The Canadian Mineralogist* **35**, 219–246.

Leclair, A. (2008). *Contexte géologique régional du nord-est de la Province du Supérieur*. In: Simard, M. (ed.) *Synthèse Du Nord-Est de La Province Du Supérieur*. Ministère de Ressources Naturelles et de la Faune, Québec MM2008-2, 13–22.

Lugmair, G.W. & Marti, K. (1978). Lunar initial $^{143}Nd/^{144}Nd$: differential evolution of the lunar crust and mantle. *Earth and Planetary Science Letters* **39**, 349-357.

Maurice, C., David, J., Bédard, J.H. & Francis, D. (2009). Evidence for a widespread mafic cover sequence and its implications for continental growth in the Northeastern Superior Province. *Precambrian Research* **168**, 45–65.

Maurice, C., Francis, D. & Madore, L. (2003). Constraints on early Archean crustal extraction and tholeiitic – komatiitic volcanism in greenstone belts of the Northern Superior Province. *Canadian Journal of Earth Sciences* **40**, 431–445.

Milidragovic, D. & Francis, D. (2014). Ferropicrite-driven reworking of the Ungava craton and the genesis of Neoarchean pyroxene-granitoids. *Earth and Planetary Science Letters* **386**, 138–148.

Moorbath, S. (2005). Oldest rocks, earliest life, heaviest impacts, and the Hadean–Archaean transition. *Applied Geochemistry* **20**, 819–824.

O'Neil, J., Carlson, R.W., Francis, D. & Stevenson, R.K. (2008). Neodymium-142 evidence for Hadean mafic crust. *Science* **321**, 1828–1831.

Pearce, J.A. (2008). Geochemical fingerprinting of oceanic basalts with applications to ophiolite classification and the search for Archean oceanic crust. *Lithos* **100**, 14–48.

Pearce, J.A. & Peate, D.W. (1995). Tectonic implications of the composition of volcanic arc magmas. *Annual Review of Earth and Planetary Sciences* **23**, 251–285.

Percival, J.A. & Mortensen, J.K. (2002). Water-deficient calc-alkaline plutonic rocks of Northeastern Superior Province, Canada: significance of charnockitic magmatism. *Journal of Petrology* **43**, 1617–1650.

Percival, J.A., Stern, R.A. & Skulski, T. (2001). Crustal growth through successive arc magmatism: reconnaissance U – Pb SHRIMP data from the Northeastern Superior Province, Canada. *Precambrian Research* **109**, 203– 238.

Polat, A. (2009). The geochemistry of Neoarchean (ca. 2700 Ma) tholeiitic basalts, transitional to alkaline basalts, and gabbros, Wawa Subprovince, Canada: Implications for petrogenetic and geodynamic processes. *Precambrian Research* **168**, 83–105.

Pretorius, W., Weis, D., Williams, G., Hanano, D., Kieffer, B. & Scoates, J. (2006). Complete Trace Elemental Characterisation of Granitoid (USGS G-2, GSP-2) Reference Materials by High Resolution Inductively Coupled Plasma-Mass Spectrometry. *Geostandards and Geoanalytical Research* **30**, 39–54.

Putirka, K. (2008). Thermometers and barometers for volcanic systems. *Reviews in Mineralogy and Geochemistry* **69**, 61–120.

Putirka, K.D., Perfit, M., Ryerson, F.J. & Jackson, M.G. (2007). Ambient and excess mantle temperatures, olivine thermometry, and active vs. passive upwelling. *Chemical Geology* **241**, 177 – 206.

Richter, F.M. (1988). A Major change in the thermal state of the Earth at the Archean-Proterozoic boundary: Consequences for the nature and preservation of continental lithosphere. *Journal of Petrology Special Lithosphere Issue*, 39–52.

Rino, S., Komiya, T., Windley, B.F., Katayama, I., Motoki, A. & Hirata, T. (2004). Major episodic increases of continental crustal growth determined from zircon ages of river sands; implications for mantle overturns in the Early Precambrian. *Physics of the Earth and Planetary Interiors* **146**, 369–394.

Roeder, P.L. & Emslie, R.F. (1970). Olivine-Liquid Equilibrium. *Contributions to Mineralogy and Petrology* **29**, 275–289.

Rudnick, R.L. & Gao, S. (2003). *Composition of the continental crust*. In: Rudnick, R.L. (ed.) *The Crust*, Elsevier, pp. 1–64.

Russell, J.K. & Nicholls, J. (1988). Analysis of petrologic hypotheses with Pearce elemeent ratios. *Contributions to Mineralogy and Petrology* **99**, 25–35.

Schmitz, M.D., Vervoort, J.D., Bowring, S. A. & Patchett, P.J. (2004). Decoupling of the Lu-Hf and Sm-Nd isotope systems during the evolution of granulitic lower crust beneath southern Africa. *Geology* **32**, 405.

Simard, M. (2008). *Stratigraphie et géochronologie du nord-est de la Province du Supérieur*. In: Simard, M. (ed.), *Synthèse Du Nord-Est de La Province Du Supérieur*. Ministère de Ressources Naturelles et de la Faune, Québec MM2008-2, pp. 23–86.

Smith, P.M. & Asimow, P.D. (2005). Adiabat_1ph: A new public front-end to the MELTS, pMELTS, and pHMELTS models. *Geochemistry, Geophysics, Geosystems* **6**, 1–8.

Söderlund, U., Patchett, P.J., Vervoort, J.D. & Isachsen, C.E. (2004). The ^{176}Lu decay constant determined by Lu-Hf and U-Pb isotope systematics of Precambrian mafic intrusions. *Earth and Planetary Science Letters* **219**, 311-324.

Stein, M. & Hofmann, A.W. (1994). Mantle plumes and episodic crustal growth. *Nature* **372**, 63–68.

Stern, R.A., Percival, J.A. & Mortensen, J.K. (1994). Geochemical evolution of the Minto block: a 2. 7 Ga continental magmatic arc built on the Superior proto-craton. *Precambrian Research* **65**, 115–153.

Stone, W.E., Crocket, J.H., Dickin, A.P. & Fleet, M.E. (1995). Origin of Archean ferropicrites: geochemical constraints from the Boston Creek Flow, Abitibi greenstone belt, Ontario, Canada. *Chemical Geology* **121**, 51–71.

Stone, W.E., Jensen, L.S. & Church, W.R. (1987). Petrography and geochemistry of an unusual Fe-rich basaltic komatiite from Boston Township, northeastern Ontario. *Canadian Journal of Earth Sciences* **24**, 2537–2550.

Sun, S.S. & McDonough, W.F. (1989). Chemical and isotopic systematics of oceanic basalts: implications for mantle composition and processes. In: Saunders, A.D. & Norry, M.J. (eds) Magmatism in the Ocean Basins. Geological Society, London, Special Publication **42**, 313-345.

Takahashi, E. & Kushiro, I. (1983). Melting of a dry peridotite at high pressures and basalt magma genesis. *American Mineralogist* **68**, 859–879.

Tuff, J., Takahashi, E. & Gibson, S.A. (2005). Experimental constraints on the role of garnet pyroxenite in the genesis of high-Fe mantle plume derived melts. *Journal of Petrology* **46**, 2023–2058.

Van Kranendonk, M.J., Altermann, W., Beard, B.L., Hoffman, P.F., Johnson, C.M., Kasting, J.F., Melezhik, V.A., Nutman, A.P., Papineau, D. & Pirajno, F. (2012). *A Chronostratigraphic Division of the Precambrian*, In: Gradstein, F.M., Ogg, J.G., Schmitz, M. & Ogg, G. (eds), *The Geologic Time Scale 2012*. Elsevier, 299–392.

Vervoort, J.D., Plank, T. & Prytulak, J. (2011). The Hf–Nd isotopic composition of marine sediments. *Geochimica et Cosmochimica Acta* **75**, 5903–5926.

Von Seckendorff, V. & O'Neill, H.S.C. (1993). An experimental study of Fe-Mg partitioning between olivine and orthopyroxene at 1173, 1273 and 1423 K and 1.6 GPa. *Contributions to Mineralogy and Petrology* **113**, 196–207.

Wall, C.J., Scoates, J.S., Friedman, R.M. & Meurer, W.P. (2012). Age of the Stillwater Complex. *Mineralogical Magazine* **76**, 2506.

Watson, E.B. (1979). Zircon saturation in felsic liquids: experimental results and applications to trace element geochemistry. *Contributions to Mineralogy and Petrology* **419**, 407–419.

Weis, D., Kieffer, B., Maerschalk, C., Barling, J., de Jong, J., Williams, G.A., Hanano, D., Pretorius, W., Mattieli, N., Scoates, J.S., Goolaerts, A., Friedman, R.M. & Mahoney, J.B. (2006). High-precision isotopic characterization of USGS reference materials by TIMS and MC-ICP-MS. *Geochemistry, Geophysics, Geosystems* **7**, 1-30.

Weis, D., Kieffer, B., Hanano, D., Nobre Silva, I., Barling, J., Pretorius, W., Maerschalk, C. & Mattieli, N. (2007). Hf isotope compositions of U.S. Geological Survey reference materials. *Geochemistry, Geophysics, Geosystems* **8**, 1-15.

SUPPLEMENTARY ON-LINE MATERIAL

Table 2-7: Geochemistry of the subalkaline DASH (Q-suite) intrusion

Sample	DH-03B	DH-05	DH-06	DH-07	DH-08	DH-09	DH-10	DH-11	DH-13	DH-14	DH08-3	DH08-5	DH08-6
Zone	18	18	18	18	18	18	18	18	18	18	18	18	18
Easting	359203	359198	359190	359182	359175	359153	359153	359143	359135	359134	359137	359156	359173
Northing	6460881	6460876	6460862	6460825	6460812	6460817	6460817	6460816	6460820	6460823	6460804	6460806	6460807
Lithology	*gabnor*	*web*	*web*	*perid*	*harzb*	*perid*	*web*	*web*	*web*	*web*	*web*	*web*	*perid*
Major elements (wt. %)													
SiO_2	56.86	50.47	51.86	45.78	39.24	38.23	50.47	51.58	57.51	58.77	56.18	51.11	46.62
TiO_2	0.22	0.16	0.25	0.17	0.09	0.07	0.2	0.23	0.29	0.36	0.25	0.22	0.17
Al_2O_3	11.56	3.3	5.69	3.24	2.53	2.03	4.16	4.8	6.22	6.75	5.84	4.12	3.4
MgO	9.03	24.34	18.46	25.74	32.6	30.01	22.29	18.66	13.75	12.38	15.63	18.39	22.85
FeO	6.8	11.71	8.94	10.1	13.48	13.29	8.34	9.96	7.51	7.71	8	8.11	9.47
MnO	0.12	0.21	0.17	0.14	0.16	0.18	0.12	0.18	0.16	0.15	0.15	0.19	0.2
CaO	8.29	6.8	10.34	8.4	1.09	3.12	7.96	9.67	10.45	9.89	8.98	14.58	11.53
Na_2O	2.86	0.33	0.98	0.43	0.18	0.2	0.62	1.07	1.49	1.58	1.17	0.65	0.51
K_2O	1.76	0.25	0.61	0.11	0.17	0.11	0.23	0.53	1.25	1.27	1.85	0.17	0.11
P_2O_5	0.03	0.02	0.06	0.03	0.03	0.03	0.04	0.11	0.07	0.09	0.05	0.03	0.02
LOI	1.76	1.29	1.57	4.55	9.15	11.11	3.92	1.87	0.65	0.59	0.84	1.55	3.91
Total	99.35	99.2	99.19	99.07	99.15	98.75	98.97	99.06	99.52	99.68	99.23	99.37	99.28
Trace elements (ppm)													
S	-	-	-	3650	-	-	-	-	-	-	-	-	-
Th	0.8	1.12	1.2	0.25	0.73	0.41	0.62	2.88	0.68	4.81	-	-	-
U	0.14	0.17	0.21	0.08	0.1	0.07	0.1	0.3	0.06	0.09	-	-	-
Rb	51.1	11.9	29.2	3.2	8.1	1.9	9.6	18	40.3	47.4	67	3.9	2.7
Ba	720.8	58	74.8	32.8	53.7	33.9	56.2	335.5	435.2	383.5	647.7	34.6	38.2
Pb	7.7	2	2.4	3.2	3.5	<1.0	1.2	4	5.2	5.8	5.4	2.5	2.6
Sr	287.7	28.8	103	68	40.7	64.5	76.8	172.4	100.4	110.5	106.9	91.3	79.1
Nb	1.8	0.7	1.6	0.3	0.5	0.4	0.3	0.9	1.8	2.6	2.1	0.3	<0.3
Ta	0.02	0.02	0.08	<0.01	0.03	0.01	0.01	0.02	0.03	0.04	-	-	-
Zr	39.6	12.6	23.4	13.0	1.0	9.0	14.3	37.1	57.2	101.1	68.0	12.3	10.0
Hf	2.1	0.5	0.9	0.4	0.3	0.2	0.5	1.3	2.2	2.1	-	-	-
Y	13.7	4.2	7.4	4.6	1.8	1.5	5.3	6	7.3	8.1	6.1	6.1	5.2
Cr	347	1414	1496	1723	1648	1358	3642	1589	974	875	1434	1155	2261
Ni	88	967	507	1051	1572	1283	651	1406	189	173	699	643	1173
La	17	4.92	14.8	2.64	3.27	3.19	4.45	19.6	22.2	41.1	-	-	-
Ce	44.2	10.9	31.2	5.84	6.53	6.07	8.56	41.7	43.3	79.4	-	-	-
Pr	5.74	1.15	3.14	0.74	0.68	0.63	1.01	4.56	4.35	7.83	-	-	-
Nd	23.7	4.6	11.1	3.6	2.49	2.32	4.69	16.3	15.3	24.5	-	-	-
Sm	5.69	1.07	2.25	1.05	0.5	0.5	1.26	3.21	3.08	4.41	-	-	-
Eu	0.72	0.227	0.51	0.31	0.14	0.11	0.34	0.75	0.65	0.67	-	-	-
Gd	4.16	0.87	1.76	0.9	0.41	0.39	1.14	2.18	2.24	3.1	-	-	-
Tb	0.59	0.14	0.27	0.15	0.05	0.05	0.18	0.26	0.3	0.38	-	-	-
Dy	2.95	0.77	1.54	0.82	0.3	0.28	1.05	1.28	1.56	1.85	-	-	-
Ho	0.53	0.15	0.3	0.16	0.06	0.05	0.21	0.22	0.28	0.32	-	-	-
Er	1.4	0.42	0.84	0.43	0.18	0.15	0.59	0.61	0.76	0.83	-	-	-
Tm	0.19	0.061	0.12	0.063	0.027	0.022	0.084	0.087	0.11	0.115	-	-	-
Yb	1.17	0.39	0.73	0.4	0.19	0.14	0.54	0.54	0.65	0.71	-	-	-
Lu	0.18	0.062	0.11	0.065	0.033	0.024	0.085	0.081	0.096	0.11	-	-	-

Table 2-7: Subalkaline DASH (Q-suite) intrusion (cont.)

Sample	DH08-7	DH08-8	DH08-9	DH08-10	DH08-11	DH08-12
Zone	18	18	18	18	18	18
Easting	359177	359200	359211	359216	359190	359201
Northing	6460809	6460809	6460802	6460811	6460867	6460889
Lithology	*harzb*	*perid*	*perid*	*perid*	*web*	*gabnor*
Major elements (wt. %)						
SiO_2	38.38	42.29	41.27	42.64	52.05	50.1
TiO_2	0.1	0.15	0.17	0.18	0.29	0.48
Al_2O_3	2.78	2.97	2.9	3.4	5.74	14.24
MgO	32.82	28.09	28.51	25.06	16.86	9.46
FeO	13.42	11.2	13.34	12.24	7.82	8.65
MnO	0.17	0.2	0.2	0.18	0.16	0.17
CaO	1.64	5.3	3.52	7.98	12.66	10.17
Na_2O	0.25	0.37	0.37	0.46	1.04	3.2
K_2O	0.22	0.14	0.1	0.11	0.92	0.94
P_2O_5	0.03	0.03	0.03	0.03	0.05	0.1
LOI	8.76	7.93	8.04	5.95	1.43	1.52
Total	98.95	99.09	98.84	98.66	99.31	99.2
Trace elements (ppm)						
S	-	1175	-	-	-	-
Th	0.76	-	0.9	-	-	-
U	0.18	0	0.13	-	-	-
Rb	7.9	5.2	2.7	2.8	55.5	11.6
Ba	83.5	49.8	50.3	41.7	137	266.9
Pb	3.2	2.1	2.5	2.8	7.5	13.1
Sr	62.6	53.3	58.4	74.1	105.5	268.2
Nb	0.5	0.4	0.4	0.5	2.2	1.9
Ta	0.06	-	0.62	-	-	-
Zr	16.0	12.0	22	11.9	33.4	41.6
Hf	0.4	-	0.5	-	-	-
Y	2.2	4.4	3.3	4.8	9.3	10.5
Cr	1590	1993	1692	1560	1643	909
Ni	1184	980	1164	1684	375	151
La	4.01	-	3.37	-	-	-
Ce	8.26	-	7.52	-	-	-
Pr	0.92	-	0.92	-	-	-
Nd	3.85	-	4.17	-	-	-
Sm	0.7	-	0.89	-	-	-
Eu	0.18	-	0.24	-	-	-
Gd	0.57	-	0.78	-	-	-
Tb	0.08	-	0.12	-	-	-
Dy	0.43	-	0.68	-	-	-
Ho	0.09	-	0.14	-	-	-
Er	0.24	-	0.38	-	-	-
Tm	0.041	-	0.051	-	-	-
Yb	0.25	-	0.37	-	-	-
Lu	0.024	-	0.038	-	-	-

Table 2-8: Geochemistry of the subalkalkine Pinguk Hill (Q-suite) intrusion

Sample	PK-1	PK-2	PK-3	PK-4	PK09-1	PK09-2	PK09-3	PK09-4	PK09-5	PK09-6	PK09-7	PK09-8	PK09-10
Zone	18	18	18	18	18	18	18	18	18	18	18	18	18
Easting	355427	355588	355669	356031	356360	356320	356285	356237	356198	356169	356122	356155	355597
Northing	6471416	6471627	6472095	6472583	6473144	6473162	6473205	6473230	6473268	6473303	6473357	6470136	6471295
Lithology	*web*	*gabnor*	*web*	*gabnor*	*gabnor*	*gabnor*	*gabnor*	*gabnor*	*gabnor*	*gabnor*	*gabnor*	*web*	*web*
Major elements (wt. %)													
SiO_2	50.21	53.08	51.41	51.58	46.02	45.03	45.33	47.77	49.05	47.77	51.79	52.09	51.54
TiO_2	0.24	0.56	0.33	0.23	0.86	0.93	0.89	0.67	0.56	0.71	0.26	0.23	0.3
Al_2O_3	8.35	11.01	7.04	17.66	18.09	17.49	17.84	18.3	18.99	17.43	19.05	4.11	6.12
MgO	14.21	10.57	15.44	7.44	5.58	5.82	5.7	6.49	6.38	6.93	7.95	18.95	16.43
FeO	8.9	9.6	9.2	6.97	14.34	15.09	14.34	12.04	11.01	13.04	8.18	9.14	9.13
MnO	0.19	0.17	0.19	0.15	0.14	0.14	0.14	0.15	0.15	0.17	0.18	0.21	0.18
CaO	13.46	10.54	13.44	10.78	10.86	10.91	10.95	10.76	10.1	10.45	9.02	13.8	13.01
Na_2O	1.36	1.94	1.11	2.95	2.69	2.73	2.79	2.58	2.85	2.57	2.96	0.68	0.92
K_2O	0.43	1.19	0.2	0.47	0.3	0.43	0.5	0.25	0.31	0.31	0.43	0.15	0.32
P_2O_5	0.03	0.04	0.08	0.05	0.03	0.03	0.03	0.02	0.03	0.03	0.03	0.02	0.04
LOI	1.32	0.33	0.67	0.86	0.16	0.15	0.24	0.19	0.14	0.2	0.13	0.29	1.57
Total	98.77	99.08	99.28	99.15	99.07	98.76	98.76	99.23	99.57	99.63	100	99.83	99.66
Trace elements (ppm)													
S	-	-	-	-	-	-	-	-	-	-	-	-	-
Th	1.07	-	0.41	-	-	-	-	-	-	-	-	-	-
U	0.2	-	0.05	-	-	-	-	-	-	-	-	-	-
Rb	12.2	48.7	<1.0	4.3	7.3	4.7	5.9	5.7	6.6	5	6.1	3.1	10.2
Ba	104.8	207.5	57.1	135.8	132.2	122.5	125.8	104.9	123.9	112.4	141.1	<10.8	50.8
Pb	2.1	5.9	1.2	5.2	1	3.2	2.9	<1.0	2.3	<1.0	1.4	<1.0	2.2
Sr	221.7	296.8	188.4	585.4	720.2	693.9	715.4	731.9	777.7	703.9	668.8	72.2	115
Nb	0.6	2.1	0.9	1.2	0.6	0.9	0.7	0.5	0.7	0.6	0.7	0.5	0.8
Ta	0.04	-	0.04	-	-	-	-	-	-	-	-	-	-
Zr	16	42.5	21.3	13	8.4	8.1	6.8	5.8	6.9	8.4	8.6	11	20.2
Hf	0.6	-	0.9	-	-	-	-	-	-	-	-	-	-
Y	7.9	7.9	9.7	8.4	6	6.3	5.9	5.6	5	6.2	4.8	7.2	9
Cr	416.3	311.7	863.5	38.4	20.6	15.7	13.9	32.9	36.1	31.9	63	846	628.3
Ni	109	86	352	35	10	9	13	26	16	54	56	244	170
La	6.24	-	7.15	-	-	-	-	-	-	-	-	-	-
Ce	13.9	-	17.8	-	-	-	-	-	-	-	-	-	-
Pr	1.76	-	2.34	-	-	-	-	-	-	-	-	-	-
Nd	8.22	-	10.7	-	-	-	-	-	-	-	-	-	-
Sm	2.03	-	2.51	-	-	-	-	-	-	-	-	-	-
Eu	0.56	-	0.64	-	-	-	-	-	-	-	-	-	-
Gd	1.88	-	2.19	-	-	-	-	-	-	-	-	-	-
Tb	0.28	-	0.33	-	-	-	-	-	-	-	-	-	-
Dy	1.53	-	1.88	-	-	-	-	-	-	-	-	-	-
Ho	0.31	-	0.38	-	-	-	-	-	-	-	-	-	-
Er	0.87	-	1.03	-	-	-	-	-	-	-	-	-	-
Tm	0.13	-	0.15	-	-	-	-	-	-	-	-	-	-
Yb	0.78	-	0.99	-	-	-	-	-	-	-	-	-	-
Lu	0.10	-	0.13	-	-	-	-	-	-	-	-	-	-

Table 2-8: Subalkaline Pinguk Hill (Q-suite) intrusion (cont.)

Sample	PK09-11	PK09-12	PK09-14	PK09-16	PK09-17	PK09-18	PK09-21
Zone	18	18	18	18	18	18	18
Easting	355597	355597	356107	355794	355746	355789	354886
Northing	6471295	6471295	6469901	6469801	6469786	6469860	6471946
Lithology	*web*	*web*	*web*	*web*	*web*	*web*	*web*
Major elements (wt. %)							
SiO_2	51.79	50.19	52.52	49.63	48.56	50.00	51.94
TiO_2	0.29	0.29	0.22	0.24	0.27	0.24	0.26
Al_2O_3	6.22	6.27	3.84	7.34	3.39	6.08	5.39
MgO	16.67	16.38	19.14	15.00	22.27	16.12	16.33
FeO	9.42	8.88	8.86	9.9	10.34	11.32	9.34
MnO	0.20	0.20	0.21	0.23	0.19	0.21	0.22
CaO	12.84	13.36	14.01	13.02	12.91	11.33	14.23
Na_2O	1.11	0.84	0.62	1.36	0.47	1.30	0.99
K_2O	0.34	0.28	0.11	0.22	0.19	0.34	0.36
P_2O_5	0.04	0.04	0.03	0.03	0.04	0.04	0.03
LOI	0.67	2.92	0.33	2.66	0.69	1.42	0.80
Total	99.71	99.75	100.06	99.7	99.59	99.15	100.05
Trace elements (ppm)							
S	-	-	-	-	-	-	-
Th	-	-	-	-	0.62	-	-
U	-	-	-	-	0.1	-	-
Rb	14.2	11.7	3.3	3.3	5.1	10.2	14.4
Ba	76.6	52.1	20.7	<10.8	62.7	41	35.4
Pb	2.8	1.5	2.3	2.2	2.1	8.6	1.3
Sr	141.2	95.9	74.1	61.9	81.5	107.6	117
Nb	0.7	0.7	0.3	1.5	0.9	1	1.3
Ta	-	-	-	-	<0.01	-	-
Zr	18.7	22.2	12.9	30.8	24.1	20	17.7
Hf	-	-	-	-	0.6	-	-
Y	9	9	7.1	14.2	6.5	7.3	10.8
Cr	601.1	618.8	1030	274.9	1454	2131	918.5
Ni	173	165	196	153	490	3405	183
La	-	-	-	-	6.55	-	-
Ce	-	-	-	-	14.7	-	-
Pr	-	-	-	-	2.15	-	-
Nd	-	-	-	-	10.1	-	-
Sm	-	-	-	-	2.13	-	-
Eu	-	-	-	-	0.51	-	-
Gd	-	-	-	-	1.64	-	-
Tb	-	-	-	-	0.25	-	-
Dy	-	-	-	-	1.28	-	-
Ho	-	-	-	-	0.25	-	-
Er	-	-	-	-	0.69	-	-
Tm	-	-	-	-	0.10	-	-
Yb	-	-	-	-	0.62	-	-
Lu	-	-	-	-	0.11	-	-

Table 2-9: Geochemistry of the subalkaline Lac Muraalaavik (Q-suite) intrusions

Sample	LM1-1	LM1-2	LM1-3	LM1-4	LM1-5	LM1-6	LM1-8	LM2-1	LM2-2	LM2-3	LM2-4	LM2-5	LM2-6
Zone	18	18	18	18	18	18	18	18	18	18	18	18	18
Easting	433888	433875	433861	433841	433806	433779	433742	434173	434180	434186	434193	434206	434171
Northing	6488688	6488688	6488684	6488671	6488657	6488659	6488668	6492037	6492036	6492037	6492035	6492038	6492089
Lithology	*gabnor*	*web*	*gabnor*	*web*	*web*	*gabnor*	*gabnor*	*gabnor*	*web*	*web*	*perid*	*web*	*web*
Major elements (wt. %)													
SiO_2	41.44	48.07	45.55	48.99	49.12	39.90	44.67	49.01	51.26	50.02	47.00	50.45	49.48
TiO_2	1.33	0.67	1.07	0.38	0.35	1.47	1.57	0.47	0.33	0.38	0.21	0.37	0.34
Al_2O_3	15.08	8.20	17.81	6.83	6.14	12.64	15.13	20.05	5.90	6.62	3.72	6.30	4.77
MgO	7.56	13.96	5.91	15.34	16.43	8.29	6.44	6.29	14.03	15.2	25.6	16.1	18.79
FeO	18.24	11.92	12.66	9.48	9.82	20.48	15.61	7.96	7.29	8.62	15.21	10.6	12.16
MnO	0.17	0.19	0.14	0.17	0.17	0.17	0.21	0.12	0.16	0.17	0.23	0.21	0.18
CaO	9.41	13.19	9.87	14.73	14.52	11.61	8.58	9.63	17.27	15.25	5.09	12.52	10.63
Na_2O	1.88	1.07	3.14	1.03	0.76	1.04	2.9	3.06	1.12	1.00	0.33	1.04	0.50
K_2O	2.08	0.77	1.10	0.65	0.63	1.21	1.59	1.10	0.72	0.82	0.18	0.68	0.36
P_2O_5	0.08	0.08	0.37	0.12	0.10	0.14	0.17	0.12	0.06	0.07	0.04	0.06	0.04
LOI	1.43	0.91	1.42	1.45	1.15	1.38	1.65	1.73	1.32	1.42	1.45	0.72	1.45
Total	98.73	99.24	99.03	99.44	99.46	98.35	98.53	99.57	99.86	99.85	99.4	99.23	98.89
Trace elements (ppm)													
S	-	-	-	-	-	-	-	-	-	-	1475	-	-
Th	-	-	-	-	-	-	-	-	1.75	-	0.21	-	-
U	-	-	-	-	-	-	-	-	0.32	-	0.06	-	-
Rb	139.7	27.1	42.7	18.6	23.9	70	75.9	36.4	35.5	34	5.4	35.3	16.7
Ba	350.6	159.2	201.3	92.3	107.5	203	302.4	308.1	134.8	215.6	53.6	134.2	87.6
Pb	4.8	3.7	7.7	1.5	2.9	3.5	4.4	3.9	3	4.2	2.5	2.9	2.1
Sr	404.2	171.9	656.2	77.9	88.2	497.3	479.3	795.3	158	157.8	57.4	161.4	58.3
Nb	1.7	2.5	6.4	1.7	1.3	1.1	5.3	2.9	1.3	1.3	<0.3	1.4	0.7
Ta	-	-	-	-	-	-	-	-	0.09	-	<0.01	-	-
Zr	30.7	43.8	44.1	41.2	37.3	27.7	39.3	39.9	28.9	36.4	13.0	29.7	27
Hf	-	-	-	-	-	-	-	-	0.9	-	0.3	-	-
Y	9.4	14.8	20.5	11.4	10.7	10.7	15.7	11.8	10.3	10.7	4.1	12	8.8
Cr	42.9	1174	23.9	1582	1637	62.8	51.8	52.1	2612	1695	1764	994.9	738.1
Ni	78	271	37	256	302	69	76	62	205	291	680	321	623
La	-	-	-	-	-	-	-	-	10	-	2.51	-	-
Ce	-	-	-	-	-	-	-	-	19.3	-	5.09	-	-
Pr	-	-	-	-	-	-	-	-	2.62	-	0.73	-	-
Nd	-	-	-	-	-	-	-	-	12.1	-	3.49	-	-
Sm	-	-	-	-	-	-	-	-	2.76	-	0.83	-	-
Eu	-	-	-	-	-	-	-	-	0.77	-	0.24	-	-
Gd	-	-	-	-	-	-	-	-	2.41	-	0.79	-	-
Tb	-	-	-	-	-	-	-	-	0.37	-	0.12	-	-
Dy	-	-	-	-	-	-	-	-	2.02	-	0.74	-	-
Ho	-	-	-	-	-	-	-	-	0.41	-	0.16	-	-
Er	-	-	-	-	-	-	-	-	1.22	-	0.50	-	-
Tm	-	-	-	-	-	-	-	-	0.18	-	0.080	-	-
Yb	-	-	-	-	-	-	-	-	1.06	-	0.55	-	-
Lu	-	-	-	-	-	-	-	-	0.18	-	0.091	-	-

Table 2-9: Subalkaline Lac Muraalaavik (Q-suite) intrusions (cont.)

Sample	LM2-9	LM2-10	LM2-11	LM3-1	LM3-2	LM3-3	LM3-4	LM3-5	LM3-5*	LM3-6	LM3-7	LM3-8	LM3-9
Zone	18	18	18	18	18	18	18	18	18	18	18	18	18
Easting	434088	434116	434129	440102	439199	439299	439401	439483	439483	439573	439569	439512	439659
Northing	6492164	6492175	6492172	6491570	6490163	6490192	6490283	6490421	6490421	6490525	6490750	6490843	6490883
Lithology	*web*	*gabnor*	*web*	*gabnor*	*web*	*web*	*web*	*web*	*web*	*web*	*web*	*web*	*web*
Major elements (wt. %)													
SiO_2	49.95	47.66	49.61	50.36	51.3	51.43	51.17	49.61	-	49.55	50.66	50.23	50.38
TiO_2	0.41	0.81	0.41	0.30	0.21	0.21	0.23	0.35	-	0.29	0.32	0.32	0.34
Al_2O_3	6.29	18.89	5.49	10.64	3.56	3.38	3.69	4.79	-	4.71	6.72	7.04	6.97
MgO	14.54	6.25	15.9	13.08	18.21	18.04	17.48	17.68	-	17.58	14.28	14.47	14.35
FeO	10.35	9.87	10.69	7.93	6.7	6.67	7.26	9.5	-	9.44	7.94	7.87	8.28
MnO	0.20	0.12	0.19	0.17	0.17	0.17	0.18	0.2	-	0.2	0.17	0.17	0.18
CaO	13.34	10.2	14.22	13.61	18.09	18.6	17.94	16.38	-	16.22	17.29	17.18	17.48
Na_2O	0.87	2.74	0.78	0.96	0.46	0.42	0.44	0.53	-	0.54	0.62	0.58	0.58
K_2O	0.60	0.93	0.55	0.83	0.17	0.13	0.17	0.22	-	0.25	0.32	0.29	0.31
P_2O_5	0.07	0.27	0.06	0.06	0.03	0.02	0.03	0.03	-	0.03	0.04	0.03	0.03
LOI	2.35	1.52	0.86	1.33	0.30	0.38	0.81	0.25	-	0.34	1.19	1.19	0.71
Total	99.05	99.27	98.89	99.39	99.61	99.72	99.58	99.68	-	99.28	99.64	99.46	99.67
Trace elements (ppm)													
S	-	-	-	-	-	-	-	-	-	-	-	-	-
Th	-	0.80	-	-	-	-	-	0.81	0.93	0.96	-	0.75	-
U	-	0.13	-	-	-	-	-	0.22	0.26	0.27	-	0.2	-
Rb	28.1	27.6	24.6	38.9	4.5	5.3	7.7	8.5	-	8.4	11.5	9.9	13.1
Ba	103.6	290.2	110.8	110.8	<10.8	<10.8	<10.8	13.5	-	26.1	21.4	26.7	20.5
Pb	16.9	4.7	2	2.3	<1.0	2.5	2.2	2	-	2.3	21.2	2.4	1.2
Sr	120.3	764.8	104.9	299.5	67.4	60.8	63.7	83	-	84.9	139.2	153.4	150.5
Nb	1.7	5.1	1.2	1	0.4	0.4	0.4	0.6	0.67	0.8	0.9	0.6	0.8
Ta	-	0.2	-	-	-	-	-	0.02	0.05	0.02	-	0.01	-
Zr	32.6	60	32.3	26.6	12.7	12.7	15	22.8	22.98	23.8	24.3	20.8	21
Hf	-	2	-	-	-	-	-	0.8	0.91	0.7	-	0.7	-
Y	13.0	16.4	12	9.3	6.6	6.7	7.5	9.8	11.39	8.9	9.3	9.2	10.5
Cr	329.5	36.4	529.9	752.1	2541	1606	1099	802.6	-	776.4	540.5	442.3	316.4
Ni	295	62	393	136	226	220	229	213	-	207	140	114	83
La	-	27.9	-	-	-	-	-	4.87	4.84	5.55	-	5.15	-
Ce	-	58.4	-	-	-	-	-	12.00	13.86	12.8	-	11.7	-
Pr	-	7.56	-	-	-	-	-	1.94	2.08	1.95	-	1.8	-
Nd	-	29.9	-	-	-	-	-	9.99	10.34	9.45	-	9.03	-
Sm	-	5.48	-	-	-	-	-	2.46	2.69	2.36	-	2.28	-
Eu	-	1.20	-	-	-	-	-	0.58	0.67	0.54	-	0.57	-
Gd	-	3.99	-	-	-	-	-	2.14	2.51	2.03	-	2.05	-
Tb	-	0.55	-	-	-	-	-	0.33	0.35	0.31	-	0.32	-
Dy	-	2.85	-	-	-	-	-	1.80	2.16	1.71	-	1.73	-
Ho	-	0.55	-	-	-	-	-	0.37	0.40	0.35	-	0.35	-
Er	-	1.73	-	-	-	-	-	1.09	1.13	1.01	-	1.05	-
Tm	-	0.26	-	-	-	-	-	0.16	0.17	0.15	-	0.15	-
Yb	-	1.58	-	-	-	-	-	0.96	1.05	0.91	-	0.94	-
Lu	-	0.26	-	-	-	-	-	0.15	0.15	0.14	-	0.15	-

Table 2-9: Subalkaline Lac Muraalaavik (Q-suite) intrusions (cont.)

Sample	LM3-10	LM3-11	LM3-12	LM3-13	LM3-14	LM3-15	LM3-16	LM4-2	LM4-3	LM4-4	LM4-5	LM4-6	LM4-8
Zone	18	18	18	18	18	18	18	18	18	18	18	18	18
Easting	439898	439008	439023	438980	438981	440283	440156	439596	439602	439661	439700	439741	438721
Northing	6490746	6490276	6490410	6490612	6490824	6491730	6491348	6497034	6497035	6496918	6496830	6496820	6496111
Lithology	*web*	*gabnor*	*web*	*web*	*web*	*web*	*web*	*perid*	*web*	*web*	*gabnor*	*web*	*gabnor*
Major elements (wt. %)													
SiO_2	51.04	45.27	43.64	51.11	51.49	50.94	50.6	42.42	49.59	50.96	48.86	52.01	49.59
TiO_2	0.31	0.80	0.29	0.26	0.29	0.32	0.39	0.16	0.31	0.25	0.24	0.42	0.33
Al_2O_3	5.68	18.31	5.08	4.43	4.92	6.48	7.96	4.33	5.40	5.71	20.58	6.34	12.26
MgO	16.12	7.02	15.98	16.75	17.26	15.35	13.46	27.11	18.76	15.44	7.16	13.82	13.46
FeO	9.37	11.67	6.93	7.74	9.62	8.70	8.67	13.29	9.19	6.91	5.78	7.86	8.59
MnO	0.21	0.15	0.21	0.18	0.22	0.21	0.18	0.21	0.17	0.18	0.13	0.21	0.18
CaO	15.43	11.04	18.29	17.67	14.27	13.53	15.25	4.97	13.57	16.64	9.00	14.97	12.87
Na_2O	0.55	1.94	0.84	0.55	0.54	1.21	0.93	0.47	0.61	1.29	3.05	1.53	1.07
K_2O	0.23	0.88	0.28	0.33	0.32	0.37	1.00	0.25	0.34	0.55	1.97	0.25	0.34
P_2O_5	0.03	0.12	0.03	0.03	0.03	0.02	0.05	0.05	0.04	0.07	0.09	0.08	0.04
LOI	0.52	1.70	7.20	0.69	0.30	1.92	1.12	5.38	1.35	1.17	2.75	2.11	0.98
Total	99.59	98.9	99.07	99.89	99.34	99.11	99.66	98.8	99.53	99.61	99.64	99.83	99.78
Trace elements (ppm)													
S	-	-	-	-	-	-	-	-	-	-	-	-	-
Th	-	-	-	-	0.80	-	-	0.90	-	1.37	-	-	-
U	-	-	-	-	0.25	-	-	0.16	-	0.29	-	-	-
Rb	8.3	34.4	4	18.9	16.4	8.4	29.6	8.1	15.5	19.5	100	10.7	7.3
Ba	<10.8	147.8	<10.8	14.1	26.3	<10.8	103.2	83.4	54.4	177.2	437.5	26.8	59.3
Pb	2.7	5.9	9.1	4.4	1.3	7.1	4	2	2.1	8.5	9.6	1.2	1.9
Sr	98.2	488.1	78.7	50.7	88.8	51.5	123	101.6	92.7	112.2	683.6	114	291.6
Nb	0.6	3.1	0.7	0.8	0.9	2.3	1.1	0.5	0.7	1.1	1.9	3.6	0.6
Ta	-	-	-	-	0.01	-	-	0.02	-	0.03	-	-	-
Zr	21.3	36.3	19.5	18.9	21.5	38.8	32.1	20	21.9	33.1	23.9	53.1	17.9
Hf	-	-	-	-	0.6	-	-	0.4	-	0.7	-	-	-
Y	8.8	11	8.1	8.2	8.9	10.8	11.6	3.8	9.5	9.2	6	15.8	9
Cr	527.5	19.4	1781	744.2	304.7	364.6	302.1	436.2	1097	2731	121.4	1422	322.1
Ni	145	26	192	226	155	141	80	813	391	377	96	227	180
La	-	-	-	-	4.97	-	-	5.17	-	10.1	-	-	-
Ce	-	-	-	-	11.6	-	-	9.38	-	19	-	-	-
Pr	-	-	-	-	1.78	-	-	1.16	-	2.45	-	-	-
Nd	-	-	-	-	8.62	-	-	4.63	-	10.3	-	-	-
Sm	-	-	-	-	2.13	-	-	0.94	-	2.18	-	-	-
Eu	-	-	-	-	0.49	-	-	0.26	-	0.56	-	-	-
Gd	-	-	-	-	1.77	-	-	0.78	-	1.87	-	-	-
Tb	-	-	-	-	0.28	-	-	0.12	-	0.3	-	-	-
Dy	-	-	-	-	1.6	-	-	0.69	-	1.65	-	-	-
Ho	-	-	-	-	0.33	-	-	0.14	-	0.36	-	-	-
Er	-	-	-	-	0.98	-	-	0.45	-	1.05	-	-	-
Tm	-	-	-	-	0.15	-	-	0.070	-	0.15	-	-	-
Yb	-	-	-	-	0.96	-	-	0.45	-	1.00	-	-	-
Lu	-	-	-	-	0.15	-	-	0.076	-	0.16	-	-	-

Table 2-10: Geochemistry of the Qullinaaraaluk-suite type location

Sample	JY9142	JY9143A	JY9145A	JY9146	JY9150	JY9152	JY9153	JY9155	JY9158	JY9160	JY9161	JY9163	TSB107
Zone	18	18	18	18	18	18	18	18	18	18	18	18	18
Easting	518660	518708	518731	518735	518837	518698	518691	518524	518572	518424	518340	518366	518799
Northing	6393156	6393172	6393205	6393262	6393131	6393047	6393017	6392924	6393092	6393153	6393121	6392975	6393152
Lithology	*f. web*	*f. web*	*f. web*	*f. web*	*f. web*	*f. web*	*f. web*	*qf. web*	*f. web*	*f. web*	*f. web*	*f. web*	*f. web*
Major elements (wt. %)													
SiO_2	52.88	50.85	52.41	52.65	52.01	51.43	51.66	52.76	51.86	51.37	50.87	50.72	50.85
TiO_2	0.35	0.35	0.18	0.2	0.28	0.36	0.32	0.28	0.32	0.33	0.23	0.36	0.35
Al_2O_3	5.24	6.28	2.92	4.49	3.31	4.87	4.65	4.35	4.12	6.98	3.78	4.48	6.28
MgO	15.2	18.41	23.12	23.4	20.51	20.02	18.52	19.52	19.52	16.06	22.83	17.51	18.41
FeO	9.04	13.24	9.19	10.09	10.77	11.07	9.78	11.62	9.89	9.8	13.23	8.93	13.24
MnO	0.17	0.23	0.19	0.15	0.2	0.2	0.19	0.21	0.2	0.17	0.21	0.18	0.23
CaO	12.88	5.61	8.17	2.79	10.93	10.28	12.96	8.6	11.81	12.1	6.05	14.47	5.61
Na_2O	0.92	0.81	0.39	0.42	0.46	0.62	0.66	0.63	0.57	1.01	0.41	0.56	0.81
K_2O	0.67	0.47	0.13	0.33	0.1	0.17	0.17	0.2	0.13	0.35	0.17	0.23	0.47
P_2O_5	0.03	0.09	0.03	0.08	0.02	0.03	0.03	0.01	0.03	0.02	0.03	0.02	0.09
LOI	2.07	2.82	2.42	4.56	0.79	0.44	0.47	1.16	0.74	0.94	0.68	1.5	1.55
Total	99.51	99.45	99.65	99.55	99.61	99.81	99.67	99.5	99.44	99.4	99.18	99.41	99.39
Trace elements (ppm)													
S	-	-	-	-	-	-	-	-	-	-	-	-	-
Th	-	-	-	-	-	-	-	-	-	-	-	-	-
U	-	-	-	-	-	-	-	-	-	-	-	-	-
Rb	33.8	24.6	3.3	21.7	1.6	<1.0	1.4	4.6	1	11.4	1.4	4.4	5.3
Ba	86.4	39.9	<10.8	32.2	<10.8	15.1	<10.8	36.9	<10.8	126.7	26.9	16.2	<10.8
Pb	1.2	2.1	<1.0	1.1	<1.0	<1.0	<1.0	1.9	<1.0	1.7	1	1.4	1.1
Sr	63.9	94.1	36.6	37.5	56.4	76.2	67.5	44.7	47.5	109.2	48.7	54	32.4
Nb	0.7	1.8	1	0.7	0.9	0.8	0.7	1.5	1.1	1.4	0.7	0.8	1.2
Ta	-	-	-	-	-	-	-	-	-	-	-	-	-
Zr	34.8	24.2	11.5	17.7	16.6	18.9	18.7	13.9	15.9	16.8	11.5	20.8	16.1
Hf	-	-	-	-	-	-	-	-	-	-	-	-	-
Y	9	6.1	3.6	3.1	6.7	7.7	7.9	9	7.7	11.9	4.3	8.6	7.4
Cr	288.5	1348	3050	2228	1227	1729	1449	845.8	1583	1307	2441	2435	1574
Ni	126	837	425	660	373	574	271	327	274	568	2619	621	318
La	-	-	-	-	-	-	-	-	-	-	-	-	-
Ce	-	-	-	-	-	-	-	-	-	-	-	-	-
Pr	-	-	-	-	-	-	-	-	-	-	-	-	-
Nd	-	-	-	-	-	-	-	-	-	-	-	-	-
Sm	-	-	-	-	-	-	-	-	-	-	-	-	-
Eu	-	-	-	-	-	-	-	-	-	-	-	-	-
Gd	-	-	-	-	-	-	-	-	-	-	-	-	-
Tb	-	-	-	-	-	-	-	-	-	-	-	-	-
Dy	-	-	-	-	-	-	-	-	-	-	-	-	-
Ho	-	-	-	-	-	-	-	-	-	-	-	-	-
Er	-	-	-	-	-	-	-	-	-	-	-	-	-
Tm	-	-	-	-	-	-	-	-	-	-	-	-	-
Yb	-	-	-	-	-	-	-	-	-	-	-	-	-
	-	-	-	-	-	-	-	-	-	-	-	-	-

Table 2-10: Q-suite type locality (cont.)

Sample	TSB108	TSB112	TSB117	TSB118	TSB119	QB1205	QB1207	QB1208	QB1210	QB1211	QB1212
Zone	18	18	18	18	18	18	18	18	18	18	18
Easting	518746	518431	518808	518853	518862	518834	518706	518672	518626	518529	518233
Northing	6393147	6393056	6393228	6393102	6393087	6393127	6393108	6393096	6393085	6393075	6393083
Lithology	*f. web*	*f. web*	*f. web*	*f. web*	*gabnor*	*f. web*	*f. web*	*f. web*	*f. web*	*f. web*	*gabnor*
Major elements (wt. %)											
SiO_2	51.41	52.14	52.84	51.94	52.97	52.07	51.52	51.13	51.45	51.64	51.32
TiO_2	0.27	0.29	0.30	0.25	0.27	0.28	0.29	0.31	0.30	0.30	0.40
Al_2O_3	3.40	4.42	4.09	5.07	5.17	3.86	4.07	4.75	3.15	3.97	5.47
MgO	20.07	19.53	18.54	18.61	16.4	19.88	17.54	17.79	19.47	19.52	16.57
FeO	9.32	9.66	8.78	8.83	9.57	10.20	8.51	8.92	9.48	9.87	9.52
MnO	0.19	0.19	0.14	0.18	0.19	0.19	0.17	0.18	0.19	0.19	0.18
CaO	12.22	12.27	12.00	11.91	12.45	11.17	14.89	13.56	12.76	12.41	13.73
Na_2O	0.48	0.51	0.5	0.83	0.87	0.58	0.66	0.73	0.47	0.48	0.87
K_2O	0.14	0.10	0.38	0.14	0.32	0.14	0.19	0.17	0.15	0.12	0.20
P_2O_5	0.02	0.02	0.04	0.07	0.03	0.03	0.02	0.06	0.02	0.02	0.05
LOI	1.40	0.37	1.84	1.49	1.09	0.91	1.20	1.52	1.67	0.50	0.74
Total	99.29	99.76	99.72	99.6	99.57	99.52	99.28	99.47	99.46	99.27	99.26
Trace elements (ppm)											
S	-	-	-	-	-	-	-	-	-	-	-
Th	-	-	-	-	-	-	-	-	-	-	-
U	-	-	-	-	-	-	-	-	-	-	-
Rb	1.5	1.1	21	1.3	13.2	3.7	3	3.5	2.4	<1.0	2.2
Ba	<10.8	<10.8	14.8	18.6	100.6	23.6	<10.8	<10.8	<10.8	<10.8	21.1
Pb	1.2	<1.0	<1.0	1.4	1.1	<1.0	2	1.4	<1.0	<1.0	<1.0
Sr	47	64.1	38.3	98.9	158	75	97.5	87.3	37.8	48.7	83
Nb	1.0	0.3	1.5	0.8	1.0	0.8	0.9	0.8	0.7	0.4	1.3
Ta	-	-	-	-	-	-	-	-	-	-	-
Zr	17.1	15.8	25.9	18.2	32.8	18.1	19.1	19.1	16.7	15.1	24
Hf	-	-	-	-	-	-	-	-	-	-	-
Y	6.5	6.8	7.6	6.8	9.3	6.3	8.2	8	7	7.3	10.3
Cr	1611	1712	1821	1487	1644	1659	1720	1882	1772	1788	2426
Ni	2236	1589	1530	1688	1443	1189	1162	2046	2115	1507	1158
La	-	-	-	-	-	-	-	-	-	-	-
Ce	-	-	-	-	-	-	-	-	-	-	-
Pr	-	-	-	-	-	-	-	-	-	-	-
Nd	-	-	-	-	-	-	-	-	-	-	-
Sm	-	-	-	-	-	-	-	-	-	-	-
Eu	-	-	-	-	-	-	-	-	-	-	-
Gd	-	-	-	-	-	-	-	-	-	-	-
Tb	-	-	-	-	-	-	-	-	-	-	-
Dy	-	-	-	-	-	-	-	-	-	-	-
Ho	-	-	-	-	-	-	-	-	-	-	-
Er	-	-	-	-	-	-	-	-	-	-	-
Tm	-	-	-	-	-	-	-	-	-	-	-
Yb	-	-	-	-	-	-	-	-	-	-	-
Lu	-	-	-	-	-	-	-	-	-	-	-

Table 2-11: Miscellaneous subalkaline Q-suite samples

Sample	UM02-08	UM03-08	UM03-08*	UM01-08	PT-7	PT-8	PT-9	QB1160	JY9175A
Zone	18	18	18	18	18	18	18	18	18
Easting	468830	468878	486236	477058	360550	360550	360083	515459	555498
Northing	6446176	6446039	6673793	6490124	6470992	6470992	6470915	6390188	6404290
Lithology	*web*	*web*	*weh*	*gabnor*	*gabnor*	*web*	*web*	*f. web*	*f. web*
Major elements (wt. %)									
SiO_2	53.65	50.98	-	45.31	51.26	51.56	51.88	50.12	51.62
TiO_2	0.20	0.23	-	1.02	0.22	0.31	0.25	0.28	0.25
Al_2O_3	3.81	4.2	-	17.75	12.57	6.53	5.34	4.74	2.26
MgO	25.16	23.35	-	5.86	13.27	16.31	17.15	18.11	18.54
FeO	9.76	10.07	-	13.41	8.65	10.15	8.5	12.57	10.73
MnO	0.2	0.19	-	0.15	0.18	0.22	0.22	0.22	0.23
CaO	4.97	8.74	-	10.68	11.29	12.99	13.6	10.21	14.86
Na_2O	0.55	0.55	-	2.61	1.41	0.85	1.21	0.90	0.45
K_2O	0.40	0.40	-	0.92	0.17	0.14	0.38	0.45	0.09
P_2O_5	0.03	0.04	-	0.05	0.02	0.03	0.04	0.02	0.02
LOI	0.00	0.28	-	0.83	0.09	0.03	0.71	1.21	0.60
Total	99.26	99.5	-	98.58	99.23	99.29	99.49	98.97	99.73
Trace elements (ppm)									
S	-	-	-	-	-	-	-	-	-
Th	0.63	1.59	1.57	-	-	-	1.47	-	-
U	0.23	0.74	0.84	-	-	-	0.27	-	-
Rb	24.6	17.2	-	24	1.1	<1.0	8.9	20	1.1
Ba	67.1	70.3	-	164.6	77.2	37.2	42.6	56.3	<10.8
Pb	1.4	3.8	-	7.0	2.1	<1.0	3.14	1.8	<1.0
Sr	54.7	81.7	-	462.6	375.7	151.8	83.6	91.6	34.2
Nb	0.9	1.08	1.08	2.1	0.4	<0.3	1.8	0.5	0.4
Ta	0.07	0.21	0.18	-	-	-	0.18	-	-
Zr	13.9	23.0	23.36	28.5	11.3	18.1	22.2	15.9	13.9
Hf	0.5	0.8	0.78	-	-	-	1.1	-	-
Y	4.1	6.1	7.19	7.9	6.2	9.1	16.1	7.4	8.7
Cr	3092	2530	-	11.3	511	956.5	1226	567	314.6
Ni	578	805	-	3	167	233	284	405	210
La	3.32	4.71	4.74	-	-	-	11.7	-	-
Ce	7.5	10.6	11.61	-	-	-	30.5	-	-
Pr	0.88	1.28	1.53	-	-	-	4.07	-	-
Nd	3.89	5.83	6.87	-	-	-	18.1	-	-
Sm	0.83	1.34	1.53	-	-	-	4.48	-	-
Eu	0.21	0.32	0.35	-	-	-	0.69	-	-
Gd	0.76	1.23	1.34	-	-	-	3.86	-	-
Tb	0.12	0.19	0.21	-	-	-	0.61	-	-
Dy	0.68	1.1	1.22	-	-	-	3.22	-	-
Ho	0.14	0.23	0.23	-	-	-	0.64	-	-
Er	0.43	0.65	0.71	-	-	-	1.7	-	-
Tm	0.06	0.095	0.11	-	-	-	0.25	-	-
Yb	0.47	0.63	0.71	-	-	-	1.53	-	-
Lu	0.054	0.086	0.11	-	-	-	0.19	-	-

Table 2-12: Geochemistry of the transitional Lac Couture (Q-suite) intrusion

Sample	C1-01	C1-02	C1-03	C1-04	C1-05	C1-06	C1-07	C1-08	C1-09	C1-10	C1-12	C1-13	C1-14
Zone	18	18	18	18	18	18	18	18	18	18	18	18	18
Easting	485922	486032	486050	486026	486007	485975	485967	485970	485993	486005	486012	486000	485982
Northing	6674639	6674633	6674604	6674602	6674678	6674695	6674539	6674527	6674534	6674496	6674402	6674385	6674385
Lithology	*amphblt*	*bt. weh*	*gabbro*	*amphblt*	*weh*	*bt. weh*	*weh*	*amphblt*	*gabbro*	*amphblt*	*weh*	*weh*	*dun*
Major elements (wt. %)													
SiO_2	50.77	41.29	45.74	49.46	43.56	46.23	45.97	44.48	49.05	44.82	44.52	43.49	38.08
TiO_2	0.38	0.33	0.96	0.44	0.23	0.25	0.30	0.27	0.73	1.52	0.31	0.29	0.10
Al_2O_3	3.56	4.79	16.56	5.12	2.56	4.40	3.03	2.52	15.05	11.78	3.20	2.88	1.04
MgO	17.64	26.78	8.86	18.47	26.50	22.09	22.25	24.68	8.40	12.19	21.96	23.81	33.61
FeO	10.08	13.33	10.55	8.26	12.95	11.40	10.72	11.81	10.24	11.43	12.76	12.01	11.05
MnO	0.2	0.22	0.16	0.17	0.23	0.20	0.21	0.18	0.18	0.16	0.22	0.21	0.21
CaO	14.41	4.78	10.02	14.03	10.1	10.25	12.99	10.39	10.27	12.67	11.65	10.9	4.62
Na_2O	0.55	0.81	3.04	1.02	0.33	0.74	0.49	0.2	2.55	1.59	0.49	0.41	0.08
K_2O	0.21	0.56	1.41	0.29	0.14	0.52	0.2	0.78	1.18	1.15	0.16	0.09	0.01
P_2O_5	0.02	0.07	0.54	0.04	0.03	0.06	0.02	0.03	0.31	0.18	0.03	0.03	0.02
LOI	1.44	5.84	0.87	1.71	2.10	2.64	2.96	3.70	0.91	1.33	2.95	4.49	9.73
Total	99.41	98.95	98.75	99.28	99.02	98.93	99.35	99.29	98.9	98.84	98.44	98.86	99.2
Trace elements (ppm)													
S	-	-	-	-	-	-	-	-	-	-	-	-	400
Th	-	-	-	-	-	-	-	-	-	-	-	-	-
U	-	-	-	-	-	-	-	-	-	-	-	-	-
Rb	-	-	-	-	-	-	-	-	-	-	-	-	-
Ba	22.8	198.3	1709	34.7	47.9	221.6	66.6	42.9	662.9	199.5	13.3	18.2	<10.8
Pb	1.5	2.9	8.1	2.2	1.3	2.4	1.8	3.2	5.9	2.6	6.3	2.5	2.5
Sr	58	148.7	1227	106.9	62	125.9	59.7	26.6	730	304.5	62.2	60.6	15.5
Nb	0.6	1.4	3.6	1	0.3	0.9	0.3	0.5	2	3.3	0.5	0.3	<0.3
Ta	-	-	-	-	-	-	-	-	-	-	-	-	-
Zr	18	22.6	29.1	21.1	11.8	27.2	14.4	13.4	29.6	48.3	17.7	14.3	2.6
Hf	-	-	-	-	-	-	-	-	-	-	-	-	-
Y	11.2	5.5	15.3	9	5.3	5.7	7.6	7.1	12.8	19.5	7.8	7.7	2
Cr	818.1	697.4	240.8	1553	1655	784.9	1168	1477	132.9	138.8	1105	1341	3413
Ni	186	417	91	195	426	252	280	373	57	56	276	334	1170
La	-	-	-	-	-	-	-	-	-	-	-	-	-
Ce	-	-	-	-	-	-	-	-	-	-	-	-	-
Pr	-	-	-	-	-	-	-	-	-	-	-	-	-
Nd	-	-	-	-	-	-	-	-	-	-	-	-	-
Sm	-	-	-	-	-	-	-	-	-	-	-	-	-
Eu	-	-	-	-	-	-	-	-	-	-	-	-	-
Gd	-	-	-	-	-	-	-	-	-	-	-	-	-
Tb	-	-	-	-	-	-	-	-	-	-	-	-	-
Dy	-	-	-	-	-	-	-	-	-	-	-	-	-
Ho	-	-	-	-	-	-	-	-	-	-	-	-	-
Er	-	-	-	-	-	-	-	-	-	-	-	-	-
Tm	-	-	-	-	-	-	-	-	-	-	-	-	-
Yb	-	-	-	-	-	-	-	-	-	-	-	-	-
Lu	-	-	-	-	-	-	-	-	-	-	-	-	-

Table 2-12: Transitional Lac Couture (Q-suite) intrusion (cont.)

Sample	C1-15	C1-16	C1-17	C1-18	C1-20	C1-21	C1-22	C1-23	C1-24	C1-25	C1-28	C1-29	C1-29a
Zone	18	18	18	18	18	18	18	18	18	18	18	18	18
Easting	485990	486034	486074	486077	486082	486092	486092	486099	486100	486111	486119	486133	486133
Northing	6674374	6674335	6674192	6674192	6674190	6674183	6674183	6674177	6674177	6674123	6674027	6674105	6674105
Lithology	*dun*	*dun*	*weh*	*dun*	*dun*	*weh*	*weh*	*dun*	*weh*	*weh*	*weh*	*weh*	*weh*
Major elements (wt. %)													
SiO_2	36.9	37.87	44.46	36.43	36.33	45.16	42.96	36.39	46.19	46.79	48.71	47.84	48.01
TiO_2	0.16	0.08	0.27	0.10	0.09	0.23	0.24	0.09	0.28	0.34	0.31	0.30	0.31
Al_2O_3	1.21	0.92	2.61	0.80	0.84	2.23	2.22	0.84	2.91	3.13	3.33	2.91	3.01
MgO	31.52	37.68	22.77	34.71	35.50	23.10	24.34	34.87	21.21	20.21	18.69	20.16	19.48
FeO	18.35	14.5	11.02	16.13	15.09	10.74	12.58	15.99	11.06	10.37	9.15	9.77	9.25
MnO	0.22	0.28	0.22	0.25	0.24	0.19	0.24	0.27	0.21	0.21	0.20	0.20	0.19
CaO	3.06	2.19	12.02	2.22	1.73	12.67	10.94	2.02	14.13	15.43	16.71	15.99	16.62
Na_2O	0.09	0.10	0.3	0.04	0.03	0.27	0.19	0.04	0.36	0.4	0.48	0.36	0.38
K_2O	0.04	0.03	0.09	0.02	0.01	0.07	0.03	0.03	0.14	0.11	0.15	0.09	0.08
P_2O_5	0.02	0.02	0.02	0.01	0.02	0.02	0.01	0.02	0.03	0.03	0.02	0.02	0.02
LOI	6.51	4.67	5.07	7.55	8.26	4.19	5.01	7.67	2.77	2.07	1.30	1.73	1.45
Total	98.48	99.09	99.04	98.92	98.84	99.05	99.07	98.93	99.42	99.24	99.31	99.52	98.95
Trace elements (ppm)													
S	<350	440	-	450	430	-	-	360	-	-	-	-	-
Th	-	-	-	-	0.09	-	-	<0.05	-	-	-	-	-
U	-	-	-	-	0.08	-	-	0.02	-	-	-	-	-
Rb	<1	<1	2	<1	<1	2	<1	<1	4.7	2.9	3.4	2.2	1.9
Ba	<10.8	15.7	15.4	<10.8	<10.8	<10.8	<10.8	<10.8	36.9	14.5	20.2	<10.8	13.4
Pb	3	1.4	6.1	1.1	<1.0	2.5	3.1	2	2.5	2.1	2.9	1	1.7
Sr	18.6	11.3	57.1	9.5	6.4	51.4	36	8.3	71.2	79.9	78.5	64	66.2
Nb	<0.3	<0.3	<0.3	<0.3	<0.3	<0.3	<0.3	<0.3	<0.3	<0.3	<0.3	<0.3	0.3
Ta	-	-	-	-	<0.01	-	-	<0.01	-	-	-	-	-
Zr	3.7	2.1	11.8	1.1	1.1	9.1	9.2	1.2	13.7	15.8	15.9	13.5	14
Hf	-	-	-	-	<0.1	-	-	<0.1	-	-	-	-	-
Y	2.3	<1.0	6.1	1.1	1	5.8	5.9	<1.0	7.2	9.1	8.5	7.7	8.1
Cr	2205	3908	1114	3484	3613	994.8	1747	3623	733.3	930.5	1516	831.2	864.8
Ni	581	1460	291	1144	1414	300	415	1292	222	200	225	180	162
La	-	-	-	-	2.14	-	-	0.41	-	-	-	-	-
Ce	-	-	-	-	3.02	-	-	0.98	-	-	-	-	-
Pr	-	-	-	-	0.41	-	-	0.18	-	-	-	-	-
Nd	-	-	-	-	1.7	-	-	1.01	-	-	-	-	-
Sm	-	-	-	-	0.38	-	-	0.28	-	-	-	-	-
Eu	-	-	-	-	0.075	-	-	0.074	-	-	-	-	-
Gd	-	-	-	-	0.34	-	-	0.25	-	-	-	-	-
Tb	-	-	-	-	0.05	-	-	0.04	-	-	-	-	-
Dy	-	-	-	-	0.26	-	-	0.19	-	-	-	-	-
Ho	-	-	-	-	0.05	-	-	0.04	-	-	-	-	-
Er	-	-	-	-	0.14	-	-	0.12	-	-	-	-	-
Tm	-	-	-	-	0.022	-	-	0.017	-	-	-	-	-
Yb	-	-	-	-	0.15	-	-	0.11	-	-	-	-	-
Lu	-	-	-	-	0.026	-	-	0.020	-	-	-	-	-

Table 2-12: Transitional Lac Couture (Q-suite) intrusion (cont.)

Sample	C1-30	C1-31	C1-32	C1-33	C1-34	C1-37	C1-38	C1-39	C1-39*	C1-43	C1-44	C1-45	C1-47
Zone	18	18	18	18	18	18	18	18	18	18	18	18	18
Easting	486159	486158	486168	486168	486186	486211	486151	486236	486236	486316	486340	486298	486258
Northing	6674107	6674113	6674122	6674123	6674120	6674018	6673919	6673793	6673793	6674690	6674630	6674708	6674744
Lithology	*bt. weh*	*bt. weh*	*amphblt*	*amphblt*	*gabbro*	*gabbro*	*amphblt*	*weh*	*weh*	*gabbro*	*dun*	*amphblt*	*gabbro*
Major elements (wt. %)													
SiO_2	44.78	45.5	42.51	47.45	51.94	51.17	49.42	44.46	-	49.59	39.9	46.51	53.85
TiO_2	0.35	0.74	1.18	0.71	0.69	0.56	0.43	0.34	-	0.6	0.09	0.84	0.71
Al_2O_3	2.77	5.35	13.39	7.01	15.18	14.33	6.23	3.17	-	13.64	1.22	6.43	15.96
MgO	23.66	18.51	10.34	16.72	7.31	8.20	14.93	23.9	-	10.17	32.62	17.36	5.52
FeO	12.62	11.92	13.66	10.91	8.69	8.82	9.08	12.43	-	9.78	17.83	12.02	8.23
MnO	0.24	0.16	0.17	0.2	0.17	0.17	0.20	0.22	-	0.18	0.27	0.21	0.15
CaO	10.4	11.49	13.59	12.58	9.00	9.91	16.15	10.41	-	11.19	3.74	12.63	7.81
Na_2O	0.15	0.14	1.53	1.15	3.63	3.12	0.93	0.37	-	2.3	0.14	0.9	3.33
K_2O	1.47	3.08	0.89	0.49	1.30	1.56	0.41	0.14	-	0.49	0.08	0.63	2.40
P_2O_5	0.02	0.04	0.49	0.03	0.32	0.29	0.09	0.02	-	0.14	0.02	0.04	0.33
LOI	2.68	1.90	0.99	1.43	0.73	0.89	1.14	3.54	-	0.84	2.57	1.18	0.67
Total	99.3	98.94	98.77	98.8	98.99	99.06	99.14	99.18	-	98.96	98.63	98.89	98.99
Trace elements (ppm)													
S	-	-	-	-	-	-	-	-	-	-	<350	-	-
Th	-	-	-	-	-	-	-	0.09	0.13	-	-	-	3.07
U	-	-	-	-	-	-	-	0.03	0.04	-	-	-	1.02
Rb	76.3	181.5	9.7	3.9	42.7	33.5	5.2	1.7	-	10.1	3	10.5	64.5
Ba	16.9	159.1	144.2	94.7	200.5	1053	52.5	<10.8	-	412.3	30.2	117.2	1180
Pb	2.3	1.8	3.7	1.4	10.8	7.4	1.6	3.6	-	6.9	1.6	1.1	12.6
Sr	13.7	21.7	476.4	169.3	505.7	733.8	131.1	69.7	-	694.4	25	108.2	710.4
Nb	0.5	0.7	2.1	1.7	3.6	1.4	1.6	0.6	0.44	0.6	<0.3	1.8	3.6
Ta	-	-	-	-	-	-	-	<0.01	0.03	-	-	-	0.2
Zr	21.9	22.5	28.3	29.7	46.2	25.2	28.7	11.6	12.46	15.5	5.6	29.9	84.7
Hf	-	-	-	-	-	-	-	0.4	0.59	-	-	-	2.3
Y	10.1	11	18.6	13.3	14.6	12	12.5	7.2	8.63	10.2	2.3	14.1	16.2
Cr	939.6	629.3	218.9	729.1	188.2	268.3	790.1	970.1	-	264.7	474.3	720.3	104.3
Ni	288	181	64	183	43	51	148	308	-	83	511	193	32
La	-	-	-	-	-	-	-	2.21	1.99	-	-	-	29.1
Ce	-	-	-	-	-	-	-	7.11	8.11	-	-	-	60.4
Pr	-	-	-	-	-	-	-	1.39	1.53	-	-	-	7.28
Nd	-	-	-	-	-	-	-	7.96	8.86	-	-	-	30.8
Sm	-	-	-	-	-	-	-	2.29	2.54	-	-	-	6.09
Eu	-	-	-	-	-	-	-	0.58	0.61	-	-	-	1.56
Gd	-	-	-	-	-	-	-	2.00	2.17	-	-	-	4.51
Tb	-	-	-	-	-	-	-	0.28	0.28	-	-	-	0.58
Dy	-	-	-	-	-	-	-	1.43	1.62	-	-	-	2.93
Ho	-	-	-	-	-	-	-	0.27	0.33	-	-	-	0.56
Er	-	-	-	-	-	-	-	0.76	0.87	-	-	-	1.71
Tm	-	-	-	-	-	-	-	0.11	0.10	-	-	-	0.26
Yb	-	-	-	-	-	-	-	0.65	0.7	-	-	-	1.56
Lu	-	-	-	-	-	-	-	0.11	0.10	-	-	-	0.26

Table 2-12: Transitional Lac Couture (Q-suite) intrusion (cont.)

Sample	C1-48	C1-50	C1-53	C2-01	C2-02	C2-03	C3-02	C3-03	C4-01
Zone	18	18	18	18	18	18	18	18	18
Easting	486252	486420	486289	489040	489021	488176	484169	484128	488949
Northing	6674786	6674097	6674810	6669212	6669208	6669175	6685259	6686419	6673011
Lithology	*weh*	*dun*	*gabbro*	*amphblt*	*gabbro*	*amphblt*	*amphblt*	*bt. weh*	*gabbro*
Major elements (wt. %)									
SiO_2	43.64	39.00	49.18	51.17	40.65	48.46	51.66	47.84	50.64
TiO_2	0.22	0.14	0.59	0.33	1.00	0.47	0.56	0.25	0.63
Al_2O_3	2.86	1.08	13.66	5.16	18.65	4.29	8.92	5.22	19.39
MgO	29.68	33.88	10.21	14.05	7.43	17.59	12.42	21.47	5.32
FeO	12.83	17.59	9.99	7.95	12.76	11.82	10.38	9.68	7.24
MnO	0.22	0.28	0.19	0.21	0.16	0.22	0.21	0.18	0.12
CaO	7.68	4.16	11.33	18.41	11.85	13.25	11.33	10.87	9.64
Na_2O	0.38	0.08	2.32	1.05	1.55	0.57	1.55	0.89	4.59
K_2O	0.15	0.02	0.43	0.39	2.15	0.36	0.62	0.57	0.57
P_2O_5	0.04	0.02	0.18	0.03	0.22	0.03	0.16	0.06	0.44
LOI	1.03	1.89	0.90	0.74	2.31	1.87	1.40	1.69	0.63
Total	99.19	98.75	99.03	99.61	98.74	99.03	99.29	99	99.23
Trace elements (ppm)									
S	-	<350	-	-	-	-	-	-	-
Th	0.25	0.08	0.18	-	-	-	-	-	-
U	0.13	0.06	0.08	-	-	-	-	-	-
Rb	2.6	<1	6.5	7.9	77.8	8.5	8.3	15.7	7.7
Ba	73.1	20	347.1	24.3	229.2	29.3	174.5	225.6	209.5
Pb	2.4	1	4.1	2.9	5.7	1.7	3.8	5.2	15.2
Sr	73.1	16	730.5	120	550	71	185.4	171.6	1506
Nb	0.6	<0.3	0.4	1.2	1.7	0.4	3.4	0.9	3.7
Ta	<0.01	< 0.01	<0.01	-	-	-	-	-	-
Zr	15.9	3	12.7	25.4	26.1	17.4	50.1	27.7	89.1
Hf	0.5	0.1	0.5	-	-	-	-	-	-
Y	5.5	2.1	9.9	9.3	16.5	9.8	14.1	6.7	16.8
Cr	2510	3248	265.5	609.7	55.1	529.8	297.8	1556	67.5
Ni	723	1055	87	188	50	183	129	347	21
La	3.31	0.48	8.45	-	-	-	-	-	-
Ce	8.69	1.73	17.1	-	-	-	-	-	-
Pr	1.44	0.32	2.58	-	-	-	-	-	-
Nd	7.3	1.75	12.5	-	-	-	-	-	-
Sm	1.75	0.57	2.93	-	-	-	-	-	-
Eu	0.44	0.15	1.00	-	-	-	-	-	-
Gd	1.45	0.5	2.48	-	-	-	-	-	-
Tb	0.2	0.08	0.35	-	-	-	-	-	-
Dy	1.01	0.39	1.84	-	-	-	-	-	-
Ho	0.2	0.07	0.36	-	-	-	-	-	-
Er	0.58	0.2	1.06	-	-	-	-	-	-
Tm	0.086	0.029	0.15	-	-	-	-	-	-
Yb	0.55	0.19	0.96	-	-	-	-	-	-
Lu	0.082	0.029	0.15	-	-	-	-	-	-

Table 2-13: Geochemistry of the transitional Lac Duquet (Q-suite) intrusion

Sample	D-02	D-03	D-04	D-05	D-06	D-07	D-08	D-09	D-10	D-11	D-13	D-14	D-16
Zone	18	18	18	18	18	18	18	18	18	18	18	18	18
Easting	495059	495059	495155	494877	494859	495285	495142	495057	495052	495029	495019	494805	494548
Northing	6701080	6701080	6701248	6700168	6700185	6700263	6700170	6700188	6700187	6699603	6699277	6699625	6698884
Lithology	*gabbro*	*amphblt*	*bt. weh*	*gabbro*	*gabbro*	*bt. weh*	*amphblt*	*amphblt*	*amphblt*	*bt. weh*	*amphblt*	*amphblt*	*amphblt*
Major elements (wt. %)													
SiO_2	50.02	48.58	47.69	48.93	50.64	47.41	46.81	45.87	48.31	47.69	50.68	48.67	47.86
TiO_2	0.53	0.58	0.30	0.61	0.57	0.34	0.36	0.40	0.46	0.31	0.32	0.43	0.49
Al_2O_3	18.11	8.74	4.99	14.37	16.10	5.34	5.85	4.63	8.07	4.93	4.19	8.84	7.81
MgO	6.48	13.56	22.14	9.30	7.25	21.26	20.3	19.97	15.36	20.56	15.59	14.36	15.95
FeO	8.28	9.59	8.75	9.80	9.03	9.29	8.94	12.42	10.48	7.89	5.62	10.48	11.19
MnO	0.15	0.20	0.17	0.19	0.18	0.17	0.17	0.23	0.21	0.16	0.14	0.21	0.22
CaO	8.29	13.8	11.87	9.99	10.17	11.47	12.38	11.39	12.47	13.10	20.32	11.46	11.6
Na_2O	3.12	1.40	0.81	2.63	3.55	0.82	0.86	0.64	1.08	0.77	0.55	1.34	0.98
K_2O	2.76	1.10	0.82	1.57	0.79	1.05	0.66	0.74	1.13	0.64	0.26	0.9	1.23
P_2O_5	0.32	0.13	0.12	0.34	0.15	0.12	0.12	0.12	0.14	0.08	0.03	0.14	0.13
LOI	1.01	1.15	1.57	1.06	0.73	1.71	2.20	1.71	1.18	2.81	1.47	1.59	1.25
Total	99.09	98.98	99.51	98.85	99.19	99.25	98.92	98.34	99.03	99.24	99.46	98.55	98.85
Trace elements (ppm)													
S	-	-	-	-	-	-	-	-	-	-	-	-	-
Th	-	-	-	-	0.95	-	-	-	-	-	0.46	-	2.11
U	-	-	-	-	0.45	-	-	-	-	-	0.13	-	0.83
Rb	67	45.9	27.3	68.7	21.5	36.7	21.4	31.6	55.7	25	10.1	29.1	58.7
Ba	1560	269	309.7	433.5	163.7	414.8	213.1	188	219.1	275.8	29.5	230.5	296.3
Pb	11.2	4.9	5.3	8.7	9.4	5.1	4.4	2.1	3.6	3.6	1.3	3.9	3.4
Sr	863.3	276.7	151.8	638	596.6	133.4	165.9	89.9	152.2	182.3	94.4	289.5	152.6
Nb	1.3	1.5	1.1	2.5	0.9	1.5	1	1.1	1.6	0.9	0.5	1.9	1.5
Ta	-	-	-	-	<0.01	-	-	-	-	-	<0.01	-	0.1
Zr	21.9	38.1	33.9	50.8	28.1	33.1	34.3	32.9	49.4	30	20.5	58	45.7
Hf	-	-	-	-	0.9	-	-	-	-	-	0.6	-	1.3
Y	10.6	14.6	6.6	14.4	10.5	7.1	8.5	11.7	12.9	7.1	7.6	13.3	12.3
Cr	109.4	852.9	1519	368.9	164.3	1457	1534	1254	806.8	1684	1910	706.3	753.2
Ni	85	155	467	114	62	450	401	376	198	391	205	184	214
La	-	-	-	-	11.2	-	-	-	-	-	5.69	-	16.7
Ce	-	-	-	-	23.2	-	-	-	-	-	14.6	-	37.5
Pr	-	-	-	-	3.32	-	-	-	-	-	2.32	-	4.39
Nd	-	-	-	-	15.4	-	-	-	-	-	11.5	-	19.8
Sm	-	-	-	-	3.49	-	-	-	-	-	2.72	-	4.32
Eu	-	-	-	-	1.31	-	-	-	-	-	0.74	-	1.1
Gd	-	-	-	-	2.71	-	-	-	-	-	2.26	-	3.5
Tb	-	-	-	-	0.38	-	-	-	-	-	0.31	-	0.48
Dy	-	-	-	-	2.01	-	-	-	-	-	1.56	-	2.48
Ho	-	-	-	-	0.39	-	-	-	-	-	0.30	-	0.48
Er	-	-	-	-	1.14	-	-	-	-	-	0.87	-	1.38
Tm	-	-	-	-	0.16	-	-	-	-	-	0.13	-	0.20
Yb	-	-	-	-	1.02	-	-	-	-	-	0.73	-	1.26
Lu	-	-	-	-	0.16	-	-	-	-	-	0.12	-	0.21

Table 2-13: Transitional Lac Duquet (Q-suite) intrusion (cont.)

Sample	D-19	D-20	D-21	D-22	D-24	D-25	D-27
Zone	18	18	18	18	18	18	18
Easting	495157	494927	494988	495060	494903	494914	494894
Northing	6700509	6699887	6699939	6699951	6700128	6700627	6701169
Lithology	*amphblt*	*amphblt*	*gabbro*	*bt. weh*	*amphblt*	*amphblt*	*bt. weh*
Major elements (wt. %)							
SiO_2	49.57	47.6	54.27	43.88	49.38	46.64	47.26
TiO_2	0.24	0.59	0.74	0.29	0.30	0.41	0.41
Al_2O_3	4.01	8.60	15.17	4.33	5.89	6.01	5.30
MgO	19.78	15.12	4.57	25.57	17.01	20.11	21.29
FeO	8.00	10.96	8.35	11.46	10.97	9.65	9.19
MnO	0.17	0.21	0.13	0.21	0.28	0.18	0.18
CaO	13.93	11.71	8.13	8.73	11.97	10.83	12.1
Na_2O	0.39	1.03	3.57	0.55	0.61	0.62	0.83
K_2O	0.13	1.15	2.26	0.56	0.25	1.71	0.91
P_2O_5	0.06	0.14	0.68	0.08	0.04	0.15	0.16
LOI	2.69	1.67	1.17	3.44	2.22	2.09	1.18
Total	99.23	98.91	99.06	99.31	99.13	98.65	99.08
Trace elements (ppm)							
S	-	-	-	-	-	-	-
Th	-	-	-	1.1	0.38	0.77	-
U	-	-	-	0.31	0.23	0.39	-
Rb	1.1	51.8	52.7	16.6	2.1	83.8	34.7
Ba	<10.8	384.7	759.4	190.1	<10.8	448.2	445.1
Pb	3.1	4.6	16.5	4.2	3.7	2.1	5.8
Sr	52.2	298.5	642.5	135.9	113.9	92.6	131.3
Nb	0.9	2.1	6.1	0.6	4.9	1.1	1.6
Ta	-	-	-	<0.01	0.3	<0.01	-
Zr	14.6	54.2	83.1	28.1	16.2	24	37.6
Hf	-	-	-	0.8	0.6	0.8	-
Y	5.3	13.3	19.8	7.5	8.6	8.9	8.0
Cr	1398	766.4	95.7	1010	1152	1409	1527
Ni	366	196	41	580	328	395	439
La	-	-	-	7.55	4.05	7.27	-
Ce	-	-	-	16.3	11.8	17.7	-
Pr	-	-	-	2.43	1.98	2.81	-
Nd	-	-	-	11.7	10	13.7	-
Sm	-	-	-	2.6	2.6	3.22	-
Eu	-	-	-	0.66	0.744	0.81	-
Gd	-	-	-	2.08	2.28	2.61	-
Tb	-	-	-	0.28	0.32	0.35	-
Dy	-	-	-	1.39	1.62	1.78	-
Ho	-	-	-	0.27	0.31	0.34	-
Er	-	-	-	0.78	0.93	0.99	-
Tm	-	-	-	0.12	0.14	0.14	-
Yb	-	-	-	0.75	0.87	0.88	-
Lu	-	-	-	0.12	0.14	0.13	-

Table 2-14: Geochemistry of the ultramafic enclave near Gladel River intrusion

Sample	GR3-1	GR3-2	GR3-4	GR3-8[?]
Zone	18	18	18	18
Easting	359780	359780	359781	359069
Northing	6465460	6465460	6465440	6465453
Lithology	*dun*	*opxite*	*dun*	*dun*
Major elements (wt. %)				
SiO_2	38.34	59.28	39.98	40.26
TiO_2	0.02	0.02	0.03	0.01
Al_2O_3	0.45	1.08	0.48	0.2
MgO	45.02	28.36	43.61	47.96
FeO	10.04	8.31	9.24	6.45
MnO	0.14	0.37	0.16	0.13
CaO	0.05	0.65	0.07	0.05
Na_2O	0.01	0.05	0.02	0.02
K_2O	0.15	0.41	0.14	0.03
P_2O_5	0.01	0.01	0.01	0.01
LOI	4.48	0.74	4.97	3.97
Total	99.65	99.82	99.63	99.73
Trace elements (ppm)				
S	-	-	-	-
Th	0.89	-	-	1.15
U	0.52	-	-	2.14
Rb	9	26.4	9.9	3
Ba	34.5	39.3	22.9	22.4
Pb	<1.0	<1.0	<1.0	<1.0
Sr	<1.0	2.1	1.1	<1.0
Nb	0.3	1.4	0.3	<0.3
Ta	0.05	-	-	0.16
Zr	<1.0	<1.0	<1.0	<1.0
Hf	0.7	-	-	2.9
Y	<1.0	4.1	<1.0	<1.0
Cr	3586	2236	3581	1179
Ni	3164	1686	3116	3662
La	0.5	-	-	0.63
Ce	0.96	-	-	0.91
Pr	0.1	-	-	0.07
Nd	0.34	-	-	0.23
Sm	0.08	-	-	0.05
Eu	0.014	-	-	<0.005
Gd	0.08	-	-	0.06
Tb	0.01	-	-	<0.01
Dy	0.08	-	-	0.07
Ho	0.02	-	-	0.02
Er	0.06	-	-	0.08
Tm	0.012	-	-	0.02
Yb	0.11	-	-	0.14
Lu	0.01	-	-	0.013

Tables 2-7 to2-14. See caption to Table 2-1 for analytical details.

All REE, Hf, Ta, U, and Th were analyzed at Activation Laboratories, unless indicated with (*). Samples with (*) were analyzed at PCIGR.

? Sample GR3-8 was collected from a m-sized boulder of float

Table 2-15: Average olivine analyses from the Mg-rich enclave near GR intrusion

Sample:	GR3-1	GR3-3	GR3-4	GR3-8[1]
n	7	2	7	9
Rock	*dun*	*dun*	*dun*	*dun*
SiO_2	40.5 ± 0.3	40.5 ± 0.1	40.2 ± 0.4	40.64 ± 0.2
TiO_2	<0.04.	<0.04	<0.04	<0.04
Al_2O_3	<0.02	<0.02	<0.02	<0.02
MgO	50.4 ± 0.3	50.5 ± 0.3	50.4 ± 0.3	52.1 ± 0.2
FeO	8.5 ± 0.3	8.6 ± 0.1	8.5 ± 0.2	6.7 ± 0.1
MnO	0.15 ± 0.02	0.14 ± 0.01	0.13 ± 0.02	0.13 ± 0.02
CaO	<0.02	<0.02	<0.02	<0.02
Na_2O	<0.02	<0.02	<0.02	<0.02
NiO	0.43 ± 0.02	0.42 ± 0.06	0.45 ± 0.05	0.43 ± 0.03
Cr_2O_3	<0.05	<0.05	<0.05	<0.05
P_2O_5	-	-	-	-
Total	100.1 ± 0.7	100.3 ± 0.5	99.7 ± 0.3	100.0 ± 0.3
Fo	91.3 ± 0.2	91.2 ± 0.0	91.3 ± 0.2	93.3 ± 0.1
Ni (ppm)	3344 ± 140	3332± 489	3511 ± 367	3402 ± 233
Mg# liq	0.76	0.76	0.76	0.81

[1] float

Table 2-16: Average compositions of orthopyroxene from subalkaline Q-suite intrusions

Sample:	GR-2	GR2-1	GR2-2	GR-8	GR-10	GR-11	GR-13	GR2-4	GR4-2	DH08-7	DH-07	DH-08	DH-09
n	11	25	8	8	10	13	8	10	9	7	11	12	9
Area	1	1	1	1	1	1	1	1	1	1	1	1	1
Rock	web.	web.	web.	gabnor.	gabnor.	gabnor.	gabnor.	gabnor.	px-qmzt	harzb.	per.	harzb.	per.
WR Mg-	0.78	0.77	0.76	0.73	0.71	0.69	0.64	0.60	0.50	0.81	0.82	0.81	0.81
SiO_2	54.2 ± 0.5	53.6 ±	53.8 ±	53.3 ±	52.9 ±	52.7 ±	52.0 ±	51.9 ±	52.0 ±	54.0 ±	54.7 ± 1.1	54.3 ±	55.3 ±
TiO_2	<0.05	<0.05	<0.05	<0.05	<0.05	<0.05	<0.05	0.06 ±	0.06 ±	<0.05	<0.05	<0.05	<0.05
Al_2O_3	1.8 ± 0.5	1.8 ± 0.3	0.97 ±	0.98 ±	1.0 ± 0.2	1.0 ± 0.2	1.1 ± 0.2	1.0 ± 0.2	0.81 ±	2.8 ± 0.3	1.7 ± 0.3	2.4 ± 0.8	1.5 ± 0.2
MgO	29.3 ± 0.7	27.6 ±	26.7 ±	25.2 ±	24.8 ±	24.1 ±	22.2 ±	21.8 ±	20.5 ±	30.7 ±	30.8 ± 1.1	30.9 ±	30.9 ±
FeO	13.2 ± 0.4	15.6 ±	17.1 ±	19.0 ±	19.8 ±	20.6 ±	22.4 ±	23.6 ±	25.0 ±	11.1 ±	11.8 ± 0.6	11.1 ±	11.7 ±
MnO	0.33 ±	0.36 ±	0.44 ±	0.47 ±	0.50 ±	0.52 ±	0.55 ±	0.63 ±	0.87 ±	0.12 ±	0.29 ±	0.24 ±	0.31 ±
CaO	0.46 ±	0.49 ±	0.38 ±	0.42 ±	0.44 ±	0.45 ±	0.48 ±	0.42 ±	0.54 ±	0.21 ±	0.59 ± 1.8	0.21 ±	0.32 ±
Na_2O	<0.03	<0.03	<0.03	<0.03	<0.03	<0.03	<0.03	<0.03	<0.03	<0.03	<0.03	<0.03	<0.03
K_2O	<0.02	<0.02	<0.02	<0.02	<0.02	<0.02	<0.02	<0.02	<0.02	<0.02	<0.02	<0.02	<0.02
NiO	<0.03	<0.03	<0.03	<0.03	<0.03	<0.03	<0.03	<0.03	<0.03	0.14 ±	-	0.15 ±	-
Cr_2O_3	<0.06	<0.06	<0.06	<0.06	<0.06	<0.06	<0.06	<0.06	<0.06	0.18 ±	0.12 ±	0.23 ±	0.09 ±
Total	99.4 ± 0.4	99.5 ±	99.5 ±	99.5 ±	99.5 ±	99.5 ±	98.8 ±	99.5 ±	99.7 ±	99.3 ±	99.9 ± 1.1	99.5 ±	100.2 ±
[1]100Mg#	79.4 ± 0.7	75.6 ±	73.0 ±	69.7 ±	68.5 ±	67.0 ±	63.8 ±	61.6 ±	58.5 ±	82.8 ±	82.0 ± 0.5	82.9 ±	82.1 ±
[2]Fe^{3+}/SFe	0.1 ± 0.0	0.1 ± 0.1	0.1 ± 0.0	0.1 ± 0.0	0.1 ± 0.0	0.1 ± 0.0	<0.05	0.1 ± 0.0	<0.05	0.2 ± 0.0	0.2 ± 0.1	0.2 ± 0.1	0.1 ± 0.1

Sample:	DH-11	DH-13	DH-14	PK09-17	LM3-2	LM3-3	UM03-08
n	11	8	11	4	12	15	7
Area	1	1	1	1	2	2	5
Rock	web.	web.	web.	web.	web.	web.	web.
WR Mg-	0.77	0.77	0.74	0.79	0.83	0.83	0.81
SiO_2	54.5 ± 0.6	54.1 ±	53.7 ±	54.3 ±	54.4 ±	54.5 ±	54.3 ±
TiO_2	<0.05	0.05 ±	0.05 ±	<0.05	<0.05	<0.05	<0.05
Al_2O_3	0.64 ±	0.53 ±	0.54 ±	1.5 ± 0.1	1.3 ± 0.3	1.1 ± 0.6	1.6 ± 0.4
MgO	28.3 ± 0.5	26.5 ±	25.2 ±	29.2±	29.1 ±	29.0 ±	29.5 ±
FeO	15.6 ± 0.5	17.6 ±	19.1 ±	13.4 ±	13.8 ±	14.2 ±	12.8 ±
MnO	0.33 ±	0.38 ±	0.41 ±	0.30 ±	0.36 ±	0.37 ±	0.26 ±
CaO	0.36 ±	0.37 ±	0.48 ±	0.64 ±	0.30 ±	0.31 ±	0.58 ±
Na_2O	<0.03	<0.03	<0.03	<0.03	<0.03	<0.03	<0.03
K_2O	<0.02	<0.02	<0.02	<0.02	<0.02	<0.02	<0.02
NiO	-	<0.03	<0.03	0.08 ±	<0.03	0.03 ±	0.12 ±
Cr_2O_3	0.09 ±	0.07 ±	<0.06	0.10 ±	0.12 ±	<0.06	0.12 ±
Total	99.8 ± 0.7	99.6 ±	99.7 ±	99.6 ±	99.4 ±	99.6 ±	99.3 ±
[1]100Mg#	76.1 ± 0.9	72.4 ±	69.7 ±	79.1 ±	78.1 ±	78.5 ±	80.1 ±
[2]Fe^{3+}/SFe	0.1 ± 0.1	<0.05	<0.05	0.1 ± 0.0	0.1 ± 0.0	0.1 ± 0.0	0.1 ± 0.0

Table 2-17: Average compositions of clinopyroxene from Q-suite intrusions

Sample:	GR-2	GR2-1	GR2-2	GR-08	GR-10	GR-11	GR-13	GR2-4	GR4-2	DH-09	DH-11	DH-13	DH-14
n	6	5	7	6	8	6	4	8	3	12	9	9	16
Area	1	1	1	1	1	1	1	1	1	1	1	1	1
Rock	web.	web.	web.	gabnor.	gabnor.	gabnor.	gabnor.	gabnor.	px-qmzt	per.	web.	web.	web.
WR Mg-	0.78	0.77	0.76	0.73	0.71	0.69	0.64	0.60	0.50	0.81	0.77	0.77	0.74
SiO_2	52.1 ± 0.5	52.5 ±	52.8 ±	52.5 ±	52.6 ±	52.4 ±	51.6 ±	51.9 ±	52.0 ±	53.0 ±	53.5 ± 0.8	53.5 ±	53.2 ±
TiO_2	0.16 ±	0.05 ±	0.11 ±	0.11 ±	0.10 ±	0.09 ±	0.14 ±	0.18 ±	0.14 ±	0.08 ±	0.08 ±	0.11 ±	0.09 ±
Al_2O_3	2.2 ± 0.8	1.8 ± 0.4	1.5 ± 0.7	1.5 ± 0.1	1.6 ± 0.1	1.6 ±	1.9 ± 0.1	1.7 ± 0.5	1.7 ± 0.1	1.6 ± 0.4	1.1 ± 0.3	1.1 ± 0.1	1.0 ± 0.1
MgO	16.2 ± 0.4	16.0 ±	16.0 ±	15.5 ±	15.3 ±	15.1 ±	14.1 ±	14.3 ±	13.7 ±	16.8 ±	16.1 ± 0.4	16.0 ±	15.5 ±
FeO	4.5 ± 0.2	5.5 ± 0.2	5.5 ± 1.1	6.5 ± 0.3	7.0 ± 0.2	7.5 ±	8.3 ± 0.3	8.3 ± 0.8	9.8 ± 1.1	3.6 ± 0.5	4.8 ± 0.3	5.7 ± 0.4	6.2 ± 0.3
MnO	0.14 ±	0.16 ±	0.17 ±	0.19 ±	0.21 ±	0.23 ±	0.23 ±	0.24 ±	0.35 ±	0.12 ±	0.14 ±	0.15 ±	0.16 ±
CaO	23.6 ± 0.7	23.1 ±	23.1 ±	23.0 ±	22.8 ±	22.7 ±	22.7 ±	22.7 ±	22.0 ±	24.1 ±	23.2 ± 0.4	23.1 ±	23.1 ±
Na_2O	0.26 ±0.17	0.33 ±	0.35 ±	0.36 ±	0.39	0.40 ±	0.44 ±	0.4 ±	0.47 ±	0.15	0.46	0.50 ±	0.47 ±
K_2O	<0.02	<0.02	<0.02	<0.02	<0.02	<0.02	<0.02	<0.02	<0.02	<0.02	<0.02	<0.02	<0.02
Cr_2O_3	0.12 ±	0.07 ±	0.09 ±	<0.06	<0.06	<0.06	<0.06	<0.06	<0.06	0.18 ±	0.25 ±	0.22 ±	0.19 ±
Total	99.4 ± 0.3	99.5 ±	99.7 ±	99.6 ±	100.1 ±	100.0 ±	99.4 ±	99.6 ±	100.1 ±	99.7 ±	99.7 ± 0.7	100.3 ±	100.0 ±
[1]100Mg#	86.2 ± 0.8	81.2 ±	83.4 ±	80.5 ±	79.0 ±	77.7 ±	74.7 ±	75.0 ±	70.6 ±	88.6 ±	85.4 ± 1.1	82.9 ±	81.3 ±
[2]Fe^{3+}/SFe	0.6 ± 0.3	0.4 ± 0.1	0.4 ± 0.2	0.4 ± 0.2	0.4 ± 0.1	0.4 ± 0.1	0.4 ± 0.1	0.3 ± 0.1	0.3 ± 0.1	0.5 ± 0.3	0.3 ± 0.2	0.4 ± 0.2	0.3 ± 0.1

Sample:	PK09-17	LM4-2	UM03-	C1-05	C1-13	C1-15	C1-18	C1-20	C1-23	C1-39	C1-44	C1-50	D-22
n	6	4	3	8	9	10	9	4	4	2	4	5	8
Area	1	2	5	3	3	3	3	3	3	3	3	3	3
Rock	web.	web.	web.	weh.	weh.	dun.	dun.	dun.	dun.	weh.	dun.	dun.	bt. weh.
WR Mg-	0.79	0.79	0.81	0.78	0.78	0.75	0.81	0.81	0.8	0.77	0.77	0.77	0.8
SiO_2	52.7 ± 0.7	52.5 ±	51.9 ±	53.8 ±	53.8 ±	51.8 ±	52.3 ±	51.4 ±	52.7 ±	53.3 ±	52.9 ± 1.7	52.5 ±	52.6 ±
TiO_2	0.12 ±	0.10 ±	0.08 ±	0.05 ±	0.06 ±	0.19 ±	0.14 ±	0.15 ±	0.14 ±	0.07 ±	0.08 ± 0.1	0.19 ±	0.29 ±
Al_2O_3	1.8 ± 0.6	2.5 ± 0.5	2.1 ± 0.4	0.39 ±	0.53 ±	1.0 ± 0.3	1.0 ± 0.6	1.2 ± 0.3	1.1 ± 0.2	1.2 ± 0.1	0.48 ±	1.8 ± 0.8	2.7 ± 2.7
MgO	16.5 ± 0.3	16.5 ±	16.9 ±	17.3 ±	17.5 ±	16.9 ±	17.3 ±	17.3 ±	17.0 ±	16.8 ±	17.5 ± 1.1	16.9 ±	16.7 ±
FeO	4.4 ± 0.6	4.3 ± 0.5	5.1 ± 0.9	3.5 ± 0.2	3.1 ± 0.4	5.4 ± 3.1	4.1 ± 3.1	4.7 ± 2.4	3.7 ± 1.0	4.2 ± 0.1	5.0 ± 4.03	3.8 ± 1.4	4.3 ± 1.0
MnO	0.13 ±	0.13 ±	0.12 ±	0.15 ±	0.13 ±	0.11 ±	0.11 ±	0.09 ±	0.11 ±	0.16 ±	0.12 ±	0.11 ±	0.13 ±
CaO	23.7 ± 0.4	23.9 ±	22.1 ±	24.7 ±	25.0 ±	23.9 ±	24.1 ±	24.1 ±	24.5 ±	24.3 ±	23.7 ± 0.7	23.6 ±	22.7 ±
Na_2O	0.22 ±0.06	0.17	0.41	0.06 ±	0.05 ±	0.04	0.06	0.04 ±	0.04 ±	0.10	0.10 ±	0.15 ±	0.06
K_2O	<0.02	<0.02	<0.02	<0.02	<0.02	<0.02	<0.02	<0.02	<0.02	<0.02	<0.02	<0.02	0.03 ±
Cr_2O_3	0.20 ±	0.15 ±	0.52 ±	<0.06	<0.06	0.45 ±	0.53 ±	0.81 ±	0.51 ±	0.07 ±	0.19 ±	0.39 ±	0.29 ±
Total	99.8 ± 0.8	100.3 ±	99.3 ±	100.0 ±	100.3 ±	99.7 ±	99.7 ±	99.7 ±	99.8 ±	100.1 ±	100.1 ±	99.5 ±	100.1 ±
[1]100Mg#	86.6 ± 1.7	87.2 ±	85.2 ±	89.3 ±	90.7 ±	84.5 ±	88.0± 7.7	86.7 ±	89.0 ±	87.3±	86.3 ±	88.8 ±	87.0± 3.1
[2]Fe^{3+}/SFe	0.5 ± 0.2	0.6 ± 0.1	0.7 ± 0.1	0.6 ± 0.2	0.7 ± 0.3	0.8 ± 0.3	0.8 ± 0.2	1.0 ± 0.1	0.7 ± 0.2	0.5 ± 0.1	0.8 ± 0.1	0.5 ± 0.4	0.5 ± 0.4

Table 2-18: Average compositions of amphibole from Q-suite intrusions

Sample	GR-2	GR2-1	GR2-2	GR-08	GR-10	GR-11	GR-13	GR2-4	DH08-7	DH-05	DH-08	DH-09	LM4-2
n	4	3	5	6	3	6	5	4	5	7	8	19	2
Area	1	1	1	1	1	1	1	1	1	1	1	1	2
Rock	web.	web.	web.	gabnor.	gabnor.	gabnor.	gabnor.	gabnor.	harzb.	web.	harzb.	per.	web.
WR Mg-	0.78	0.77	0.76	0.73	0.71	0.69	0.64	0.60	0.81		0.81	0.81	0.79
SiO_2	42.2 ± 0.5	43.1 ±	47.6 ±	47.3 ±	48.1 ±	46.7 ±	44.7 ±	44.9 ±	48.9 ±	45.9 ±	42.5 ± 0.7	44.6 ±	45.1 ±
TiO_2	0.99 ±	0.66 ±	0.81 ±	0.94 ±	0.75 ±	0.92 ±	1.2 ± 0.1	1.8 ± 0.2	0.65 ±	0.49 ±	0.51 ±	0.51 ±	0.32 ±
Al_2O_3	13.3 ± 0.3	12.6 ±	8.4 ± 0.5	8.3 ± 0.2	7.8 ± 1.1	8.8 ±	9.6 ± 0.3	9.7 ± 0.8	13.2 ±	10.3 ±	13.9 ± 1.0	11.9 ±	12.0 ±
MgO	15.9 ± 0.3	15.5 ±	17.0 ±	16.4 ±	16.5 ±	15.5 ±	13.7 ±	13.6 ±	17.4 ±	17.6 ±	17.3 ± 0.4	17.6 ±	17.3 ±
FeO	8.4 ± 0.6	9.4 ± 0.4	8.9 ± 0.4	10.0 ±	10.2 ±	13.3 ±	13.1 ±	13.3 ±	6.8 ± 0.4	7.4 ± 0.6	7.0 ± 0.3	6.8 ± 0.7	7.7 ± 0.1
MnO	0.09 ±	0.09 ±	0.10 ±	0.11 ±	0.11 ±	0.13 ±	0.13 ±	0.13 ±	0.10 ±	0.07 ±	0.12 ±	0.07 ±	0.08 ±
CaO	12.1 ± 0.3	11.9 ±	12.0 ±	11.9 ±	12.1 ±	11.8 ±	11.8 ±	11.8 ±	11.8 ±	12.3 ±	11.4 ± 0.1	12.3 ±	12.4 ±
Na_2O	2.4 ± 0.3	2.0 ± 0.1	1.2 ± 0.1	1.1 ± 0.1	0.97 ±	1.1 ± 0.1	1.2 ± 0.2	1.2 ± 0.1	2.5 ± 0.2	1.8 ± 0.3	2.7 ± 0.2	2.0 ±0.4	2.1 ±
K_2O	0.73 ±	1.1 ± 0.1	0.75 ±	0.73 ±	0.63 ±	0.82 ±	0.96 ±	0.98 ±	0.49 ±	0.83 ±	0.33 ±	0.58 ±	0.19 ±
Cr_2O_3	0.31 ±	0.23 ±	0.25 ±	0.09 ±	<0.06	<0.06	<0.06	<0.06	0.68 ±	0.40 ±	0.78 ±	0.68 ±	0.18 ±
Total	96.3 ± 0.5	96.6 ±	96.8 ±	96.8 ±	97.3 ±	97.0 ±	96.4 ±	97.4 ±	96.6 ±	97.4 ±	96.7 ± 1.7	96.9 ±	97.4 ±
Structural formula [3]													
Si	6.12 ±	6.24 ±	6.81 ±	6.78 ±	6.86 ±	6.71 ±	6.57 ±	6.55 ±	6.11 ±	6.53 ±	6.03 ±	6.31 ±	6.39 ±
Al^{IV}	1.88 ±	1.76 ±	1.19 ±	1.22 ±	1.14 ±	1.29 ±	1.43 ±	1.45 ±	1.89 ±	1.47 ±	1.97 ±	1.69 ±	1.61 ±
Ti	0.11 ±	0.07 ±	0.09 ±	0.10 ±	0.08 ±	0.10 ±	0.13 ±	0.19 ±	0.07 ±	0.05 ±	0.05 ±	0.06 ±	0.03 ±
Al^{VI}	0.39 ±	0.39 ±	0.20 ±	0.17 ±	0.17 ±	0.21 ±	0.23 ±	0.22 ±	0.33 ±	0.27 ±	0.35 ±	0.34 ±	0.39 ±
Cr	0.04 ±	0.03 ±	0.03 ±	0.01 ±	-	-	-	-	0.08 ±	0.05 ±	0.08 ±	0.08 ±	0.02 ±
Fe^{3+}	0.69 ±	0.73 ±	0.66 ±	0.73 ±	0.73 ±	0.81 ±	0.71 ±	0.64 ±	0.81 ±	0.68 ±	0.84 ±	0.75 ±	0.75 ±
Fe^{2+}	0.33 ±	0.41 ±	0.39 ±	0.47 ±	0.49 ±	0.55 ±	0.90 ±	0.98 ±	0.00 ±	0.18 ±	0.00 ±	0.08 ±	0.16 ±
Mn	0.01 ±	0.01 ±	0.01 ±	0.01 ±	0.01 ±	0.02 ±	0.02 ±	0.02 ±	0.01 ±	0.01 ±	0.01 ±	0.01 ±	0.01 ±
Mg	3.44 ±	3.36 ±	3.61 ±	3.50 ±	3.51 ±	3.31 ±	3.00 ±	2.95 ±	3.70 ±	3.73 ±	3.67 ±	3.71 ±	3.64 ±
Ca	1.87 ±	1.85 ±	1.83 ±	1.83 ±	1.85 ±	1.81 ±	1.85 ±	1.84 ±	1.79 ±	1.87 ±	1.73 ±	1.87 ±	1.89 ±
Na	0.67 ±	0.55 ±	0.33 ±	0.31 ±	0.27 ±	0.29 ±	0.35 ±	0.34 ±	0.69 ±	0.49 ±	0.76 ±	0.55 ±	0.57 ±
K	0.13 ±	0.21 ±	0.14 ±	0.13 ±	0.11 ±	0.15 ±	0.18 ±	0.18 ±	0.09 ±	0.15 ±	0.06 ±	0.10 ±	0.03 ±
Total	15.68 ±	15.61 ±	15.29 ±	15.26 ±	15.11 ±	15.25 ±	15.38 ±	15.36 ±	15.57 ±	15.47 ±	15.57 ±	15.56 ±	15.49 ±

Table 2-18: Average compositions of amphibole from Q-suite intrusions (cont.)

Sample	C1-05	C1-13	C1-15	C1-16	C1-20	C1-44	C1-50	D-22
n	2	3	4	3	4	6	2	2
Area	3	3	3	3	3	3	3	3
Rock	weh.	weh.	dun.	dun.	dun.	dun.	dun.	bt. weh.
WR Mg-	0.78	0.78	0.75	0.82	0.81	0.77	0.77	0.80
SiO_2	51.2 ± 4.2	51.3 ±	52.4 ±	51.1 ±	51.0 ±	51.7 ±	49.6 ±	42.8 ±
TiO_2	0.28 ±	0.27 ±	0.18 ±	0.24 ±	0.21 ±	0.14 ±	0.38 ±	1.7 ± 0.8
Al_2O_3	5.8 ± 3.4	5.7 ± 2.0	5.0 ± 2.4	5.4 ± 3.0	5.3 ± 0.9	4.4 ± 1.7	7.2 ± 2.5	13.1 ±
MgO	20.0 ± 1.4	20.7 ±	20.8 ±	21.0 ±	20.8 ±	20.6 ±	19.1 ±	15.5 ±
FeO	5.5 ± 1.3	4.8 ± 0.5	4.5 ± 1.2	3.8 ± 1.1	3.8 ± 0.4	4.5 ± 0.8	5.6 ± 1.5	8.0 ± 1.2
MnO	0.09± 0.01	0.08 ±	0.07 ±	0.06 ±	0.09 ±	0.08 ±	0.09 ±	0.09 ±
CaO	12.9 ± 0.3	13.1 ±	13.0 ±	12.8 ±	13.1 ±	13.6 ±	14.3 ±	12.4 ±
Na_2O	0.99 ±	1.1 ± 0.6	0.67 ±	1.3 ± 0.6	0.64 ±	0.83 ±	0.99 ±	2.1 ±0.03
K_2O	0.21 ±	0.22 ±	0.09 ±	0.29 ±	0.16 ±	0.25 ±	0.06 ±	0.98 ±
Cr_2O_3	0.20 ±	0.12 ±	0.26 ±	0.57 ±	0.49 ±	0.18 ±	0.67 ±	0.45 ±
Total	97.2 ± 0.2	97.2 ±	96.9 ±	96.6 ±	95.6 ±	96.4 ±	97.9 ±	97.2 ±
Structural formula [3]								
Si	7.17 ±	7.14 ±	7.30 ±	7.16 ±	7.20 ±	7.33 ±	7.00 ±	6.20 ±
Al^{IV}	0.83 ±	0.86 ±	0.70 ±	0.84 ±	0.80 ±	0.67 ±	1.00 ±	1.80 ±
Ti	0.03 ±	0.03 ±	0.02 ±	0.03 ±	0.02 ±	0.02 ±	0.04 ±	0.18 ±
Al^{VI}	0.13 ±	0.05 ±	0.12 ±	0.06 ±	0.08 ±	0.07 ±	0.20 ±	0.43 ±
Cr	0.02 ±	0.01 ±	0.03 ±	0.06 ±	0.05 ±	0.02 ±	0.08 ±	0.05 ±
Fe^{3+}	0.45 ±	0.47 ±	0.45 ±	0.41 ±	0.42 ±	0.40 ±	0.19 ±	0.32 ±
Fe^{2+}	0.20 ±	0.05 ±	0.07 ±	0.04 ±	0.03 ±	0.13 ±	0.47 ±	0.65 ±
Mn	0.01 ±	0.01 ±	0.01 ±	0.01 ±	0.01 ±	0.01 ±	0.01 ±	0.01 ±
Mg	4.16 ±	4.31 ±	4.31 ±	4.40 ±	4.39 ±	4.35 ±	4.02 ±	3.36 ±
Ca	1.94 ±	1.95 ±	1.94 ±	1.93 ±	1.98 ±	2.08 ±	2.16 ±	1.92 ±
Na	0.27 ±	0.26 ±	0.18 ±	0.35 ±	0.17 ±	0.23 ±	0.27 ±	0.60 ±
K	0.04 ±	0.03 ±	0.02 ±	0.05 ±	0.03 ±	0.05 ±	0.01 ±	0.18 ±
Total	15.21 ±	15.19 ±	15.13 ±	15.33 ±	15.19 ±	15.35 ±	15.44 ±	15.71 ±

Tables 2-15 to 2-18. See caption to Table 2-2 for analytical details.

n = number of analyses/sample. Reported uncertainties are 2 s.d. deviations from the mean calculated from n samples.

[1] Mg-number of pyroxenes = $Mg/(Mg+Fe^{TOT}+Mn)$; [2] Fe^{3+}/Fe^{TOT} was calculated using the program CALCMIN (Brandelik, 2009)

[3]Amphibole structural formula calculated to the basis of 23 O using amphibole_MAS routine of CALCMIN (Brandelik, 2009)

CHAPTER 3. Ferropicrite-driven reworking of the Ungava Craton and the genesis of the Neoarchean pyroxene-granitoids

Chapter 2 described the petrology of ca. 2.72-2.70 Ga Q-suite intrusions of Northeaster Superior Province's Ungava craton. The Q-suite plutons were derived from at least two distinct parental magma types. The parental magmas were Fe-rich high-Mg basalts and ferropicrites that require mantle sources considerably richer in iron than the "pyrolitic" mantle. Trace element and isotopic data suggest that the Q-suite plutons experienced late metasomatism by felsic anatectic melts, which may have imparted the "calc-alkaline" trace element signatures on the Q-suite cumulates. Chapter 3 presents evidence of extensive assimilation of TTG-derived melts by Q-suite parental magmas from a zoned intrusion in western Ungava craton. Simultaneous assimilation of crustal melts and fractional crystallization produced a margin of pyroxene-bearing diorite to granodiorite, indistinguishable from intermediate-SiO_2 ($\leq$65 wt. %) members of the regionally widespread pyroxene-bearing plutonic suite. Chapter 3 provides a new model for the petrogenesis of Ungava craton's pyroxene-granitoids and suggests an important role of Q-suite magmas in the cratonization of Northeastern Superior Province.

Abstract

Voluminous, pyroxene-bearing, intermediate to felsic plutons were emplaced during a 20-50 million year long, spatially extensive Neoarchean igneous event that culminated in the cratonization of North America's ~500 km-wide Ungava craton. The crystallization ages of pyroxene-bearing plutons coincide with the emplacement of numerous ca. 2.72-2.70 Ga, Fe-rich, ultramafic/mafic intrusions of the Qullinaaraaluk suite (Q-suite) that are scattered across the disparate domains of the Ungava craton. A high proportion of relatively sodic pyroxene-bearing granitoids with intermediate silica contents fall in a compositional gap between the Q-suite and pyroxene-free granitoids, suggesting that the pyroxene-granitoids may be formed by the simultaneous fractional crystallization and assimilation of older tonalitic and trondhjemitic (TT) crust by the Q-suite magmas. We estimate that pyroxene-granitoids containing ~65 wt. % SiO_2 may reflect ~40-50 wt. % contamination of mantle-derived picritic magma by trondhjemitic melts of the pre-2.74 Ga TTG crust. The craton-wide occurrence of the Q-suite intrusions and pyroxene-granitoids suggests that underplating by ferropicritic magmas played a key role in the cratonization of the Ungava craton at the end of Archean. A major contribution of mantle-derived magmas to the petrogenesis of the ca. 2.74-2.70 Ga pyroxene-granitoids is consistent with the proposed global generation of voluminous juvenile continental crust ca. 2.7 Ga.

Keywords: Neoarchean, AFC, ferropicrite, crustal growth, charnockite

1. Introduction

The Neoarchean Ungava craton (Fig. 3-1A) is a largely plutonic domain of the

Archean Superior Province composed of the pre-2.74 Ga tonalite-trondhjemite-granodiorite (TTG), and the ≤ 2.74 Ga high-K granite-granodiorite-monzogranite (GGM) and low-K pyroxene-granitoid suites (Boily et al., 2009; Maurice et al., 2009). Most of the pyroxene-granitoids and the GGM plutons of the Ungava craton were emplaced ca. 2.74 – 2.70 Ga, during an episode of extensive igneous activity, increased crustal contamination of mafic volcanic suites, and comprehensive reworking of the Ungava craton (Maurice et al., 2009). During this same time period, numerous, small, ultramafic to mafic intrusions (locally termed the Qullinaaraaluk, Couture, and Chateguay suites, herein collectively referred to as the Q-suite) were emplaced across the width of the craton (Simard, 2008). These intrusions commonly contain peridotitic cores inferred to have crystallized from Fe-rich, high-Mg basaltic to picritic parental magmas (MgO = 10-14 wt. %). In this paper, we present a geochemical model in which the voluminous pyroxene-granitoid suites of the Ungava craton are produced by craton-wide underplating by the mantle-derived magmas that were parental to the Q-suite. The pyroxene-granitoids are thus the mid-crustal expression of juvenile, mantle-derived magmatism that drove the reworking of the Northeastern Superior Province during a time of enhanced global formation of continental crust at ca. 2.7 Ga (Condie, 2000; Hawkesworth et al., 2009).

2. Plutonic rocks of the Ungava Craton

The relatively sodic (K/(K+Na) = 0.20 +0.29/-0.10) TTG suites of the Ungava craton have positive Sr anomalies and steep REE profiles (Bédard, 2006; Boily et al.,

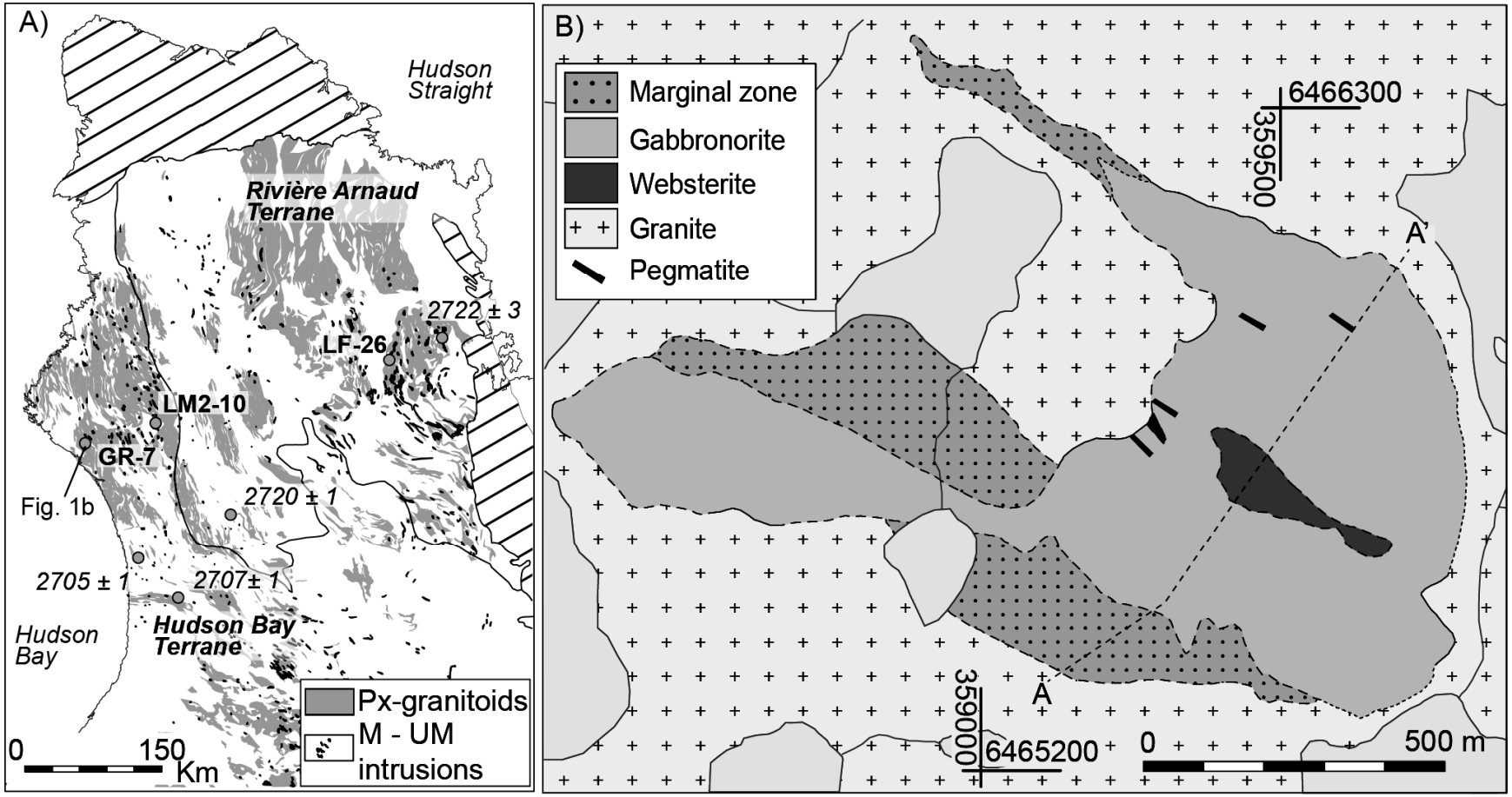

Figure 3-1: Maps of the Ungava craton and the Gladel River intrusion.
A) Map of the Ungava Craton showing the distribution of the pyroxene-granitoids and the mafic/ultramafic intrusive rocks, adapted from Simard (2008). Grey circles – previously dated MRNF Q-suite samples (ages shown) and samples dated in this study (bold labels). Location of map in Figure 3-1B is shown for reference. **B)** Geological map of the Gladel River intrusion, and the location of transect A-A' shown in Figure 3-5.

2009; Bédard et al., 2013), characteristic of the majority of Archean TTGs (Martin, 1986; Moyen and Stevens, 2006; Moyen and Martin, 2012). Although there is a broad consensus that the geochemical signature of TTGs reflects an origin through fluid-absent partial melting of metabasite at pressures > 1000 MPa where garnet is stable as a residual mineral, there are differing views regarding the geodynamic setting of Archean TTG (Moyen and Stevens, 2006; Moyen, 2011; Moyen and Martin, 2012). The end-member models call for: 1) A high pressure (2000 MPa) origin by partial melting of subducted oceanic crust, requiring geothermal gradients lower than 10 °C/km; 2) a medium pressure (1000-1500 MPa) origin, requiring geotherms of 10-12 °C; or 3) a low pressure origin (<1000 MPa) by partial melting of overthickened oceanic crust or underplated hydrous basalt, requiring steep geothermal gradients of 20-30 °C/km. In contrast to the TTG suite, the granitoids of the GGM suite are significantly more potassic (K/(K+Na) = 0.40 +0.18/-0.30) and show stronger enrichments in the light rare-earth (LREE) and large ion lithophile (LILE) elements. Isotopic and geochemical data indicate that partial melting of the pre-existing TTG in the middle-upper crust is the dominant process for the genesis of the GGM suite (Bédard, 2006; Boily et al., 2009; Huang et al., 2013).

Plutonic suites containing primary magmatic pyroxene were initially recognized in the Ungava by Percival et al. (1992). Such rocks have subsequently been referred to as charnockites (Percival and Mortensen, 2002; Frost and Frost, 2008), enderbites and clinopyroxene-tonalites (Bédard, 2003), or more simply pyroxene-granitoids (Boily and Maurice, 2008) or pyroxene-TTGs (Boily et al., 2009). The pyroxene-granitoid rocks range in composition from diorite to granite (SiO_2 ≥50–78 wt. %), and are a volumetrically significant component of the Ungava craton, accounting for more than

20% of its exposed surface (Fig. 3-1A; Simard, 2008; Maurice et al., 2009).

The pyroxene-granitoids were emplaced at mid-crustal pressures (500 ±100 MPa) at high temperatures (1100-810°C), and subsequently underwent prolonged cooling during which sub-solidus mineral re-equilibration and hydration occurred (Percival and Mortensen, 2002; Bédard, 2003). The pyroxene-granitoids have a wide range of SiO_2 contents that are positively correlated with light rare-earth element/heavy rare-earth element (LREE/HREE) ratios (Boily and Maurice, 2008). In contrast to the GGM and TTG suites, the pyroxene-granitoid suite includes a significant proportion (37%) of rocks with intermediate-SiO_2 (<65 wt. %) contents (Fig. 3-2). Pyroxene-granitoids with intermediate-SiO_2 are characterized by relatively uniform Y + HREE contents (Yb_{MORB} = 0.5 +0.4/-0.3; Gd/Yb_{MORB} = 3 +3/-1) and La/Yb_{MORB} (<80) ratios that in most cases fall outside the range of Archean TTGs (Martin, 1986; Moyen and Martin, 2012), suggesting that garnet did not have a significant role in their petrogenesis. Furthermore, the Mg-numbers (0.45 ±0.15; defined as Mg/(Mg+Fe)) of the intermediate-SiO_2 pyroxene-granitoids are lower than those of the globally widespread late Archean high-Mg sanukitoids (Shirey and Hanson, 1984; Martin et al., 2005; Rapp et al., 2010). The felsic pyroxene-granitoids (SiO_2 >65 wt. %) exhibit a systematic decrease in Y+HREE concentration and a concomitant increase in REE fractionation with increasing SiO_2 content.

The majority of the Ungava pyroxene-granitoids are relatively sodic (K/(K+Na) = 0.22 +0.32/-0.12) and geochemically similar to deep plutons formed in Phanerozoic magmatic arcs (Percival and Mortensen, 2002; Boily and Maurice, 2008; Frost and Frost,

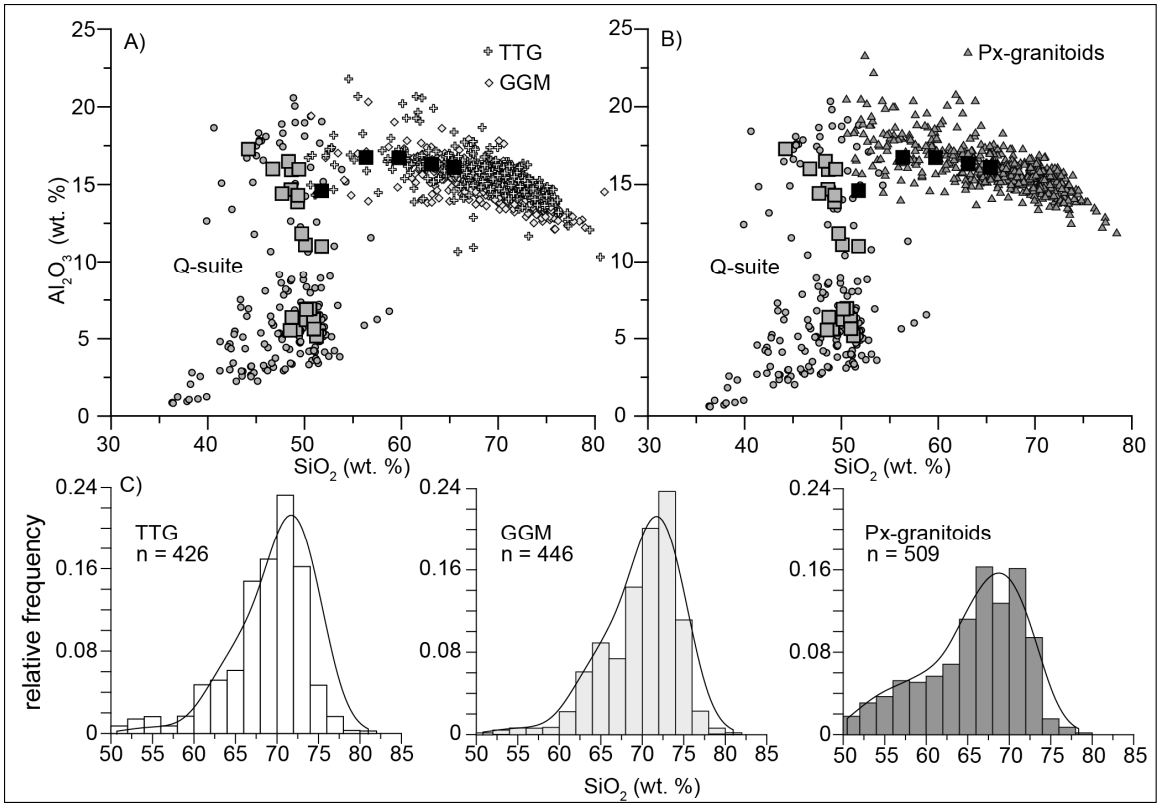

Figure 3-2: SiO_2 concentrations of the main plutonic suites of the Ungava craton. Al_2O_3 vs. SiO_2 plot of the Q-suite intrusions and the major plutonic suites of the Ungava craton. Large squares - Gladel River intrusion analyses; Small circles – other Q-suite; Black squares - marginal rocks of the Gladel River intrusion. **A)** Comparison of the Q-suite and marginal rock compositions with the TTG (crosses) and GGM (diamonds) suites. **B)** Comparison of the Q-suite and Gladel margin compositions with pyroxene-granitoids (triangles). **C)** SiO_2 (wt. %) relative probability histograms and density plots of the TTG, GGM and pyroxene-granitoid suites. Data sources: Stern et al., 1994; Percival and Mortensen, 2002; Bédard, 2006; Stevenson et al., 2006; Boily et al., 2009, MRNF E-Sigéom database.

2008). This similarity has led to the development of plate tectonic models that argue for their evolution in a supra-subduction zone environment during the docking and assembly of the NNE-SSW trending domains that make up the Ungava craton ((Stern et al., 1994; Percival et al., 2001; Percival and Mortensen, 2002). Percival and Mortensen (2002) originally proposed a model in which dry (<2 wt. % H_2O), mantle-derived, dioritic parental liquids evolved through early crystallization of pyroxenes, plagioclase, and biotite to form the intermediate-SiO_2 compositions of the pyroxene-granitoids. Percival and Mortensen (2002) argued that the fusion of a hot Neoarchean mantle wedge would generate voluminous, water-undersaturated melts that would evolve to dioritic compositions through the assimilation (10-20 %) of mid-lower felsic crust. Implicit in this model is the existence of a number of simultaneously active subduction zones in order to generate voluminous, coeval pyroxene-granitoids across the Ungava craton, and the dominant role of fractional crystallization in producing the compositional spectrum of the pyroxene-granitoid suites.

More recent studies (Bédard, 2003; Boily et al., 2009; Maurice et al., 2009) have argued against a plate tectonic model for the development of the Ungava craton. The identification of isotopically-distinct Rivière Arnaud and Hudson Bay terranes (Fig. 3-1A; Boily et al., 2009) and greenstone belts that once formed a laterally continuous ca. 2.78 Ga volcanic cover sequence on the Rivière Arnaud terrane (Maurice et al., 2009) provide a compelling argument against a major episode of arc assembly ca. 2.74-2.70 Ga. A tectonic model presented by Maurice et al. (2009), suggests the amalgamation of Rivière Arnaud and Hudson Bay terranes between 2.76 and 2.74 Ga, and subsequent large-scale melting of the proto-craton ca. 2.74-2.70 Ga. Furthermore, the presence of

widespread inherited zircon cores and enriched isotopic signatures (Boily et al., 2009) require the recycling of older felsic crust in the genesis of the pyroxene-granitoids. In an attempt to explain the geochemical similarities between the pyroxene-granitoids and the dominant, pre- 2.74 Ga TTG suite, Boily et al. (2009) proposed two alternative mechanisms for the generation of the pyroxene- granitoids: 1) melting of dehydrated lower crustal metabasites to produce dry dioritic parental melts, which then evolved through coupled fractional crystallization and assimilation; or 2) bulk re-melting of older TTG parents.

Experimental evidence (Rushmer, 1991; Wolf and Wyllie, 1994; Rapp and Watson, 1995; López and Castro, 2001) suggests that relatively high (~20-40 %) degrees of dehydration melting of amphibolite at relatively low pressures (<1000 MPa) and temperatures of 950-1075 °C are required to generate HREE-undepleted liquids of intermediate-SiO_2 composition. Furthermore, despite the low initial H_2O contents (0.7-1.7 wt. %) of amphibolite, the experimental melts of Rapp and Watson (1995) were H_2O -rich (3-15 wt. %). The generation of dry dioritic melts from dehydrated metabasites, as proposed by Boily et al. (2009), would require even higher temperatures and craton-scale geothermal gradients in excess of 80 °C/km that are required for amphibole breakdown below the wet basaltic solidus at upper to mid-crustal pressures (≤300 MPa; Peacock et al., 1994). Assuming complete dehydration, middle crustal metabasites would yield small-degree silicic melts at ~1100° (Harry and Green, 1999), and larger-degree melts of intermediate-SiO_2 content at higher temperatures. The development of such extreme craton-scale geothermal gradients is, however, not supported by the widespread presence of >2.74 Ga amphibolite-facies greenstone belts, and biotite-rich TTG at the present level

of exposure. Alternatively, dehydration of amphibole could occur under cool, high pressure conditions (~2500 MPa; Peacock et al., 1994) that require relatively low geothermal gradients (≤10°C/km). Such low geothermal gradients are, however, inconsistent with the hotter regional geothermal gradients required by the widespread > 2.75 Ga TTG suites. Relatively dry, Fe and Al-rich dioritic (jotunitic) magmas, parental to some Proterozoic anorthositic suites, were generated by melting of anhydrous plagioclase and pyroxene-dominated mafic granulites in the lower crust (1000-1300 MPa; Longhi et al., 1999). However, the scarcity of anorthosite (Simard, 2008) and pyroxene-bearing diorites with SiO_2 <55 wt. % in the Ungava craton, and the less pronounced Fe-enrichment of the intermediate-SiO_2 pyroxene-granitoids compared to the jotunitic parental magma (Mg-number = 0.38) of Longhi et al. (1999), suggest that the intermediate -SiO_2 pyroxene-granitoids were not derived by melting of Fe-rich mafic granulites.

The alternative hypothesis (Boily et al., 2009) that the pyroxene-granitoid suite is a product of bulk re-melting of older TTG crust does not offer an adequate explanation for the high abundance of the intermediate-SiO_2 pyroxene-granitoids, which require parental magmas that are more mafic than the majority of TTG.

3. The Q-Suite

The Q-suite intrusions are amphibole ± biotite-rich mafic/ultramafic bodies that commonly include lenses of dunite or peridotite composed of 85-90 % accumulated olivine ±orthopyroxene ±clinopyroxene, which represent the most primitive magmatic cumulates. The abundance of interstitial amphibole in the most magnesian cumulates, and the frequently observed partial replacement of clinopyroxene by amphibole, suggests that

the Q-suite magmas attained relatively high H_2O contents. Field relations, such as the absence of chilled contacts against surrounding granitoids, symmetrically-zoned dyke-like morphologies, and ubiquitous brecciation by late-stage granitic dykes and veins suggest that the Q-suite intrusions are coeval with the granitic rocks that surround them.

3.1 U-Pb zircon geochronology of the Q-suite intrusions

Two previously dated Qullinaaraaluk suite (sensu stricto) plutons from the southwestern Ungava craton (2705 ±1, 2707 ±1, 2720 ±2 Ma U-Pb zircon; Simard, 2008) indicate that the emplacement of Q-suite intrusions was coeval with the ca. 2.74-2.70 Ga reworking of the Ungava craton. A gabbronorite located in the easternmost Ungava craton has a zircon crystallization age of 2722 ±3 Ma (Simard, 2008), consistent with the Q-suite ages from the western Ungava craton. Zircon grains from two Q-suite gabbronorites from the Hudson Bay Terrane, and from a single websterite in the eastern Rivière Arnaud Terrane (Fig. 3-1A) were analyzed at the University of British Columbia's Pacific Institute for Isotopic and Geochemical Research (PCIGR) using the Chemical Abrasion-Thermal Ion Mass Spectrometry (CA-TIMS) procedure (Mundil et al., 2004; Mattinson, 2005; Scoates and Friedman, 2008). The analyzed zircon grains (Table 3-1; Fig. 3-3) have irregular, elongate to "wormy" habits.

Four chemically abraded zircons from a gabbronorite (sample GR-7) situated within a zoned mafic-ultramafic plutonic body in the westernmost Hudson Bay Terrane (the Gladel River intrusion, see section 3.3), are slightly discordant (-0.2 - 0.2 %) and yield overlapping $^{207}Pb/^{206}Pb$ ages ranging from 2717.8 – 2719.2 Ma. The mean weighted $^{207}Pb/^{206}Pb$ age of 2718.9 ±0.7 (error quoted as 2σ) is interpreted to be the crystallization

Table 3-1: U-Pb TIMS analytical data for zircon from mafic and ultramafic intrusive rocks of the Ungava craton

								Isotopic ratios (2σ, %)[d]				Apparent ages (2σ, Ma)[e]			
Sample[a]	**Wt. µg**	**U ppm**	**Pb ppm**	**$^{206}Pb/^{204}Pb$[b]**	**Pb_c[c] pg**	**Th/U**	**Pb^*/Pb_c[c]**	**$^{206}Pb/^{238}U$**	**$^{207}Pb/^{235}U$**	**$^{207}Pb/^{206}Pb$**	**rho**	**$^{206}Pb/^{238}U$**	**$^{207}Pb/^{235}U$**	**$^{207}Pb/^{206}Pb$**	**% disc.[f]**
GR-7 *(UTM NAD27 zone 18, 359545E, 6465849N)*															
A	79	39	23.4	7063516	0.01	0.466	132872	0.52495 (0.11)	13.5566 (0.17)	0.18730 (0.10)	0.812	2720.1 (2.5)	2719.2 (1.6)	2718.6 (1.6)	-0.1
B	80	14	8.6	349661	0.10	0.480	6597	0.52343 (0.14)	13.5112 (0.20)	0.18721 (0.14)	0.714	2713.7 (3.0)	2716.1 (1.9)	2717.8 (2.3)	0.2
D	22	68	41.7	7063516	0.02	0.580	42387	0.52602 (0.12)	13.5897 (0.16)	0.18737 (0.06)	0.944	2724.7 (2.7)	2721.5 (1.5)	2719.2 (1.0)	-0.2
E	13	91	54.1	243764	0.15	0.451	4571	0.52464 (0.15)	13.5495 (0.18)	0.18731 (0.07)	0.935	2718.7 (3.2)	2718.7 (1.7)	2718.7 (1.1)	0.0
Mean weighted $^{207}Pb/^{206}Pb$ age = 2718.9 ± 0.7 Ma (2σ, decay constant error not included; MSWD = 0.53, probability = 0.66)															
LM2-10 *(UTM NAD27 zone 18, 434116E, 6492175N)*															
A	38	44	29.2	134331	0.41	1.041	2688	0.52224 (0.11)	13.4160 (0.15)	0.18632 (0.05)	0.959	2708.7 (2.3)	2709.4 (1.4)	2709.9 (0.9)	0.0
B	23	54	37.0	51424	0.79	1.167	1053	0.52283 (0.11)	13.4326 (0.15)	0.18634 (0.06)	0.932	2711.2 (2.5)	2710.6 (1.5)	2710.1 (1.1)	0.0
C	30	36	25.3	76555	0.47	1.318	1612	0.52229 (0.11)	13.4201 (0.15)	0.18636 (0.05)	0.972	2708.9 (2.4)	2709.7 (1.4)	2710.3 (0.8)	0.1
D	23	109	78.1	272265	0.30	1.505	5934	0.51832 (0.10)	13.3119 (0.15)	0.18627 (0.07)	0.913	2692.0 (2.2)	2702.0 (1.4)	2709.5 (1.1)	0.6
Mean weighted $^{207}Pb/^{206}Pb$ age = 2710.0 ± 0.5 Ma (2σ, decay constant error not included; MSWD = 0.44, probability = 0.73)															
LF-26 *(UTM NAD27 zone 19, 342152E, 6549087N)*															
A	998	188	131.7	13865	3.07	0.466	278	0.55017 (0.11)	15.1218 (0.15)	0.199343 (0.06)	0.945	2825.9 (2.6)	2822.9 (1.5)	2820.8 (1.0)	-0.2
B	729	24	16.1	3658	1.45	0.480	69	0.54684 (0.17)	14.9762 (0.21)	0.198627 (0.07)	0.947	2812.0 (3.9)	2813.7 (2.0)	2815.0 (1.1)	0.1
C	663	217	141.7	10029	1.28	0.580	188	0.54704 (0.13)	14.9529 (0.17)	0.198244 (0.07)	0.931	2812.9 (2.9)	2812.2 (1.6)	2811.8 (1.1)	0.0
E	271	33	18.9	3951	0.86	0.451	67	0.52473 (0.22)	13.6021 (0.24)	0.188005 (0.03)	0.999	2719.2 (4.8)	2722.4 (2.3)	2724.8 (0.4)	0.2

[a] A, B etc. are labels for fractions composed of single zircon grains or fragments; all fractions annealed and chemically abraded after Mattison (2005) and Scoates and Friedman (2008).

[b] Measured ratio corrected for spike and fractionation only. Mass discrimination of 0.25%/amu based on analysis of NBS-982; all Daly analyses.

[c] Pb* and Pb_c represent radiogenic and common Pb, respectively.

[d] Corrected for fractionation, spike, and common Pb; up to 0.2 pg of common Pb was assumed to be procedural blank: $^{206}Pb/^{204}Pb = 18.50 \pm 1.0\%$; $^{207}Pb/^{204}Pb = 15.50 \pm 1.0\%$; $^{208}Pb/^{204}Pb = 38.40 \pm 1.0\%$ (all uncertainties 1σ). Excess over blank was assigned to initial common Pb with Stacey and Kramers (1975) model Pb composition at 2719 Ma. Errors are 2σ.

[e] Calculations are based on the decay constants of Jaffey et al. (1971). $^{206}Pb/^{238}U$ and $^{207}Pb/^{206}Pb$ ages corrected for initial disequilibrium in $^{230}Th/^{238}U$ using Th/U [magma] = 3.

[f] % discordance calculated as $100 - 100 \times (^{206}Pb/^{238}U / ^{207}Pb/^{206}Pb)_{age.}$

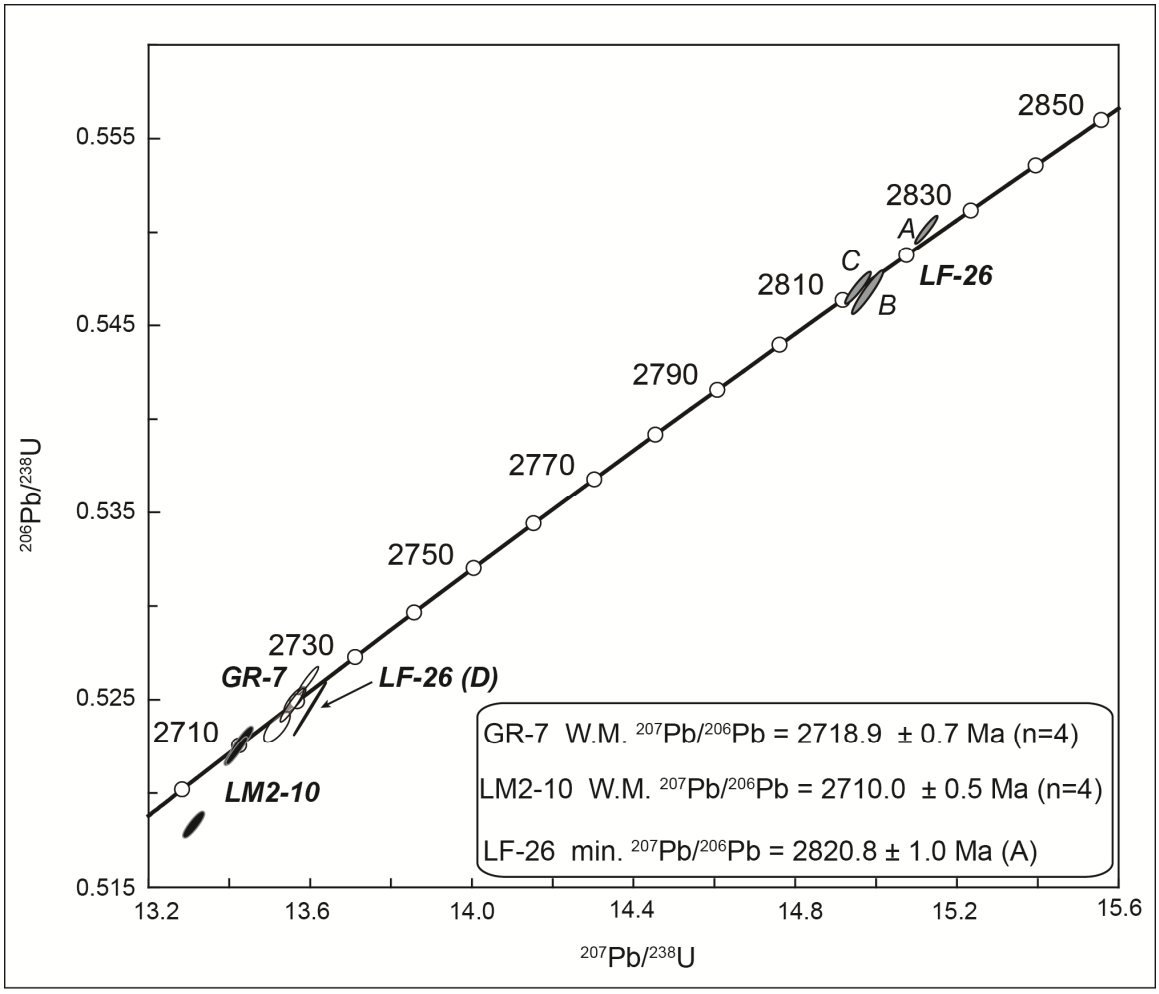

Figure 3-3: U-Pb concordia diagrams.

Concordia diagram of CA-TIMS U-Pb data (ellipses at 2σ) for Q-suite gabbronorites GR-7 (white ellipses) and LM2-10 (black ellipses) and older websterite LF-26 (grey-ellipses).

age of the intrusion, assuming the closure temperature for diffusion of Pb in zircon is greater than 950°C (Cherniak and Watson, 2000). The mean weighted $^{207}Pb/^{206}Pb$ age of four nearly concordant (0-0.6 %) zircons from a gabbronorite sample (LM2-10) collected in the eastern Hudson Bay Terrane, near the inferred contact with the Rivière Arnaud Terrane, yields a crystallization age of 2710.0 ±0.5 Ma.

In contrast to the zircon analyses from Q-suite intrusions within the Hudson Bay terrane, four analyzed zircon grains from a websterite (sample LF-26) in the Rivière Arnaud Terrane indicate both significant Pb-loss and a significantly older emplacement age. The measured $^{207}Pb/^{206}Pb$ ages range from 2724.8 to 2820.8 Ma, suggesting that the heating associated with the ca. 2.74-2.70 Ga reworking of the Ungava craton may have facilitated Pb-loss from the zircon grains. The oldest measured $^{207}Pb/^{206}Pb$ age (2820.8 ±1.0 Ma) is considered to be the minimum emplacement age of the websterite, coinciding with the crystallization ages of the tholeiitic metavolcanics in the Duquet and Buet greenstone belts (Maurice et al., 2009).

3.2 Geochemistry of the Q-suite intrusions

The Q-suite intrusions located in the Hudson Bay Terrane and the southern Rivière Arnaud Terrane contain ubiquitous cumulate orthopyroxene and are strongly orthopyroxene-normative, whereas the Q-suite plutons from the north–central Rivière Arnaud Terrane are orthopyroxene-poor and straddle the plane of critical silica-undersaturation. This difference in mineralogy indicates the existence of at least two magma types; a subalkaline magma parental to the orthopyroxene-rich intrusions, and a transitional magma parental to the orthopyroxene-poor intrusions. The major phases crystallizing out of the subalkaline magmas were olivine, followed by orthopyroxene,

clinopyroxene, plagioclase and finally amphibole, whereas the transitional magmas followed the crystallization sequence: olivine, clinopyroxene, plagioclase and amphibole. Despite these differences, the whole rock (Mg-number <0.84) and olivine compositions (Fo_{max} ~0.84) of the most primitive ultramafic rocks indicate that both magma types were enriched in Fe (Mg-number ≤ 0.61) relative to most modern-day mantle-derived magmas, and the estimated parental magmas of most of the world's ultramafic plutonic rocks.

The cumulate rocks of the Q-suite are depleted in most incompatible trace elements relative to their parental magmas (Fig. 3-4A). Mid-ocean ridge basalt (MORB; Sun and McDonough, 1989) –normalized trace element profiles of the Q-suite rocks are enriched in LREE relative to MREE and display relatively unfractionated Y + HREE contents. They are also depleted in high field strength elements (HFSE) relative to the REE of similar compatibility (Nb/La_{MORB} <0.3, Zr/Sm_{MORB} <0.8, Ti/Gd_{MORB} <0.8), a characteristic commonly associated with magmas generated in Phanerozoic arc environments (Pearce and Peate, 1995). The wide range of Th/Yb_{MORB} ratios (~5-170) of the ultramafic rocks suggests, however, that Q-suite magmas were variably contaminated by granitic country rocks during ascent and/or emplacement. A small amount of contamination (<10 %) by LREE-enriched, HREE-depleted granitoids could have imparted the Ta-Nb-Ti depleted, LREE-enriched "calc-alkaline" geochemical signature of the Q-suite magmas and their resulting cumulates. Most importantly, the Y + HREE concentrations of the Q-suite cumulates (Yb_{MORB} = 0.26 +0.26/-0.10; n = 61) are elevated relative to most of the Ungava's TTG (Yb_{MORB} =0.18 +0.73/-0.15) and GGM (Yb_{MORB} = 0.15 +0.76/-0.12) granitoids, implying that the HREE content of the Q-suite parental magmas was relatively insensitive to the addition of crustal material.

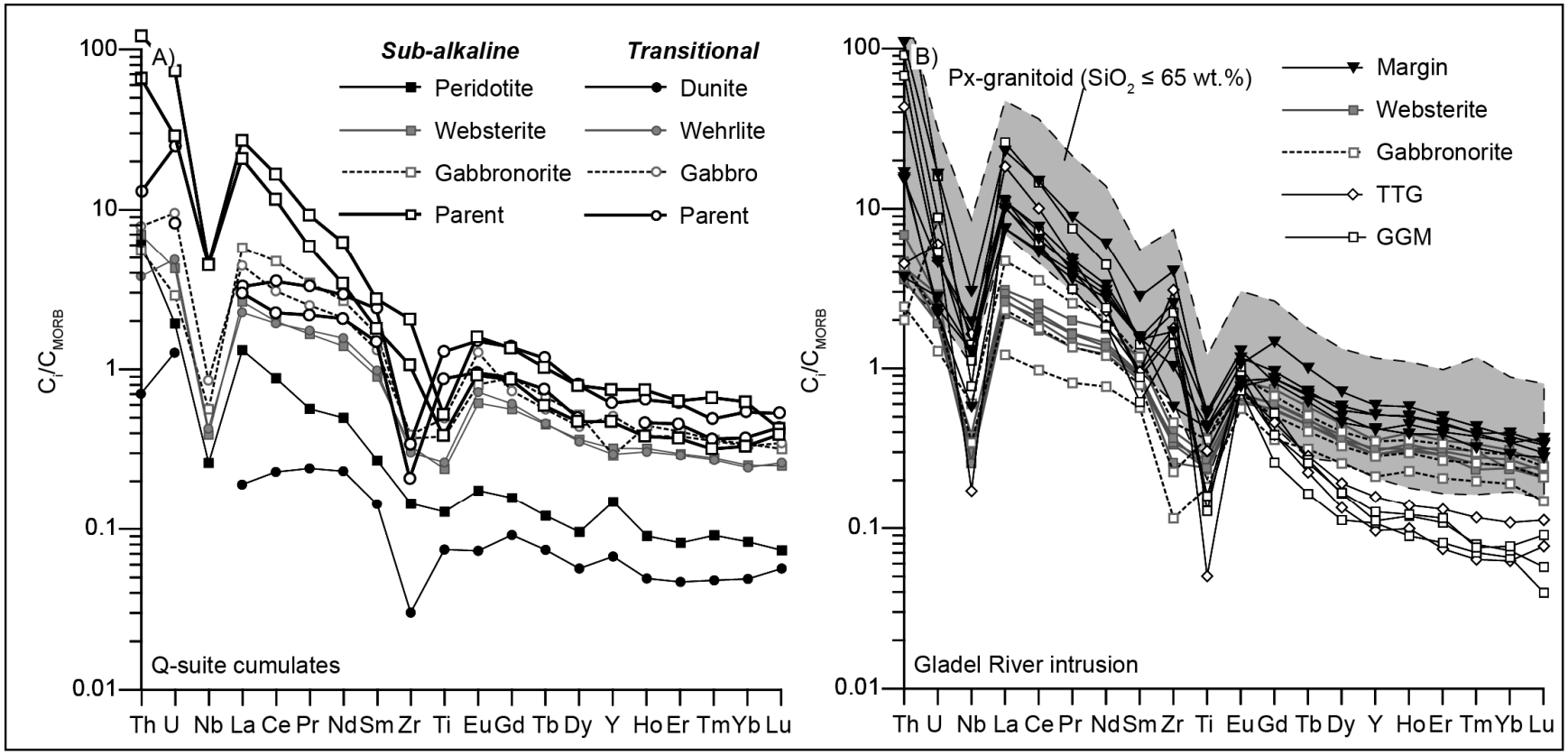

Figure 3-4: MORB-normalized trace element spidergrams.

A) Median abundances in the subalkaline and transitional-type Q-suite intrusions, by lithology, along with the parental magma compositions (thick lines) calculated from the most primitive cumulates using the method of (Bédard, 1994), assuming a trapped liquid fraction of 0.05. **B)** Trace element abundances of selected websterites, gabbronorites and marginal-facies rocks from the Gladel River intrusion along with nearby TTG and GGM granites and the range of intermediate-SiO2 (≤65 wt. %) pyroxene-granitoids (n =60 at 95 % confidence interval).

3.3 The Gladel River Intrusion

Some Q-suite intrusions are spatially associated with pyroxene-bearing granitoids that are mineralogically and chemically distinct from the predominant, surrounding TTG- and GGM-series granitoids. The Gladel River intrusion (Fig. 3-1B, Table 3-2) is a zoned Q-suite intrusion that exhibits a particularly well developed pyroxene-granitoid margin, providing a potential link between the Q-suite magmas and the petrogenesis of pyroxene-granitoids.

The 2717.8 ±0.7 Ma Gladel River intrusion is situated in the Hudson Bay terrane, approximately 45 km east from the town of Inukjuak (Fig. 3-1A). The intrusion is composed of a brecciated websterite core that contains oikocrystic amphibole, rare orthopyroxene-armoured olivine (Fo ~78), and outward-increasing amounts of interstitial plagioclase. The Mg-numbers of the subhedral to euhedral orthopyroxene grains decrease away from the center of the websterite core (0.78 to 0.74). Euhedral clinopyroxene is partially replaced by amphibole and displays extensive exsolution of Cr-rich spinel, contributing to elevated clinopyroxene Mg-numbers (0.89 -0.93). The appearance of interstitial plagioclase in the Gladel River websterites is accompanied by a change in amphibole composition from magnesio-hastingsite to magnesiohornblende (Leake et al., 1997). The transition of websterite into hornblende gabbronorite marks the onset of plagioclase accumulation. The gabbronorite contains rare enclaves of websterite and displays an outward increase in magnetite and normative apatite content. Across the gabbronorite orthopyroxene Mg-numbers range from 0.72 -0.64, with a general decrease away from the center of the intrusion. The clinopyroxene in the gabbronorite has undergone partial amphibole replacement and contains sub-microscopic exsolved oxides,

Table 3-2: Representative Q-suite and Gladel River intrusion samples

Sample	C1-16	C1-50	DH08-7	GR2-12	GR2-10*	GR2-9*	GR2-8*	GR2-4	GR2-3	GR2-2	GR2-1	GR-2*	Chron2	GR4-2
Easting	486034	486420	359177	359125	359158	359213	359272	359361	359396	359430	359439	359468	358690	358839
Northing	6674335	6674097	6460809	6465326	6465396	6465435	6465456	6465593	6465620	6465641	6465659	6465693	6465413	6465733
Transect (m)	-	-	-	0	71	135	185	349	391	426	449	491	-	-
Lithology	dunite	dunite	harzb.	granite	Px-grdt	Px-qmzt	Px-diorite	mt.gabnor	gabnor	f.web	web	web	Px-grdt	Px-qmzt
Major elements (wt. %)														
SiO_2	37.87	39.00	38.38	72.65	63.11	59.73	51.77	48.65	47.69	50.17	49.1	48.52	65.40	56.35
TiO_2	0.08	0.14	0.10	0.16	0.69	0.66	0.54	0.47	0.23	0.34	0.31	0.3	0.55	0.55
Al_2O_3	0.92	1.08	2.78	14.79	16.31	16.72	14.6	15.95	14.42	6.24	5.62	5.56	16.11	16.74
MgO	37.68	33.88	32.82	0.62	1.87	2.44	7.24	8.64	12.12	16.3	17.99	18.99	1.42	4.3
FeO	14.50	17.59	13.42	0.92	5.35	7.28	9.87	10.29	7.17	9.2	9.36	9.6	4.27	7.56
MnO	0.28	0.28	0.17	0.02	0.09	0.1	0.14	0.18	0.16	0.18	0.18	0.18	0.08	0.12
CaO	2.19	4.16	1.64	1.64	4.54	5.99	9.74	12.16	13.44	14.12	14.83	13.7	3.89	7.7
Na_2O	0.1	0.08	0.25	3.97	4.17	4.13	3.15	1.85	0.83	0.84	0.77	0.81	5.03	3.63
K_2O	0.03	0.02	0.22	4.04	1.62	1.3	0.95	0.27	0.35	0.35	0.32	0.33	1.7	1.26
P_2O_5	0.02	0.02	0.03	0.07	0.18	0.19	0.05	0.04	0.02	0.07	0.06	0.06	0.29	0.1
LOI	4.67	1.89	8.76	0.8	1.19	0.56	0.99	0.6	2.63	1.02	0.58	0.66	0.6	0.91
Total	99.09	98.75	98.95	99.68	99.12	99.1	99.04	99.1	99.06	98.83	99.12	98.71	99.34	99.22
Trace elements (ppm)														
Cs	-	<0.1	0.2	<0.1	0.1	0.1	0.1	<0.1	0.1	<0.1	<0.1	0.09	0.5	<0.1
Rb	<1	<1	7.9	83	29.5	25.4	22.9	2.9	6.0	5.0	7.3	6.6	67.7	21.7
Ba	15.7	20	83.5	1171	914.0	1013.4	366.5	144.0	123.2	166.5	190.9	149.0	402.2	708.4
Th	-	0.08	0.76	32.6	1.82	0.44	2.01	0.5	0.2	0.5	0.8	0.51	13.0	1.9
U	-	0.06	0.18	0.75	0.22	0.13	0.10	0.1	0.4	0.1	0.1	0.14	0.8	0.1
Nb	<0.3	<0.3	0.7	1.8	4.65	3.06	1.61	0.8	<0.3	0.7	0.6	0.68	7.0	3.0
Ta	-	< 0.01	0.06	0.06	0.12	0.08	0.07	0.03	0.01	0.09	0.04	0.04	0.30	0.11
Pb	1.4	1	3.2	17.7	9.6	9.3	6.9	2.0	<1.0	1.8	1.9	2.2	15.6	9.6
Sr	11.3	16	62.6	361.0	501.6	566.5	481.0	690.6	553.8	154.4	138.8	129.4	410.2	544.7
Zr	2.1	2.4	12.8	164.2	188.0	124.9	42.3	16.7	8.5	25.7	27.4	19.2	298.0	75.9
Hf	-	0.1	0.4	4.6	4.52	3.00	1.33	0.7	0.5	1.3	0.9	0.60	8.6	2.2
Ga	1.5	1.9	2.9	15.1	22.1	22.1	17.2	16.1	11.3	7.7	6.6	7.3	21.2	18.2
Sc	13.6	22.6	8.3	<1.0	12.88	17.41	31.45	42.8	46.2	64.9	64.7	53.44	11.5	23.7
V	58.2	98.7	38.5	16.6	89.9	133.6	232.0	197.5	146.5	174.3	159.6	143.9	58.9	149.5
Co	142	147	139	<10	15	24	50	55	58	94	85	87	<10	32
La	-	0.48	4.01	64.7	27.66	25.02	18.70	5.76	3.03	7.35	6.69	6.51	57	18.6
Ce	-	1.73	8.26	109	57.28	48.25	40.83	13.3	7.3	16.6	14.8	15.74	111	39.8
Pr	-	0.32	0.92	9.89	6.3	5.65	5.21	1.79	1.07	2.2	1.93	2.17	11.7	4.76
Nd	-	1.75	3.85	32.4	24.14	22.31	20.84	8.73	5.61	10.6	9.58	10.07	43.9	19.9
Sm	-	0.57	0.70	3.7	4.07	3.98	4.13	2.07	1.49	2.47	2.34	2.39	7.36	4.04
Eu	-	0.15	0.18	1.03	1.31	1.18	0.78	0.70	0.57	0.71	0.65	0.69	1.08	0.85
Gd	-	0.5	0.57	1.93	2.98	3.51	3.16	1.85	1.32	2.23	2.03	2.25	5.35	3.16

Tb	-	0.08	0.08	0.18	0.41	0.48	0.46	0.27	0.21	0.32	0.3	0.33	0.67	0.45
Dy	-	0.39	0.43	0.75	2.08	2.48	2.65	1.49	1.16	1.76	1.6	1.65	3.24	2.28
Y	<1.0	1.8	2.5	3.1	11.77	14.31	14.33	7.9	5.9	8.6	8.2	8.92	16.4	11.5
Ho	-	0.07	0.09	0.12	0.39	0.51	0.50	0.3	0.23	0.34	0.31	0.32	0.58	0.45
Er	-	0.2	0.24	0.32	1.15	1.36	1.32	0.79	0.61	0.91	0.86	0.95	1.48	1.19
Tm	-	0.029	0.041	0.036	0.15	0.18	0.18	0.12	0.09	0.13	0.11	0.14	0.20	0.17
Yb	-	0.19	0.25	0.22	0.88	1.05	1.21	0.75	0.58	0.83	0.73	0.72	1.14	1.05
Lu	-	0.029	0.024	0.026	0.13	0.17	0.16	0.095	0.067	0.11	0.095	0.11	0.15	0.14
Cr	3908	3248	1590	19.3	12.6	13.3	79.4	158.5	739.8	814.1	971.4	1255	24.1	23.4
Ni	1460	1055	1184	3	4	<3	76	72	167	491	421	451	6	14

Major elements, Cr and Ni for all samples, as well as Ba, Co and V for samples not labeled with an (*) were analyzed by X-ray fluorescence spectrometry at McGill University using a Philips PW1400 spectrometer on 32-mm fused lithium tetraborate beads. The Rb, Sr, Pb, Zr, Nb, Y and Sc analyses of the samples not labeled with (*) were performed on 40 mm-diameter pressed powder pellets at McGill University; REE, Hf, Ta, U, Th were analyzed at Activation Laboratories by inductively coupled - plasma mass spectrometry (ICP-MS) using a Perkin Elmer SCIEX ELAN 6000 system and lithium metaborate/tetraborate fusion technique. *All trace elements, with the exception of Cr and Ni were analyzed at the University of British Columbia's Pacific Institute for Isotopic and Geochemical Research (PCIGR) using a high-resolution (HR)-ICP-MS Thermo Finnigan ELEMENT2 machine. UTM coordinates for sample locations based on North American Datum 1927 (NAD27). The complete dataset for the Gladel River intrusion, including mineral analysis data may be found in Appendix 1.

Abbreviations: harzb. – harzburgite; mt. gabnor- magnetite gabbronorite; gabnor – gabbronorite; f. web – feldspathic websterite; web. –websterite; px-qmzt – pyroxene-bearing quartz monzodiorite; px-grdt – pyroxene-bearing granodiorite.

resulting in clinopyroxene Mg-numbers (0.88 -0.82) that are significantly higher than those of the coexisting orthopyroxene. Although not systematically zoned, cumulus plagioclase is highly heterogeneous and on average An-rich (0.71 ±0.07). The crystallization sequence in the intrusion was: olivine, followed by orthopyroxene, clinopyroxene, amphibole, plagioclase, and finally magnetite. The Gladel River rocks have elevated Y and HREE concentrations (Yb_{MORB} =0.25 +0.22/-0.05; n =10) relative to most of the Ungava's felsic plutons and exhibit relative HFSE depletions and weakly fractionated REE and incompatible trace element ratios (Ce/Yb_{MORB} =5 –12; Zr/Y_{MORB} =0.6 –2.2), characteristic of the Q-suite.

The gabbronorite grades outwards into a relatively sodic (K/(K+Na) ~0.20), pyroxene-bearing, granitoid margin of variable width (Fig. 3-1B). The marginal pyroxene-granitoids are composed of orthopyroxene +clinopyroxene +plagioclase +biotite +quartz +Fe-Ti-oxide ±hornblende ±alkali feldspar, and closely match the pyroxene-bearing granitoids from the central (Percival and Mortensen, 2002) and eastern (Bédard, 2003) Ungava craton. The modal abundances of orthopyroxene and clinopyroxene decrease outwards across the margin, while biotite, alkali feldspar and quartz increase. The most distal and evolved marginal samples contain antiperthitic plagioclase that resembles the plagioclase in the pyroxene-tonalites of the eastern Ungava craton (Bédard, 2003). There is a concomitant outward increase in SiO_2 and incompatible/ compatible ratios (e.g. K/Ti, Zr/Y, La/Sm), and a decrease in CaO, MgO, Cr, Ni and Mg-number (Fig. 3-5). The pyroxene-bearing dioritic to granodioritic compositions (SiO_2 = 52.0 – 65.5 wt. %) of the Gladel margin span the compositional gap between the mafic rocks of the Q-suite and the TTG and GGM suites (Fig. 3-2A), and

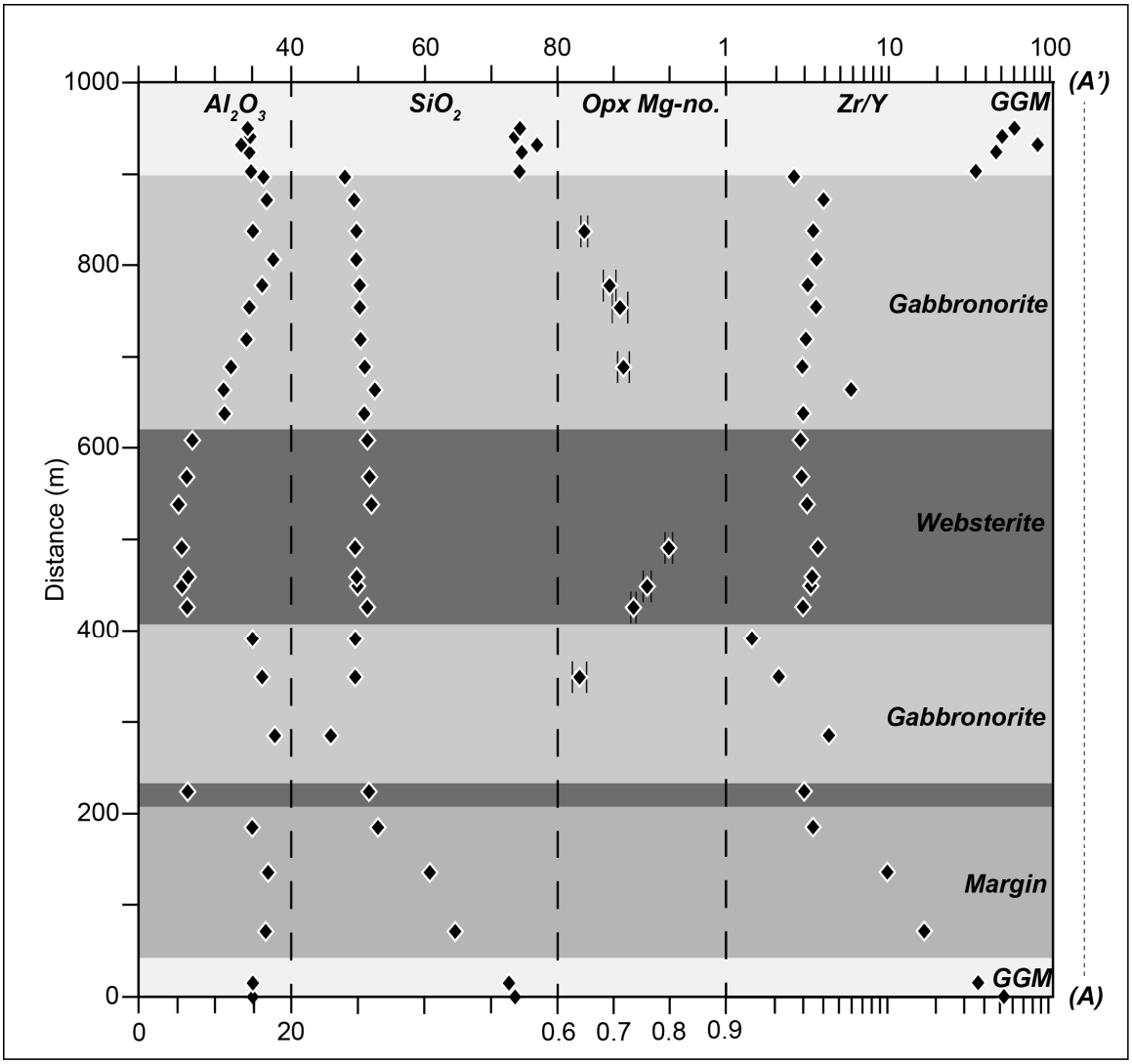

Figure 3-5: Key compositional parameters of the Gladel River intrusion.
Key compositional parameters of the Gladel River intrusion plotted as a function of distance along transect A-A' (Fig. 3-1B).

overlap the intermediate-SiO_2 pyroxene-granitoids of the Ungava craton (Fig. 3-2B). The Y + HREE contents (Yb_{MORB} = 0.3– 0.4) and weakly to moderately fractionated HREE (Gd/Yb_{MORB} = 2-4) of the marginal rocks are indistinguishable from those of pyroxene-granitoids with ≤ 65 wt. % SiO_2 (Fig. 3-4B).

4. Duration of Q-suite magmatism

The $^{207}Pb/^{206}Pb$ crystallization ages of 2718.9 ± 0.7 and 2710 ± 0.5 Ma fall within the range of the previous age determinations for the emplacement of Q-suite intrusions (Simard, 2008), suggesting that Q-suite magmatism may have been long-lived and continuous between ≤2705 Ma and ≥2720 Ma. The older (> 2.82 Ga) websterite from the eastern Ungava craton significantly predates the reworking of the Ungava craton, and therefore should not be included in the Q-suite. The age of the websterite suggests that it may be related to the ca. 2.82 Ga supracrustal metavolcanics of the Duquet or Buet greenstone belts, and highlights the long and complex tectonic history of the Ungava craton.

5. Assimilation-Fractional Crystallization (AFC) model for pyroxene-granitoidss

The chemical and mineralogical characteristics of the marginal rocks of the Gladel River intrusion suggest that it represents an analogue for the petrogenesis of the intermediate-SiO_2 pyroxene-granitoids. The ~ 5-fold increase in Zr/Y (3 -16) across the ~150 m wide margin (Fig. 3-1B, Transect A-A'; Fig. 3-5) cannot be produced by closed system fractionation of assemblages dominated by olivine, pyroxenes, plagioclase, or amphibole, as illustrated by the mass balance and thermodynamic models in Figure 3-6. The positive correlation between Zr/Hf ratios (30 -40) and SiO_2 suggests that zircon

accumulation has not produced the trend of increasing Zr/Y in the marginal rocks (Deering and Bachmann, 2010). Thus, the assimilation of a high Zr/Y contaminant provides the best explanation for the sharp outward increase in Zr/Y ratios and SiO_2 content (52 –63 wt. %) across the marginal zone, and forms the basis of our model for the genesis of pyroxene-granitoids.

The relative contributions of the Q-suite parental magma and a granitic component in the petrogenesis of the marginal facies of the Gladel River intrusion were evaluated by modeling the effects of simultaneous assimilation and fractional crystallization, over a range of assimilation/ crystallization rates (r-values). In the absence of rocks that approach liquid compositions, the major element composition of the subalkaline Q-suite parental magma was estimated using the thermodynamic-based program alphaMELTS (Appendix 3-3; Ghiorso and Sack, 1995; Smith and Asimow, 2005). Equilibrium melting calculations were performed until the last non-cumulus phase (clinopyroxene) was melted out of the most magnesian harzburgite, and extended until the Mg-number (Mg/(Mg+Fe2+)) of the model liquid reached a value that would be in equilibrium with the earliest crystallized olivine (Fo83), assuming an olivine-liquid Fe-Mg distribution coefficient of 0.3 (KD; Roeder and Emslie, 1970). The modeling results indicate that the magmas parental to the subalkaline Q-suite plutons were Fe-rich, high-Mg basalts (FeOTOT > 13.5 wt. %; Mg/(Mg+Fe) ≤ 0.59; Table 3-3).The trace element composition of the subalkaline Q-suite parental magmas, calculated using the method of Bédard (1994), display a wide range of incompatible trace element enrichments and Zr/Y ratios (~3-9) that exceed the Zr/Y ratio of the most primitive pyroxene-diorite of the Gladel River intrusion's margin. Consequently, the trace element concentrations of the least

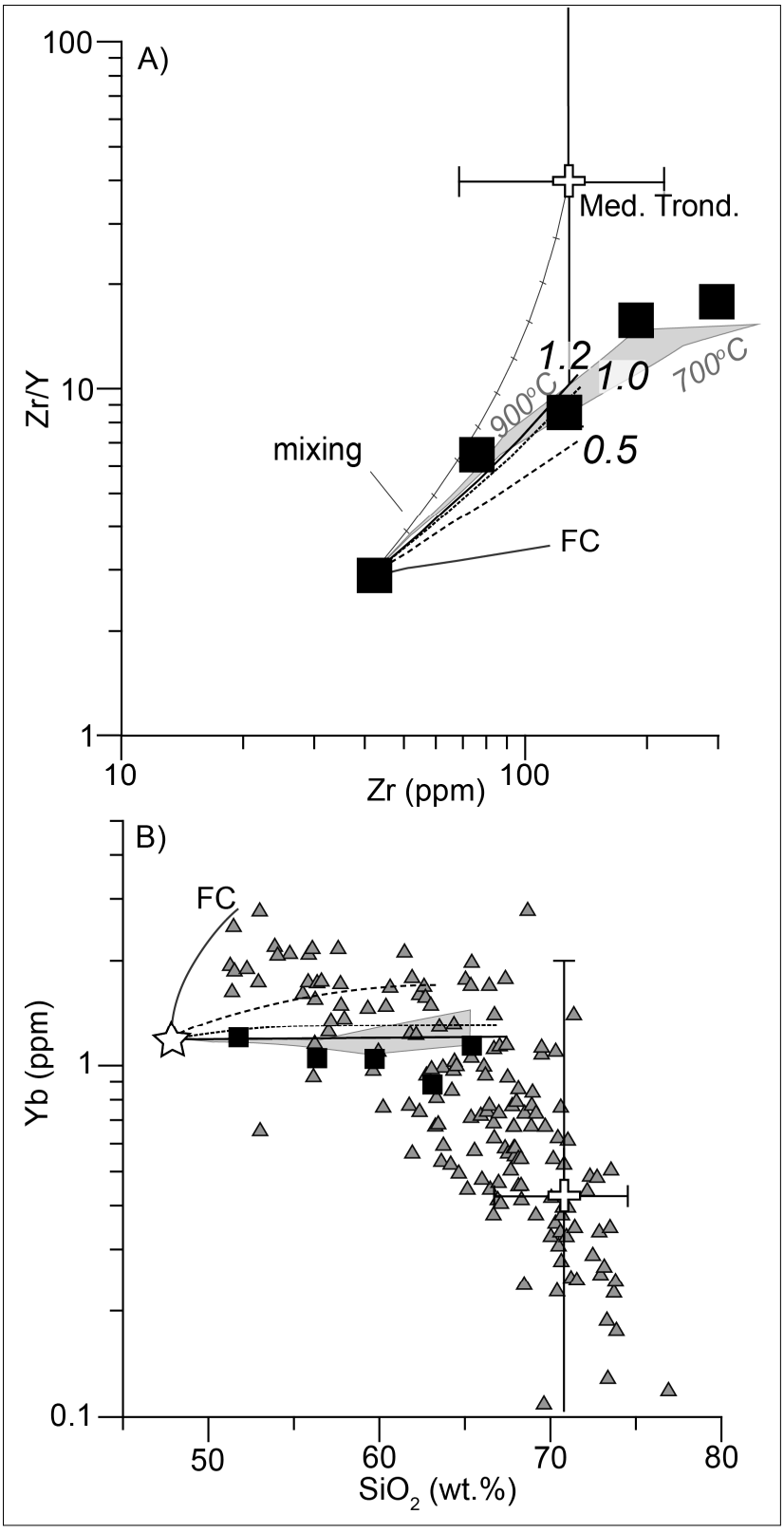
A)
100
10
1
Zr/Y
10
100
Zr (ppm)
Med. Trond.
1.2
1.0
0.5
900°C
700°C
mixing
FC
B)
FC
1
0.1
Yb (ppm)
50
60
70
80
SiO2 (wt.%)

Figure 3-6: Trace element modeling of the Gladel River margin.
A) Zr/Y vs. Zr plot of the marginal rocks of the Gladel River intrusion and the results of both mass balance and thermodynamic modeling using alphaMELTS. Mass-balance constrained fractional crystallization of the Q-suite parental liquid and simple binary mixing with the median trondhjemite are shown as thin grey solid lines. AFC curves are for r-values of 0.5 (thick coarsely-dashed black line), 1.0 (thick, finely-dashed black line) and 1.2 (thick solid black line). Isenthalpic alphaMELTS AFC models using starting contaminant (median trondhjemite) temperatures between 700 and 900°C are included in the shaded field. Mass-balance modeled fractional crystallization is shown by the grey line. **B)** Yb vs. SiO_2 plot, superimposed onto pyroxene-bearing granitoids (triangles). The upper limit and lower limits of the grey field correspond to the starting contaminant temperatures of 700 and 900°C, respectively. Data sources as in Figure 3-2. E-Sigéom data has been filtered to include only ICP-MS analyses from ACME Analytical Laboratories and McGill Geochemical Laboratories.

Table 3-3: End-member compositions used in AFC modeling

	Subalk. Q-suite	Trondhjemite*
SiO_2	47.9	71± 4
TiO_2	0.6	0.3 ±0.2
Al_2O_3	14.8	15.4 +1.0/-1.2
MgO	10.9	0.9 +1.1/-0.5
FeO^T	14.1	2.5+ 1.9/-1.4
CaO	8.4	3.2 +1.4/-1.0
Na_2O	1.6	4.6 +0.9/-0.8
K_2O	0.5	1.5 +1.7/-0.7
P_2O_5	0.2	0.1 ± 0.1
NiO	0.02	-
Cr_2O_3	0.1	-
Zr	42.3	128 +93/-60
Y	14.3	3.3 +19/-2.3
Yb	1.2	0.43 +1.57/-0.35
Zr/Y	2.95	39 +96/-32

*Median and +/- 2 IQR range calculated from 109 analyses

evolved, marginal sample (GR2-8; Ce/Yb_{MORB} ~14; Gd/Yb_{MORB} =2.3, Zr/Y ~3.5, Y_{MORB} ~0.4; Yb_{MORB} ~0.4) were used as the model parental composition in AFC modeling of the Gladel River pyroxene-granitoids.

The relatively sodic compositions of both the Gladel River marginal rocks and the majority of pyroxene-granitoids prohibit the significant assimilation of relatively K-rich GGM-suite rocks in their genesis (Fig. 3-7). In the absence of relatively sodic felsic plutonic rocks in the vicinity of the Gladel River intrusion, we used the median trondhjemite composition (Table 3; SiO_2 =69.4 +1.4/-2.0; K/(K+Na) =0.17 +0.03/-0.02) from 109 previously published analyses (Stern et al., 1994; Bédard, 2006; Stevenson et al., 2006; Boily et al., 2009) and data from Québec's Ministère de Ressources Naturelles et de la Faune (MRNF) E-Sigéom database. The Na-rich trondhjemitic rocks (~61 % sodic-feldspar, ~29 % quartz, ~10% biotite) form a tight cluster plotting on the Ab-rich side of the water-saturated granite minimum of the Qtz-Ab-Or projection (Blundy and Cashman, 2001), and thus likely represent the most easily fusible plutonic rocks of the TTG suite.

The AFC model comprises three crystallization stages; an initial harzburgitic cumulate assemblage ($olivine_{0.75}opx_{0.25}$), followed by a websteritic ($olivine_{0.10}$ $opx_{0.25}cpx_{0.65}$), and finally amphibole-bearing gabbronoritic ($opx_{0.20}cpx_{0.15}amph_{0.15}plag_{0.40}$ $mt_{0.10}$) assemblages. The fraction of cumulus amphibole, as opposed to interstitial amphibole that may contain a trapped melt component (Bédard, 1994; Charlier et al., 2005), is difficult to constrain, but for amphibole fractions less than ~0.4 this choice is not critical. The proportions of the major minerals in the cumulate assemblages were

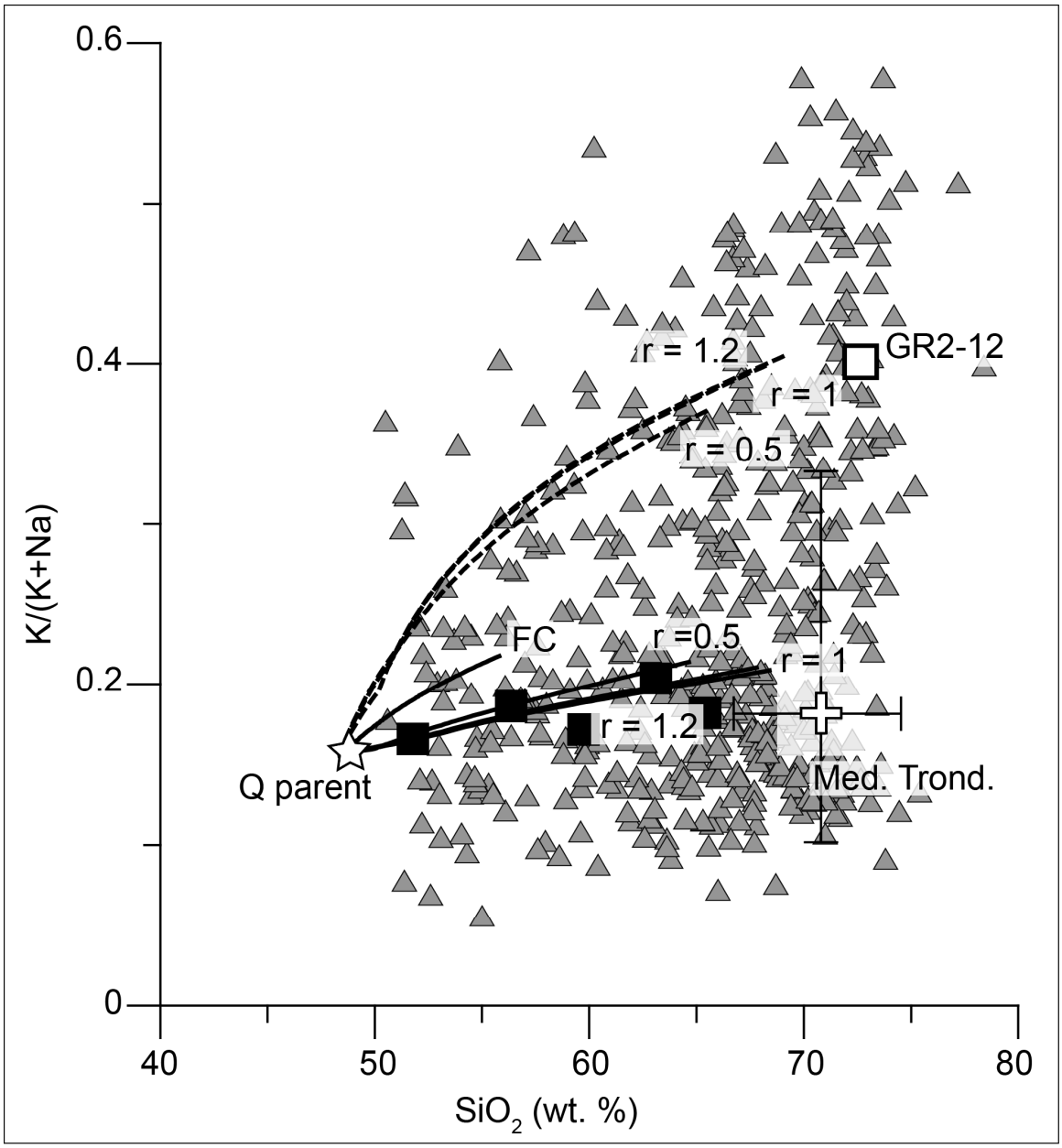

Figure 3-7: K/(K+Na) vs. SiO_2 plot.
Heavy solid lines: mass balance models for r values of 0.5, 1.0 and, 1.2, in which median trondhjemite is the contaminant (error bars at 95 % confidence interval). Heavy dashed lines: mass balance AFC models using the relatively potassic sample GR2-12 sampled adjacent to the Gladel River intrusion. Data sources for the pyroxene-granitoids (triangles) as in figure 3-6. The white star denotes the approximate composition of the Q-suite parental magma.

calculated by the least-squares fitting of the measured mineral compositions to the whole-rock compositions of the Gladel River cumulate rocks.

The modeling results indicate that large assimilation rates (r >1) of the trondhjemitic contaminant by the subalkaline Q-suite magmas are required to reproducethe elevated Zr/Y ratios and relatively constant Y concentrations of the marginal rocks of the Gladel River intrusion (Fig. 3-6). Mass balance suggests that the most evolved Gladel River margin rock (65.4 wt. % SiO_2) could represent the addition of ~40 wt. % trondhjemite component to a Q-suite parental magma, accompanied by a similar amount of fractional crystallization (Fig. 3-8). The steep decrease in the Y +HREE concentrations in the more felsic (>65 wt. % SiO_2) members of the pyroxene-suite may reflect a transition to fractional crystallization-controlled evolution that includes trace phases such as apatite and titanite (Bachmann et al., 2005; Wyman et al., 2011).

Isenthalpic simulations using the thermodynamic-based alphaMELTS software package (Ghiorso and Sack, 1995; Smith and Asimow, 2005) indicate that the initial temperature of the contaminant is the strongest control on the AFC evolution of the Q-suite parental magma. The high r-values require high middle-crustal temperatures of 700 - 900°C, approaching the fluid-absent dehydration temperatures of hornblende and biotite in granitic rocks (Clemens and Vielzeuf, 1987). The calculated instantaneous r-values are greatest during the earliest olivine-only stage of the AFC process (~2.0 and ~2.8 at 700°C and 900°C, respectively), but decrease rapidly once the contaminated magma reaches pyroxene-saturation to steady-state values ~1.0 and 1.3 for initial contaminant temperatures of 700°C and 900°C, respectively. The predicted emplacement temperatures

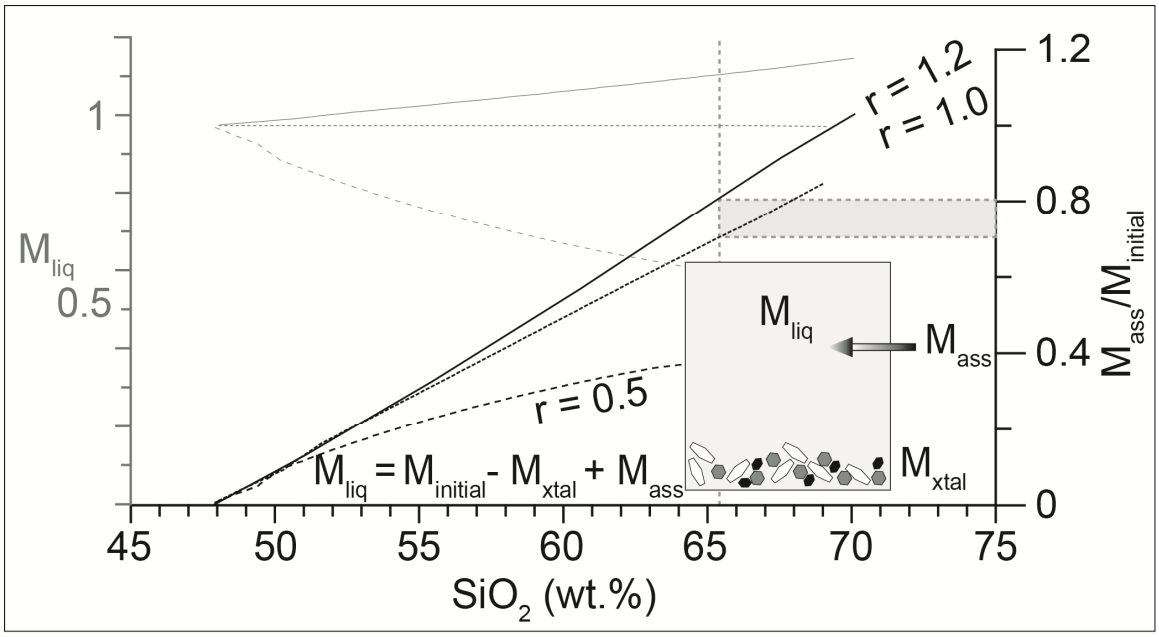

Figure 3-8: Hybrid liquid composition as a function of magma mass, contaminant fraction and rate of assimilation.

SiO_2 content as a function of total magma mass normalized to the mass of Q-suite parental magma (M_{liq}; grey curves), and as a function of the mass of crustal contaminant relative to the mass of Q-suite parent ($Ma/M_{initial}$; black curves) for r values of 0.5, 1.0 and 1.2. The grey dashed line at ~65.4 wt. % represents the SiO_2 content of the Gladel River margin's most evolved sample.

of ~1030-1070 °C for the most evolved marginal pyroxene-granodiorite is in agreement with the temperature estimates of our mass-balance model and the petrogenetic studies of Percival and Mortensen (2002) and Bédard (2003).

The high assimilation rates implied by the AFC models are difficult to reconcile with both present-day and estimates of Archean continental geothermal gradients, which would limit the crustal temperatures to ~300-500°C at lithostatic pressures of 500 MPa (Sclater et al., 1980; Martin, 1986; Rapp et al., 1991; Harder and Russell, 2006). The high required temperatures are, however, consistent with the wholesale reworking of the amalgamated Paleo-to Mesoarchean proto-Ungava craton ca. 2.74-2.70 Ga (Maurice et al., 2009) and may reflect a combination of processes, including: 1) conductive heating by craton-wide underplating of hot (~1300°C) ferropicritic Q-suite magmas; 2) deep crustal release of latent heat through crystallization of Q-suite magmas; 3) gravitational collapse and thinning of the felsic crust leading to advective heat transfer. Although processes such as episodic delamination (Bédard, 2006) may have facilitated the ascent of the Q-suite magmas, our results suggest that ferropicritic underplating was the main driving force reworking the Ungava craton. Such an underplating model provides a tangible source of heat, and is supported by the craton-wide occurrence of the Q-suite cumulates and the significant inferred juvenile component in the pyroxene-granitoid suite. “Softening” of the dominantly TTG proto-crust would make the AFC process even more efficient, as proposed by Maurice et al. (2009) for the post-2.75 Ga LREE-enriched supracrustal mafic volcanics.

Our calculations suggest that the Ungava craton experienced a significant addition of a mantle-derived, Q-suite component during its Neoarchean stabilization. The addition

of this juvenile component in the Ungava craton coincides with the peak in global zircon crystallization ages ca. 2.7 Ga (e.g. Condie, 1998, 2000; Rino et al., 2004; Hawkesworth et al., 2009, 2010). Although some have argued that global peaks in crystallization ages represent periods of enhanced zircon preservation, or crustal recycling (Hawkesworth et al., 2009, 2010; Lancaster et al., 2011), our findings support a significant addition of a mantle-derived component to the northeastern Superior Province ca. 2.7 Ga.

6. Concluding remarks

The U-Pb geochronological results from two Q-suite intrusions located within the Hudson Bay Terrane, along with field relationships indicate that the Q-suite intrusions were emplaced over a prolonged period (>15 M.y), contemporaneous with the reworking of the Ungava craton.

The mineralogical and geochemical similarities between the pyroxene-bearing margin of the Gladel River intrusion and the intermediate pyroxene-granitoids of the Ungava craton indicate that the latter represent heavily contaminated ferropicritic magmas undergoing AFC processes operating on a craton-wide scale. The relatively sodic compositions of the pyroxene-granitoids indicate that the assimilant was likely a trondhjemitic partial melt of the proto- TTG crust, rather than the younger, relatively potassic GGM granitoids. Our calculations indicate that pyroxene-granitoids with ≤65 % SiO_2 may represent up to 50 % contamination of the mantle-derived ferropicritic magma (Fig. 3-8) parental to the widespread Q-suite mafic/ultramafic bodies across the Ungava craton. The large required amounts of assimilated trondhjemitic crust suggest near-solidus ambient crustal temperatures. The craton-wide extent and large inferred volume of the pyroxene-granitoids is consistent with a tectonic model in which large volumes of

ferropicrite magma underplated and intruded the proto- Ungava crust, supplying heat for crustal-scale anatexis and reworking. This conclusion is consistent with a global period of enhanced formation of juvenile continental crust at ~ 2.7 Ga.

Appendix

Complete list of whole-rock and mineral analyses from the Gladel River intrusion and surrounding rocks is presented in appendix A3-1. Analyses of additional Ungava granitoids, collected by the authors are supplied in appendix A3-2. Details of AFC modeling are presented in appendix A3-3.

Acknowledgments

P. Antonechkina is thanked for assistance with alphaMELTS software. We thank R. Friedman and C. Wall for chemical abrasion of the zircons and U-Pb measurements. Comments by A. Hynes and C. Rowe improved the clarity of the manuscript. We thank J. Bédard and an anonymous reviewer for their insightful comments. This work was supported by the Natural Science and Research Council of Canada (NSERC) and Polar Continental Shelf grants to D.F. and the Northern Scientific Training Program (NSTP) grant to D.M.

References

Bachmann, O., Dungan, M.A., Bussy, F., 2005. Insights into shallow magmatic processes in large silicic magma bodies: the trace element record in the Fish Canyon magma body, Colorado. Contributions to Mineralogy and Petrology 149, 338–349.

Bédard, J.H., 1994. A procedure for calculating the equilibrium distribution of trace elements among the minerals of cumulate rocks, and the concentration of trace elements in the coexisting liquids. Chemical Geology 118, 143–153.

Bédard, J.H., 2003. Metamorphism in the Archaean Minto Block, Northern Superior Province, Canada. Journal of Geology 111, 183–205.

Bédard, J.H., 2006. A catalytic delamination-driven model for coupled genesis of Archaean crust and sub-continental lithospheric mantle. Geochimica et Cosmochimica Acta 70, 1188–1214.

Bédard, J.H., Harris, L.B., Thurston, P.C., 2013. The hunting of the snArc. Precambrian Research 229, 20-48.

Blundy, J., Cashman, K., 2001. Ascent-driven crystallisation of dacite magmas at Mount St Helens, 1980–1986. Contributions to Mineralogy and Petrology 140, 631–650.

Boily, M., Leclair, A., Maurice, C., Bédard, J.H., David, J., 2009. Paleo- to Mesoarchean basement recycling and terrane definition in the Northeastern Superior Province, Québec, Canada. Precambrian Research 168, 23–44.

Boily, M., Maurice, C., 2008. Géochemie et données isotopiques du Néodyme du nord-est de la Province du Supérieur, *in*: Simard, M. (Ed.), Synthèse Du Nord-est de La Province Du Supérieur. Ministère de Ressources Naturelles et de la Faune, Québec, MM2008-2, pp. 87–129.

Charlier, B., Vander Auwera, J., Duchesne, J.-C., 2005. Geochemistry of cumulates from the Bjerkreim – Sokndal layered intrusion (S. Norway) Part II. REE and the trapped liquid fraction. Lithos 83, 255 – 276.

Cherniak, D.J., Watson, E.B., 2000. Pb diffusion in zircon. Chemical Geology 172, 5–24.

Clemens, J.D., Vielzeuf, D., 1987. Constraints on melting and magma production in the crust. Earth and Planetary Science Letters 86, 287–306.

Condie, K.C., 1998. Episodic continental growth and supercontinents: a mantle avalanche connection? Earth and Planetary Science Letters 163, 97–108.

Condie, K.C., 2000. Episodic continental growth models: afterthoughts and extensions. Tectonophysics 322, 153–162.

Deering, C.D., Bachmann, O., 2010. Trace element indicators of crystal accumulation in silicic igneous rocks. Earth and Planetary Science Letters 297, 324–331.

Frost, B.R., Frost, C.D., 2008. On charnockites. Gondwana Research 13, 30–44.

Ghiorso, M.S., Sack, R.O., 1995. Chemical mass transfer in magmatic processes IV. A revised and internally consistent thermodynamic model for the interpolation and extrapolation of liquid-solid equilibria in magmatic systems at elevated temperatures and pressures. Contributions to Mineralogy and Petrology 119, 197–212.

Harder, M., Russell, J.K., 2006. Thermal state of the upper mantle beneath the Northern Cordilleran Volcanic Province (NCVP), British Columbia, Canada. Lithos 87, 1–22.

Harry, D.L., Green, N.L., 1999. Slab dehydration and basalt petrogenesis in subduction systems involving very young oceanic lithosphere. Chemical Geology 160, 309–333.

Hawkesworth, C., Cawood, P., Kemp, T., Storey, C., Dhuime, B., 2009. A matter of preservation. Science 323, 49–50.

Hawkesworth, C.J., Dhuime, B., Pietranik, A.B., Cawood, P.A., Kemp, A.I.S., Storey, C.D., 2010. The generation and evolution of the continental crust. Journal of the Geological Society, London 167, 229–248.

Huang, H., Polat, A., Fryer, B.J., 2013. Origin of Archean tonalite–trondhjemite–granodiorite (TTG) suites and granites in the Fiskenæsset region, southern West Greenland: Implications for continental growth. Gondwana Research 23, 452–470.

Jaffey, A.H., Flynn, K.F., Glendenin, L.E., Bentley, W.C., Essling, A.M., 1971. Precision measurement of half-lives and specific activities of 235U and 238U. Phys. Rev. C4, 1889-1906.

Lancaster, P.J., Storey, C.D., Hawkesworth, C.J., Dhuime, B., 2011. Understanding the roles of crustal growth and preservation in the detrital zircon record. Earth and Planetary Science Letters 305, 405–412.

Leake, B.E., Wooley, A.R., Arps, C.E.S., Birch, W.D., Gilbert, M.C., Grice, J.D., Hawthorne, F.., Kato, A., Kisch, H.J., Krivovichev, V.G., Linthout, K., Laird, J., Mandarino, J.A., Maresch, W.V., Nickel, E.., Rock, N.M.S., Schumacher, J.S., Smith, D.C., Stephenson, N.C.N., Whittaker, E.J.W., Youzhi, G., 1997. Nomenclature of amphiboles: report of the subcommittee on amphiboles of the International Mineralogical Association Commission on New Minerals and Mineral Names. The Canadian Mineralogist 35, 219–246.

Longhi, J., Vander Auwera, J., Fram, M.S., Duchesne, J.-C., 1999. Some phase equilibrium constraints on the origin of Proterozoic (massif) anorthosites and related rocks. Journal of Petrology 40, 339–362.

López, S., Castro, A., 2001. Determination of the fluid – absent solidus and supersolidus phase relationships of MORB-derived amphibolites in the range 4 – 14 kbar. American Mineralogist 86, 1396–1403.

Martin, H., 1986. Effect of steeper Archean geothermal gradient on geochemistry of subduction-zone magmas. Geology 20, 753–756.

Martin, H., Smithies, R.H., Rapp, R., Moyen, J.-F., Champion, D., 2005. An overview of adakite, tonalite–trondhjemite–granodiorite (TTG), and sanukitoid: relationships and some implications for crustal evolution. Lithos 79, 1–24.

Mattinson, J.M., 2005. Zircon U–Pb chemical abrasion ("CA-TIMS") method: Combined annealing and multi-step partial dissolution analysis for improved precision and accuracy of zircon ages. Chemical Geology 220, 47–66.

Maurice, C., David, J., Bédard, J.H., Francis, D., 2009. Evidence for a widespread mafic cover sequence and its implications for continental growth in the Northeastern Superior Province. Precambrian Research 168, 45–65.

Moyen, J.-F., 2011. The composite Archaean grey gneisses: Petrological significance, and evidence for a non-unique tectonic setting for Archaean crustal growth. Lithos 123, 21–36.

Moyen, J.-F., Martin, H., 2012. Forty years of TTG research. Lithos 148, 312–336.

Moyen, J.-F., Stevens, G., 2006. Experimental constraints on TTG petrogenesis: implications for Archean geodynamics. American Geophysical Union, Geophysical Monograph 164, 149–175.

Mundil, R., Ludwig, K.R., Metcalfe, I., Renne, P.R., 2004. Age and timing of the Permian mass extinctions: U/Pb dating of closed-system zircons. Science 305, 1760–1763.

Peacock, S.M., Rushmer, T., Thompson, A.B., 1994. Partial melting of subducting oceanic crust. Earth and Planetary Science Letters 121, 227–244.

Pearce, J.A., Peate, D.W., 1995. Tectonic implications of the composition of volcanic arc magmas. Ann. Rev. Earth Planet. Sci. 23, 251–285.

Percival, J.A., Mortensen, J.K., 2002. Water-deficient calc-alkaline plutonic rocks of Northeastern Superior Province , Canada: significance of charnockitic magmatism. Journal of Petrology 43, 1617–1650.

Percival, J.A., Mortensen, J.K., Stern, R.A., Card, K.D., 1992. Giant granulite terranes of northeastern Superior Province: the Ashuanipi complex and Minto block. Can. J. Earth Sci. 2308, 2287–2308.

Percival, J.A., Stern, R.A., Skulski, T., 2001. Crustal growth through successive arc magmatism : reconnaissance U – Pb SHRIMP data from the Northeastern Superior Province, Canada. Precambrian Research 109, 203– 238.

Rapp, R.P., Norman, M.D., Laporte, D., Yaxley, G.M., Martin, H., Foley, S.F., 2010. Continent Formation in the Archean and Chemical Evolution of the Cratonic Lithosphere: Melt-Rock Reaction Experiments at 3-4 GPa and Petrogenesis of Archean Mg-Diorites (Sanukitoids). Journal of Petrology 51, 1237–1266.

Rapp, R.P., Watson, E.B., 1995. Dehydration melting of metabasalt at 8-32 kbar: implications for continental growth and crust-mantle recycling. Journal of Petrology 36, 891–931.

Rapp, R.P., Watson, E.B., Miller, C.F., 1991. Partial melting of amphibolite/eclogite and the origin of Archean trondhjemites and tonalites. Precambrian Researche 511-25.

Rino, S., Komiya, T., Windley, B.F., Katayama, I., Motoki, A., Hirata, T., 2004. Major episodic increases of continental crustal growth determined from zircon ages of river sands; implications for mantle overturns in the Early Precambrian. Phys. Earth Planet. Int. 146, 369–394.

Roeder, P.L., Emslie, R.F., 1970. Olivine-Liquid Equilibrium. Contributions to Mineralogy and Petrology 29, 275–289.

Rushmer, T., 1991. Partial melting of two amphibolites: contrasting experimental results under fluid-absent conditions. Contributions to Mineralogy and Petrology 107, 41–59.

Sclater, J.G., Jaupart, C., Galson, D., 1980. The heat flow through oceanic and continental crust and the heat loss of the Earth. Reviews of Geophysics and Space Physics 18, 269.

Scoates, J.S., Friedman, R.M., 2008. Precise age of the platiniferous Merensky Reef, Bushveld Complex, South Africa, by the U-Pb zircon chemical abrasion ID-TIMS technique. Economic Geology 103, 465–471.

Shirey, S.B., Hanson, G.N., 1984. Mantle-derived Archaean monzodiorites and trachyandesites. Nature 310, 222–224.

Simard, M., 2008. Stratigraphie et géochronologie du nord-est de la Province du Supérieur, *in*: Simard, M. (Ed.), Synthèse Du Nord-est de La Province Du Supérieur. Ministère de Ressources Naturelles et de la Faune, Québec, MM2008-2, pp. 23–86.

Smith, P.M., Asimow, P.D., 2005. Adiabat_1ph: A new public front-end to the MELTS, pMELTS, and pHMELTS models. Geochemistry Geophysics Geosystems 6, 1–8.

Stacey, J.S. and Kramers, J.D., 1975. Approximation of terrestrial lead isotope evolution by a 2-stage model. Earth and Planetary Science Letters 26, 207-221.

Stern, R.A., Percival, J.A., Mortensen, J.K., 1994. Geochemical evolution of the Minto block: a 2. 7 Ga continental magmatic arc built on the Superior proto-craton. Precambrian Research 65, 115–153.

Stevenson, R.K., David, J., Parent, M., 2006. Crustal evolution of the western Minto Block, northern Superior Province, Canada. Precambrian Research 145, 229–242.

Sun, S., McDonough, W.F., 1989. Chemical and isotopic systematics of oceanic basalts: implications for mantle composition and processes. Spec. Publ. Vol. Geol. Soc. Lond 42, 313–345.

Wolf, M.B., Wyllie, P.J., 1994. Dehydration-melting of amphibolite at 10 kbar: the effects of temperature and time. Contributions to Mineralogy and Petrology 115, 369–383.

Wyman, D.A., Hollings, P., Biczok, J., 2011. Crustal evolution in a cratonic nucleus: Granitoids and felsic volcanic rocks of the North Caribou Terrane, Superior Province Canada. Lithos 123, 37–49.

SUPPLEMENTARY ON-LINE MATERIAL

Appendix 3-1: Geochemistry of the Gladel River intrusion samples

Table 3-4: Geochemistry of the Gladel River intrusion samples

Sample	GR2-12	GR2-11	GR2-11*	GR2-10	GR2-10*	GR2-9	GR2-9*	GR2-8	GR2-8*
Easting	359125	359090		359158		359213		359272	
Northing	6465326	6465367		6465396		6465435		6465456	
Transect (m)	0	15		71		135		185	
Lithology	granite	granite		Px-grdt		Px-qmzt		Px-drt	
Major elements (wt. %)									
SiO_2	72.65	72.03	-	63.11	-	59.73	-	51.77	-
TiO_2	0.16	0.2	-	0.69	-	0.66	-	0.54	-
Al_2O_3	14.79	14.87	-	16.31	-	16.72	-	14.6	-
MgO	0.62	0.71	-	1.87	-	2.44	-	7.24	-
FeO	0.92	1.88	-	5.35	-	7.28	-	9.87	-
MnO	0.02	0.02	-	0.09	-	0.1	-	0.14	-
CaO	1.64	2.13	-	4.54	-	5.99	-	9.74	-
Na_2O	3.97	4.12	-	4.17	-	4.13	-	3.15	-
K_2O	4.04	3.25	-	1.62	-	1.3	-	0.95	-
P_2O_5	0.07	0.07	-	0.18	-	0.19	-	0.05	-
LOI	0.8	0.47	-	1.19	-	0.56	-	0.99	-
Total	99.68	99.75	-	99.12	-	99.1	-	99.04	-
Trace elements (ppm)									
Cs	<0.1	0.1	0.1	0.2	0.1	<0.1	0.1	0.4	0.1
Rb	83	77.3	79.1	28.5	29.5	26.3	25.4	23.3	22.9
Ba	1171	1028.0	1091.6	886.7	914.0	1030.0	1013.4	368.1	366.5
Th	32.6	11.4	10.84	2.5	1.82	0.4	0.44	2.0	2.01
U	0.75	0.5	0.41	0.3	0.22	0.1	0.13	0.1	0.10
Nb	1.8	2.0	1.76	4.3	4.65	3.2	3.06	1.7	1.61
Ta	0.06	0.05	0.04	0.34	0.12	0.06	0.08	0.09	0.07
Pb	17.7	17.3	21.6	8.5	9.6	8.1	9.3	5.4	6.9
Sr	361.0	382.2	392.3	472.9	501.6	602.1	566.5	489.1	481.0
Zr	164.2	120.8	120.9	171.1	188.0	114.9	124.9	42.8	42.3
Hf	4.6	5.1	3.27	5.2	4.52	2.4	3.00	1.4	1.33
Ga	15.1	16	18.6	19.5	22.1	19.7	22.1	16.2	17.2
Sc	<1.0	1	0.98	13.4	12.88	15.3	17.41	29.9	31.45
V	16.6	26.4	14.4	97.4	89.9	136.7	133.6	234.3	232.0
Co	<10	<10	3	16	15	25	24	51	50
La	64.7	30.5	28.24	28.8	27.66	25.4	25.02	17.8	18.70
Ce	109	52.5	53.86	53.5	57.28	44.5	48.25	38.4	40.83
Pr	9.89	4.93	5.31	5.64	6.3	5.36	5.65	4.57	5.21
Nd	32.4	16.7	17.38	22.1	24.14	21.3	22.31	19.2	20.84
Sm	3.7	2.32	2.31	3.7	4.07	3.82	3.98	3.87	4.13
Eu	1.03	0.83	0.92	1.18	1.31	1.12	1.18	0.72	0.78
Gd	1.93	1.44	1.41	2.91	2.98	3.02	3.51	3.09	3.16
Tb	0.18	0.16	0.17	0.38	0.41	0.42	0.48	0.43	0.46
Dy	0.75	0.72	0.76	1.98	2.08	2.25	2.48	2.37	2.65
Y	3.1	3.3	3.54	10.1	11.77	11.5	14.31	12.4	14.33
Ho	0.12	0.13	0.12	0.38	0.39	0.45	0.51	0.46	0.50
Er	0.32	0.33	0.34	1.04	1.15	1.33	1.36	1.26	1.32
Tm	0.036	0.037	0.034	0.14	0.15	0.19	0.18	0.18	0.18
Yb	0.22	0.29	0.23	0.87	0.88	1.19	1.05	1.09	1.21
Lu	0.026	0.032	0.041	0.11	0.12	0.19	0.17	0.15	0.16
K	33540	26980	-	13450	-	10790	-	7886	-
P	283.7	323	-	781.2	-	842.3	-	226.9	-
Ti	970	1209	-	4108	-	3944	-	3215	-
Cr	19.3	19	4.9	12.6	6.5	13.3	11.6	79.4	65.8
Ni	3	<3	4	4	9	<3	8	76	76
Zr/Y	53.0	36.6	34.2	16.9	16.0	10.0	8.7	3.5	3.0
K/(K+Na)	0.40	0.34	-	0.20	-	0.17	-	0.17	-

Table 3-4. Geochemistry of the Gladel River intrusion samples (cont.)

Sample	GR2-7	GR2-5	GR2-4	GR2-3	GR2-2	GR2-1	GR-1	GR-2	GR-2*
Easting	359298	359330	359361	359396	359430	359439	359461	359468	
Northing	6465485	6465536	6465593	6465620	6465641	6465659	6465657	6465693	
Transect (m)	224	285	349	391	426	449	459	491	
Lithology	f.web.	mt.gabnor	mt.gabnor	mt.gabnor	f.web.	web	web	web	
Major elements (wt. %)									
SiO_2	50.66	44.22	48.65	47.69	50.17	49.1	48.71	48.52	-
TiO_2	0.36	0.95	0.47	0.23	0.34	0.31	0.34	0.3	-
Al_2O_3	6.34	17.28	15.95	14.42	6.24	5.62	6.39	5.56	-
MgO	15.07	5.68	8.64	12.12	16.3	17.99	17.25	18.99	-
FeO	8.07	14.28	10.29	7.17	9.2	9.36	9.68	9.6	-
MnO	0.18	0.15	0.18	0.16	0.18	0.18	0.18	0.18	-
CaO	16.06	10.69	12.16	13.44	14.12	14.83	14.15	13.7	-
Na_2O	1.07	2.64	1.85	0.83	0.84	0.77	0.92	0.81	-
K_2O	0.36	0.84	0.27	0.35	0.35	0.32	0.34	0.33	-
P_2O_5	0.07	0.04	0.04	0.02	0.07	0.06	0.06	0.06	-
LOI	0.98	1.75	0.6	2.63	1.02	0.58	0.85	0.66	-
Total	99.22	98.52	99.1	99.06	98.83	99.12	98.87	98.71	-
Trace elements (ppm)									
Cs	<0.1	-	<0.1	0.1	<0.1	<0.1	-	0.9	0.09
Rb	5.3	17.4	2.9	6.0	5.0	7.3	8.3	7.0	6.6
Ba	144.1	328.2	144.0	123.2	166.5	190.9	166.9	140.5	149.0
Th	0.6	-	0.5	0.2	0.5	0.8	-	0.8	0.51
U	0.1	-	0.1	0.4	0.1	0.1	-	0.2	0.14
Nb	0.9	1.7	0.8	<0.3	0.7	0.6	0.7	0.8	0.68
Ta	0.06	-	0.03	0.01	0.09	0.04	-	0.06	0.04
Pb	1.8	4.4	2.0	<1.0	1.8	1.9	3.6	1.2	2.2
Sr	160.7	637.3	690.6	553.8	154.4	138.8	172.8	135.3	129.4
Zr	30.4	32.5	16.7	8.5	25.7	27.4	27.3	28.5	19.2
Hf	1.1	-	0.7	0.5	1.3	0.9	-	1.2	0.60
Ga	7.6	21.5	16.1	11.3	7.7	6.6	7.5	6.3	7.3
Sc	64.4	32.7	42.8	46.2	64.9	64.7	61.2	60.2	53.44
V	174.7	480.8	197.5	146.5	174.3	159.6	180.2	146.7	143.9
Co	61	67	55	58	94	85	83	88	87
La	7.76	-	5.76	3.03	7.35	6.69	-	6.57	6.51
Ce	19.1	-	13.3	7.3	16.6	14.8	-	14.9	15.74
Pr	2.64	-	1.79	1.07	2.2	1.93	-	1.96	2.17
Nd	13.0	-	8.73	5.61	10.6	9.58	-	9.56	10.07
Sm	3.07	-	2.07	1.49	2.47	2.34	-	2.22	2.39
Eu	0.85	-	0.70	0.57	0.71	0.65	-	0.64	0.69
Gd	2.75	-	1.85	1.32	2.23	2.03	-	1.93	2.25
Tb	0.39	-	0.27	0.21	0.32	0.3	-	0.28	0.33
Dy	2.07	-	1.49	1.16	1.76	1.6	-	1.53	1.65
Y	10.0	7.5	7.9	5.9	8.6	8.2	8.0	7.7	8.92
Ho	0.4	-	0.3	0.23	0.34	0.31	-	0.3	0.32
Er	1.06	-	0.79	0.61	0.91	0.86	-	0.8	0.95
Tm	0.16	-	0.12	0.09	0.13	0.11	-	0.12	0.14
Yb	0.95		0.75	0.58	0.83	0.73		0.69	0.72
Lu	0.12	-	0.095	0.067	0.11	0.095	-	0.091	0.11
K	2989	6973	2241	2906	2906	2656	2823	2739	-
P	296.8	178.9	165.8	69.8	296.8	257.5	261.9	253.1	-
Ti	2179	5705	2797	1376	2038	1833	2031	1826	-
Cr	1219	9	158.5	739.8	814.1	971.4	982.4	1255	1344
Ni	291	97	72	167	491	421	367	451	439
Zr/Y	3.0	4.3	2.1	1.4	3.0	3.3	3.4	3.7	2.2
K/(K+Na)	0.18	0.17	0.09	0.22	0.21	0.22	0.20	0.21	-

Table 3-4. Geochemistry of the Gladel River intrusion samples (cont.)

Sample	GR-3	GR-4	GR-5	GR-6	GR-7	GR-8	GR-9	GR-10	GR-11
Easting	359492	359516	359498	359546	359545	359552	359573	359588	359612
Northing	6465731	6465800	6465764	6465818	6465849	6465874	6465896	6465927	6465939
Transect (m)	538	568	608	638	664	689	719	754	778
Lithology	f.web.	f.web.	f.web.	gabnor	gabnor	gabnor	gabnor	gabnor	gabnor
Major elements (wt. %)									
SiO_2	51.24	50.94	50.57	50.1	51.77	49.72	49.29	49.33	49.42
TiO_2	0.29	0.33	0.35	0.28	0.4	0.31	0.32	0.33	0.32
Al_2O_3	5.18	6.25	6.96	11.12	11.02	11.84	13.88	14.31	15.98
MgO	17.45	16.7	16.31	13.85	13	13.03	12.12	11.71	10.43
FeO	8.85	9.39	9.77	8.96	8.35	8.72	8.52	8.64	8.52
MnO	0.19	0.2	0.2	0.18	0.17	0.17	0.17	0.17	0.16
CaO	14.36	13.75	13.34	12.81	12.19	12.46	12.19	12.24	11.79
Na_2O	0.81	0.87	0.85	1.11	1.66	1.24	1.37	1.45	1.65
K_2O	0.26	0.23	0.23	0.22	0.23	0.24	0.27	0.26	0.37
P_2O_5	0.06	0.06	0.06	0.06	0.08	0.07	0.08	0.09	0.08
LOI	0.45	0.4	0.52	0.4	0.44	0.9	0.72	0.81	0.65
Total	99.14	99.12	99.16	99.09	99.31	98.7	98.93	99.34	99.37
Trace elements (ppm)									
Cs	-	-	-	-	-	<0.1	-	-	-
Rb	2.4	<1.0	1.3	1.6	1.1	1.7	2.2	2.3	3.2
Ba	101.9	91.1	68.3	116.5	66.5	148.8	143.1	176.4	262.5
Th	-	-	-	-	-	3.6	-	-	-
U	-	-	-	-	-	1.4	-	-	-
Nb	0.9	0.8	0.9	0.8	2.1	0.9	1.3	1.0	1.0
Ta	-	-	-	-	-	0.68	-	-	-
Pb	1.3	2.0	<1.0	2.1	1.9	1.6	2.4	1.4	1.1
Sr	121.8	161.1	182.9	369.3	316.7	397.8	488.4	522.1	625.1
Zr	25.4	25.8	26.8	22.5	55.3	24.0	24.3	28.5	25.6
Hf	-	-	-	-	-	1.4	-	-	-
Ga	6.8	8.1	9.2	11	11.6	11.6	12.7	13.1	14.4
Sc	68.5	65.7	64.9	54.8	52.2	51	45.8	48	42.6
V	163	174.8	179.6	146.1	160.9	148.5	144.1	138.1	130.6
Co	75	67	79	65	67	70	65	64	60
La	-	-	-	-	-	71	-	-	-
Ce	-	-	-	-	-	124	-	-	-
Pr	-	-	-	-	-	13	-	-	-
Nd	-	-	-	-	-	51.3	-	-	-
Sm	-	-	-	-	-	8.3	-	-	-
Eu	-	-	-	-	-	2.18	-	-	-
Gd	-	-	-	-	-	6.76	-	-	-
Tb	-	-	-	-	-	0.91	-	-	-
Dy	-	-	-	-	-	4.74	-	-	-
Y	8	8.8	9.3	7.5	9.3	8.1	7.8	7.9	8
Ho	-	-	-	-	-	0.9	-	-	-
Er	-	-	-	-	-	2.16	-	-	-
Tm	-	-	-	-	-	0.28	-	-	-
Yb						1.58			
Lu	-	-	-	-	-	0.19	-	-	-
K	2138	1909	1909	1826	1909	1992	2241	2158	3072
P	253.1	274.9	279.3	244.4	331.7	283.7	331.7	371	331.7
Ti	1730	2008	2118	1701	2369	1879	1928	1979	1926
Cr	845.7	593.8	497.3	236.1	218.4	189	142.7	127.1	81.5
Ni	349	258	265	179	169	167	136	138	96
Zr/Y	3.2	2.9	2.9	3.0	5.9	3.0	3.1	3.6	3.2
K/(K+Na)	0.17	0.15	0.15	0.12	0.08	0.11	0.11	0.11	0.13

Table 3-4. Geochemistry of the Gladel River intrusion samples (cont.)

Sample	GR-12	GR-13	GR-14	GR-15	GR-17	GR-18	GR-19	GR-20	GR-21
Easting	359622	359648	359658	359669	359683	359689	359724	359739	359752
Northing	6465967	6465987	6466021	6466046	6466040	6466064	6466051	6466052	6466055
Transect (m)	806	837	872	897	903	924	932	941	950
Lithology	gabnor	mt.gabnor	mt.gabnor	mt.gabnor	granite	granite	granite	granite	granite
Major elements (wt. %)									
SiO_2	48.82	48.61	48.35	46.74	73.53	73.83	76.16	72.46	73.79
TiO_2	0.37	0.46	0.54	0.87	0.09	0.09	0.06	0.13	0.09
Al_2O_3	17.38	14.68	16.49	16	14.62	14.38	13.33	14.44	14.21
MgO	9.15	10.17	8.88	8.36	0.24	0.29	0.22	0.42	0.34
FeO	8.52	10.00	10.2	11.31	0.89	0.57	0.54	1.22	1.1
MnO	0.15	0.17	0.17	0.17	0.01	0.01	0.01	0.02	0.01
CaO	11.73	11.69	10.91	10.83	1.31	1.31	1.38	1.49	1.57
Na_2O	1.95	1.76	2.08	2.37	3.88	3.62	3.56	3.78	3.74
K_2O	0.36	0.40	0.47	0.69	4.6	5.04	3.92	4.68	4.56
P_2O_5	0.11	0.11	0.15	0.41	0.02	0.01	0.02	0.04	0.03
LOI	0.58	1.01	0.37	0.95	0.4	0.36	0.41	0.8	0.34
Total	99.12	99.07	98.61	98.7	99.59	99.51	99.61	99.48	99.78
Trace elements (ppm)									
Cs	-	<0.1	-	-	-	-	-	-	-
Rb	3.0	2.8	3.0	10.2	93.6	97.4	76.5	93.5	85.2
Ba	224.5	258.8	302.8	394.8	1518.0	1633.0	1278.0	1576.0	1693.0
Th	-	0.29	-	-	-	-	-	-	-
U	-	0.06	-	-	-	-	-	-	-
Nb	1.4	1.4	1.7	2.8	1.1	0.7	0.4	0.7	<0.3
Ta	-	0.07	-	-	-	-	-	-	-
Pb	2.2	2.6	2.6	4.5	30.5	33.7	26.7	28.0	28.9
Sr	719.5	589.2	692.3	650.6	315.9	326.3	302.4	317.5	339.8
Zr	30.5	33.9	36.9	41.8	67.3	56.9	85.9	72.3	67.7
Hf	-	1.2	-	-	-	-	-	-	-
Ga	16.1	14.9	16.7	18.4	14	13.1	12.9	13.6	13.4
Sc	38.7	46.5	37.2	39.7	<1.0	<1.0	<1.0	1.3	<1.0
V	140.4	181	203.1	227.2	14.6	12.5	11.5	14.5	15.3
Co	55	59	58	56	<10	<10	<10	<10	<10
La	-	11.70	-	-	-	-	-	-	-
Ce	-	26.50	-	-	-	-	-	-	-
Pr	-	3.35	-	-	-	-	-	-	-
Nd	-	15.10	-	-	-	-	-	-	-
Sm	-	3.09	-	-	-	-	-	-	-
Eu	-	0.91	-	-	-	-	-	-	-
Gd	-	2.47	-	-	-	-	-	-	-
Tb	-	0.34	-	-	-	-	-	-	-
Dy	-	1.83	-	-	-	-	-	-	-
Y	8.4	9.8	9.2	15.9	1.9	1.2	1	1.4	1.1
Ho	-	0.36	-	-	-	-	-	-	-
Er	-	1.00	-	-	-	-	-	-	-
Tm	-	0.14	-	-	-	-	-	-	-
Yb		0.89							
Lu	-	0.11	-	-	-	-	-	-	-
K	2989	3321	3902	5728	38190	41840	32540	38850	37850
P	475.7	463	641.5	1798	82.9	65.5	69.8	161.5	130.9
Ti	2247	2730	3252	5200	549.2	521.6	362.7	758.4	535.4
Cr	55	106.4	51.5	58.3	<7.0	9.6	8.5	10.9	9.3
Ni	79	101	67	56	<3	<3	<3	<3	<3
Zr/Y	3.6	3.5	4.0	2.6	35.4	47.4	85.9	51.6	61.5
K/(K+Na)	0.11	0.13	0.13	0.16	0.44	0.48	0.42	0.45	0.45

Table 3-4. Geochemistry of the Gladel River intrusion samples (cont.)

Sample	Chron2	GR4-2	Chron1	GR4-1	GR2-6	GR3-5	GR3-6	GR3-7
Easting	358690	358839	358752	358633	359329	359609	359440	359353
Northing	6465413	6465733	6465681	6465670	6465532	6465937	6465953	6465704
Transect (m)	-	-	-	-	-	-	-	-
Lithology	Px-grdt	Px-qmzt	f.web.	f.web.	pegmatite	pegmatite	pegmatite	pegmatite
Major elements (wt. %)								
SiO_2	65.40	56.35	50.98	50.19	73.53	73.87	74.81	73.42
TiO_2	0.55	0.55	0.3	0.34	0.3	0.07	0.1	0.04
Al_2O_3	16.11	16.74	5.64	6.91	14.08	13.79	14.44	14.99
MgO	1.42	4.3	16.16	15.65	1.23	0.45	0.64	0.48
FeO	4.27	7.56	8.13	8.83	1.47	0.38	0.57	0.37
MnO	0.08	0.12	0.19	0.2	0.03	0.01	0.01	0.02
CaO	3.89	7.7	15.34	14.31	3.38	0.36	4.02	3.19
Na_2O	5.03	3.63	0.91	0.96	3.8	2.16	3.58	3.94
K_2O	1.7	1.26	0.25	0.35	0.88	7.96	0.59	1.52
P_2O_5	0.29	0.1	0.04	0.05	0.01	0.01	0.01	0.01
LOI	0.6	0.91	1.36	1.3	1.06	0.56	1.16	1.65
Total	99.34	99.22	99.3	99.09	99.77	99.62	99.93	99.63
Trace elements (ppm)								
Cs	0.5	<0.1	<0.1	-	<0.1	-	-	<0.1
Rb	67.7	21.7	2.0	2.4	27.6	121.1	11.0	31.8
Ba	402.2	708.4	70.9	86.2	313.6	3695.0	294.1	730.9
Th	13.0	1.9	0.4	-	0.2	-	-	0.3
U	0.8	0.1	0.1	-	0.1	-	-	0.0
Nb	7.0	3.0	0.6	1.0	1.8	0.5	0.8	<0.3
Ta	0.30	0.11	0.09	-	0.01	-	-	<.01
Pb	15.6	9.6	2.0	1.1	6.5	55.6	5.3	5.5
Sr	410.2	544.7	123.5	138.1	460.9	467.8	507.7	518.1
Zr	298.0	75.9	24.8	27.0	76.9	<1.0	<1.0	9.6
Hf	8.6	2.2	0.9	-	2	-	-	0.2
Ga	21.2	18.2	7	7.9	15.6	9.1	14.6	14.4
Sc	11.5	23.7	61.9	60.7	2.3	<1.0	<1.0	1.9
V	58.9	149.5	166.3	166	32.7	8.5	13.8	8.4
Co	<10	32	60	70	12	<10	<10	<10
La	57	18.6	5.45	-	7.93	-	-	12.8
Ce	111	39.8	12.9	-	9.08	-	-	14.3
Pr	11.7	4.76	1.78	-	0.76	-	-	1.15
Nd	43.9	19.9	8.96	-	2.15	-	-	3.19
Sm	7.36	4.04	2.23	-	0.23	-	-	0.28
Eu	1.08	0.85	0.62	-	0.57	-	-	0.64
Gd	5.35	3.16	2.05	-	0.13	-	-	0.17
Tb	0.67	0.45	0.3	-	0.02	-	-	0.02
Dy	3.24	2.28	1.64	-	0.08	-	-	0.06
Y	16.4	11.5	8.1	9.3	<1.0	<1.0	<1.0	<1.0
Ho	0.58	0.45	0.32	-	0.02	-	-	0.01
Er	1.48	1.19	0.86	-	0.07	-	-	0.03
Tm	0.197	0.171	0.116	-	0.011	-	-	<0.005
Yb	1.14	1.05	0.76		0.09			0.03
Lu	0.15	0.14	0.096	-	0.017	-	-	0.003
K	14110	10460	2075	2906	7305	66080	4898	12620
P	1266	414.6	187.7	218.2	39.3	39.3	34.9	34.9
Ti	3324	3283	1786	2043	1813	397.5	593.5	233.8
Cr	24.1	23.4	1206	1006	26.8	15.9	20	24
Ni	6	14	366	347	16	5	8	7
Zr/Y	18.2	6.6	3.1	2.9	-	-	-	-
K/(K+Na)	0.18	0.19	0.15	0.19	0.13	0.71	0.10	0.20

Details of whole rock analyses:

Major element, and select trace element analyses (Ba, Co, Cr, Ni , V, Ga, Nb, Pb, Rb, Sc, Sr, Y, and Zr) were performed at the McGill University Geochemical Laboratories using a Philips PW2440 X-ray fluorescence (XRF) spectrometer

REE, Hf, Ta, Th, U, Cs were analyzed by Activation Laboratories using a Perkin Elmer SCIEX ELAN 6000 ICP-MS system

* duplicate trace lement analyses performed at the Pacific Institute for Isotopic and Geochemical Research (PCIGR) at the University of British Columbia in Vancouver, B.C., Canada using a high-resolution (HR)-ICP-MS Thermo Finnigan ELEMENT2 machine

when available, data obtained from PCIGR were plotted preferentially

Table 3-5: Average plagioclase compositions of select Gladel River intrusion samples

Sample	GR2-11	GR2-10	GR2-9	GR2-8	GR2-4
PLAGIOCLASE	n=5	n=7	n=10	n=11	n=5
SiO2	62.85 (0.33)	60.44 (0.68)	60.24 (0.86)	58.32 (1.17)	51.65 (0.52)
Al_2O_3	23.19 (0.21)	24.66(0.40)	25.09 (0.29)	26.21 (0.60)	30.75 (0.44)
MgO	-	-	-	-	0.00 (0.01)
FeO	0.05 (0.04)	0.07 (0.03)	0.07 (0.05)	0.08 (0.03)	0.12 (0.03)
CaO	4.53 (0.64)	6.55 (0.59)	6.94 (0.41)	8.30 (0.70)	13.76 (0.38)
Na_2O	8.50 (0.09)	7.44 (0.40)	7.17 (0.36)	6.41 (0.40)	3.70 (0.20)
K_2O	0.41 (0.33)	0.35 (0.15)	0.46 (0.43)	0.32 (0.05)	0.14 (0.03)
BaO	0.02 (0.06)	0.02 (0.02)	0.03 (0.07)	0.03 (0.06)	-
SrO	-	-	-	-	0.18 (0.05)
Total	99.55 (0.52)	99.53 (0.47)	100.00 (0.84)	99.68 (0.56)	100.31 (0.18)
An	*0.22 (0.03)*	*0.32 (0.03)*	*0.34 (0.02)*	*0.41 (0.04)*	*0.67 (0.02)*
Ab	*0.75 (0.01)*	*0.66 (0.03)*	*0.63 (0.02)*	*0.57 (0.03)*	*0.33 (0.02)*
Or	*0.02 (0.02)*	*0.01 (0.01)*	*0.02 (0.03)*	*0.02 (0.00)*	*0.01 (0.00)*

All analyses performed on McGill University's JEOL 8900 Electron Microprobe

Table 3-6: Average mafic mineral compositions of select Gladel River intrusion samples

Sample	GR2-2	GR2-1	GR-2	GR2-4
ORTHOPYROXENE	n=8	n=25	n=11	n=10
SiO2	53.83 (0.49)	53.57 (0.56)	54.22 (0.50)	51.90 (0.54)
TiO_2	0.03 (0.02)	0.02 (0.02)	0.05 (0.02)	0.06 (0.02)
Al_2O_3	0.97 (0.15)	1.78 (0.27)	1.75 (0.46)	1.03 (0.19)
MgO	26.69 (0.33)	27.60 (0.56)	29.33 (0.66)	21.84 (0.33)
FeO	17.12 (0.34)	15.55 (0.56)	13.20 (0.38)	23.59 (0.32)
MnO	0.44 (0.02)	0.36 (0.02)	0.33 (0.03)	0.63 (0.03)
CaO	0.38 (0.06)	0.49 (0.69)	0.46 (0.53)	0.42 (0.06)
Na_2O	0.02 (0.05)	0.02 (0.06)	0.00 (0.01)	0.01 (0.02)
K_2O	0.00 (0.00)	0.00 (0.00)	0.00 (0.00)	0.00 (0.01)
Cr_2O_3	0.02 (0.01)	0.05 (0.05)	0.03 (0.05)	0.00 (0.01)
NiO	0.03 (0.07)	0.02 (0.02)	0.02 (0.01)	0.02 (0.07)
Total	99.52 (0.83)	99.46 (0.71)	99.40 (0.44)	99.49 (0.60)
˙En	*0.70 (0.01)*	*0.71 (0.02)*	*0.75 (0.02)*	*0.59 (0.01)*
˙FS	*0.23 (0.01)*	*0.20 (0.02)*	*0.17 (0.01)*	*0.33 (0.02)*
˙Cpx	*0.01 (0.00)*	*0.02 (0.03)*	*0.02 (0.02)*	*0.02 (0.00)*
Mg-number	*0.75 (0.01)*	*0.78 (0.01)*	*0.82 (0.01)*	*0.64 (0.01)*
CLINOPYROXENE	n=6	n=5	n=5	n=8
SiO2	53.02 (0.51)	52.54 (0.46)	52.22 (0.36)	51.86 (0.86)
TiO_2	0.09 (0.03)	0.05 (0.02)	0.17 (0.06)	0.18 (0.06)
Al_2O_3	1.41 (0.12)	1.80 (0.42)	2.08 (0.21)	1.67 (0.48)
MgO	15.96 (0.42)	15.99 (0.41)	16.18 (0.26)	14.33 (0.43)
FeO	5.72 (0.28)	5.48 (0.20)	4.52 (0.20)	8.28 (0.79)
MnO	0.18 (0.02)	0.16 (0.02)	0.14 (0.01)	0.24 (0.03)
CaO	22.96 (0.48)	23.09 (0.45)	23.77 (0.26)	22.67 (0.53)
Na_2O	0.38 (0.04)	0.33 (0.06)	0.23 (0.03)	0.40 (0.04)
K_2O	0.00 (0.01)	0.00 (0.01)	0.00 (0.01)	0.00 (0.01)
Cr_2O_3	0.08 (0.05)	0.07 (0.06)	0.12 (0.07)	0.01 (0.03)
Total	99.81 (0.79)	99.52 (0.39)	99.42 (0.28)	99.63 (0.72)
†*Di*	*0.75 (0.03)*	*0.76 (0.02)*	*0.80 (0.02)*	0.71 (0.07)
†*Hd*	*0.10 (0.01)*	*0.08 (0.01)*	*0.06 (0.02)*	0.15 (0.01)
†*Opx*	*0.07 (0.02)*	*0.07 (0.02)*	*0.05 (0.01)*	0.07 (0.01)
†*Tsch*	*0.05 (0.01)*	*0.07 (0.01)*	*0.08 (0.01)*	0.04 (0.07)
†Fe^{3+}/Fe^{tot}	*0.36 (0.07)*	*0.44 (0.09)*	*0.54 (0.13)*	0.34 (0.06)
Mg-number	*0.89 (0.01)*	*0.90 (0.02)*	*0.93 (0.02)*	0.82 (0.02)
AMPHIBOLE	n=5	n=3	n=4	n=4
SiO2	47.65 (0.66)	43.08 (0.80)	42.18 (0.46)	44.93 (0.50)
TiO_2	0.81 (0.06)	0.66 (0.01)	0.99 (0.62)	1.76 (0.24)
Al_2O_3	13.26 (0.32)	12.59 (0.15)	13.26 (0.32)	9.68 (0.84)
MgO	16.96 (0.24)	15.53 (0.35)	15.92 (0.28)	13.59 (0.26)
FeO	8.85 (0.42)	9.41 (0.44)	8.38 (0.58)	13.26 (0.26)
MnO	0.10 (0.02)	0.09 (0.02)	0.09 (0.01)	0.13 (0.03)
CaO	11.95 (0.48)	11.91 (0.07)	12.06 (0.31)	11.78 (0.12)
Na_2O	1.18 (0.07)	1.96 (0.11)	2.39 (0.29)	1.20 (0.11)
K_2O	0.74 (0.06)	1.13 (0.05)	0.73 (0.48)	0.98 (0.07)
Cr_2O_3	0.25 (0.07)	0.23 (0.09)	0.31 (0.18)	0.04 (0.06)
Total	96.76 (0.60)	96.59 (0.97)	96.29 (0.53)	97.36 (1.00)
§*Tr*	0.92 (0.04)	*0.92 (0.01)*	*0.94 (0.03)*	*0.92 (0.02)*
§*Gl*	0.06 (0.05)	*0.06 (0.02)*	*0.04 (0.03)*	*0.05 (0.02)*
§*Ri*	0.03 (0.01)	*0.02 (0.01)*	*0.02 (0.01)*	*0.03 (0.00)*
§Fe^{3+}/Fe^{tot}	0.63 (0.19)	*0.64 (0.14)*	*0.68 (0.14)*	*0.40 (0.05)*
Mg-number	0.90 (0.04)	*0.89 (0.03)*	*0.91 (0.03)*	*0.75 (0.01)*

Table 3-6. Average mafic mineral compositions of Gladel River samples (cont.)

Sample	GR2-2	GR2-1	GR-2	GR2-4
OLIVINE	-	-	n=7	-
SiO2	-	-	38.79 (0.13)	-
TiO_2	-	-	0.01 (0.01)	-
Al_2O_3	-	-	0.00 (0.01)	-
MgO	-	-	40.86 (0.38)	-
FeO	-	-	20.48 (0.70)	-
MnO	-	-	0.32 (0.03)	-
CaO	-	-	0.01 (0.01)	-
Na_2O	-	-	0.00 (0.01)	-
P_2O_5	-	-	0.02 (0.01)	-
Cr_2O_3	-	-	0.00 (0.01)	-
NiO	-	-	0.13 (0.02)	-
Total	-	-	100.62 (0.55)	-
Mg-number	-	-	*0.79 (0.01)*	-

* calculated using program Calcmin (Brandelik, 2009) using orthopyroxen_MAS routine
† calculated using program Calcmin (Brandelik, 2009) using clinopyroxen_MAS routine
§ calculated using program Calcmin (Brandelik, 2009) using amphibole_MAS routine

Appendix 3-2: Geochemistry of Ungava granitoids (2008-2011)

Table 3-7: Geochemistry of Ungava Granitoids

Sample	DH-15	DH08-1	DH08-2	DH08-13	DH08-14	DH-12	DH08-4	LM1-7	LM2-7
Easting	359073	359042	359134	359202	359241	359136	359149	433906	434067
Northing	6460827	6460822	6460803	6460889	6460859	6460820	6460816	6488672	6492174
Suite	*GGM*	*GGM*	*GGM*	*GGM*	*GGM*	*pegmatite*	*pegmatite*	*GGM*	*GGM*
Major elements (wt. %)									
SiO_2	70.36	67.43	68.84	72.05	72.29	69.08	74.68	73.85	73.94
TiO_2	0.39	0.44	0.25	0.14	0.12	0.16	0.09	0.22	0.19
Al_2O_3	15.29	16.07	16.16	15.25	15.47	16.54	14.58	13.64	13.93
MgO	0.98	1.29	1.37	0.96	0.60	1.18	0.61	0.41	0.49
FeO	2.54	3.45	2.09	1.08	0.77	1.45	0.60	1.58	1.40
MnO	0.02	0.03	0.03	0.02	0.01	0.02	0.02	0.02	0.02
CaO	3.46	3.63	4.24	2.56	2.22	3.62	2.67	1.30	1.65
Na_2O	4.19	4.47	4.71	4.40	3.93	4.98	4.91	3.05	3.83
K_2O	1.51	1.90	1.31	2.30	3.77	1.54	1.03	5.46	4.01
P_2O_5	0.09	0.16	0.10	0.04	0.03	0.07	0.01	0.07	0.07
LOI	0.95	0.64	0.63	0.92	0.59	1.23	0.75	0.28	0.38
Total	99.79	99.51	99.75	99.73	99.81	99.89	99.96	99.88	99.91
Trace elements (ppm)									
Cs	0	-	-	-	-	<0.1	-	-	0.1
Rb	35	45.8	33.7	45.1	75.9	27.4	24.4	135.4	98.4
Ba	411.3	544.7	623.9	971.3	1560	539.5	395.9	817.0	682.0
Th	5.17	-	-	-	-	1.34	-	-	25.70
U	0.22	-	-	-	-	0.19	-	-	0.56
Nb	3.8	4.6	2.3	1.8	1.2	1.9	1.2	2.4	2.1
Ta	0.06	-	-	-	-	0.05	-	-	0.06
Pb	8.5	10.5	8.8	13.1	13.3	14.5	10.4	30.3	22.2
Sr	357.1	423.3	455.9	457.6	422.3	466.8	364.0	210.2	272.4
Zr	131	214.2	96.8	84.4	93.8	75.7	23.5	147.9	101.0
Hf	3.6	-	-	-	-	2.3	-	-	3.4
Ga	18.8	20.3	18.4	16.3	15.6	18.7	17.0	16.1	16.9
Sc	3.9	5.3	4.3	1.3	1.1	3.4	<1.0	3.0	1.3
V	46.6	43.3	36.6	16.6	14.9	20.9	9.1	20.3	26.3
Co	<10	<10	<10	<10	<10	<10	<10	<10	<10
La	45.7	-	-	-	-	22.9	-	-	31.70
Ce	75.1	-	-	-	-	35.0	-	-	52.40
Pr	6.39	-	-	-	-	2.97	-	-	5.58
Nd	16.6	-	-	-	-	8.5	-	-	18.70
Sm	2.51	-	-	-	-	1.29	-	-	2.46
Eu	0.79	-	-	-	-	0.67	-	-	0.83
Gd	1.42	-	-	-	-	0.78	-	-	1.45
Tb	0.15	-	-	-	-	0.09	-	-	0.16
Dy	0.61	-	-	-	-	0.38	-	-	0.72
Y	2.7	6.1	2.9	1.5	1.4	2.3	<1.0	4.6	3.6
Ho	0.10	-	-	-	-	0.07	-	-	0.13
Er	0.22	-	-	-	-	0.19	-	-	0.37
Tm	0.029	-	-	-	-	0.027	-	-	0.051
Yb	0.19	-	-	-	-	0.16	-	-	0.30
Lu	0.035	-	-	-	-	0.026	-	-	0.049
K	12540	15770	10870	19090	31300	12780	8551	45330	33290
P	406	690	454	166	122	288	57	292	288
Ti	2316	2638	1526	818	729	977	532	1316	1168
Cr	16.1	27.6	30.7	31.4	22.4	34.8	24.7	14.7	<6.8
Ni	7	8	17	9	5	19	12	<3	<3
Zr/Y	48.5	35.1	33.4	56.3	67.0	32.9	-	32.15	28.06
K/(K+Na)	0.19	0.22	0.15	0.26	0.39	0.17	0.12	0.54	0.41

Table 3-7: Geochemistry of Ungava granitoids (cont.)

Sample	LM2-8	LM3-17	LM4-7	C1-27B	C1-51	*C1-51**	D-01	C1-46	D-17
Easting	434077	438948	439658	486078	486104		494992	486258	494187
Northing	6492166	6490070	6496926	6674100	6674755		6701526	6674709	6698489
Suite	*GGM*	*GGM*	*pegmatite*	*TTG*	*TTG*		*TTG*	*TTG*	*TTG*
Major elements (wt. %)									
SiO_2	65.40	71.69	63.07	61.25	63.88		65.93	65.14	66.30
TiO_2	0.70	0.28	0.53	0.59	0.53		0.46	0.48	0.44
Al_2O_3	16.43	14.99	15.72	17.63	16.26		15.56	16.67	15.00
MgO	1.58	0.72	3.05	2.60	2.49		2.00	1.87	1.85
FeO	4.27	2.07	4.46	4.83	4.93		4.08	3.97	3.88
MnO	0.06	0.03	0.07	0.13	0.11		0.08	0.09	0.07
CaO	3.00	2.16	4.68	3.81	4.85		4.14	4.49	3.58
Na_2O	4.69	4.59	4.33	4.31	4.12		3.83	4.45	4.12
K_2O	3.03	2.56	2.47	2.74	1.83		2.98	1.86	3.40
P_2O_5	0.27	0.17	0.22	0.19	0.14		0.13	0.14	0.12
LOI	0.39	0.63	1.24	1.25	0.64		0.55	0.59	0.52
Total	99.83	99.90	99.86	99.33	99.78		99.75	99.75	99.28
Trace elements (ppm)									
Cs	0.2	0.5	0.3	-	3.6	3.55	-	-	-
Rb	93.0	81.0	63.6	193.0	81.1	83.6	97.7	70.8	105.4
Ba	550.3	693.8	931.3	377.9	402.3	392.5	943.6	504.5	740.6
Th	14.00	12.00	5.90	-	3.72	4.16	-	-	-
U	0.54	0.55	0.1	-	1.59	1.77	-	-	-
Nb	11.3	2.6	4.8	7.2	5.8	5.76	6.2	5.4	7.9
Ta	0.49	0.08	0.05	-	0.4	0.43	-	-	-
Pb	19.9	16.3	8.3	7.6	9.4	8.63	15.1	11.3	18.2
Sr	331.4	326.0	522.0	405.3	349.7	363.1	378.5	403.2	285.4
Zr	204.2	162.9	154.9	116.6	121.9	131.6	181.9	108.3	188.9
Hf	6.2	4.4	3.6	-	3.4	3.72	-	-	-
Ga	24.0	19.3	19.5	21.0	18.6	21.7	17.4	19.7	17.5
Sc	6.8	3.0	11.9	8.0	11.6	10.9	11.3	7.8	10.4
V	60.0	30.7	85.5	86.2	91.8	82.3	75.2	74.8	71.5
Co	<10	<10	13	11	17	15	12	11	<10
La	73.20	55.6	52.2	-	21.60	20.28	-	-	-
Ce	147.00	85.1	88.8	-	40.90	45.22	-	-	-
Pr	17.60	10.4	10.4	-	5.07	5.40	-	-	-
Nd	66.50	36.6	38.8	-	20.50	21.66	-	-	-
Sm	11.20	4.81	6.41	-	3.86	4.14	-	-	-
Eu	1.21	0.86	1.27	-	0.91	0.99	-	-	-
Gd	7.44	2.58	4.08	-	2.95	3.11	-	-	-
Tb	0.97	0.26	0.48	-	0.43	0.46	-	-	-
Dy	4.90	1.04	2.28	-	2.27	2.81	-	-	-
Y	25.8	5.0	11.2	6.8	13.5	16.03	12.9	10.2	15.4
Ho	0.91	0.17	0.4	-	0.46	0.53	-	-	-
Er	2.63	0.46	1.16	-	1.40	1.60	-	-	-
Tm	0.36	0.064	0.16	-	0.21	0.21	-	-	-
Yb	2.00	0.42	0.94	-	1.35	1.39	-	-	-
Lu	0.30	0.072	0.15	-	0.23	0.21	-	-	-
K	25150	21250	20500	22750	15190		24740	15440	28230
P	1183	759	969	834	620		580	598	511
Ti	4218	1686	3184	3537	3179		2741	2876	2629
Cr	12.6	7.8	81.5	22.4	26.1	20.3	33.1	15.9	27.8
Ni	5	<3	44	11	10	13	7	5	6
Zr/Y	7.91	32.58	13.83	17.15	9.03	8.21	14.10	10.62	12.27
K/(K+Na)	0.30	0.27	0.27	0.30	0.23		0.34	0.22	0.35

Table 3-7: Geochemistry of Ungava granitoids (cont.)

Sample	C1-55B	D-12	C1-52	C2-04	C1-40	C1-54	C1-49	C1-27A	C1-36
Easting	486160	495161	487492	488785	486320	486375	486255	486078	486253
Northing	6674724	6699394	6672796	6668319	6674699	6674369	6674832	6674100	6674011
Suite	*TTG*	*TTG*	*GGM*	*GGM*	*GGM*	*GGM*	*GGM*	*GGM*	*GGM*
Major elements (wt. %)									
SiO_2	67.32	68.78	75.39	74.26	64.18	73.53	75.63	75.09	73.23
TiO_2	0.43	0.40	0.03	0.06	0.13	0.06	0.02	0.05	0.02
Al_2O_3	16.74	15.54	13.84	14.67	20.58	13.95	13.40	14.56	14.26
MgO	1.47	1.19	0.18	0.25	0.93	0.45	0.22	0.20	0.13
FeO	2.93	2.75	0.31	0.73	1.03	0.51	0.17	0.70	0.19
MnO	0.04	0.05	0.01	0.01	0.02	0.01	0.00	0.02	0.00
CaO	3.63	3.30	1.65	2.24	4.74	0.37	0.86	2.47	0.20
Na_2O	4.95	4.36	3.17	4.05	6.47	2.16	2.63	4.91	1.85
K_2O	1.52	2.36	4.66	3.28	0.99	8.34	6.51	1.25	9.36
P_2O_5	0.16	0.11	0.02	0.03	0.01	0.01	0.01	0.01	0.01
LOI	0.64	0.63	0.47	0.29	0.56	0.43	0.37	0.38	0.32
Total	99.84	99.47	99.73	99.86	99.64	99.82	99.82	99.64	99.57
Trace elements (ppm)									
Cs	3.9	-	-	-	-	-	1.1	-	-
Rb	88.6	81.9	95.5	61.6	30.8	175.1	134.0	31.0	185.9
Ba	240.2	784.0	1875.0	1520.0	306.3	2555.0	1342.0	482.5	1497.0
Th	12.40	-	-	-	-	-	9.37	-	-
U	0.77	-	-	-	-	-	1.49	-	-
Nb	6.0	5.2	0.9	0.6	3.2	1.7	<0.3	1.8	0.3
Ta	0.2	-	-	-	-	-	<0.01	-	-
Pb	8.3	13.1	19.1	13.7	320.7	36.4	24.5	12.7	27.8
Sr	433.6	414.4	311.8	324.7	858.6	383.4	314.2	278.1	301.7
Zr	211.3	94	49.7	45.5	84.7	14.9	55.9	35.8	0
Hf	5.1	-	-	-	-	-	1.4	-	-
Ga	21.8	18.9	12.0	13.9	19.4	10.0	11.5	15.3	12.1
Sc	2.3	4.9	<1	<1	1.4	<1	<1	1.2	0.0
V	48.0	46.8	10.7	19.1	27.2	10.2	<7	15.5	7.6
Co	<10	<10	<10	<10	<10	<10	<10	<10	<10
La	64.50	-	-	-	-	-	4.19	-	-
Ce	109.00	-	-	-	-	-	10.80	-	-
Pr	11.70	-	-	-	-	-	0.75	-	-
Nd	38.40	-	-	-	-	-	2.62	-	-
Sm	4.58	-	-	-	-	-	0.61	-	-
Eu	0.79	-	-	-	-	-	0.34	-	-
Gd	2.14	-	-	-	-	-	0.43	-	-
Tb	0.18	-	-	-	-	-	0.05	-	-
Dy	0.61	-	-	-	-	-	0.15	-	-
Y	3.1	7.3	1.4	<1.0	12.6	<1.0	1.0	1.2	<1.0
Ho	0.09	-	-	-	-	-	0.02	-	-
Er	0.23	-	-	-	-	-	0.07	-	-
Tm	0.033	-	-	-	-	-	0.011	-	-
Yb	0.25	-	-	-	-	-	0.11	-	-
Lu	0.046	-	-	-	-	-	0.024	-	-
K	12620	19590	38680	27230	8218	69230	54040	10380	77700
P	698	476	83	118	39	35	44	52	31
Ti	2605	2405	160	366	774	381	100	320	134
Cr	20.7	21.6	<6.8	11.4	15.9	<7	<7	<7	<7.0
Ni	10	<3	<3	<3	<3	<3	<3	<3	<3
Zr/Y	68.16	12.88	35.50	-	6.72	-	55.90	29.83	-
K/(K+Na)	0.17	0.26	0.49	0.35	0.09	0.72	0.62	0.14	0.77

Table 3-7: Geochemistry of Ungava granitoids (cont.)

Sample	D-23	C1-11	C1-26	C1-35	C1-55A	D-15	D-26	PK09-13	PK09-15
Easting	494903	486005	486117	486177	486160	494552	494914	355633	356186
Northing	6700128	6674496	6674125	6674112	6674724	6698882	6700627	6470101	6469910
Suite	*X-cutting*	*X-cutting*	*X-cutting*	*X-cutting*	*leucosome*	*X-cutting*	X-cutting	*GGM*	*GGM*
Major elements (wt. %)									
SiO_2	65.08	77.04	74.56	73.40	75.45	63.54	80.44	71.86	71.20
TiO_2	0.10	0.03	0.05	0.02	0.03	0.02	0.03	0.19	0.25
Al_2O_3	20.65	13.85	14.33	16.34	14.20	22.01	11.48	15.44	15.92
MgO	0.59	0.17	0.24	0.15	0.12	0.15	0.37	0.67	0.68
FeO	0.68	0.19	0.65	0.14	0.28	0.15	0.26	1.42	1.91
MnO	0.01	0.01	0.02	0.01	0.01	0.01	0.03	0.02	0.02
CaO	4.07	2.74	1.51	3.50	2.04	3.36	2.38	2.07	3.09
Na_2O	7.32	4.79	4.14	5.65	3.52	8.40	4.03	4.49	5.00
K_2O	0.59	0.60	3.75	0.29	3.93	1.32	0.26	2.92	1.48
P_2O_5	0.02	0.01	0.01	0.01	0.01	0.01	0.01	0.05	0.07
LOI	0.52	0.33	0.38	0.32	0.32	0.47	0.45	0.77	0.30
Total	99.63	99.74	99.65	99.83	99.91	99.44	99.75	99.90	99.94
Trace elements (ppm)									
Cs	-	-	-	-	1	0.4	-	-	-
Rb	29.5	7.6	79.2	3.1	75.0	23.3	7.7	67.8	35
Ba	375.3	91.9	1100.0	198.0	1820.0	1045.0	213.9	951.5	419.8
Th	-	-	-	-	1.72	30.90	-	-	-
U	-	-	-	-	0.52	7.81	-	-	-
Nb	1.6	0.5	1.2	<0.3	0.6	0.9	1.5	1.1	1.8
Ta	-	-	-	-	<0.01	0.2	-	-	-
Pb	22.2	11.9	12.9	22.4	13.2	36.0	17.7	16.2	14.5
Sr	1423	344.1	195.5	701.5	414.6	1693	554.7	460.0	485.3
Zr	111.5	1	28.6	28	49.2	147.3	46.9	126.4	138.6
Hf	-	-	-	-	1.3	4.5	-	-	-
Ga	19.6	15.8	15.9	16.3	12.8	22.0	12.9	16.1	18.6
Sc	<1	<1	1.4	1.6	1.4	<1	<1	1.6	1.1
V	15.2	10.4	12.1	10.5	8.5	8.0	12.4	18.9	24.4
Co	<10	<10	<10	<10	<10	<10	<10	<10	<10
La	-	-	-	-	11.40	11.5	-	-	-
Ce	-	-	-	-	25.10	15.2	-	-	-
Pr	-	-	-	-	1.81	1.94	-	-	-
Nd	-	-	-	-	5.86	6.76	-	-	-
Sm	-	-	-	-	0.69	0.85	-	-	-
Eu	-	-	-	-	0.41	0.32	-	-	-
Gd	-	-	-	-	0.38	0.55	-	-	-
Tb	-	-	-	-	0.02	0.07	-	-	-
Dy	-	-	-	-	0.07	0.39	-	-	-
Y	2.4	<1.0	1.3	1.3	<1.0	4.1	2.6	1.7	2.6
Ho	-	-	-	-	0.01	0.08	-	-	-
Er	-	-	-	-	0.04	0.29	-	-	-
Tm	-	-	-	-	0.005	0.048	-	-	-
Yb	-	-	-	-	0.05	0.40	-	-	-
Lu	-	-	-	-	0.011	0.081	-	-	-
K	4898	4981	31130	2407	32620	10960	2158	24240	12290
P	87	31	66	44	44	35	31	214	327
Ti	578	152	292	112	185	149	207	1141	1520
Cr	24.4	<7	9.0	10.8	9.5	14.3	15.0	11.2	10.7
Ni	12	<3	<3	<3	<3	<3	6	<3	<3
Zr/Y	46.46	-	22.00	21.54	-	35.93	18.04	74.4	53.3
K/(K+Na)	0.05	0.08	0.37	0.03	0.42	0.09	0.04	0.30	0.16

Table 3-7: Geochemistry of Ungava granitoids (cont.)

Sample	LF-9	LF-9*	LF-29	LF-31	LF-41	LF-3	LF-19	LF-40	LF14-1
Easting	343297		343214	342205	343020	342065	343218	342992	344591
Northing	6549614		6550087	6548457	6549977	6549039	6551062	6549997	6552467
Suite	*Px-diorite*		*Px-tonalite*	*Px-tonalite*	*Px-tonalite*	*X-cutting*	*Px-tonalite*	*TTG*	*TTG*
Major elements (wt. %)									
SiO_2	54.04		63.05	66.00	68.31	77.21	70.58	66.26	66.68
TiO_2	1.24		0.29	0.62	0.47	0.07	0.43	0.48	0.50
Al_2O_3	16.70		17.04	16.06	15.92	12.66	15.60	16.26	16.55
MgO	3.99		2.46	1.53	1.25	0.91	0.88	1.33	1.39
FeO	8.28		4.15	4.12	3.19	0.90	2.04	3.69	3.39
MnO	0.14		0.10	0.07	0.05	0.02	0.02	0.05	0.05
CaO	7.82		5.87	4.01	3.94	3.14	3.85	4.22	3.83
Na_2O	4.28		4.69	4.53	4.37	3.71	4.31	4.49	4.39
K_2O	0.78		1.00	1.33	1.24	0.64	1.26	1.30	1.95
P_2O_5	0.30		0.08	0.19	0.15	0.01	0.07	0.17	0.13
LOI	0.46		0.29	0.44	0.47	0.40	0.67	0.76	0.41
Total	98.05		99.02	98.91	99.36	99.68	99.71	99.01	99.28
Trace elements (ppm)									
Cs	0.2	0.16	< 0.1	0.2	-	0.1	0.2	-	0.5
Rb	12.8	13.3	17.5	32.3	29.1	11.2	30.9	30.1	48.3
Ba	344.0	329.4	683.6	851.1	957.2	224.0	588.8	1099.0	600.0
Th	1.87	1.99	3.31	5.37	-	2.82	1.87	-	3.57
U	0.65	0.54	0.17	0.44	-	0.36	0.22	-	0.98
Nb	5.7	6.20	1.6	5.9	2.8	<0.3	2.5	2.2	5.0
Ta	0.23	0.24	0.04	0.2	-	0.04	0.09	-	0.23
Pb	8.4	7.8	10.7	11.9	10.7	10.2	10.1	11.1	13.8
Sr	483.2	501.9	358.6	371.8	358.0	358.0	399.0	386.4	352.1
Zr	85.9	107.3	74.7	190.2	202.9	9.6	141.5	223.8	175.4
Hf	2.5	2.55	1.9	4.5	-	0.5	3.5	-	5.6
Ga	20.9	24.0	20.0	20.2	18.5	15.1	17.3	19.1	20.2
Sc	24.5	22.53	18	9	7.1	2.4	4.1	7.5	5.9
V	188.4	194.1	42.9	48.2	45.8	19.1	45.7	51.9	55.0
Co	32	27	20	12	13	8	13	13	15
La	23.8	25.02	26.8	37.6	-	11.6	16.9	-	27.5
Ce	55.0	57.23	49.3	64.3	-	14.5	25.4	-	49.1
Pr	6.94	7.28	5.57	6.50	-	1.11	2.39	-	5.30
Nd	28.6	30.43	22.0	21.8	-	2.99	7.49	-	19.1
Sm	5.80	5.90	4.45	3.03	-	0.24	0.97	-	3.06
Eu	1.53	1.66	1.32	1.20	-	0.47	0.72	-	1.11
Gd	5.19	5.54	3.70	2.04	-	0.17	0.58	-	2.28
Tb	0.76	0.76	0.51	0.24	-	0.02	0.06	-	0.29
Dy	4.22	4.52	2.65	1.05	-	0.09	0.30	-	1.50
Y	22.5	26.44	12.5	5.7	4.5	<1.0	1.7	5.9	8.4
Ho	0.81	0.93	0.49	0.19	-	0.02	0.05	-	0.28
Er	2.25	2.46	1.26	0.53	-	0.05	0.13	-	0.79
Tm	0.31	0.35	0.17	0.076	-	0.006	0.017	-	0.11
Yb	1.96	2.10	0.99	0.48	-	0.05	0.12	-	0.79
Lu	0.31	0.28	0.15	0.080	-	0.009	0.024	-	0.13
K	6475		8302	11040	10290	5313	10460	10790	16190
P	1305		340	847	642	44	284	759	576
Ti	7434		1733	3723	2830	438	2596	2854	3004
Cr	119	112.3	62.5	26.3	19.2	33.3	13.7	17.7	11.2
Ni	53	56	22	<3	3	15	<3	<3	<3
Zr/Y	3.8	4.1	6.0	33.4	45.1	-	83.2	37.9	20.9
K/(K+Na)	0.11		0.12	0.16	0.16	0.10	0.16	0.16	0.23

Table 3-7: Geochemistry of Ungava granitoids (cont.)

Sample	LF8-1	LF-38	LF9-2	LF-30	LF3-5	LF1-2	LF-28	LF-18	*LF-18**
Easting	344561	342560	341723	341935	343684	346236	343401	343212	
Northing	6548907	6549856	6553358	6548344	6548783	6554749	6550086	6551048	
Suite	*TTG*	*TTG*	*TTG*	*TTG*	*TTG*	*TTG*	*TTG*	*TTG*	
Major elements (wt. %)									
SiO_2	67.54	68.67	68.93	69.64	70.13	70.32	70.62	71.30	
TiO_2	0.43	0.23	0.46	0.52	0.47	0.31	0.53	0.29	
Al_2O_3	15.93	17.77	15.76	15.32	14.92	16.04	15.61	15.37	
MgO	1.30	0.65	1.15	0.90	1.04	0.83	0.96	0.76	
FeO	2.93	1.50	2.93	2.91	2.83	1.82	2.00	2.07	
MnO	0.04	0.02	0.04	0.05	0.04	0.03	0.03	0.02	
CaO	3.90	4.23	3.56	3.60	3.34	3.45	3.74	3.30	
Na_2O	4.58	4.96	4.40	4.40	4.20	4.53	4.22	4.17	
K_2O	0.99	1.18	1.51	1.14	1.49	1.53	1.22	1.81	
P_2O_5	0.19	0.04	0.16	0.13	0.12	0.10	0.06	0.04	
LOI	1.28	0.35	0.36	0.58	0.74	0.72	0.51	0.49	
Total	99.12	99.61	99.26	99.18	99.33	99.68	99.50	99.63	
Trace elements (ppm)									
Cs	-	0.1	1.3	0.4	-	-	0.3	0.1	0.13
Rb	14.6	18.2	78.8	28.1	30.5	28.6	32.8	31.1	34.7
Ba	565.2	708.6	327.3	612.2	1138	649.0	881.5	1193	1288
Th	-	3.50	15.40	3.00	-	-	3.49	0.95	1.01
U	-	0.32	0.82	0.82	-	-	0.74	0.16	0.20
Nb	3.4	1.5	9.0	4.5	2.5	2.9	4.8	1.1	1.45
Ta	-	0.05	0.33	0.19	-	-	0.18	0.05	0.04
Pb	13.5	9.2	14.2	9.0	8.6	11.5	10.8	10.7	12.4
Sr	426.4	538.1	246.6	427.9	521.9	361.4	400.2	370.0	391.9
Zr	229.8	252.1	176.0	225.9	152.8	143.2	331.7	152.7	216.8
Hf	-	7.1	4.6	5.4	-	-	8.3	3.8	5.17
Ga	17.8	18.3	21.1	18.4	17.1	17.4	16.8	16.2	20.2
Sc	3.7	2.9	7.2	4.3	1.7	2.9	4.2	3	2.42
V	36.9	19.5	50.9	46.4	43.2	28.2	43.4	27.2	26.6
Co	11	9	13	7	16	10	11	8	6
La	-	22.9	37.9	34.5	-	-	18.7	14.9	13.2
Ce	-	33.3	66.7	51.9	-	-	27.6	20.1	19.2
Pr	-	2.84	7.00	5.05	-	-	2.46	1.74	1.66
Nd	-	8.43	23.8	16.3	-	-	7.63	5.1	5.0
Sm	-	0.89	3.97	2.07	-	-	0.91	0.59	0.57
Eu	-	0.97	0.67	1.16	-	-	0.71	0.74	0.82
Gd	-	0.61	2.77	1.29	-	-	0.64	0.37	0.36
Tb	-	0.05	0.31	0.14	-	-	0.06	0.04	0.04
Dy	-	0.26	1.34	0.67	-	-	0.31	0.20	0.19
Y	5.1	1.7	6.3	3.9	3.2	3.9	2.0	1.3	1.17
Ho	-	0.05	0.21	0.12	-	-	0.06	0.03	0.04
Er	-	0.14	0.53	0.31	-	-	0.20	0.10	0.13
Tm	-	0.023	0.069	0.046	-	-	0.032	0.016	0.017
Yb	-	0.17	0.42	0.33	-	-	0.24	0.13	0.16
Lu	-	0.031	0.069	0.060	-	-	0.043	0.021	0.024
K	8218	9796	12540	9464	12370	12700	10130	15030	
P	821	183	711	550	546	432	266	157	
Ti	2590	1379	2764	3123	2824	1876	3153	1757	
Cr	<7.0	7.8	<7.0	8.8	9.7	4.9	4.1	<7.0	3.8
Ni	<3	<3	<3	<3	<3	<3	<3	<3	4.8
Zr/Y	45.1	148.3	27.9	57.9	47.8	36.7	165.9	117.5	185.3
K/(K+Na)	0.12	0.14	0.18	0.15	0.19	0.18	0.16	0.22	

Table 3-7: Geochemistry of Ungava granitoids (cont.)

Sample	LF8-4	LF8-3	LF-10	LF9-4	LF-12	LF-22	LF-36	PT-1	PT-2
Easting	343943*	343943*	343310*	341965*	343262*	343208*	342653*	360413	360427
Northing	6548858	6548858	6549475	6552747	6550454	6551065	6549911	6470816	6470827
Suite	*TTG*	*TTG*	*TTG*	*TTG*	*pegmatite*	*pegmatite*	*pegmatite*	*GGM*	*Px-diorite*
Major elements (wt. %)									
SiO_2	71.43	71.62	71.90	74.79	72.44	70.85	75.69	71.84	53.08
TiO_2	0.30	0.25	0.32	0.19	0.13	0.32	0.08	0.12	0.74
Al_2O_3	15.90	15.99	15.13	13.75	15.07	15.14	12.93	15.84	19.44
MgO	0.56	0.55	0.64	0.52	0.76	1.85	0.10	0.53	3.28
FeO	1.37	1.34	1.46	1.25	0.64	1.75	0.70	0.67	9.10
MnO	0.02	0.02	0.02	0.02	0.02	0.03	0.01	0.01	0.11
CaO	3.28	3.37	1.45	0.66	1.85	2.82	0.58	2.13	8.05
Na_2O	4.64	4.72	6.20	4.00	4.27	4.57	2.12	4.49	4.05
K_2O	1.84	1.47	1.23	3.81	3.55	1.36	7.18	3.59	0.72
P_2O_5	0.08	0.05	0.08	0.03	0.06	0.04	0.01	0.04	0.33
LOI	0.30	0.33	1.13	0.72	0.63	0.60	0.22	0.48	0.25
Total	99.72	99.71	99.56	99.74	99.41	99.35	99.62	99.75	99.16
Trace elements (ppm)									
Cs	0.2	-	-	-	0.2	0.8	-	-	-
Rb	32.5	27.6	37.2	81.6	67.3	57.7	143.5	58.9	9.4
Ba	1149	866.2	400.4	1031	3383	609.9	2513	1348	293.7
Th	20.20	-	-	-	141	111	-	-	-
U	0.51	-	-	-	0.54	4.30	-	-	-
Nb	4.8	2.2	4.4	3.3	0.8	5.0	<0.3	1.3	1.6
Ta	0.24	-	-	-	0.04	0.35	-	-	-
Pb	17.0	14.8	6.0	7.3	35.4	28.0	25.4	21.0	6.4
Sr	507.3	516.4	236.4	126.5	458.0	389.5	355.3	570.1	851.7
Zr	155.1	132.7	254.3	88.2	136.0	225.9	27.2	41.2	18.4
Hf	4.4	-	-	-	3.3	6.1	-	-	-
Ga	16.2	17.0	14.7	13.9	11.0	17.2	10.0	15.7	23.8
Sc	3.3	2.2	2.3	2.2	<1.0	2.3	1.4	<1.0	14.5
V	11.2	17.4	23.0	14.3	<7.0	30.3	3.8	11.9	199.1
Co	5	14	9	8	9	12	8	<10	27
La	50.2	-	-	-	202.0	127.0	-	-	-
Ce	82.4	-	-	-	336.0	214.0	-	-	-
Pr	7.64	-	-	-	30.5	19.2	-	-	-
Nd	23.2	-	-	-	93.6	58.4	-	-	-
Sm	2.66	-	-	-	8.34	5.40	-	-	-
Eu	0.90	-	-	-	0.85	0.64	-	-	-
Gd	1.30	-	-	-	3.55	2.28	-	-	-
Tb	0.14	-	-	-	0.21	0.15	-	-	-
Dy	0.66	-	-	-	0.85	0.63	-	-	-
Y	4.0	2.4	5.3	1.7	3.2	2.8	<1.0	1.0	6.5
Ho	0.11	-	-	-	0.10	0.09	-	-	-
Er	0.31	-	-	-	0.21	0.23	-	-	-
Tm	0.048	-	-	-	0.025	0.034	-	-	-
Yb	0.35	-	-	-	0.15	0.23	-	-	-
Lu	0.059	-	-	-	0.023	0.040	-	-	-
K	15270	12200	10210	31630	29470	11290	59600	29800	5977
P	332	223	358	140	249	183	61	170.2	1458
Ti	1799	1511	1930	1127	755	1936	504	722.4	4453
Cr	<7.0	10.7	<7.0	<7.0	<7.0	52.1	<7.0	17.9	22.9
Ni	<3	<3	<3	<3	6	41	<3	10	12
Zr/Y	38.8	55.3	48.0	51.9	42.5	80.7	-	41.2	2.83
K/(K+Na)	0.21	0.17	0.12	0.39	0.35	0.16	0.69	0.34	0.10

Table 3-7: Geochemistry of Ungava granitoids (cont.)

Sample	**PT-3**	**PR-1**	**DH-02**
Easting	360431	354832	359282
Northing	6470848	6462489	6460855
Suite	*Px-*	*GGM*	*GGM*
Major elements (wt. %)			
SiO_2	54.66	71.03	71.45
TiO_2	0.49	0.18	0.06
Al_2O_3	17.51	15.54	15.91
MgO	5.28	0.69	0.54
FeO	8.29	1.49	1.60
MnO	0.17	0.02	0.01
CaO	8.04	2.3	2.76
Na_2O	3.44	4.13	4.53
K_2O	0.87	3.85	2.08
P_2O_5	0.03	0.07	0.12
LOI	0.33	0.53	0.91
Total	99.12	99.83	99.98
Trace elements (ppm)			
Cs	-	0.1	<0.1
Rb	18.4	91.7	25.6
Ba	311.2	1495	427.9
Th	-	8.09	0.54
U	-	0.25	0.28
Nb	1.6	2.6	0.4
Ta	-	0.08	<0.01
Pb	5.1	27.0	9.4
Sr	757.8	423.8	372.9
Zr	26.1	104.8	227.6
Hf	-	2.5	8.2
Ga	18.6	16.3	18.1
Sc	23.1	1.8	2.5
V	121.9	25.5	10.4
Co	26	<10	10
La	-	28.4	25.6
Ce	-	45.9	43.6
Pr	-	4.11	4.12
Nd	-	13.3	13.5
Sm	-	1.62	2.50
Eu	-	0.74	0.76
Gd	-	0.95	1.69
Tb	-	0.11	0.19
Dy	-	0.51	0.87
Y	5.2	3.0	4.4
Ho	-	0.09	0.14
Er	-	0.24	0.39
Tm	-	0.032	0.053
Yb	-	0.2	0.33
Lu	-	0.018	0.051
K	7222	31960	17270
P	118	305.5	546
Ti	2953	1109	381
Cr	62.8	20.2	17.1
Ni	29	<3	7
Zr/Y	5.02	34.9	51.7
K/(K+Na)	0.14	0.38	0.23

UTM locations are NAD27 zone 18N, with the exception of samples beginning with LF which were collected in zone 19N

Appendix 3-3: Geochemical Modelling

Estimation of the major element composition of the Q-suite parental magmas

The major element composition of the Q-suite magma was estimated using the MELTS algorithm of the program alphaMELTS (Ghiorso and Sack, 1995; Smith and Asimow, 2005). Equilibrium melting calculations in 1°C increments were performed on mesocumulate ultramafic rocks containing the cumulus assemblage of olivine + chromite ± orthopyroxene at a constant pressure (500 MPa) from f =0 until f =1 (where f =mass fraction of melt). To calculate the major element compositions of the transitional and subalkaline Q-suite parental magmas, we selected the most primitive (highest Mg-number, MgO, and compatible element contents) dunitic and harzburgitic samples (C1-16 and DH08-7), respectively, as the starting compositions in the melting calculations. The parental magma compositions, determined using this method, all fit the following criteria: 1) all intercumulus /oikocrystic phases were completely exhausted from the mineral assemblage, 2) calculated olivine Mg-numbers agree closely with the measured olivine Mg-numbers, 3) There is excellent agreement between the calculated melt Mg-number and the calculated olivine Mg-number ($K_D = 0.30 \pm 0.01$; c.f. Roeder and Emslie (1970), 4) The phase proportions calculated by alphaMELTS agree with the least-squares determined mineral modes. The final constraint was relaxed for the orthopyroxene-rich cumulates, in which the post-accumulation reaction-relationship olivine +$melt_1$ =opx +$melt_2$ may have increased the relative opx:olivine ratio.

The calculated melt compositions are relatively insensitive to H_2O contents, as illustrated in Fig 3-9. The bulk H_2O contents of 0.1 and 0.2 wt. % in the starting mesocumulate compositions result in the parental liquid H_2O concentrations of ~0.7 and

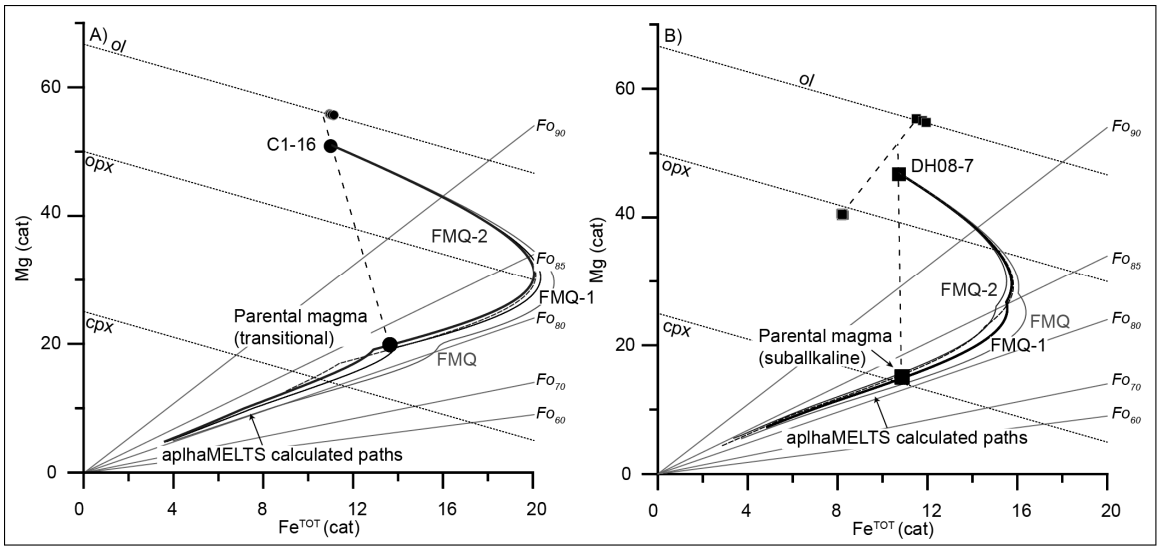

Figure 3-9: alphaMELTS Mg vs. Fe^{TOT} diagrams.
Mg vs. Fe^{TOT} diagrams in cation units illustrating the alphaMELTS-calculated melting paths of **A)** transitional and **B)** subalkaline Q-suite intrusions. Calculations performed at FMQ to FMQ-2 are shown for comparison, with the preferred solution depicted by the thick line. The effect of adding 0.2 wt. % H_2O to the starting cumulate composition at the optimal fO_2 buffer is shown by the dashed line, corresponding to ~ 1.6 and 1.0 wt. % H_2O in the parental magma. Also shown are the bulk cumulate compositions, the compositions of the constituent minerals and liquid-cumulate tielines.

~1.6 wt. % in the transitional magmas and ~0.5 and ~ 1.0 wt. % in the subalkaline magmas, respectively. The addition of ~ 1.5 wt. % H_2O to the Q-suite transitional magma reduces the stability of clinopyroxene, consequently lowering the calculated MgO and FeO^{TOT} contents by ~1.5 wt.% and increasing the calculated CaO by ~1 wt.%. The effect of adding 1 wt. % H_2O to the subalkaline magma is negligible.

The calculations were performed along a series of oxygen buffers (FMQ-2 $\leq fO_2 \leq$ FMQ+2) and compared to the petrographic observations and measured mineral compositions. Under relatively oxidizing conditions, the kink in the melting path of the transitional dunite C1-16 corresponding to the final disappearance of clinopyroxene as the intercumulus phase, occurs at very high Fe^{TOT} contents that are inconsistent with the observed phase proportions and olivine compositions. In contrast, melting paths at relatively reducing (FMQ-2) conditions are most consistent with the observed modes and measured olivine compositions (Table 3-8). The melt model for the subalkaline harzburgite yields the most consistent results at fO_2 value of FMQ-1.

The parental magmas to the transitional and subalkaline Q-suite intrusions, calculated using alphaMELTS are ferropicrites and Fe-rich high-Mg basalts, respectively (Table 3-9).

Estimation of the trace element compositions of the Q-suite parental magmas

The approximate trace-element composition of the Q-suite parental magmas were calculated following the methodology of Bédard (1994), using the partition coefficients listed in Table 3-10, and the crystal assemblage of olivine +clinopyroxene ±orthopyroxene +amphibole. Parental trace-element concentrations of the transitional and subalkaline Q-suite magmas, calculated for the trapped liquid fractions (TLF) of 0.025,

Table 3-8: Comparison of alphaMELTS-calculated parameters with observed and measured parameters

	C1-16[a]	C1-16[b]	DH08-7[a]	DH08-7[b]
Olivine	86.1	84 ± 4	70.3	63 ± 5
Spinel	1.0	2 ± 2	0.7	1 ± 0
Orthopyroxene	-	-	11.6	20 ± 8
Liquid / interstitial	12.9	14 ± 4	17.4	16 ± 6
Mg-number liquid	0.61	-	0.60	
Mg-number olivine	0.84	0.835	0.83	0.824
Calculated K_D	0.30	-	0.30	
FMQ	-2		-1	

[a] alphaMELTS calculated system coexisting with parental magma

[b] observed/measured parameters

Table 3-9: Reconstructed major element compositions of Q-suite magmas

	C1-16	DH08-7
SiO_2	46.5	47.9
TiO_2	0.6	0.6
Al_2O_3	6.6	14.8
Fe_2O_3	1.0	1.1
FeO	15.9	13.1
MgO	14.0	10.8
CaO	13.9	8.4
Na_2O	0.9	1.6
K_2O	0.2	1.4
P_2O_5	0.2	0.2
Cr_2O_3	0.2	0.11
NiO	0.02	0.02
Total	100.0	100.0
Fe^{3+}/Fe^{tot}	0.05	0.07
Fo	84.0	83.1
Fo meas.	83.5	82.4

Table 3-10: D-values used for parental liquid calculations

Element	Olivine	OPX	CPX	Amphibole
Th	0.001	0.002	0.0003	0.006
U	0.001	0.002	0.0004	0.006
Nb	0.0004	0.012	0.05	0.16
La	0.00003	0.001	0.054	0.092
Ce	0.0001	0.002	0.098	0.16
Pr	0.0003	0.004	0.15	0.26
Nd	0.0004	0.006	0.21	0.36
Sm	0.0015	0.015	0.26	0.49
Zr	0.007	0.014	0.26	0.21
Ti	0.027	0.13	0.10	1.0
Eu	0.0025	0.020	0.31	0.61
Gd	0.0040	0.027	0.30	0.69
Tb	0.0062	0.036	0.31	0.66
Dy	0.0094	0.046	0.33	0.63
Y	0.012	0.054	0.30	0.62
Ho	0.013	0.058	0.31	0.58
Er	0.018	0.070	0.30	0.64
Tm	0.024	0.083	0.41	0.58
Yb	0.029	0.095	0.28	0.52
Lu	0.035	0.11	0.28	0.31

Olivine and orthopyroxene D-values calculated after Bédard (2005, 2007) for a magma with approximate MgO content of 12 wt. %. Clinopyroxene D-values after McKenzie and O'Nions (1991). Amphibole D-values after Tiepolo et al. (2007). calculated for an estimated X_{NF}/X_{TOT} ~ 0.52 (where X_{NF} = sum of molar fractions of network forming cations and X_{TOT} = sum of all cations).

Table 3-11: Calculated transitional Q-suite parental magma trace element compositions

	C1-50 (dunite)			C1-39 (wehrlite)		
TLF	**0.025**	**0.050**	**0.10**	**0.025**	**0.050**	**0.10**
Th	3.1	1.6	0.8	3.4	1.8	0.9
U	2.3	1.2	0.6	1.1	0.6	0.3
Nb	-	-	-	7.7	6.3	4.6
La	14.0	8.2	4.5	33.8	25.4	16.9
Ce	41.5	26.6	15.5	72.7	60.8	45.7
Pr	6.2	4.3	2.7	10.2	10.1	9.9
Nd	28.7	21.3	14.0	43.5	40.8	36.3
Sm	8.1	6.3	4.3	10.0	9.7	9.2
Zr	32.1	24.9	17.5	65.4	58.5	48.3
Ti	13200	9720	6360	7540	8240	10140
Eu	1.9	1.5	1.1	2.1	2.1	2.1
Gd	6.3	5.1	3.6	7.0	7.1	7.2
Tb	1.0	0.8	0.6	1.0	1.0	1.0
Dy	4.4	3.6	2.7	4.9	4.9	4.9
Y	21.0	17.1	12.4	26.3	26.2	25.8
Ho	0.8	0.6	0.5	1.0	1.0	1.0
Er	2.2	1.8	1.3	2.7	2.7	2.7
Tm	0.3	0.2	0.2	0.3	0.3	0.3
Yb	2.0	1.6	1.2	2.6	2.5	2.4
Lu	0.3	0.2	0.2	0.5	0.5	0.4
Zr/Y	1.5	1.45	1.40	2.5	2.2	1.9
Ce/Yb	21.0	16.2	12.7	28.3	24.2	19.1

Estimated mineral modes for C1-50 and C1-39 are $Ol_{0.81}Cpx_{0.14}Amph_{0.05}$ and $Ol_{0.36}Cpx_{0.40}Amph_{0.24}$, respectively.

Table 3-12: Calculated subalkaline Q-suite parental magma trace element compositions

	DH08-7 (harz.)			DH-09 (per.)			GR-2 (web.)				GR2-1 (web.)			
TLF	0.025	0.050	0.10	0.025	0.050	0.10	0.025	0.050	0.10	0.18	0.025	0.050	0.10	0.18
Th	28.3	14.8	7.5	15.4	8.0	4.1	18.8	9.9	5.1	2.9	30.4	16.0	8.2	4.7
U	6.8	3.5	1.8	2.6	1.4	0.7	5.0	2.6	1.3	0.8	4.8	2.5	1.3	0.7
Nb	14.8	10.7	6.6	14.6	10.6	6.4	8.2	6.9	5.3	3.9	6.0	5.1	3.9	2.9
La	108.7	68.4	38.6	81.5	52.4	29.9	85.9	66.7	46.2	31.6	85.8	67.1	46.7	32.1
Ce	178.2	126.0	77.2	120.4	87.2	54.0	135	115.9	90.3	67.9	122.8	106.0	83.1	62.8
Pr	15.5	12.3	8.3	9.6	7.7	5.3	12.7	11.7	10.0	8.2	10.9	10.0	8.6	7.1
Nd	53.2	45.6	33.3	28.7	24.9	18.3	44.8	42.5	38.6	33.9	41.1	39.1	35.6	31.4
Sm	7.7	7.2	5.8	5.0	4.7	3.7	8.3	8.1	7.8	7.3	7.9	7.7	7.4	6.9
Zr	204.4	153.3	102.6	100.5	79.0	55.6	140.8	127.6	107.5	86.9	129.0	117.4	99.6	81.1
Ti	3400	3890	4180	2460	2850	2780	4530	4800	5470	6920	4540	4810	5480	6925
Eu	1.6	1.6	1.4	0.9	0.9	0.8	2.0	2.0	2.0	1.9	1.8	1.8	1.8	1.8
Gd	4.9	4.9	4.5	3.1	3.1	2.7	6.2	6.2	6.3	6.4	5.4	5.4	5.5	5.6
Tb	0.7	0.7	0.6	0.4	0.4	0.3	0.9	0.9	0.9	0.9	0.8	0.8	0.8	0.8
Dy	3.6	3,6	3.1	2.1	2.1	1.8	4.5	4.5	4.4	4.4	4.2	4.2	4.2	4.1
Y	20.9	20.6	18.1	13.1	12.9	11.1	22.0	21.9	21.7	21.4	22.7	22.6	22.4	22.1
Ho	0.8	0.7	0.6	0.4	0.4	0.3	0.9	0.9	0.9	0.9	0.9	0.9	0.8	0.8
Er	1.9	1.8	1.6	1.1	1.1	0.9	2.6	2.6	2.6	2.6	2.3	2.3	2.3	2.3
Tm	0.3	0.3	0.3	0.1	0.1	0.1	0.4	0.4	0.3	0.3	0.3	0.3	0.3	0.2
Yb	2.0	1.9	1.6	1.0	1.0	0.8	2.2	2.2	2.1	2.0	2.2	2.2	2.1	2.0
Lu	0.2	0.2	0.1	0.2	0.2	0.1	0.4	0.4	0.4	0.3	0.4	0.3	0.3	0.3
Zr/Y	9.8	7.4	5.7	7.7	6.1	5.0	6.4	5.8	5.0	4.1	5.7	5.2	4.4	3.7
Ce/Y	91.2	67.5	48.2	117.6	88.9	65.4	60.3	52.7	42.6	33.7	55.8	48.9	39.7	31.6

Estimated mineral modes for DH08-7, DH-09, GR-2 and GR2-1 are $Ol_{0.63}Opx_{0.20}Amph_{0.16}$, $Ol_{0.59}Opx_{0.19}Cpx_{0.07}Amph_{0.15}$, $Ol_{0.02}Opx_{0.23}Cpx_{0.40}Amph_{0.35}$ and $Opx_{0.21}Cpx_{0.44}Amph_{0.35}$, respectively.

Table 3-13: Fractionating assemblages and mineral modes

Q magma type	Assemblage	Olivine	Opx	Cpx	Amph.	Plag.
Subalkaline*	Harzburgite	0.75	0.25	-	-	-
	Websterite[a]	0.10	0.25	0.65	-	-
	Gabbronorite[b]	-	0.10	0.10	0.45	0.35
	Gabbronorite[c]	-	0.25	0.15	0.20	0.40

[a] websterite mode was corrected to the amphibole-free assemblage by applying the backstripping equation 2 amphibole = 1 TLF + 1 clinopyroxene (Bédard, 1994).

[b] Least-squares calculated mode of amphibole-rich sample GR-10.

[c] Least-squares calculated mode of amphibole-poor sample GR-13.

0.05 and 0.10 are shown in Tables 3-11 and 3-12, respectively. Amphibole was treated as a non-cumulus product of the reaction between the TLF and clinopyroxene in the ultramafic rocks; the cumulus mode was corrected accordingly, assuming the reaction: TLF = 2 amphibole – 1 clinopyroxene (Bédard, 1994). At greater melt fractions, following the complete exhaustion of amphibole, TLF is backstripped according to the equation TLF = 0.33 olivine + 0.67 clinopyroxene.

The calculated Q-suite parental compositions are plotted in Fig. 3-10. The calculated parental liquids for most of the subalkaline ultramafic samples display higher Zr/Y ratios than the most primitive marginal facies samples. This discrepancy may be explained in two ways. First, the parental liquids are backstripped from depleted ultramafic samples in which Zr concentrations range from 10-30 ppm and Y is < 10 ppm. As emphasized by Bédard (1994), analytical error is the largest source of uncertainty in the trapped-liquid backstripping technique, and its effects are most pronounced for samples with the lowest trace element concentrations. Second, the technique assumes the closed-system behaviour in which all of the minerals equilibrated with the same melt. The migration of trace-element enriched fluids through the Q-suite cumulates during the final stages of solidification may negate this assumption.

Because the Zr/Y ratios of the calculated parental liquids are higher than those of the most primitive marginal pyroxene-diorite, we selected the trace-element composition of sample GR2-8 for the starting trace-element composition in the AFC modeling of the Gladel River margin. This least evolved marginal sample represents an appropriate starting composition in the assessment of the rates of assimilation required to generate the increase in Zr/Y ratios across the margin of the Gladel River intrusion.

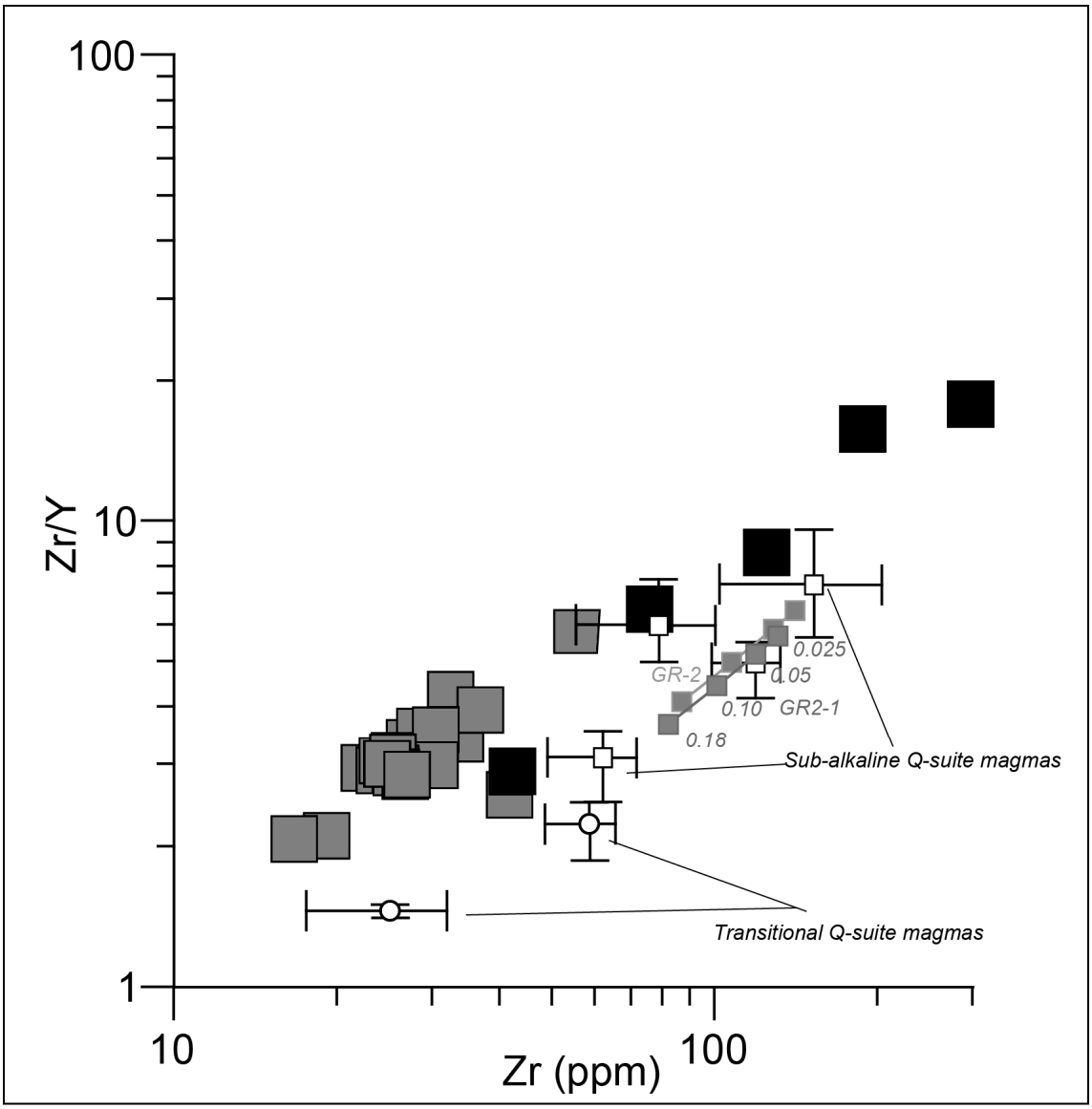

Figure 3-10: Zr/Y vs. Zr diagram of Gladel River intrusion rocks and calculated parental compositions.

Zr/Y vs. Zr showing the calculated trace-element compositions of the Q-suite parental magmas at 0.05 TLF (white circles –transitional magmas; white squares – subalkaline magmas; error bars include the range between 0.025 and 0.10 TLF). Calculations from two websteritic samples from the Gladel River intrusions at TLF values of 0.025, 0.05, 0.10 and 0.18 (the melt fraction at which amphibole is completely removed from the intercumulus assemblage) are shown by small grey squares. Large black squares: marginal rocks. Grey squares: Gladel River intrusion mafic and ultramafic cumulate rocks.

Mass-balance constrained AFC models

Fractional crystallization of the minerals present in the Gladel River intrusion does not provide an adequate mechanism of driving the Zr/Y ratio of the marginal rocks from ~3.5 to ~ 18, unless unreasonable proportion of amphibole is present in the crystallizing assemblage (Fig. 3-11). Amphibole dominated fractional crystallization is, however, inconsistent with both petrographic observations and major element constraints, which would require very high degrees of fractional crystallization ($\leq$ 90%) to drive the SiO_2 concentrations of the marginal rocks from ~52 wt. % to > 65 wt%.

Simultaneous assimilation and fractional crystallization was modelled using the program Xstaln. The program was used to calculate the stepwise evolution of the major and trace composition of the melt and the key parameters such as the melt temperature, Mg-number, and network-former/total cation ratios, which are known to influence mineral-liquid partitioning (Wood and Blundy, 2001; Bédard, 2005; Tiepolo et al., 2007; Francis and Minarik, 2008).

Crystallizing assemblages

Three crystallizing stages (Table 3-13) were simulated in the mass-balance model, using the subalkaline Q-suite parental magma as the starting composition. The initial harzburgitic ($olivine_{0.75}$ + $opx_{0.25}$) crystallizing assemblage was followed by websteritic ($olivine_{0.1}$ + $opx_{0.25}$ +$cpx_{0.65}$), and finally gabbronoritic assemblages. Given its interstitial habit and tendency to replace clinopyroxene in the ultramafic rocks, the first two modeling stages were free of amphibole. AFC calculations using a harzburgitic assemblage were carried out until the liquid composition attained an Mg-Fe ratio that would crystallize olivine/orthopyroxene with an Mg-number of 0.78, assuming a K_D

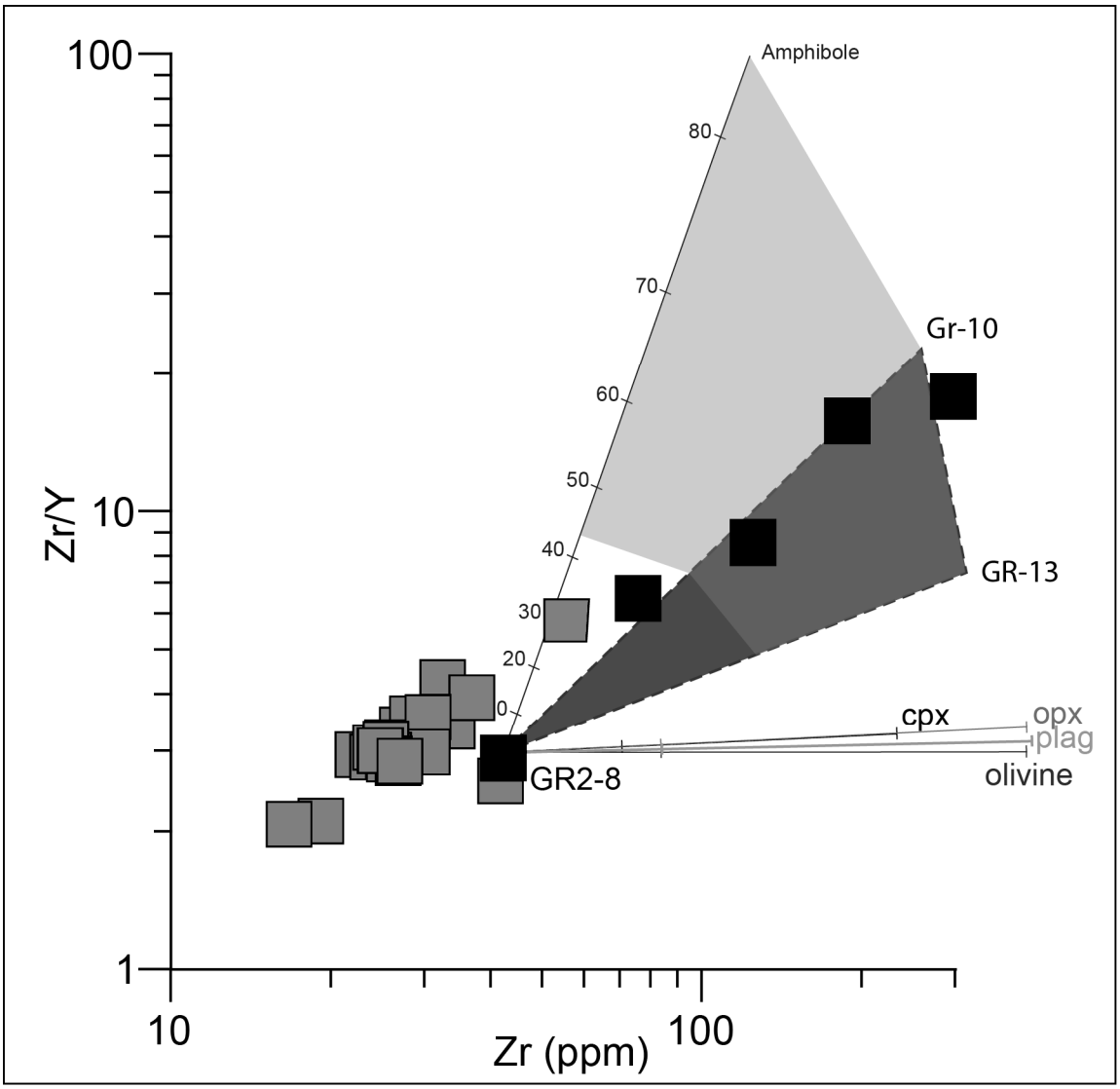

Figure 3-11: Zr/Y vs. Zr plot showing illustrating the limits of fractional crystallization. Zr/Y vs. Zr plot of the liquid evolution paths derived by fractional crystallization of olivine, orthopyroxene, clinopyroxene, plagioclase (ticks only shown for 50 % and 90% crystallization), and amphibole from pyroxene-bearing diorite GR2-8. Amphibole-only path was calculated assuming the $X^{NF}/X^{TOT} = 0.7$ using the equations of Tiepolo et al. (2007). The dark grey triangle represents the range of compositions produced by fractional crystallization of gabbronoritic compositions intermediate between amphibole-rich sample GR-10 ($opx_{12}cpx_{08}amph_{45}plag_{34}$) and a more typical gabbronorite GR-13 ($opx_{24}cpx_{16}amph_{20}plag_{40}$). The light grey shaded field that overlaps the dark grey triangle depicts unrealistic solutions in which no MgO remains in the melt. Other symbols as in Fig. 3-10.

value of 0.3. The websteritic stage was simulated until the liquid reached equilibrium with orthopyroxene having an Mg-number of 0.73.

The fraction of cumulus amphibole in the gabbronorites is difficult to constrain. Consequently, two different assemblages, corresponding to samples GR-10 ($opx_{0.10}cpx_{0.10}amph_{0.40}plag_{0.30}mt_{0.10}$) and GR-13 ($opx_{0.20}cpx_{0.15}amph_{0.15}$ $plag_{0.40}mt_{0.10}$) were used in the final gabbronoritic stage of the model, in order to asses the sensitivity of the model to amphibole crystallization. The third stage was modelled until MgO reached the concentration of the most evolved marginal facies pyroxene-granodiorite (~1.5 wt. % MgO).

Compositions of the crystallizing phases

The Xstaln program accounts for the influence of the changing liquid composition on the composition of the minerals being fractionated (e.g. (Beattie et al., 1991; Beattie, 1993; Hart and Davis, 1978; Grove et al., 1992)). In order to model amphibole fractionation, the observed compositions in the Gladel River and the nearby Dash intrusions were parameterized against the orthopyroxene Mg-number (Figures 3-12 and 3-13). The partition coefficients for the fractionating minerals used in the calculations are listed in Table 3-14.

Figure 3-14 shows the comparison of results obtained by varying the proportion of amphibole in the gabbroic assemblage from 0.15 to 0.40. Two sets of curves are presented for each assemblage. The first set of curves was calculated using the parametrization of Tiepolo et al. (2007), which accounts for the strong increase in the compatibility of HREE and Y in amphibole with the increased degree of melt polymerization. The second set of curves is calculated for the case of strongly

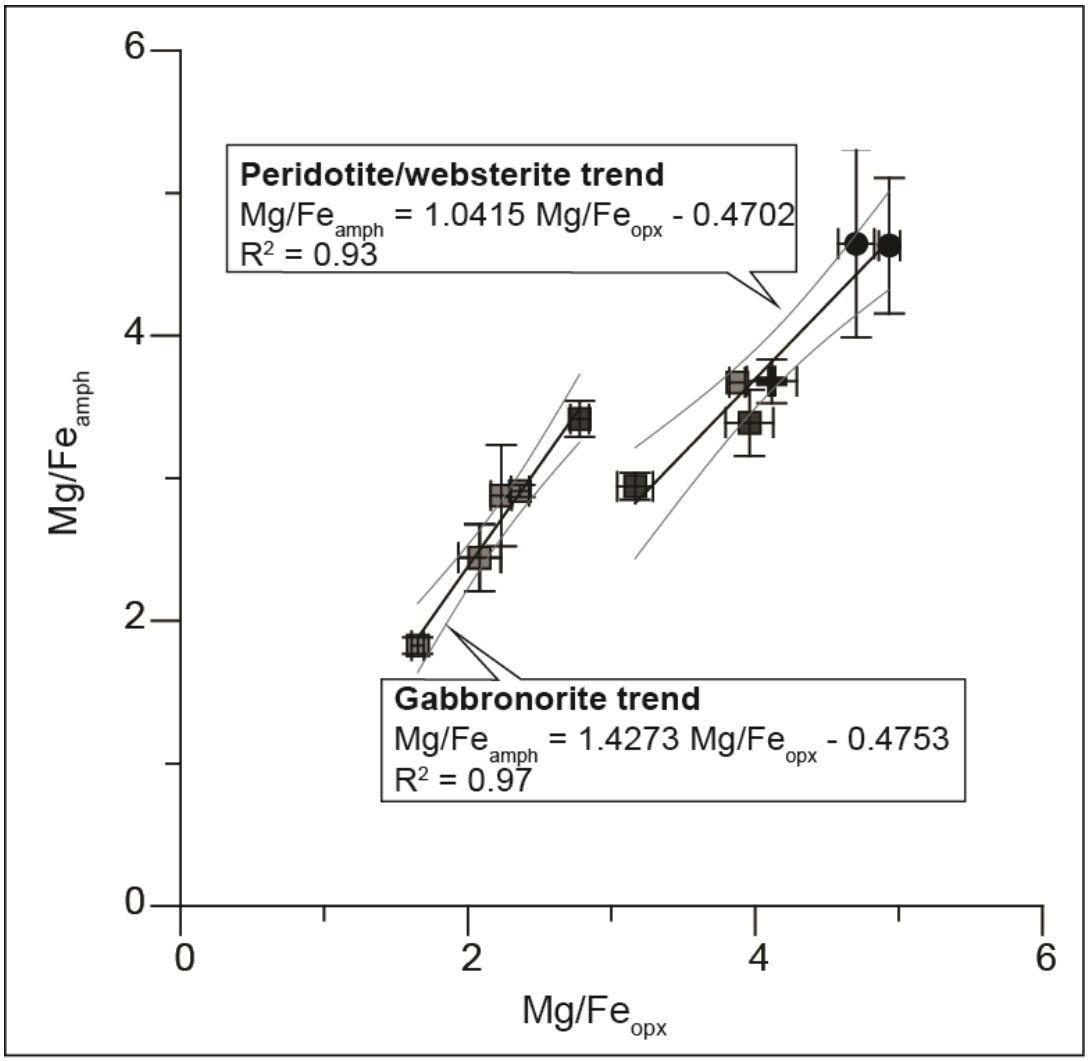

Figure 3-12: Measured Mg/Fe ratios of coexisting amphibole and orthopyroxene in samples from the western Hudson Bay Terrane.
The magnesiohornblende (step 3) trend was incorporated into the AFC model using the orthopyroxene parametrization equations. The error bars indicate the 2 s.d. deviation from the analysis average.

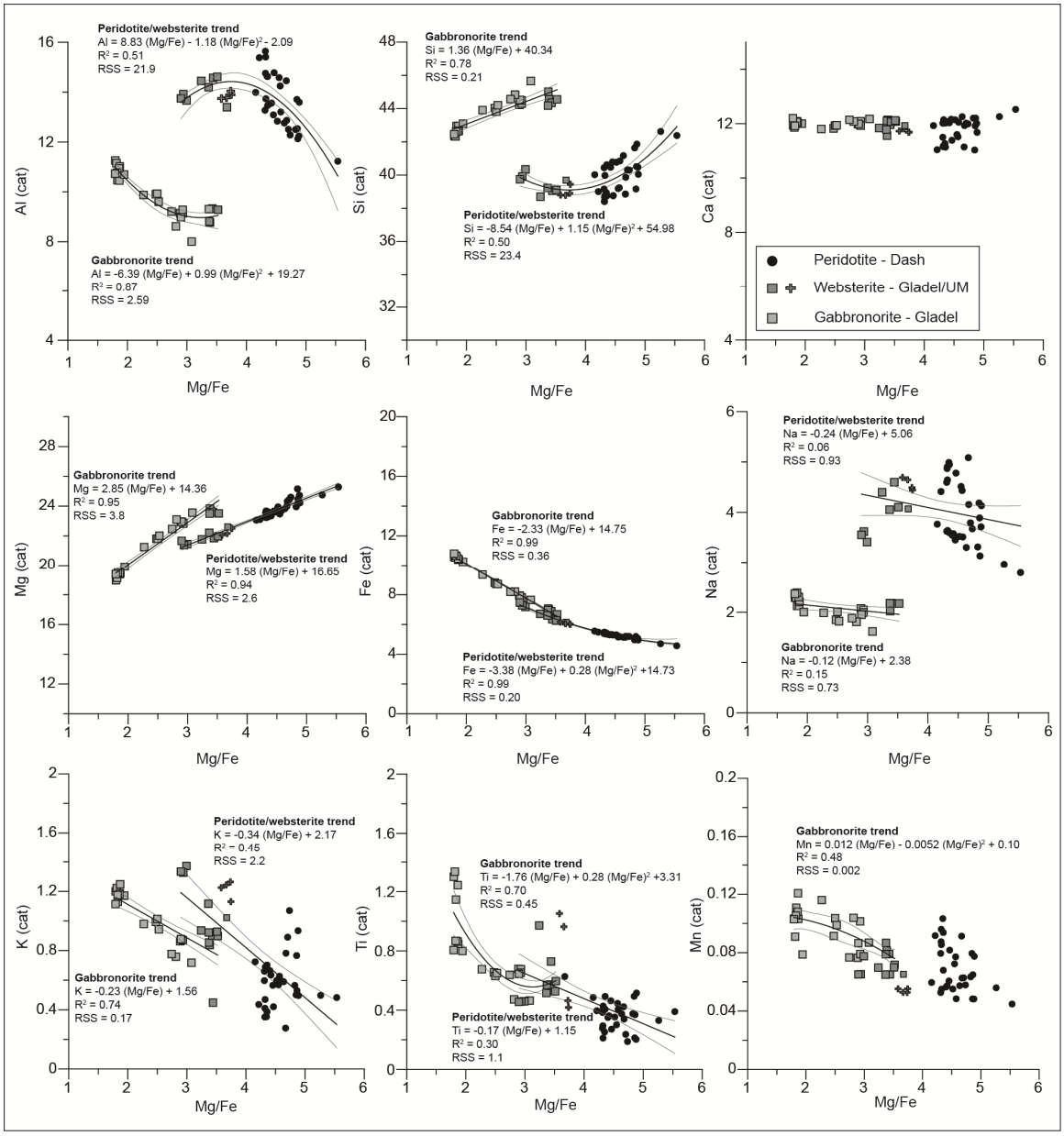

Figure 3-13: Amphibole compositional dependency on Mg/Fe ratio.
Amphibole cation abundances normalized to 100 vs. amphibole Mg/Fe ratio. The calculated regressions (black lines) were used in AFC simulations using the program Xstaln. The light grey lines indicate the field of the 95 % confidence interval.

Table 3-14: D-values used in AFC modelling

Element	Olivine[a]	OPX[b]	CPX[c]	Amphibole[d]	Plagioclase[e]
90Th	B1	B2	0.002	T	0.040
92U	B1	B2	0.002	T	0.040
41Nb	B1	B2	0.005	T	0.009
57La	B1	B2	W&B	T	0.21
58Ce	B1	B2	W&B	T	0.15
59Pr	B1	B2	W&B	T	0.14
60Nd	B1	B2	W&B	T	0.16
61Sm	B1	B2	W&B	T	0.14
40Zr	B1	B2	0.12	T	0.002
63Eu	B1	B2	W&B	T	0.14
64Gd	B1	B2	W&B	T	0.06
65Tb	B1	B2	W&B	T	0.05
66Dy	B1	B2	W&B	T	0.03
39Y	B1	B2	W&B	T	0.055
67Ho	B1	B2	W&B	T	0.025
68Er	B1	B2	W&B	T	0.02
69Tm	B1	B2	W&B	T	0.015
70Yb	B1	B2	W&B	T	0.010
71Lu	B1	B2	W&B	T	0.009

[a] Parametrized olivine D-values from Bédard (2005).

[b] Parametrized orthopyroxene D-values from Bédard (2007).

[c] Parametrized clinopyroxene values calculated using the lattice strain model (Wood and Blundy, 1997), unless noted otherwise. r_o value of 1.01 Å was assigned as the radius of the M site in clinopyroxene (Francis and Minarik, 2008). In the absence of reliable compositional data for clinopyroxene, we assigned a value of 0.5 to D_o^{3+} (the strain-free partition coefficient for a trivalent cation).

[d] Parametrized amphibole D-values from Tiepolo et al. (2007).

[e] Plagioclase D-values estimated/extrapolated for $X_{An} = 0.70$ from Bindeman et al. (1998) and Bindeman and Davis (2000).

polymerized melt (X_{NF}/X_{TOT} =0.7), in which HREE are strongly compatible (D_Y ~2) and kept constant throughout the calculation. The calculations indicate that the rate of assimilation exerts the strongest control on the Zr/Y ratio. Although higher Zr/Y ratios are attained with increased amphibole fraction, the effect is minor for X_{amph}<0.40. The choice of constant D_{HREE} vs. variable D_{HREE} (as per Tiepolo et al. (2007)) has little importance at high r-values where X_{NF} increases rapidly with progressive AFC.

AFC modelling using alphaMELTS

We used the thermodynamics-based alphaMELTS software (Ghiorso and Sack, 1995; Smith and Asimow, 2005) in order to investigate the range of initial contaminant temperatures required for the indicated assimilation rates. We performed simultaneous assimilation and fractional crystallization calculations at a pressure of 500 MPa in isenthalpic mode, at temperatures of 700, 800, and 900 °C. The calculations were performed over 200 iterations, and 1 g of contaminant was added per cycle to the initial magma mass of 100 g. The initial magma composition, previously used in the mass-balance AFC modelling, was assigned an H_2O content of 1.5 wt. %, corresponding to upper limit for the Neoarchean mafic volcanic sequences of the Ungava craton (Maurice et al. (2009). An fO_2 buffer value of FMQ-1 was assigned to the initial magma, consistent with the value used in the earlier modeling of subalkaline parental magma composition.

The contaminant, composed of ~62 % plagioclase, 30 % quartz and 8% biotite has the major element composition of the median trondhjemite used in the mass-balance calculations, and was initially buffered at fO_2 = FMQ+2. The effect of H_2O on the AFC models was evaluated by varying the parental magma's water content from 0.5 to 2.5 wt. % at 800°C (Fig. 3-15). The effect of adding or removing 1 wt. % H_2O to the initial

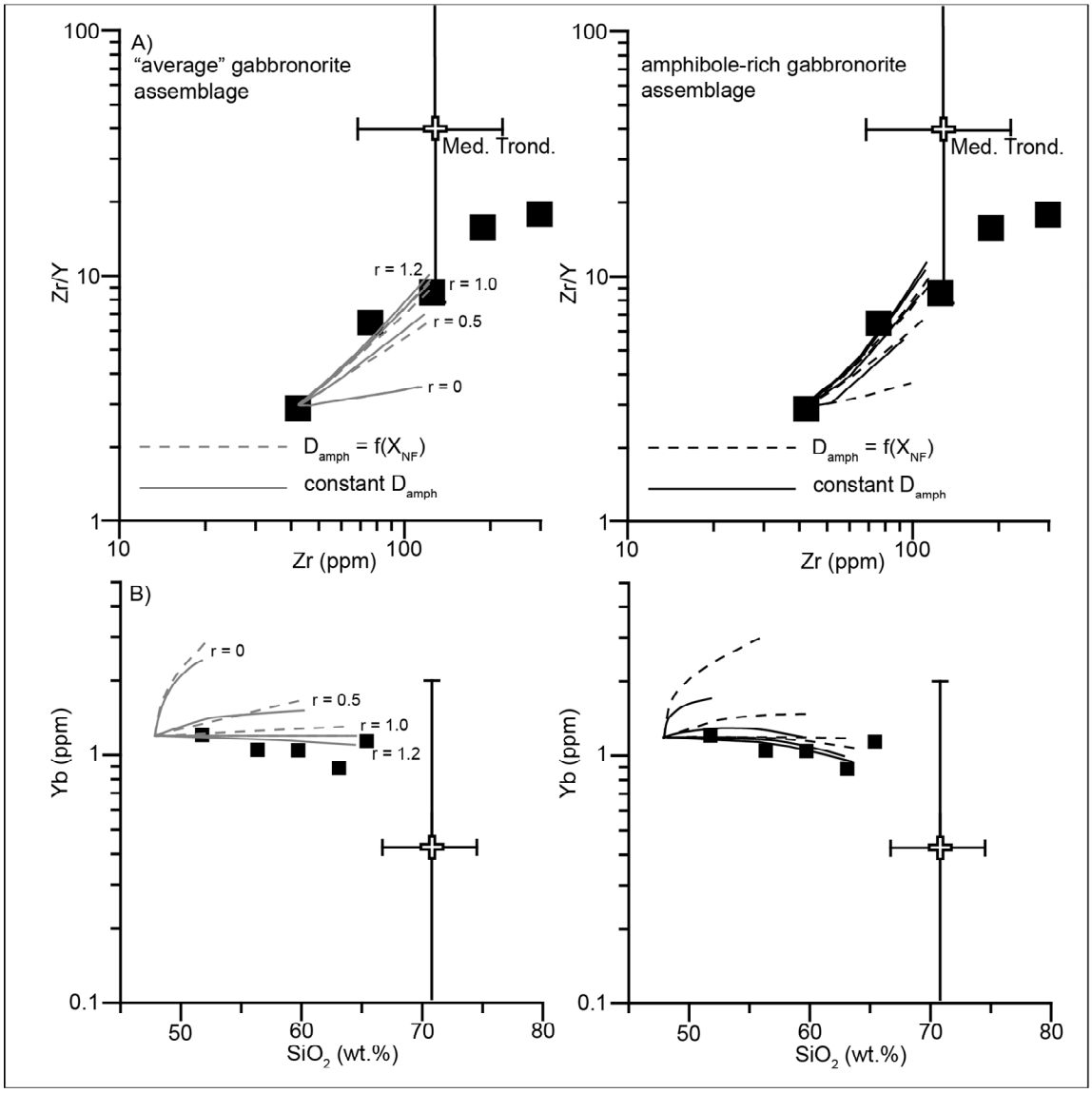

Figure 3-14: Sensitivity of Xstaln AFC models to amphibole fraction and composition. Comparison of model liquid compositions obtained using an average gabbronoritic fractionating assemblage ($opx_{20}cpx_{15}amph_{15}plag40mt_{10}$; grey curves) vs. those obtained using an amphibole-rich assemblage ($opx_{10}cpx_{10}amph_{40}plag_{30}mt_{10}$; black curves), during the 3rd stage of AFC calculation. Dashed lines represent compositions calculated using the melt polymerization dependency of D_i^{amph} of Tiepolo et al. (2007), whereas the solid lines were calculated using constant D_i^{amph} (D_{Zr} = 0.4, D_Y = 1.8, D_{Yb} =2.3). Results of AFC models with r-value set to 0 (pure FC), 0.5, 1.0 and 1.2 are shown. Median trondhjemite is the assimilant composition used in the models.

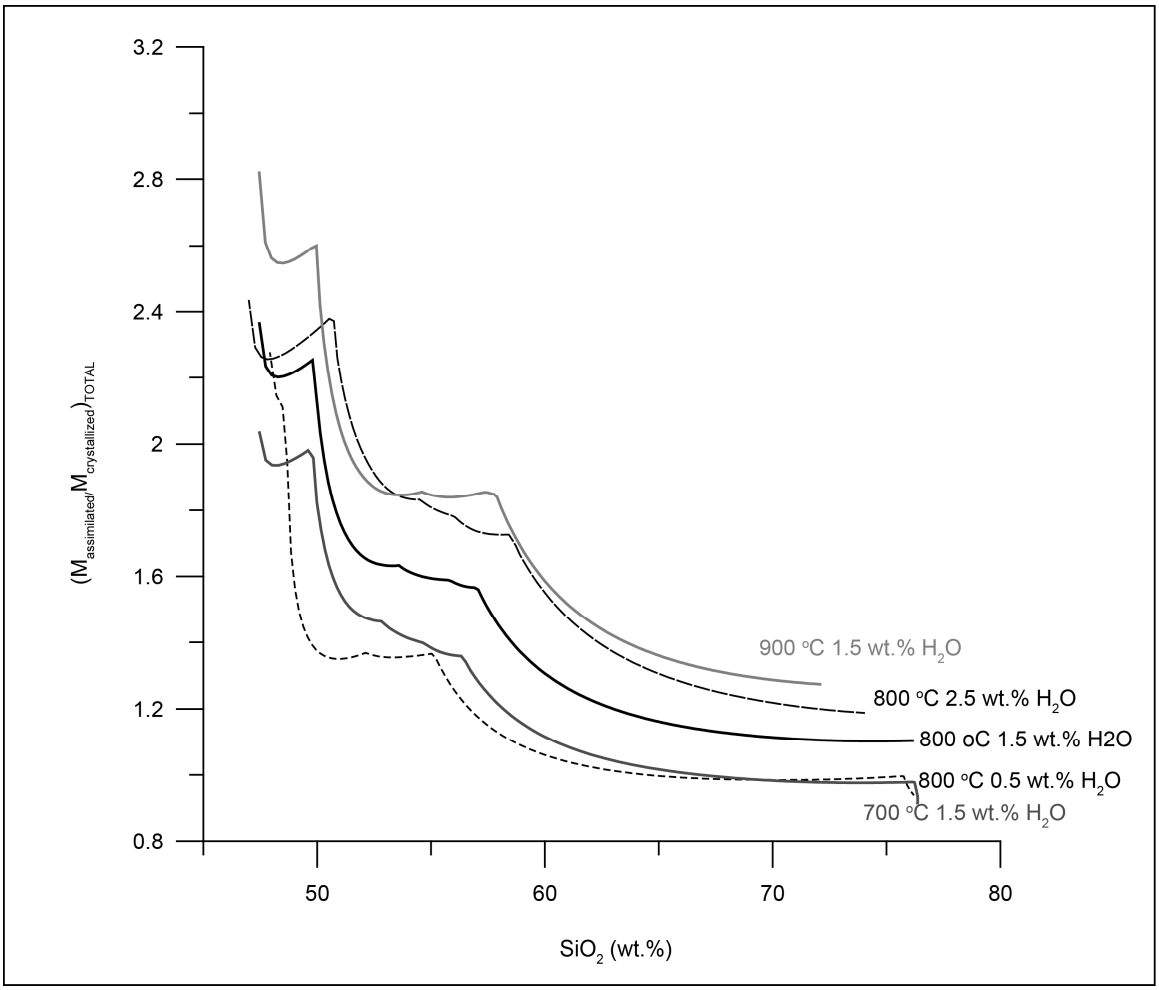

Figure 3-15: Sensitivity of alphaMELTS models to water content and initial contaminant temperature.

alphaMELTS modeling – comparison of calculated bulk r-values against SiO_2 (wt. %) as a function of parental magma water content and initial contaminant temperature. Upper solid light grey line – starting contaminant T = 900°C, starting parental magma = 1.5 wt.% H_2O; Lower solid dark grey line – starting contaminant T = 700°C, starting parental magma = 1.5 wt.% H_2O; solid black line (central) - starting contaminant T = 800°C, starting parental magma = 1.5 wt.%; long-dashed black line – starting contaminant T = 800°C, starting parental magma = 2.5 wt.%; short-dashed black line – starting contaminant T = 800°C, starting parental magma = 0.5 wt.%.

parental magma is comparable to a 100 °C increase or decrease in initial contaminant temperature, respectively.

Comparison of results obtained using the mass-balance program Xstaln with the results of alphaMELTS modelling, suggests that the inferred assimilation rates (r = 1-1.2) are most consistent with the initial contaminant temperature of 700 to 900°C.

References

Beattie, P., 1993. Olivine-melt and orthopyroxene-melt equilibria. Contributions to Mineralogy and Petrology 115, 103–111.

Beattie, P., Ford, C., and Russell, D., 1991. Partition coefficients for olivine-melt and orthopyroxene-melt systems. Contributions to Mineralogy and Petrology 109, 212–224.

Bédard, J.H., 1994. A procedure for calculating the equilibrium distribution of trace elements among the minerals of cumulate rocks, and the concentration of trace elements in the coexisting liquids. Chemical Geology 118, 143–153.

Bédard, J.H., 2005. Partitioning coefficients between olivine and silicate melts. Lithos 83, 394–419.

Bédard, J.H., 2007. Trace element partitioning coefficients between silicate melts and orthopyroxene: Parameterizations of D variations. Chemical Geology 244, 263–303.

Bindeman, I.N., and Davis, A.M., 2000. Trace element partitioning between plagioclase and melt: Investigation of dopant influence on partition behavior. Geochimica et Cosmochimica Acta 64, 2863–2878.

Bindeman, I.N., Davis, A.M., and Drake, M.J., 1998. Ion microprobe study of plagioclase-basalt partition experiments at natural concentration levels of trace elements. Geochimica et Cosmochimica Acta 62, 1175–1193.

Brandelik, A., 2009. CALCMIN – an EXCEL™ Visual Basic application for calculating mineral structural formulae from electron microprobe analyses. Comuters and Geosciences 35, 1540-1551.

Francis, D., and Minarik, W., 2008. Aluminum-dependent trace element partitioning in clinopyroxene. Contributions to Mineralogy and Petrology 156, 439–451.

Ghiorso, M.S., and Sack, R.O., 1995. Chemical mass transfer in magmatic processes IV. A revised and internally consistent thermodynamic model for the interpolation and extrapolation of liquid-solid equilibria in magmatic systems at elevated temperatures and pressures. Contributions to Mineralogy and Petrology 119, 197–212.

Grove, T.L., Kinzler, R., and Bryan, W.B., 1992. Fractionation of mid-ocean ridge basalt (MORB). Mantle flow and melt generation at mid-ocean ridges. *in* Phipps Morgan, J., Blackman, D.K., and Sinton, J.M. eds., Mantle flow and melt generation at mid-ocean ridges. Geophysical Monograph, American Geophysical Union 71, 281–310.

Hart, S.R., and Davis, K.E., 1978. Nickel partitioning between olivine and silicate melt. Earth and Planetary Science Letters 40, 203–219.

Maurice, C., David, J., Bédard, J.H., and Francis, D., 2009. Evidence for a widespread mafic cover sequence and its implications for continental growth in the Northeastern Superior Province. Precambrian Research 168, 45–65.

McKenzie, D., and O'Nions, R.K., 1991. Partial melt distributions from inversion of rare earth element concentrations. Journal of Petrology 32, 1021–1091.

Roeder, P.L., and Emslie, R.F., 1970. Olivine-Liquid Equilibrium. Contributions to Mineralogy and Petrology 29, 275–289.

Smith, P.M., and Asimow, P.D., 2005. Adiabat_1ph: A new public front-end to the MELTS, pMELTS, and pHMELTS models. Geochemistry Geophysics Geosystems 6, 1–8.

Tiepolo, M., Oberti, R., Zanetti, A., Vannucci, R., and Foley, S.F., 2007. Trace-Element Partitioning Between Amphibole and Silicate Melt. Reviews in Mineralogy and Geochemistry 67, 417–452.

Wood, B.J., and Blundy, J.D., 1997. A predictive model for rare earth element partitioning between clinopyroxene and anhydrous silicate melt. Contributions to Mineralogy and Petrology 129, 166–181.

Wood, B.J., and Blundy, J.D., 2001. The effect of cation charge on crystal- melt partitioning of trace elements. Earth and Planetary Science Letters 188, 59–71.

CHAPTER 4. Ca. 2.7 Ga ferropicritic magmatism: a record of Fe-rich heterogeneities during Neoarchean global mantle melting

Chapters 2 and 3 established that mantle-derived Fe-rich magmas parental to the ca. 2.72 Ga Q-suite intrusions comprise an important juvenile addition to the Ungava craton of the Northeastern Superior Province. Moreover, underplating by Fe-rich magmas may have, in part, driven the Neoarchean cratonization of the Ungava craton. Chapter 4 investigates the global distribution of Neoarchean ferropicritic magmas, and identifies two main types of Neoarchean ferropicritic magmas. Nickel-rich, alkaline ferropicrites are consistent with derivation from olivine-free garnet-pyroxenite sources, whereas the Ni-poor, subalkaline ferropicrites were likely derived from garnet-free peridotites.

Abstract

Although terrestrial picritic magmas with FeO^{TOT} ≥13 wt. % are rare in the geological record, they were relatively common ca. 2.7 Ga during the Neoarchean episode of enhanced global continental crust growth. Recent evidence that ferropicritic underplating played an important role in the ca. 2.74-2.70 Ga reworking of the Ungava craton provides the impetus for a comparison of ca. 2.7 Ga ferropicrite occurrences in the global Neoarchean magmatic record. In addition to the Fe-rich plutons of the Ungava craton, volumetrically minor ferropicritic flows, pyroclastic deposits, and intrusive rocks form parts of the Neoarchean greenstone belt stratigraphy of the Abitibi, Wawa, Wabigoon and Vermillion domains of the southern and western Superior Province. Neoarchean ferropicritic rocks also occur on five other Archean cratons: West Churchill, Slave, Yilgarn, Kaapvaal, and Karelia, suggesting that ca. 2.7 Ga Fe-rich magmatism was globally widespread.

Neoarchean ferropicrites form at least two distinct groups in terms of their trace element geochemistry. Alkaline ferropicrites have fractionated REE profiles (Ce/Yb_{MORB} = 9 +7/-5) and show no systematic HFSE anomalies (Nb/La_{MORB} = 1.0 +1.4/-0.3), broadly resembling the trace element character of modern-day "Ocean Island Basalt (OIB)" magmas. Magmas parental to ca. 2.7 Ga alkaline ferropicrites also had high Nb/Y_{MORB} (>2) and low Al_2O_3/TiO_2 (3 +3/-1) and Sc/Fe (≤ 3 x 10^{-4}) ratios and were enriched in Ni relative to primary pyrolite mantle-derived melts. The high Ni contents of the alkaline ferropicrites coupled with the low Sc/Fe ratios are consistent with derivation from olivine-free garnet-pyroxenite sources. A second ferropicrite group is characterized by decisively "non-alkaline" primary trace element profiles that range from flat to LREE-

depleted, resembling Archean tholeiitic basalts and komatiites. In contrast to the parental alkaline ferropicrites, the magmas parental to the subalkaline ferropicrites had flat HREE, lower Nb/Y (<2), higher Al_2O_3/TiO_2 (7-25) and Sc/Fe ($\geq 4 \times 10^{-4}$) and ratios and were depleted in Ni relative to melts of pyrolitic peridotite, suggesting they were derived from garnet-free peridotite sources. Neodymium isotopic evidence indicates that the source of alkaline ferropicrites was metasomatically enriched shortly before ($\leq$3.0 Ga) magma generation, but the sublkaline ferropicrites do not show evidence of precursor metasomatism.

The occurrence of ca. 2.7 Ga Fe-rich rocks on at least six cratons that are commonly coeval with the more ubiquitous ca.2.7 Ga komatiites and Mg-tholeiites is consistent with the existence of heterogeneous Fe-rich "plums" throughout the Neoarchean mantle. The paucity of ferropicrites in the post-2.7 Ga geological record suggests that majority of these Fe-rich "plums" have been melted out during the global Neoarchean melting of the mantle.

1. Introduction

The Neoarchean (~2.7 Ga) peak in igneous crystallization ages across the Superior Province (Condie et al., 2009; Maurice et al., 2009) represents a period of intense igneous activity during which significant volumes of granitic magmas were emplaced, resulting in the stabilization of the world's largest craton. Numerous mafic to ultramafic intrusions and large volcano-sedimentary belts containing voluminous mantle-derived komatiitic to basaltic flows were emplaced synchronously with the felsic plutonism (see Van Kranendonk et al. (2012) for recent review). There is increasing evidence that unusually Fe-rich, picritic magmas were an important component of the ca. 2.7 Ga juvenile input into the Superior Province (Kitayama and Francis, in preparation; Milidragovic et al., in preparation; Green and Schulz, 1977; Stone et al.,1987, 1995a; Goldstein and Francis, 2008; Milidragovic and Francis, 2014). These primitive Fe-rich mafic magmas require mantle source regions that were considerably enriched in iron relative to the mantle sources of the more abundant ca. 2.7 Ga komatiitic, Mg-tholeiitic, and calc-alkaline lavas, and related cumulate rocks. In this paper we compare the geochemical signatures ca. 2.7 Ga Fe-rich magmas of the Superior Province (Fig. 4-1A) and extend the survey to the global suite of ca. 2.7 Ga ferropicrites and high-Mg basalts (Fig. 4-1B). Our findings indicate that the mantle that melted during the enhanced Neoarchean crustal growth (Condie, 1998, 2000; Rino et al., 2004; Condie et al., 2009; Hawkesworth et al., 2009) contained Fe-rich plums with a variety of compositions.

2. The geology of the Superior Province

The Superior Province (Fig. 4-1A) is a composite Archean terrane composed

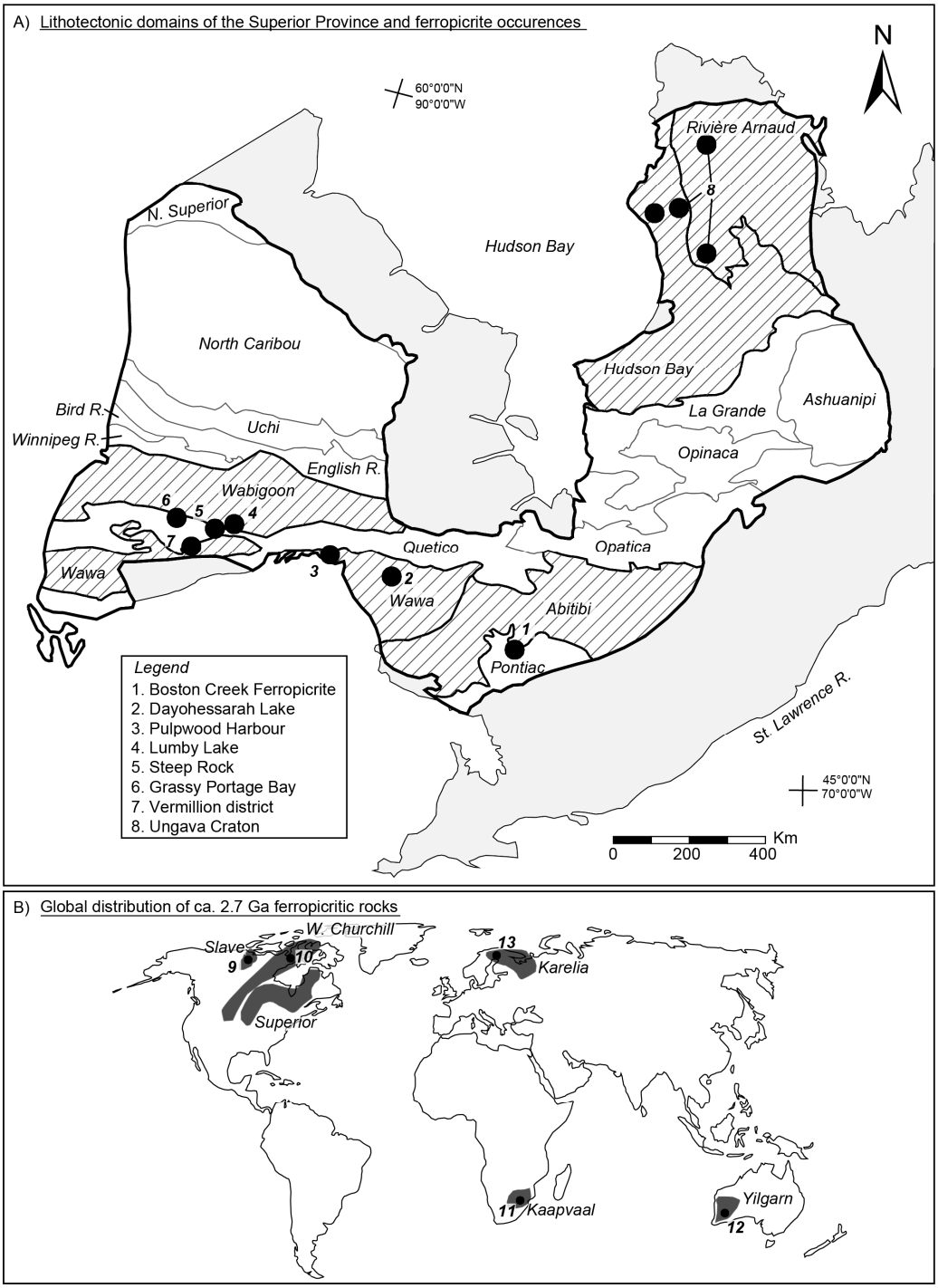

Figure 4-1: Global distribution of ca. 2.7 Ga ferropicrites.
A) The Archean Superior Province and its sub-province domains. The numbered locations refer to ferropicrite studies discussed in the paper (see Table 4-1 for details). **B)** Global distribution of Archean cratons in which ca. 2.7 Ga ferropicrites have been identified.

predominantly of supracrustal volcano-sedimentary belts and felsic plutonic complexes (Percival et al., 2006; Simard, 2008). It is a major component of North America's cratonic nucleus, and the Earth's largest craton. A compilation of zircon U-Pb data from the Superior Province shows a large ca. 2.7 Ga peak in igneous crystallization ages (Condie et al., 2009) that is widely accepted as the age of its cratonization. Rare remnants of preserved Paleo- to Mesoarchean crust are limited to isolated supracrustal belts (Cates and Mojzsis, 2007; O'Neil et al., 2008) and metamorphic domains (Böhm et al., 2000; Bickford et al., 2006), but are inferred to be an important recycled component in ca. 2.7 Ga plutonism because of the abundance of inherited zircon cores, and the unradiogenic Nd-isotopic signatures of the ca. 2.7 Ga granitoids (Tomlinson et al., 2004; Stevenson et al., 2006; Boily et al., 2009).

The Superior Province is characterized by an aeromagnetically, structurally and lithologically-defined linear fabric that generally trends east-west in the southern and western parts of the Province, and northwest-southeast in the Northeastern Superior Province. Traditionally, these fabrics have been interpreted as evidence for accretionary growth of the Superior Province through a series of collisions between oceanic and continental micro-continents ca. 2.72-2.68 Ga (Card, 1990; Percival et al., 2001, 2006). More recent work (Bédard, 2003, 2006; Boily et al., 2009; Maurice et al., 2009; Milidragovic and Francis, 2014) has argued against an accretionary plate tectonic model for the Northeastern Superior Province. The correlation of fragmented, but once laterally-continuous volcanic sequences (Maurice et al., 2009) and the identification of isotopically and seismically distinct terranes that transgress proposed arcs (Faure et al., 2008; Boily et al., 2009) indicate that the NE-SW grain of the Ungava Craton does not reflect successive

accretion of distinct arc terranes. Furthermore, the high abundance of inherited zircon cores, and the craton-wide presence of ubiquitous ca. 2.72-2.70 Ga Qullinaaraaluk suite (Q-suite) ultramafic intrusions and genetically related granitoids (Simard, 2008; Milidragovic and Francis, 2014) favour a model in which underplate-driven remelting of ≤2.74 Ga proto-cratonic crust formed the Ungava craton.

In contrast to the Northeastern Superior Province, which is characterized by dominant ca. 2.74-2.70 Ga mode in zircon crystallization ages reflecting near-complete crustal reworking, the southern and western Superior Province comprise fundamentally-different Paleo-to Mesoarchean domains, separated by fault-bounded Neoarchean metasedimentary and granite-greenstone belts (Percival et al., 2006). The ca. 2.7 Ga mafic to ultramafic rocks of the southern and western Superior Province occur within supracrustal greenstone belts and as small intrusive bodies (Polat et al., 1999; Wyman, 1999; Ayer et al., 2002; Pettigrew and Hattori, 2006; Polat, 2009; Mungall et al., 2010). Individual greenstone belts comprise, in large part, cyclically-emplaced volcanics of komatiitic, tholeiitic and calc-alkaline affinities, which have been used to develop complex tectonic and geodynamic models (Wyman, 1999; Polat, 2009). Each cycle typically displays a temporal evolution from tholeiitic and komatiitic magmatism to calc-alkaline magmatism (Ayer et al., 2002). A number of studies (Stone et al., 1987, 1995a; Polat et al., 1999; Goldstein and Francis, 2008; Polat, 2009) noted the presence of volumetrically-minor, LREE-enriched ferropicritic rocks (also referred to as transitional to alkaline basalts and Al-depleted komatiites) within the komatiite-tholeiite associations in the Abitibi and Wawa domains. The komatiitic, tholeiitic and calc-alkaline volcanic rocks, and their intrusive equivalents, define a relatively tight Mg-rich array in Mg vs. Fe

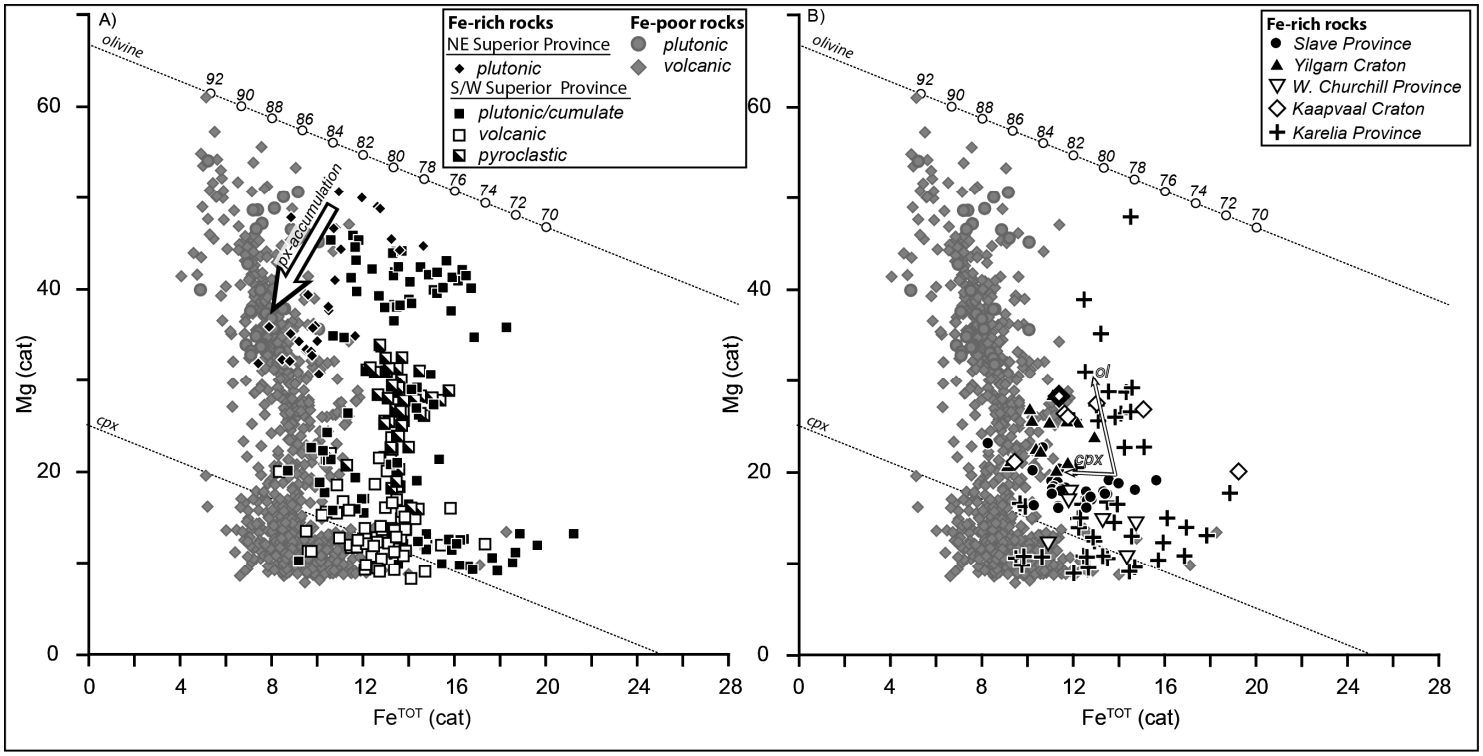

Figure 4-2: Mg vs. Fe^{TOT} cation plot of ca. 2.7 Ga ferropicrites.
A) Archean mafic and ultramafic rocks of the Superior Province. Two distinct populations are visible: 1) low-Fe main trend that includes komatiites, basaltic komatiites, and tholeiitic and calc-alkaline basalts (grey diamonds; n = 840) and their related intrusives (grey circles; n = 31) and 2) Fe-rich rocks. Accumulation of pyroxene drives the whole rock composition towards the low-Fe trend, consequently only cumulate rocks with Mg+Fe ≥40 cat. % are shown. The arrow depicts the effect of increasing amounts of clinopyroxene accumulation in ultramafic rocks. **B)** Other ca. 2.7 Ga global ferropicrite occurrences compared to the Superior Province's Mg-rich array. The arrows depict the effects of olivine and clinopyroxene accumulation by Fe-rich liquids. Data sources: GEOROC database (http://georoc.mpch-mainz.gwdg.de) and references therein, and references cited in Table 4-1. GEOROC data has been filtered to only include analyses with $SiO_2 \leq 51$ wt. %, LOI≤ 10 wt. % and MgO ≥ 6 wt. %.

Table 4-1: Global ca. 2.7 Ga ferropicrite occurrences

	Location	Age (Ga)	Rock Type	Affinity[1]	Ref[2].
1	BCF	2.72	Diff. flow/sill	alkaline	1-8
2	Dayohessarah Lk.	2.77-2.72	Intr.	alkaline	9, 10
3	Schreib.-Hem.	2.77-2.72	Intr./volc.	alkaline.	9, 11
4	Lumby Lk.	<3.0	Pyroclastic	alkaline	10, 12, 13
5	Steep Rock	<3.0	Pyroclastic	alkaline	10, 13, 14
6	GUP	2.73-2.70	Pyroclastic	alkaline	10, 14
7	Vermillion	2.72	Intr./volc.	subalkaline	15, 16
8	NESP (Q-suite)	2.72-2.70	Intr.	subalkaline	17, 18
9	Lake of Enemy	2.66	Volc.	alkaline	19
10	Central Hearne	2.71-2.69	Volc.	subalkaline	20
11	Meredale Member	2.71	Volc	alkaline	21-23
12	Kambalda Sequence	2.72-2.68	Intr.	alkaline	24-25
13	TKS	2.77-2.74	Intr./volc.	subalkaline	26

[1]Affinity of ferropicrites based on trace element profiles

[2]Data sources: 1-5. Stone et al., (1987, 1992, 1995a, 1995b, 2003); 6. Xie et al. (1993); 7. Walker and Stone (2001); 8. Crocket et al. (2005); 9. Polat et al. (1999); 10. Goldstein and Francis (2008); 11. Kitayama and Francis (in press); 12. Hollings and Wyman (1999); 13. Tomlinson et al. (1999; 14. Schaefer and Morton (1991); 15. Green and Schulz (1977); 16. Schulz (1982); 17. Milidragovic and Francis (2014); 18. Milidragovic et al. (in prep); 19. Francis et al. (1999); 20 Sandeman et al. (2004); 21. McIver et al. (1982); 22. Schweitzer and Kröner, 1985; 23. Westhuizen et. al., 1991; 24. McCuaig (1994); 25. Said and Kerrich (2010); 26. Papunen et al. (2009).

BCF= Boston Creek flow, Schreib.-Hem. = Schreiber-Hemlo greenstone belt, GUP = Grassy Portage Bay ultramafic pyroclastic unit, NESP = Northeastern Superior Province (Ungava craton), TKS = Tipasjärvi-Kuhmo-Suomussalmi greenstone belt

space (Fig. 4-2) that is similar to that formed by Phanerozoic magmas. The less common Neoarchean Fe-rich mafic-ultramafic volcanic rocks and intrusions are the main focus of this paper.

3. Ferropicritic rocks of the Superior Province

3.1 Northeastern Superior Province

Numerous Fe-rich, mafic/ultramafic intrusions are scattered across the Ungava craton of the Northeast Superior Province (Labbé et al., 2001). In different localities, they comprise the Qullinaaraaluk, Chateguay, and Couture suites (Simard, 2008) and are collectively referred to here as the Q-suite (Milidragovic et al., in preparation; Milidragovic and Francis, 2014). The ca 2.72-2.70 Ga emplacement of the Q-suite intrusions, as constrained by U-Pb dating of zircon from gabbronorites and crosscutting felsic veins (Simard, 2008; Milidragovic and Francis, 2014), is coeval with the intense felsic plutonism that reflects the near-complete remelting of the proto-cratonic TTG crust that stabilized the Ungava craton.

There are two main types of Q-suite intrusions: those with significant modal orthopyroxene and those lacking modal orthopyroxene (Milidragovic et al., in preparation). Both types of intrusions are remarkably fresh, suggesting that the observed mineralogy largely reflects the composition of their parental magmas. The orthopyroxene-rich plutons have been identified in both the Hudson Bay and Rivière Arnaud terranes. They include peridotite, websterite, and gabbronorite, and are characterized by the crystallization sequence: olivine, orthopyroxene, clinopyroxene, amphibole, plagioclase, ulvospinel. The orthopyroxene-rich Q-suite intrusions

crystallized from Fe-rich high-Mg parental basalts (MgO =10.9 wt. %, FeO^{TOT} =14.1 wt. %) of subalkaline affinity. The orthopyroxene-free Q-suite intrusions have been identified only in the Lac Couture region of north-central Rivière Arnaud Terrane. The plutons of the Lac Couture region comprise fresh dunite, wehrlite, hornblendite, and metagabbro, and are characterized by the crystallization of olivine followed by clinopyroxene, plagioclase and ulvospinel. The normative compositions of the least altered orthopyroxene-free intrusions straddle the plane of critical silica undersaturation, indicating a mildly alkaline to mildly subalkaline (transitional) ferropicritic magma (MgO =14.0 wt. %, FeO^{TOT} =16.8 wt. %). The estimated ferropicritic parental magmas are poor in Al_2O_3 (6.5 wt. %) and rich in CaO (14 wt. %), relative to the parental magmas of the subalkaline Q-suite intrusions (Al_2O_3 ~15 wt. % wt. %; CaO =8.5 wt. %).

When normalized to Mid-Ocean Ridge Basalt (MORB, Fig. 4-3), the most magnesian peridotites and dunites of the subalkaline and transitional Q-suite intrusions are characterized by relatively unfractionated heavy rare earth element (HREE) profiles that are depleted relative to the middle and light rare earth elements (MREE and LREE, respectively). The subalkaline peridotites display larger LREE/HREE ratios than the dunites of the transitional Q-suite plutons. The high field strength element (HFSE) contents of both types of Q-suite intrusions are depleted relative to REE with similar compatibility. Milidragovic et al. (in preparation) argued the subchonritic initial $\varepsilon_{Nd(2.72\ Ga)}$ values and calc-alkaline signatures of the subalkaline Q-suite plutons reflect late metasomatism by small volumes of TTG anatectic melts, following magmatic accumulation. By subtracting small amounts (~3%) of anatectic melt from bulk Q-suite harzburgite and reconstructing the parental magma compositions using the method of

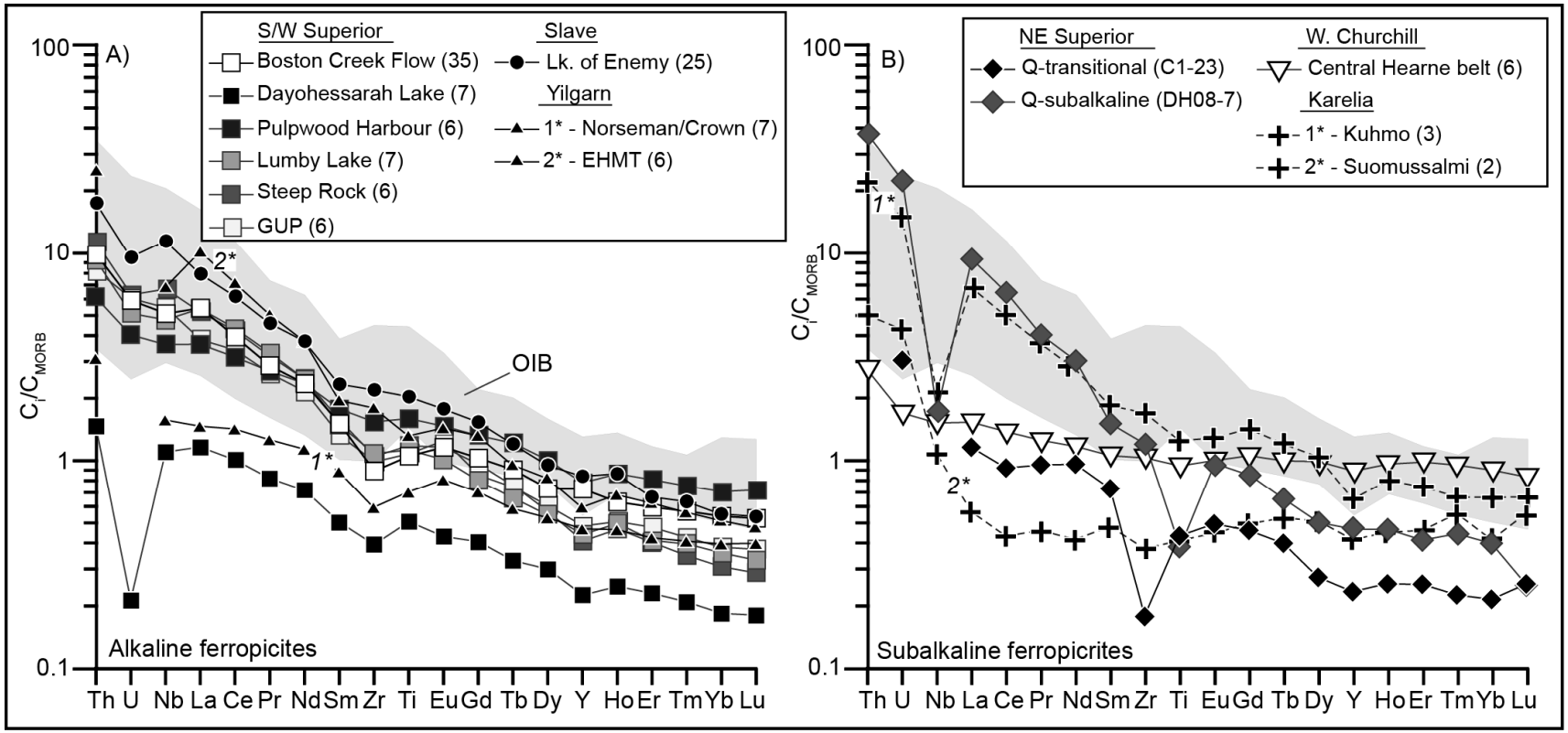

Figure 4-3: MORB-normalized spidergrams of Neoarchean ferropicrites.
With the exception of the Dayohessarah ferropicrites, which are all intrusive, an attempt was made to select samples that approach liquid compositions. **A)** Median abundances in the alkaline ferropicrites compared to the range of OIB olivine basalts (n = 106 at 95% confidence interval; source: GEOROC database). The low abundances in the Dayohessarah Lake rocks reflect their cumulate character. The low absolute abundances in the Crown and Norseman suites (Said and Kerrich, 2010), are interpreted to reflect crystal accumulation. **B)** Calculated trace element compositions of the Q-suite parental magmas (Milidragovic et al., in preparation), and the median abundances in other non-alkaline ferropicrite suites.

Bédard (1994), Milidragovic et al. (in preparation) concluded that the primary trace-element profiles of the subalkaline Q-suite magmas may have originally been relatively flat and similar to those of the Mg and Fe-tholeiites emplaced prior to ca. 2.75 Ga (Maurice et al., 2009), although at lower absolute abundances. In contrast to the subalkaline Q-suite peridotites, the transitional Q-suite dunites have flat to convex upward LREE profiles, suggesting that their parental magmas had flat to LREE-depleted trace element profiles.

3.2 Southern and western Superior Province

3.2.1 The Boston Creek Flow

Iron-rich ultramafic volcanic rocks were first identified in the ca. 2.7 Ga Abitibi domain by Stone et al. (1987; see also Stone et al., 1995a, 1995b). The 2720 ± 2 Ma (Corfu and Noble, 1992) Boston Creek flow is up to ~100 m thick and is composed of an upward succession of basal pyroxenite, peridotite, pyroxenite, gabbro, and an amygduloidal spinifex-textured layer interpreted to approach liquid composition. The flow has been metamorphosed to greenschist facies, with complete serpentinization of olivine and extensive development of chlorite and amphibole. The apparent crystallization sequence of the Boston Creek flow is olivine ± chromite, clinopyroxene, Fe-Ti oxide, and plagioclase, with no observed orthopyroxene (Stone et al., 1995b). Although the majority of the rocks of the Boston Creek flow are orthopyroxene-normative, Kitayama and Francis (in preparation) have recently argued that serpentinization of olivine can be accompanied by a significant reduction of whole rock Mg/Si ratios. Consequently, the orthopyroxene-normative composition of the Boston Creek flow rocks may reflect remobilization and loss of MgO.

The rocks of the Boston Creek flow display a large range of MgO contents (3 - 35 wt. % normalized to volatile-free concentrations), reflecting the differentiated character of the flow. The FeO^{TOT} contents of the mafic and ultramafic rocks (MgO >6 wt. %) range between 13.5 and 23 wt. %. In comparison to most Archean high-Mg ultramafic rocks, the FeO-rich rocks of the Boston Creek flow have high TiO_2 contents (1.3 +1.1/-0.8 wt. %) and relatively low abundances of Al_2O_3 (Al_2O_3 =7 +3/-5 wt. %), yielding Al_2O_3/TiO_2 ratios (6 +1.5/-2; Fig. 4-4) significantly lower than those of the primitive mantle (21.4, Palme and Neill (2004)).

The trace element profiles of the Boston Creek flow ferropicrites broadly resemble those of the mildly alkaline Ocean Island Basalts (OIB) emplaced today (Fig. 4-3A). The ferropicrites are moderately enriched in the LREE relative to the HREE (Ce/Yb_{MORB} =8 +1/-4; MORB after Sun and McDonough, 1989), have weakly fractionated HREE (Gd/Yb_{MORB} =2.0 +0.1/-0.4), and show no fractionation between the HFSE and REE with similar compatibility (Nb/La_{MORB} =0.9 +0.3/-0.2). The initial εNd (2.7 Ga) determined on three samples have suprachondritic values (+2 to +3), indicating that the magmas parental to the LREE-enriched Boston Creek Flow were derived from a source with a history of previous LREE-depletion (Stone et al., 1995a). Furthermore, the Boston Creek flow has low initial $^{187}Os/^{186}Os$ ratios (γ_{Os} (2.7 Ga) =-3.8 ± 0.5) that reflect source mantle with a long-term Re depletion (Walker and Stone, 2001).

3.2.2 The Dayohessarah Lake greenstone belt

The aluminum-poor, Fe-rich peridotites, pyroxenites and gabbros in the Dayohessarah Lake greenstone belt of the Wawa subprovince were initially classified by

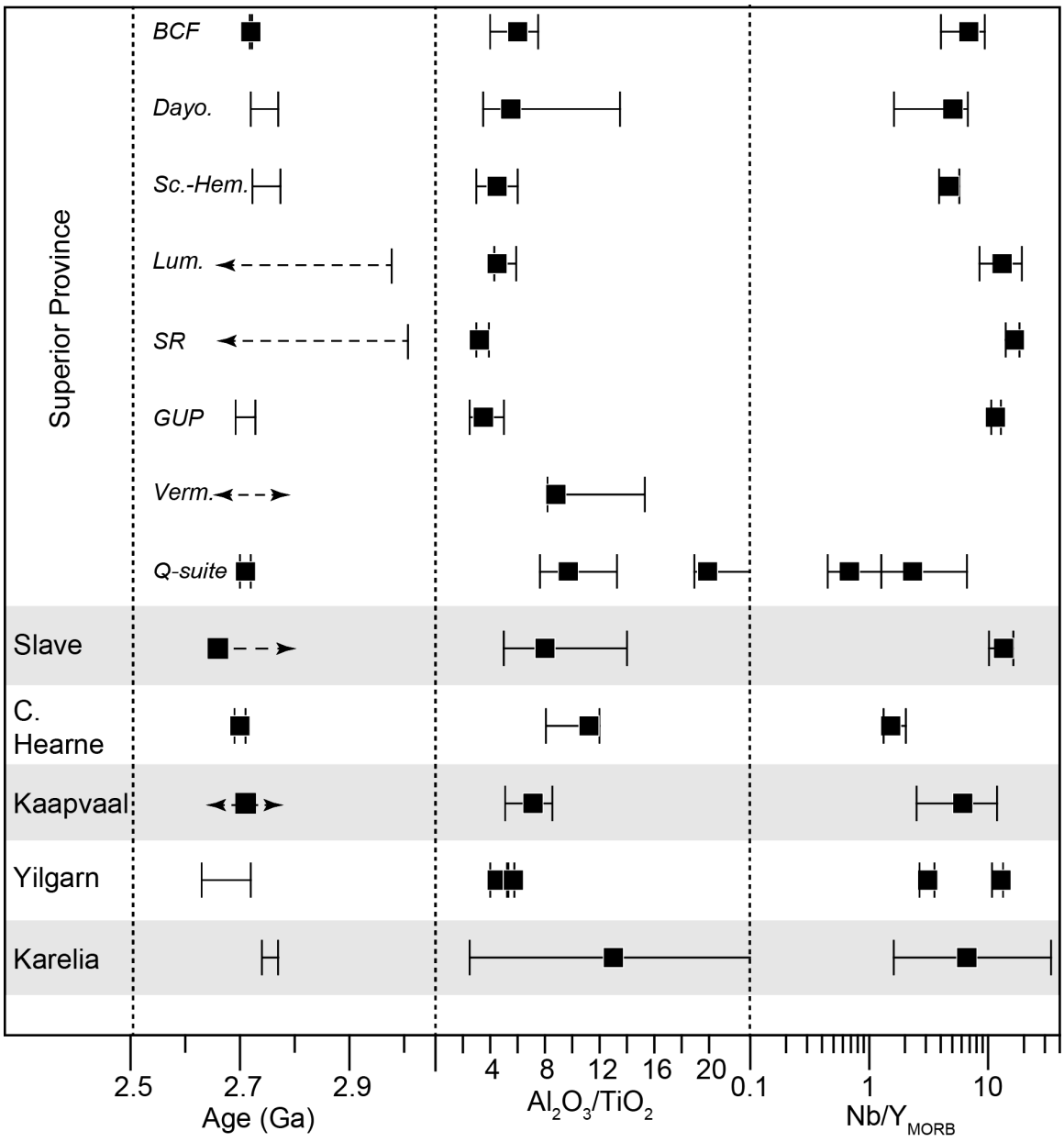

Figure 4-4: Summary of age and key chemical characteristics of Neoarchean ferropicrites

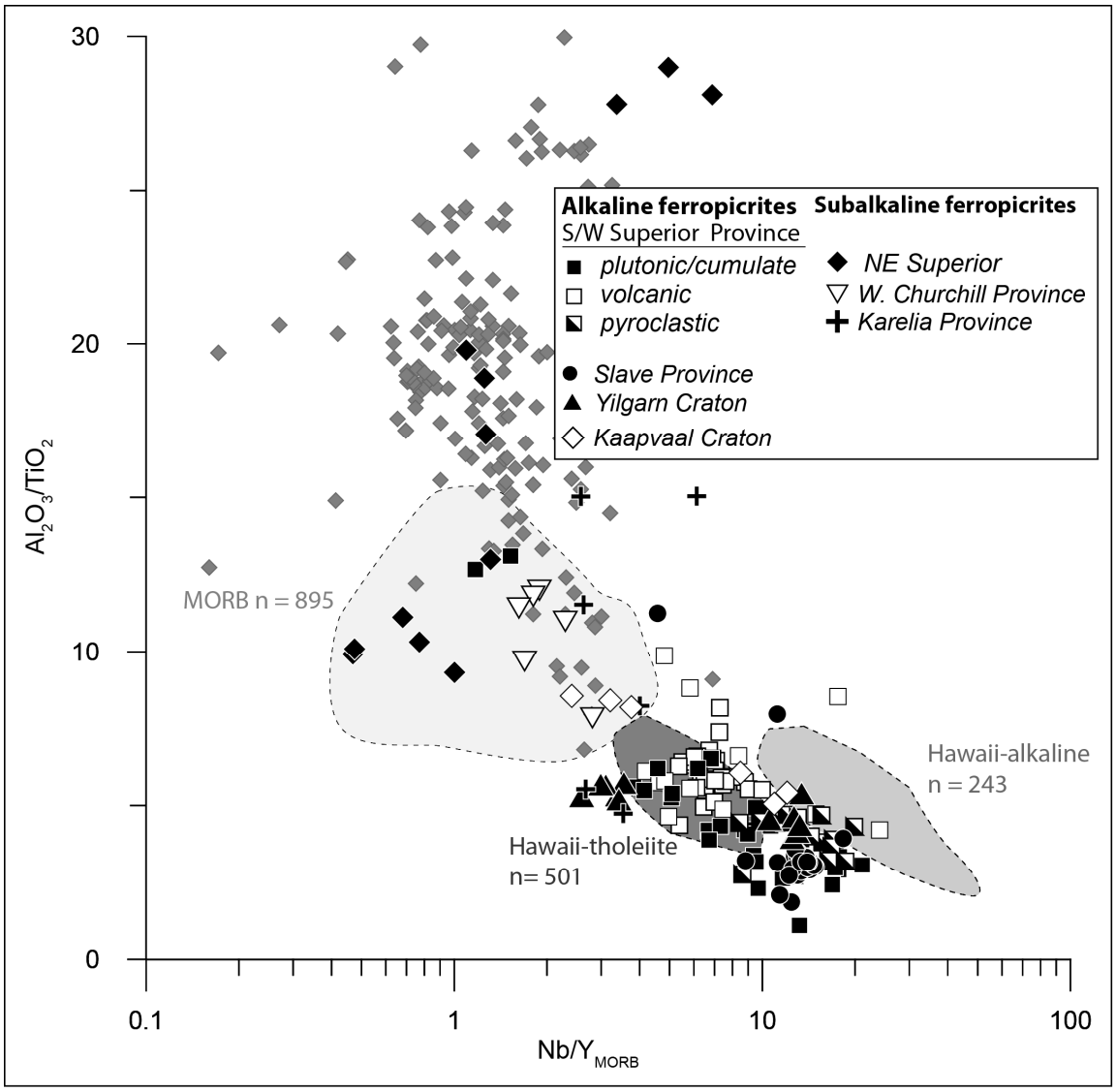

Figure 4-5: Al_2O_3/TiO_2 vs. Nb/Y_{MORB} diagram.
The plot highlights two main ca. 2.7 Ga ferropicrite sub-groups. Alkaline ferropicrites form a cluster characterized by relatively high Nb/Y ratios between E-MORB and OIB and low Al_2O_3/TiO_2 values. In contrast, the subalkaline ferropicrites plot between E-MORB and N-MORB values in terms of their Nb/Y ratios and with the exception of the subalkaline Q-suite intrusions have Al_2O_3/TiO_2 ratios that project onto the trend defined by the alkaline ferropicrites. In order to minimize the effects of crystal sorting (e.g. accumulation of amphibole, plagioclase, ulvospinel), only the most magnesian Q-suite samples are plotted. The data from Hawaii have MgO ≥ 10 wt. % and are subdivided into alkaline (pre and post-shield building) and olivine tholeiites (shield-building) lavas. MORB and Icelandic compositions have MgO > 7 wt. %. Data sources: Iceland, Hawaii - GEOROC database; MORB (Chile Ridge, East Pacific Rise, Mid-Atlantic Ridge) - PetDB database.

Polat et al. (1999) as Al-depleted komatiites and subsequently identified as metamorphosed ferropicritic cumulates by Goldstein and Francis (2008). There are no direct ages for the formation of the Dayohessarah Lake greenstone belt, but map patterns and aeromagnetic data suggest that the belt may be an extension of the Schreiber-Hemlo belt further to the west (Stott, 1999). Consequently, the Fe-rich rich rocks of the Dayohessarah Belt may be correlative with the Fe-enriched ultramafic rocks of the ca. 2.72-2.77 Ga (Corfu and Muir, 1989) Pulpwood-Playter Harbours sequence (see section 3.2.3).

The olivine-dominated (MgO >35 wt. %), Fe-rich cumulate rocks of the Deyohessarah Lake greenstone belt are significantly more Fe-enriched (Fe^{TOT} =14-19.5 wt. %) than majority of the plutonic ultramafic rocks of the Superior Province. The peridotites have relatively low Al_2O_3/TiO_2 ratios (5.5 +8/-2; Fig. 4-4). Majority of the Dayohessarah Lake peridotites plot along an $(Mg+Fe^{TOT})/Ti$ vs. Si/Ti line with a slope of 2, corresponding to covariation formed by olivine accumulation (Russell and Nicholls, 1988).

The enrichment in LREE relative to the HREE (Ce/Yb_{MORB} =1.5-6; Fig. 4-3A) and the absence of systematic HFSE-anomalies in the cumulate rocks, suggest that the magma parental to the Dayohessarah Lake ferropicritic intrusions had a fractionated REE profile and unfractionated HFSE/REE ratios, similar to the alkaline profile of the Boston Creek flow ferropicrites.

3.2.3 The Schreiber-Hemlo greenstone belt

Iron-rich mafic and ultramafic rocks form the upper part of the Pulpwood-Playter Harbours sequence of the Schreiber-Hemlo greenstone belt of the Wawa subprovince,

situated along the northern shore of Lake Superior (Polat et al., 1999; Kitayama and Francis, in preparation). The Pulpwood-Playter sequence is part of the Heron Bay assemblage that, together with the older Hemlo assemblage, comprises the eastern half of the Schreiber-Hemlo greenstone belt. The maximum age of the Pulpwood-Playter Harbours sequence is loosely constrained by the age of the Hemlo assemblage (2772 ± 2 Ma; Corfu and Muir,1989). The minimum age of the Pulpwood-Playter Harbours volcanic sequence is constrained by the earliest syn- to post- tectonic granodiorite (2719 +6/-4 Ma; Corfu and Muir, 1989) that intrudes the Schreiber-Hemlo greenstone belt. The stratigraphy of the Pulpwood-Playter Harbours sequence consists of cumulate rocks ranging from serpentinized dunite and clinopyroxenite to differentiated gabbro, bound by the underlying Mg-tholeiites and the overlying mildly-alkaline Fe-rich lavas (Kitayama and Francis, in preparation). The cumulate bodies and the mildly-alkaline overlying pillow lavas are some of the most Fe-rich rocks of the Superior Province.

The peridotite cumulates (MgO >20 wt. %) of the Pulpwood-Playter Harbours sequence and the rocks inferred to represent near-liquid compositions (MgO =6-12 wt. %), contain 15-22 wt. % FeO^{TOT}. The dunites and peridotites of the Pulpwood-Playter Harbours sequence are orthopyroxene-normative (5-45 wt. %), whereas the pyroxenites, gabbros and the overlying lavas are mildly nepheline-normative (≤12 wt. %). The discrepancy in calculated normative mineralogy appears to reflect the loss of magnesium associated with the serpentinization of olivine-dominated rocks (Kitayama and Francis, in preparation), which results in a relatively shallow $(Mg+Fe^{TOT})/Ti$ vs. Si/Ti slope ~1.50 defined by the Fe-rich dunites of the Pulpwood-Playter Harbours sequence. The Fe-rich volcanic rocks of the Pulpwood-Playter Harbours assemblage are rich in TiO_2 (2 +0.3/-

0.1 wt. %) and poor in Al_2O_3 (12 +1/-2.5 wt. %). The Al_2O_3/TiO_2 ratios (4.5 – 6; Fig. 4-4) of the Fe-rich volcanic rocks are similar to those of the Fe-rich peridotites (3-6), but are significantly lower than those of the underlying Mg-tholeiites (14-19).

Samples interpreted to represent near-liquid compositions are moderately enriched in LREE relative to the HREE (Ce/Yb_{MORB} =4 +2/-0.5), have weakly fractionated MREE/HREE ratios (Gd/Yb_{MORB} =1.8 +0.3/-0.1), and lack significant fractionation between HFSE and REE (Nb/La_{MORB} =1.0 +0.2/-0.1), thus resembling the alkaline profiles of OIB-basalts (Fig. 4-3A).

3.2.4 The Lumby Lake greenstone belt

The iron-rich ultramafic rocks of the Wabigoon subprovince's Lumby Lake greenstone belt were originally interpreted as enriched basaltic komatiites by Tomlinson et al. (1999) and Al-depleted komatiites by Hollings and Wyman (1999). Goldstein and Francis (2008) have interpreted these rocks to represent Archean pyroclastic ferropicrite deposits. The age range of the Lumby Lake greenstone belt is not well constrained, but ca. 2973 Ma zircons from a felsic tuff unit define the belt's maximum age (Tomlinson et al., 1999). The greenschist facies pyroclastic ferropicrites are pervasively sheared, clast supported, and composed of lapilli-sized aphanitic fragments set in a fine-grained matrix.

The Lumby Lake ferropicrites contain 16 - 21 wt. % FeO^{TOT}, and have high contents of MgO (11-25 wt. %) and Ni (500-1400 ppm; Fig. 4-6). They also have low Al_2O_3 (6 +5.5/-0.5 wt. %) contents and Al_2O_3/TiO_2 ratios (4.5 +1.4/-0.2; Fig.4-4). The trace element profiles of the Lumby Lake pyroclastic ferropicrites resemble those of the Boston Creek flow and the Pulpwood-Playter Harbours assemblage volcanic rocks, and are characterized by negatively sloping REE profiles (Ce/Yb_{MORB} = 11 +7/-3; Gd/Yb_{MORB}

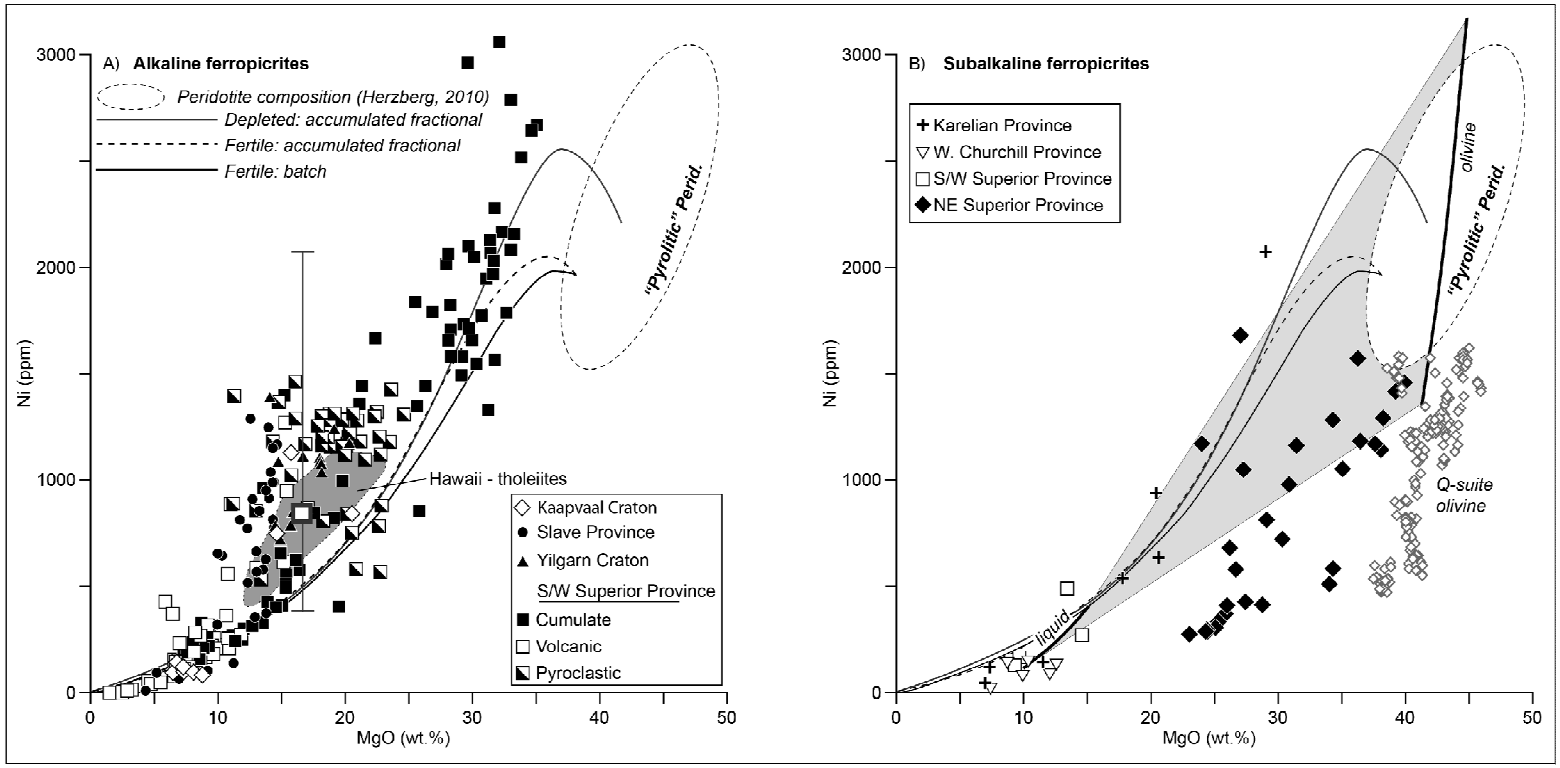

Figure 4-6: Whole rock Ni(ppm) vs MgO (wt.%) of ca. 2.7 Ga ferropicrites.
A) Comparison of alkaline ferropicrite compositions with primary melts derived from depleted and fertile mantle sources by batch and accumulated fractional melting (modified from Herzberg, 2011). The field of Hawaiian olivine tholeiites is from Sobolev et al. (2005). Median (±2 IQR) composition of extrusive ferropicrites from the Superior Province, normalized to 16 wt. % MgO is also shown (white square with thick grey outline). **B)** The compositions of subalkaline ferropicrites compared to melts of the pyrolitic mantle and model olivine cumulates formed by a hypothetical parental melt having 16 wt. % MgO, ~460 ppm Ni, and Mg-number = 0.60 (grey field) and its daughter liquids (olivine and liquid compositional paths calculated assuming D_{Ni} of Hart and Davis (1978)). Olivine accumulation from primary pyrolite-derived magmas and their differentiated liquids fails to reproduce the low Ni contents of the Q-suite olivine cumulates. Non-alkaline ferropicrites form the Vermillion District and Central Hearne greenstone belt are consistent with Ni-poor parental compositions.

= 2.4 +0.6/-0.5), and a lack of significant HFSE/REE fractionation (Nb/La_{MORB} = 1.0 +0.5/-0.3; Fig. 4-3A). In contrast to the samples interpreted to approximate liquid compositions from the Boston Creek flow (Yb_{MORB} =0.54 + 0.15/-0.16) and the Pulpwood-Playter Harbours assemblage (Yb_{MORB} =0.71 +0.09/-0.19), the Lumby Lake pyroclastic ferropicrites contain lower abundances of HREE (Yb_{MORB} =0.36 + 0.08/-0.09).

3.2.5 The Steep Rock greenstone belt

The Steep Rock greenstone belt overlies the 3003 ± 5 Ma (Davis and Jackson, 1988) Marmion Batholith and comprises five formations, including a pyroclastic Fe-rich ultramafic unit termed the Dismal Ashrock Formation (Tomlinson et al., 1999). Initially referred to as enriched komatiite (Tomlinson et al., 1999), the Dismal Ashrock Formation was later shown to be a ferropicrite by Goldstein and Francis (2008).

The Dismal Ashrock Formation pyroclastic ferropicrites are MgO, FeO, and Ni-rich (MgO =17-22 wt. %; FeO^{TOT} =16.5 -19 wt. %, Ni =1160-1300 ppm), Al_2O_3-poor (5 ±0.5 wt. %) and characterized by low Al_2O_3/TiO_2 ratios (3.2 +0.7/-0.2; Fig. 4-4). The Dismal Ashrock Formation ferropicrites have moderately fractionated LREE/HREE ratios (Ce/Yb_{MORB} =13 ±2), less steep MREE/HREE profiles (Gd/Yb_{MORB} =3.1 +0.4/-0.2), relatively low absolute HREE abundances (Yb_{MORB} =0.31 ±0.04), and slight positive to negative HFSE anomalies (Nb/La_{MORB} =1.4 +0.3/-0.4), closely resembling the Lumby Lake pyroclastic ferropicrites (Fig.4-3A). The LREE-enriched pyroclastic ferropicrites have predominantly suprachondritic initial ε_{Nd} values calculated at 2. 7 Ga (-1 to +3; Goldstein and Francis, 2008), suggesting a source with a long-term trace element depletion history.

3.2.6 The Grassy Portage Bay ultramafic pyroclastic unit

The ferropicritic Grassy Portage Bay pyroclastic rocks outcrop on the eastern edge of the fault-bounded Rice Bay Dome situated in the transition zone between the Wabigoon and Quetico subprovinces (Schaefer and Morton, 1991). The Grassy Portage Bay pyroclastic unit is a part of the Keewatin Volcanics, with an emplacement age bracketed by the oldest Keewatin rocks (2725-2728 Ma) and the overlying Coutchiching metasediments (2692-2704 Ma; Davis et al. (1989); Schaefer and Morton (1991)). Goldstein and Francis (2008) interpreted the Grassy Portage Bay ultramafic pyroclastic unit as amphibolite facies magnetite-bearing lapilli to ash tuff.

The rocks of the Grassy Bay Portage ultramafic unit display a range of MgO (11-23.5 wt. %) and FeO^{TOT} (14-20 wt. %) concentrations. The Ni contents of the Grassy Portage Bay pyroclastic rocks range from 750 ppm to 1460 ppm (Fig. 4-6. The pyroclastic rocks have low Al_2O_3/TiO_2 ratios (3.5 +1.5/-1; Fig. 4-4), owing to the low Al_2O_3 contents (< 5.5 wt. %) and high TiO_2 contents (1-2.3 wt. %). The MORB-normalized trace element profiles of the Grassy Portage Bay pyroclastics strongly resemble those of the Lumby Lake and Steep Rock greenstone belt pyroclastic ferropicrites, showing moderately sloping REE profiles (Ce/Yb_{MORB} =9 +4-/-3; Gd/Yb_{MORB} =2.2 +0.8/-0.2), relatively low abundances of HREE (Yb_{MORB} =0.38 +0.10/-0.02) and small enrichments in HFSE relative to the similarly incompatible REE (Nb/La_{MORB} =1.3 +1.8/-0.3; Fig. 4-3A). The initial ε_{Nd} (2.72 Ga) values of the Grassy Portage Bay pyroclastics are suprachondritic (+2.5), and consistent with long-term trace element depletion of their mantle source.

3.2.7 The Vermillion District ferropicrites and high Mg-basalts

Iron-rich, high-Mg basalts to picrites (basaltic komatiites of Green and Schulz (1977) and Schulz (1982)) occur in the Newton Lake Formation, the uppermost unit of the Vermillion district. The age of the Fe-rich rocks is poorly constrained, but was inferred by Corfu and Stott (1998) to be ca. 2.72 Ga. The Fe-rich ultramafic rocks of the Newton Lake Formation comprise pillowed to massive flows, ultramafic lenses and layered sills. The 100-400 m thick sills are composed of peridotite, pyroxenite and gabbronorite, and reflect the crystallization sequence of: olivine + chromite, orthopyroxene + clinopyroxene, orthopyroxene + clinopyroxene + plagioclase, and finally clinopyroxene + plagioclase + magnetite (Schulz, 1982).

In contrast to the LREE-enriched volcanic and intrusive ferropicrites of the southern Superior Province, the Fe-rich rocks (MgO = 7.5-14.5 wt. %) of the Newton Lake Formation have lower FeO^{TOT} (12-17 wt. %) at a given MgO content and higher Al_2O_3 abundances (8-12.5 wt. %). The Al_2O_3/TiO_2 ratios (8.8 +6.5/-0.6; Fig.4-4) of the Newton Lake Formation are higher than those of the other western/southern Superior Province ferropicrites. The Fe-rich rocks of the Newton Lake Formation display weakly fractionated HREE (Sm/Yb_{MORB} =1.5-2.5) and are both enriched and depleted in LREE relative to MREE (La/Sm_{MORB} = 0.7-2).

3.3 Global ca. 2.7 Ga ferropicrite occurrences

Francis et al. (1999) were the first to explicitly argue for the existence of Fe-rich domains in the Archean mantle in their study of a suite of amphibolite-facies ferropicrites located near the Lake of Enemy, in the Slave Province of the Canadian Shield. Isolated sequences and lenses of ferropicrite occur within a turbidite basin in the Yellowknife Supergroup. One ferropicrite sample produced a metamorphic zircon U-Pb of age 2613 ±

3 Ma (Bleeker and Villeneuve, 1995), constraining the minimum age of emplacement of the Lake of Enemy ferropicrites. The best age estimate for the emplacement of the ferropicrites is ca. 2.66 Ga (Bleeker and Villeneuve, 1995) based on dating of zircon grains from an ash layer in the turbidite basin. The Lake of Enemy Ferropicrites show a large range in MgO (9-18 wt. %) and FeO^{TOT} (10-21 wt. %) contents, and relatively low Al_2O_3 (8 +4/-3 wt. %) concentrations. A shallow positive correlation between MgO and FeO in primitive ferropicrites is inconsistent with the fractionation of olivine, but is similar to the trend predicted by Langmuir and Hanson (1980) for liquids produced by adiabatic mantle melting. A similar trend in the primitive olivine-phyric basalts of the Proterozoic Chukotat Group of northern Quebéc was interpreted to reflect progressively increasing degrees of adiabatic melting (Francis et al., 1981). The LREE-enriched trace element profiles of the Lake of Enemy ferropicrites lack significant HFSE anomalies (Ce/Yb_{MORB} = 12 +3/-5; Nb/La_{MORB} = 1.5 +1/-0.4; Fig. 4-3A) and are similar to the alkaline profiles of the southern and western Superior Province ferropicrites. The initial ε_{Nd} (2.72 Ga) values of the Lake of Enemy ferropicrites (+1 to +1.5; Francis et al., 1999) suggest a long-term trace element depletion of their mantle source.

Iron-rich (FeO^{TOT} = 14-18 wt. %) pillowed to massive high-Mg basaltic to basaltic rocks (MgO ≤ 12.6 wt. %) have been identified in the ca. 2711-2691 Ma Assemblage I of the Central Hearne supracrustal belt of the Western Churchill Province (Sandeman et al., 2004). These high-Mg basalts are hypersthene-normative, contain 12.5-15 wt. % Al_2O_3, and have relatively low Mg-numbers (≤0.60) and Cr (<420 ppm) and Ni (<150 ppm; Fig-4-6) concentrations, which led (Sandeman et al., 2004) to conclude that they could not have equilibrated with a peridotitic mantle source. The Fe-rich rocks of the Central

Hearne supracrustal belt have weakly fractionated REE profiles (Ce/Yb_{MORB} = 1.6 +0.8/-0.1) and lack significant HFSE/REE fractionation (Nb/La_{MORB} = 1 ±0.1), resembling the profiles of Archean tholeiites and present-day MORB (Fig. 4-3B).

The ca. 2.71 Ga Vestendorp Supergroup of the South Africa's Kaapvaal Craton is a >5 km succession composed of sub-aerial volcanic and sedimentary rocks (Armstrong et al., 1991; Van der Westhuizen et al., 1991; de Kock et al., 2012). The Westonaria Formation is ~ 80 m thick fine-grained mafic to ultramafic volcanic unit that marks the onset of the Vestendorp Supergroup deposition (Van der Westhuizen et al., 1991). The lowermost unit of the Westonaria Formation (Meredale Member) is composed of greenschist-facies metamorphosed rocks that have been interpreted as a komatiites (McIver et al., 1982). The ultramafic rocks (MgO = 13.5-20 wt. %) of the Meredale Member ((McIver et al., 1982; Schweitzer and Kröner, 1985; Van der Westhuizen et al., 1991) are Fe-rich (FeO^{TOT} =12-23 wt.%), and low in Al_2O_3 (< 9 wt.%). In contrast to the Meredale Member, the overlying volcanic rocks have low Fe-contents and plot with the main Mg-Fe array of Archean mafic/ultramafic rocks (Fig. 4-2B). Limited trace element data indicate that Meredale Member ferropicrites are characterized by moderate to high Nb/Y_{MORB} ratios (2.5-12).

The ca. 2.72-2.68 Ga Kambalda sequence of the Australia's Yilgarn Craton hosts the Fe-rich, Al-poor (MgO = 16.5-20 wt. %; FeO^{TOT} = 13-16 wt. %, Al_2O_3 < 6 wt. %) Norseman and Crown dyke-suites that have been interpreted by Said and Kerrich (2010) to be melts of metasomatized depleted lithospheric mantle. The greenschist and amphibolite-facies dykes intrude the ≥2.71 Ga Woolyeneer Formation, whose peak metamorphic age (2.65-2.63 Ga) constrains the minimum age of dyke emplacement. The

dykes are characterized by shallow REE profiles (Ce/Yb_{MORB} =3-4) and weakly fractionated HFSE/REE ratios (Nb/La_{MORB} =0.9-1.3; Fig. 3-3B). The trace-element profiles of the Norseman and Crown suite dykes of the Yilgarn Craton resemble those of the cumulate rocks of the Dayohessarah Lake ferropicrites, although at higher total concentrations. An earlier study by McCuaig et al. (1994) identified a suite of relatively Fe-enriched dykes (Enriched High-MgO Tholeiitic dykes – EHMT; MgO =14-16 wt. %, FeO^{TOT} =11-15 wt. %) in the Woolyeneer Formation that Said and Kerrich (2010) considered to be similar to the Norseman/Crown dyke suites, despite their greater LREE/HREE fractionation (Ce/Yb_{MORB} =12-14), and significantly less radiogenic initial $^{143}Nd/^{144}Nd$ ratios.

Ferropicrites are found in the Tipasjärvi-Kuhmo-Suomussalmi Greenstone complex in eastern Finland (Papunen et al., 2009) where Fe-rich, mafic to ultramafic volcanic rocks and their plutonic equivalents (MgO =6-37 wt. %; FeO^{TOT} =12-23 wt. %) were emplaced into the Karelian Province of the Baltic Shield ca. 2.77 - 2.74 Ga. The Fe-rich mafic and ultramafic rocks are characterized by highly variable Al_2O_3 contents (6-17 wt. %) and Al_2O_3/TiO_2 ratios (Fig. 4-4). Limited trace element data indicates that Fe-rich pyroxenite from the Kuhmo belt is depleted in HFSE (Nb/La_{MORB} =0.3-0.6), and moderately enriched in LREE (Ce/Yb_{MORB} ~7), suggesting that the pyroxenite's parental magma may have experienced contamination by continental crust or had a calc-alkaline affinity (Fig. 4-3B). In contrast, the trace element data from two Fe-rich ultramafic volcanic rocks from the Suomussalmi belt have markedly less fractionated trace-element patterns (Ce/Yb_{MORB} =0.5-3), and lack a systematic depletion in HFSE.

4. Discussion

4.1 Trace element character of the Neoarchean ferropicrites

Most Archean rocks have experienced greenschist to amphibolite-facies metamorphism, resulting in variable degrees of metasomatic gains and losses of mobile elements. Many of the ferropicrites discussed in this study display the apparently contradictory "alkaline" trace element profiles and "subalkaline" hypersthene-normative major element chemistry. Because of the mobility of alkalis and MgO during the ubiquitous serpentinization of Archean ultramafic rocks, the calculated normative mineralogy may not reflect the primary character of the ferropicritic magmas (Kitayama and Francis, in preparation). Consequently, ferropicrites are here divided into two groups, primarily on the basis of their immobile trace element (HFSE, REE) patterns and Al/Ti ratios.

Ca. 2.7 Ga ferropicrites from the southern and western Superior Province display negatively sloping REE profiles and unfractionated HFSE/REE ratios, features broadly similar to modern "alkaline" OIB (Fig. 4-3A; Kitayama and Francis, in preparation; Goldstein et al., 1984; Stone et al., 1995a). Neoarchean ferropicrites from the Slave Province (Francis et al., 1999) and the Fe-rich rocks from the Yilgarn Craton (McCuaig et al., 1994; Said and Kerrich, 2010) also display alkaline trace element profiles. Trace element analyses of the ferropicritic rocks from the Kaapvaal Craton are scarce but the coupled low Al_2O_3/TiO_2 ratios (5 - 8.5) and relatively high Nb/Y_{MORB} ratios (2.5 - 12) suggest an alkaline affinity (Fig. 4-4).

In contrast to the alkaline ferropicrites, the Q-suite intrusions of the Northeastern Superior Province display pronounced depletions in Nb ± Ti relative to similarly

incompatible REE. Although trace element modeling (Milidragovic et al., in preparation) indicates the calc-alkaline signature of the Q-suite intrusions cannot reflect contamination of alkaline parental liquids by HFSE-depleted, LREE enriched trondhjemitic melts, it is not possible to unequivocally determine whether the uncontaminated Q-suite liquids had flat or LREE-depleted trace element profiles. The flat trace element profiles of the Fe-rich rocks of the Central Hearne belt (Sandeman et al., 2004) are, however, decisively unfractionated. The Ti/Y_{MORB} ratios (1.2-1.6) of the Newton Lake Formation lavas are lower than those of pyroclastic alkaline ferropicrites from the Superior Province (2.8 +1.3/-0.8) or the Lake of Enemy region (2.4 +0.7/-0.5), and coupled with their low LREE/HREE ratios, indicate they do not have an alkaline affinity. The trace element data for the ferropicritic rocks of the Karelian Province of the Baltic Shield are too scarce to permit confident interpretation, but the available unfractionated to Nb-depleted trace-element profiles suggest they are not alkaline. In contrast to the alkaline ferropicrites, which display strong fractionations of LREE and mild fractionations of HREE, ferropicrites lacking the alkaline signature are characterized by unfractionated, flat HREE profiles, and flat to strongly LREE-enriched profiles (Fig. 4-3).

The trace element profiles of the Neoarchean ferropicritic rocks indicate the existence of at least two distinct magma types: 1) alkaline ferropicrites, whose trace element geochemistry resembles that of the modern-day OIB and 2) subalkaline ferropicrites, whose trace element systematics appear to resemble that of modern day MORB. The subalkaline ferropicrites range in composition from strongly subalkaline, orthopyroxene-rich suites to mildly subalkaline and transitional suites.

4.2 Relative timing of Neoarchean ferropicrites

Ferropicrites are rare in the geological record and limited to a small number of post ca. 2.7 Ga occurrences, including the Proterozoic Pechenga (Hanski and Smolkin, 1995), Jurassic Vestfjella (Heinonen and Luttinen, 2008), Cretaceous Etendeka (Gibson et al., 2000), and Permian Tamba (Ichiyama et al., 2006) ferropicrites. This paucity of post-Archean ferropicrites suggests that their high relative abundance ca. 2.7 Ga may reflect an important time in the geochemical evolution of the mantle.

Ferropicritic intrusions represent the terminal igneous pulse in the cratonization of the Northeastern Superior Province (Milidragovic et al., in preparation), and Maurice et al. (2009) showed that the chemostratigraphy of greenstone belts in the Ungava craton evolved from Mg-rich to Fe-rich. Jolly (1979) argued that within individual volcanic cycles in the Abitibi domain, a typical succession comprises Mg-tholeiitic metavolcanics that are overlain by Fe and Ti-rich tholeiites and finally lavas of calc-alkaline affinity. In the southern and western Superior Province, the late emplacement of Fe-rich magmas, relative to the Mg-rich rocks, is evident in the Dayohessarah belt where ferropicritic plugs intrude older Mg-tholeiites and komatiites (Goldstein and Francis, 2008) and in the Schreiber-Hemlo belt where the Fe-rich alkaline volcanics and underlying intrusive rocks outcrop near the top of the ca. 2.78-2.72 Ga Pulpwood-Playter Harbours sequence (Kitayama and Francis, in preparation).

Ca. 2.7 Ga ferropicrites may not be, however, universally late with respect to the Fe-poor rocks that make up the bulk of the greenstone stratigraphy. The southern Abitibi greenstone belt has been subdivided into nine assemblages (Ayer et al., 2002) that record semi-continuous, but cyclical volcanic activity. The Boston Creek flow ferropicrite is situated within the third oldest (ca. 2723-2720 Ma) Stoughton-Roquemaure Assemblage

(Ayer et al., 2002). The flow is underlain by the komatiitic Wabewawa Group and overlain by the tholeiitic Catherine Group (Stone et al., 1987), indicating ferropicritic magmatism was relatively early in the evolution of the Abitibi belt, and near-synchronous with the emplacement of komatiites and tholeiites. Similarly, the emplacement of alkaline Fe-rich basalts in the Wawa subprovince has been interpreted to be contemporaneous with the tholeiitic basalts (Polat, 2009).

The foregoing discussion of stratigraphic and age relationships between ca. 2.7 Ga mafic-ultramafic igneous rocks suggests that within individual magmatic cycles, the ferropicrites are relatively late. However, in a broader Neoarchean context, the emplacement of ferropicrites was near-synchronous with ubiquitous Mg-rich komatiites and tholeiites, suggesting that ferropicrites do not reflect secular change during the evolution of greenstone belt volcanism.

4.3 Major element compositions of alkaline ferropicrite liquids

Neoarchean alkaline Fe-rich rocks include crystal-dominated cumulates and lithologies interpreted as near-liquid compositions. Rocks interpreted to approach parental liquid compositions occur within the Boston Creek flow and the Pulpwood-Playter Harbours sequence of the Superior Province (Kitayama and Francis, in preparation; Stone et al., 1995a), and at the Lake of Enemy in the Slave Province (Francis et al., 1999). The Enriched High-MgO Tholeiite dykes (EHMT; McCuaig et al., 1994) of the Kambalda sequence in the Yilgarn carton are also interpreted to approach liquid compositions. With the exception of the Fe-rich lavas of the Pulpwood-Playter Harbours sequence, the most magnesian rocks from these localities suggest parental liquid compositions with a limited range of MgO (12-16 wt.%) and FeO^{TOT} (14-19 wt.%)

concentrations and having low Al_2O_3 (4-11 wt.%) contents and Al_2O_3/TiO_2 ratios (3-6). The Fe-rich lavas are less magnesian (MgO =6-11 wt. %) and were interpreted by Kitayama and Francis (in preparation) to be hybrids formed by mixing between tholeiitic magmas and a strongly Fe-enriched alkaline magma with a minimum MgO content of ~ 9 wt. % (FeO^{TOT} ~19 wt. %, Al_2O_3 =10.5 wt. %).

The Fe-rich intrusive rocks of the Dayohessarah Lake belt plot along a line with a slope of ~2 on the $(Mg+Fe^{TOT})/Ti$ vs. Si/Ti diagram indicating their compositional variation is chiefly controlled by olivine accumulation (Russell and Nicholls, 1988), and that serpentinization did not result in significant metasomatic gains or losses. We performed equilibrium melting calculations on the most magnesian peridotite (DY-71, MgO = 35 wt.%, Mg-number =0.81; Goldstein and Francis, 2008), using the program alphaMELTS (Ghiorso and Sack, 1995; Smith and Asimow, 2005), assuming low pressure crystallization (0.05 GPa), until olivine and Cr-rich spinel were the sole liquidus phases in equilibrium ($(Mg/Fe)_{liq}/(Mg/Fe)_{ol}$ = 0.3; Roeder and Emslie, 1970)) with the coexisting liquid. The composition of this liquid was taken to approximate the composition of the peridotite's parental magma. The estimated parental magma of the Dayohessarah Lake greenstone belt peridotites (MgO ~14.5 wt. %, FeO^{TOT} ~16 wt. % and Al_2O_3 ~11 wt. %.) is consistent with the compositions of the primitive volcanic ferropicrites from the Boston Creek flow.

The pyroclastic alkaline ferropicrites from the Lumby Lake and Steep Rock Greenstone belts and the Grassy Portage Bay ultramafic units display a range of MgO (11-24.5 wt. %) and Ni (530-1650 ppm) contents, which suggest that these rocks may include both differentiated liquid compositions and magmas that have accumulated

Table 4-2: Parental compositions of ca. 2.7 Ga ferropicrites

Loc.	BCF	Dayo	Schreib-Hem		Vermillion	Q-subalk	Q-trans	C. Hearne
Ref.	3	-	11	-	16	18	3	20
SiO_2	49.85	48.9	47.89	45.5	48.4	47.9	49.9	45.2
TiO_2	0.82	2.1	2.64	2.0	1.0	0.6	0.8	1.1
Al_2O_3	4.72	11.0	10.49	7.7	8.8	14.8	4.72	13.3
Cr_2O_3	0.18	0.6	-	-	-	0.1	0.2	0.06
FeO^{TOT}	17.00	15.7	18.59	18.5	14.0	14.1	17.0	15.0
MnO	0.21		0.72	0.7	0.2	-	0.21	0.25
MgO	15.60	14.6	9.05	17.7	13.6	10.9	15.6	12.6
NiO	0.17	-	-	-	-	-	0.17	0.02
CaO	10.89	6.8	10.10	7.5	12.1	8.4	10.9	10.8
Na_2O	0.51	0.1	0.23	0.2	1.7	1.6	0.5	1.5
K_2O	0.03	0.1	0.12	0.1	0.2	1.4	0.03	0.16
P_2O_5	0.03	0.2	0.18	0.1	0.1	0.2	0.03	0.08

olivine. The pyroclastic samples containing 1000-1500 ppm Ni show the full range of MgO contents, inconsistent with liquid compositions formed by differentiation from a common parental magma, or by different degrees of partial melting of a similar mantle source. The overall Ni vs. MgO distribution of the pyroclastic ferropicrites of the Superior Province is, however, consistent with variable degrees of pre-eruptive accumulation of olivine in a ferropicritic magma undergoing differentiation (Figure 4-6).

The aphanitic samples from the Boston Creek flow and the Lake of Enemy, thus, provide the best estimate of the parental alkaline ferropicrite compositions. The alkaline ferropicrites are considered to have ≤16 wt. % MgO, 14-19 wt. % FeO^{TOT}, low abundances of Al_2O_3 (≤ 11 wt. %) and corresponding low Al_2O_3/TiO_2 ratios (≤6).

4.4 Major element compositions of the subalkaline ferropicrite liquids

Milidragovic et al. (in preparation) demonstrated that Q-suite plutons were derived from transitional Fe-rich picritic and subalkaline high-Mg basaltic liquids. The large difference in the FeO^{TOT} concentrations and CaO/Al_2O_3 ratios of the Q-suite parental magmas precludes the derivation of the high-Mg basalts from the more magnesian transitional picrites by olivine fractionation. Furthermore, the subalkaline and transitional parental magmas show a large difference in Al_2O_3 contents at relatively similar SiO_2 concentrations, which is inconsistent with the derivation of the subalkaline basalts through coupled fractional crystallization and assimilation of tonalitic crust.

The parental magmas of the weakly fractionated ferropicrites from the Newton Lake Formation (MgO ~13.5 wt. %, FeO^{TOT} ~14 wt. %, Al_2O_3 ~9 wt. %; Sample 2, Schulz, 1982) and the Central Hearne belt (MgO ~ 12.5 wt. %, FeO^{TOT} ~15 wt. %, Al_2O_3 ~13 wt. %; sample HS426, Sandeman et al., 2004) are intermediate between the

subalkaline and transitional Q-suite parental magmas, in terms of MgO, FeO^{TOT} and Al_2O_3 contents. The Al_2O_3/TiO_2 ratios of the subalkaline ferropicrites range between ~7 and ~20-25.

4.5 Mantle sources of ferropicrites

Alkaline ferropicrites have higher Ni (Fig. 4-6A) contents than primary melts with similar MgO contents that have equilibrated with the pyrolitic mantle (Herzberg, 2011). To remove the effects of olivine fractionation and accumulation, we normalized the compositions of volcanic and pyroclastic ferropicrites to an MgO content of 16 wt.% by fractionally adding or subtracting olivine using the program PRIMEL2.xls (Herzberg and Asimow, 2008). When normalized to 16 wt. % MgO, alkaline ferropicritic rocks of the Superior Province have high Ni contents (850 + 750/-450 ppm; median +/- 2IQR) that overlap the Ni contents of the Hawaiian olivine tholeiites (Sobolev et al., 2005). The normalized Ni contents of ferropicrites from the Slave Province (1200 +500/-600 ppm), Yilgarn Craton (850+450/-100) and Kaapvaal Craton (750-1100 ppm) are also high. The normalized Ni content of the ca. 2.7 Ga alkaline ferropicrites is ~2 times higher than that of pyrolite-equilibrated melts, suggesting that parental magmas to alkaline ferropicrites were anomalously rich in nickel.

In contrast to the high Ni contents of alkaline ferropicrites, the estimated Ni contents of the Q-suite parental magmas are very low (150-200 ppm; Milidragovic et al., in preparation) and the observed Ni concentrations in the olivines from the Q-suite peridotites and dunites are significantly less than the Ni contents of olivines that would crystallize from similarly magnesian primary pyrolite-derived magmas (Fig 4-6B). When normalized to 16 wt. % MgO the calculated Ni contents of the Q-suite parental liquids

range between 200-400 ppm, significantly below the normalized Ni content of the alkaline ferropicrites and primary pyrolite melts. The limited data from the Fe-rich rocks of the Central Hearne belt and the Newton Lake Formation suggests low whole rock Ni contents, consistent with derivation from magmas depleted in Ni, relative to melts of pyrolitic mantle. When normalized to 16 wt. % MgO, the rocks of the Central Hearne belt and the Newton Lake Formation yield Ni contents of 250 +400/-100 ppm and 550 +150/-200 ppm, respectively.

Two possible petrologic scenarios could account for the observed Ni enrichment of the Neoarchean alkaline ferropicrites. The first involves melting of an olivine-dominated peridotitic mantle whose Ni content is approximately double that of the pyrolitic mantle. The second scenario involves melting of a secondary, olivine-free pyroxenite source produced by metasomatism of peridotitic mantle, as proposed by Sobolev et al. (2005) in the genesis of the Hawaii's Ni-rich olivine tholeiites. Previous studies based on melting experiments and thermodynamic data (Hanski and Smolkin, 1995; Stone et al., 1995a; Tuff et al., 2005; Goldstein and Francis, 2008) have argued that ferropicritic magmas could not have equilibrated with residues containing both olivine and garnet. Tuff et al. (2005) argued that the Early Cretaceous Etendeka ferropicrites were produced by high pressure (≥5 GPa) melting of garnet-pyroxenite, formed by metasomatism of peridotitic mantle. This model, based on the experimental results of Yaxley (2000), suggested that garnet pyroxenite formed by the reaction between ~75 % of average basaltic crust and 25 % pyrolite could yield melts similar to the most primitive Etendeka ferropicrite.

Sobolev et al. (2007) used minor elements whose concentration in silicate melt is strongly controlled by the residual mineralogy of their source to infer the relative

contributions of peridotite and pyroxenite to magmas emplaced in different tectonic settings. We used a similar approach based on the comparison with modern day magmas to evaluate the possibility that the high Ni contents of the alkaline ferropicrites reflect melting of olivine-free pyroxenite sources. Scandium is a trace element which is incompatible in olivine (D_{Sc}^{ol}<0.5, GERM database), but moderately to strongly compatible in clinopyroxene and garnet (D_{Sc}^{cpx}~1-4, D_{Sc}^{grt} ~ 1-6). Scandium/iron ratios should, therefore, behave similarly to Mn/Fe ratios which Sobolev et al. (2007) used to quantify the contributions of different sources to magmas emplaced into crust. Nickel-rich alkaline ferropicrites of the Superior and Slave provinces are characterized by relatively low Sc/Fe ratios (10000 x Sc/Fe ≤3, where both Sc and Fe are expressed in ppm), which overlap the Sc/Fe ratios and Ni contents of Hawaiian olivine tholeiites, filtered for MgO > 10 wt. % (Fig. 4-7). In contrast, the strongly alkaline low-Sc/Fe Hawaiian lavas (filtered for MgO > 10 wt. %), have relatively low Ni contents (≤400 ppm) that are consistent with the proposed melting of predominantly garnet –lherzolitic mantle (Sobolev et al., 2005). Thus, the low Sc/Fe ratios and high Ni contents of Neoarchean alkaline ferropicrites are consistent with derivation from of olivine-free garnet-pyroxenite sources, which have a relatively strong affinity for Sc and a relatively low affinity for Ni (Sobolev et al., 2007).

The relatively high Sc/Fe ratios and low Ni contents of Central Hearne ferropicrites (10000 x Sc/Fe >3) and MORB and Icelandic lavas (Fig. 4-7) are consistent with derivation by shallow (garnet-free) melting of olivine-dominated mantle. Because olivine has a much greater affinity for Fe than Sc, the Sc/Fe ratios of rocks that have accumulated olivine are lower than those of their parental magmas. We estimated the maximum Sc

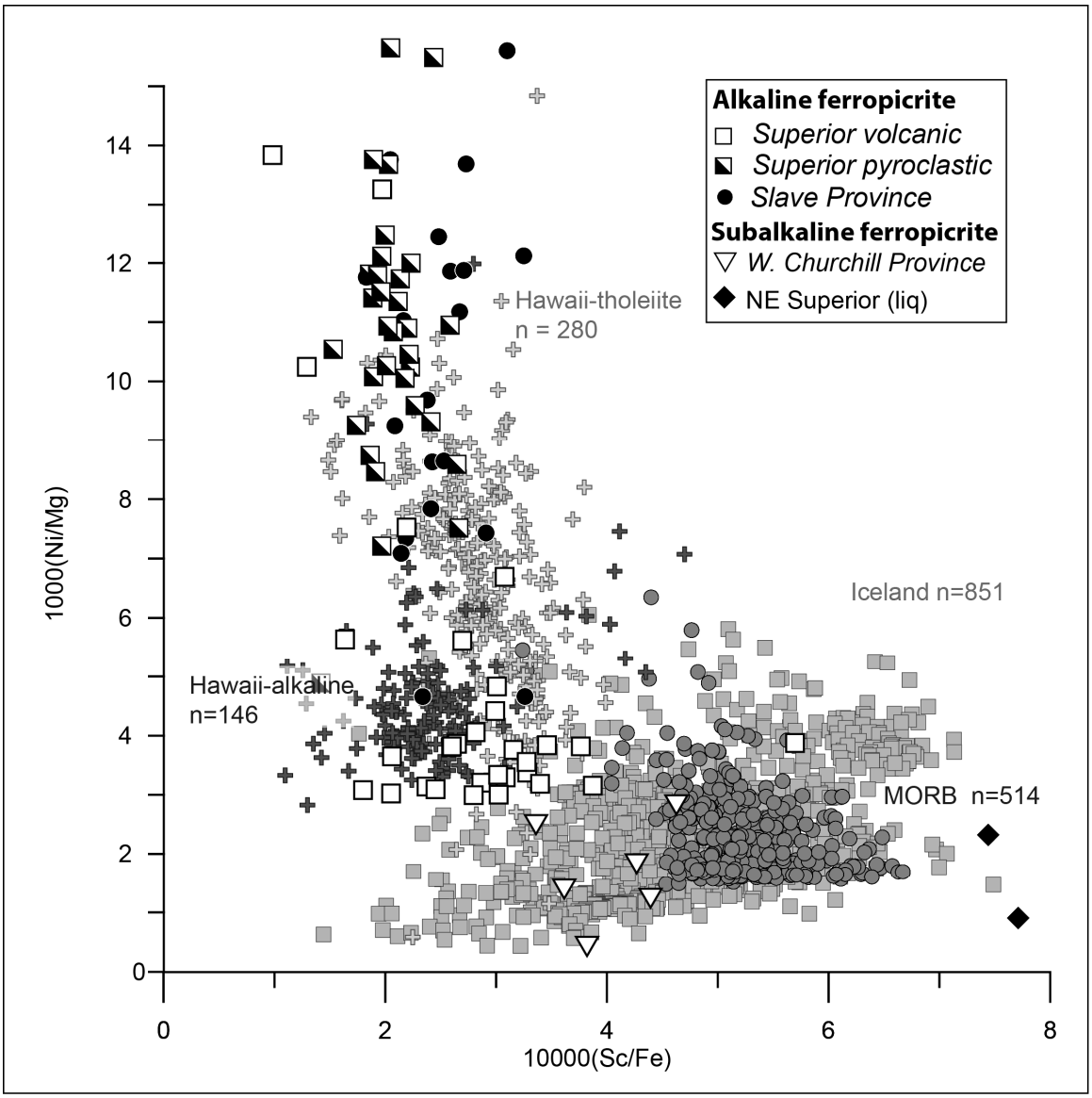

Figure 4-7: 1000 (Ni/Mg) vs. 10000 (Sc/Fe)
Comparison of alkaline and subalkaline extrusive ferropicrites to modern day MORB, and lavas from Iceland and Hawaii. All units are in ppm. Nickel concentrations were normalized to whole rock Mg content, in order to minimize the effects of olivine accumulation. Data as in Fig. 4-5.

content of the transitional Q-suite parental magma by assuming that all Sc is contained within the interstitial (trapped liquid) component of Q-suite dunites. The maximum Sc/Fe ratios of the magmas parental to the transitional Q-suite olivine cumulates are high (10000 x (Sc/Fe) ~ 7-8). The large range in the Sc/Fe ratios in ferropicritic rocks (3-7 x 10000), suggests that the Sc/Fe ratios are independent of the Fe-content of the magma, and therefore provide a suitable proxy for the mineralogy of the source.

Neoarchean alkaline ferropicrites have significantly higher FeO^{TOT} contents than the Cretaceous Etendeka ferropicrites (13.5-16 wt. %; Fig. 4-8), which Tuff et al. (2005) argued were formed by high pressure (≥5 GPa) melting of secondary garnet-pyroxenite. A bulk pyroxenite, containing an even higher proportion of crustal component would be too poor in MgO to produce the MgO contents of the parental alkaline ferropicrites. Low-degree experimental melts at 5GPa of garnet pyroxenite MIX1G (Fig. 4-8; Hirschmann et al., 2003; Kogiso et al., 2003) have MgO (13-14 wt. %) and Al_2O_3 (6-10 wt. %) contents that are similar to those of the parental alkaline ferropicrites. The melts of MIX1G, however, are poor in iron (Fe^{TOT} ≤14 wt. %) relative to the alkaline ferropicrites. MIX1G has intermediate composition within the array of mantle garnet-pyroxenite, but garnet pyroxenite xenoliths sufficiently rich in both MgO and FeO to produce magmas parental to the Neoarchean alkaline ferropicrites have been recorded (Fig. 4-8; GEOROC database).

Walker and Stone (2001) demonstrated that the initial $^{187}Os/^{188}Os$ ratios of the Boston Creek flow are significantly lower than those of the Primitive Upper Mantle or chondritic meteorites (Meisel et al., 2001; Walker et al., 2002), implying a 500-1000 m.y.-long Re-depletion in the Boston Creek Flow source. The Early Archean melting

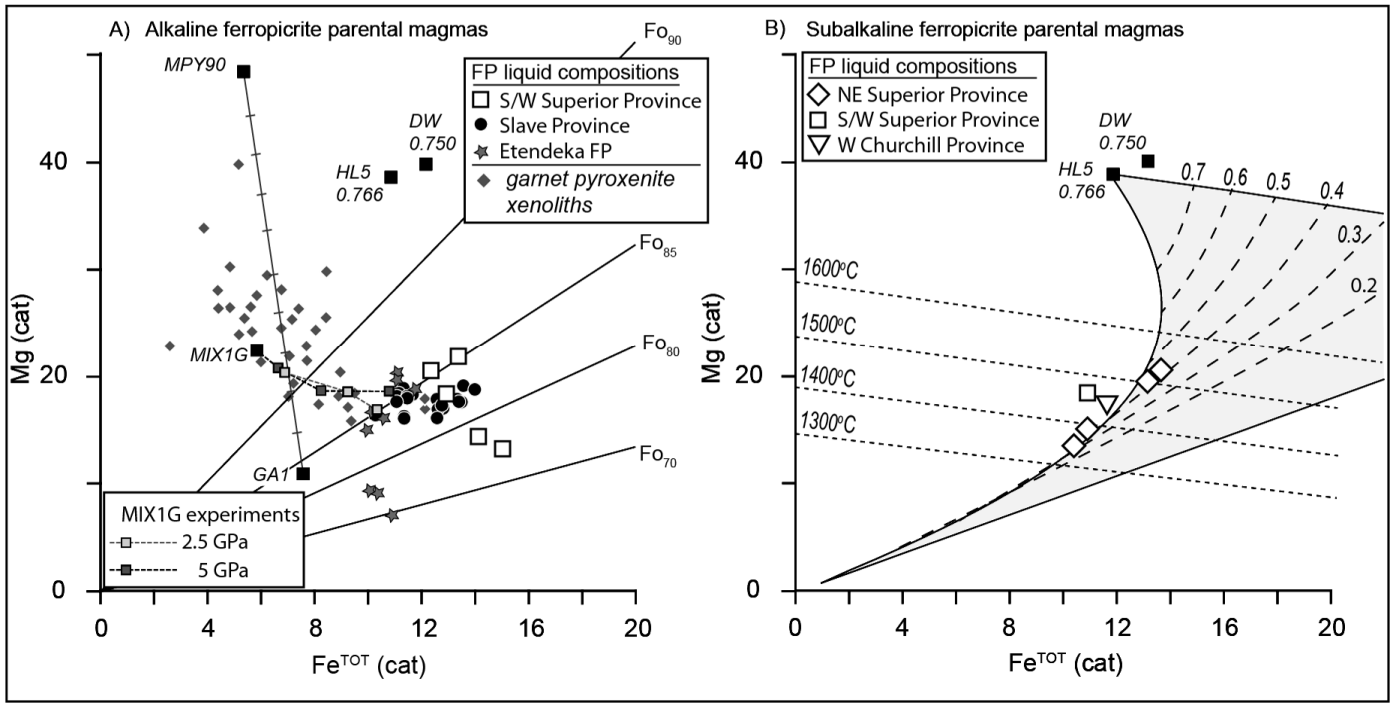

Figure 4-8: Mg vs. Fe^{TOT} cation plots of parental ferropicrite compositions.
A) Alkaline ferropicrites are compared to the Etendeka ferropicrites, which Tuff et al. (2005) argued are produced by melting of a secondary garnet-pyroxenite formed through a reaction between ~75 % oceanic crust (GA1) and ~25 % mantle peridotite (MPY90). Also shown are the results of melting experiments on garnet-pyroxenite MIX1G at pressures of 2.5 GPa (Hirschmann et al., 2003) and 5 GPa (Kogiso et al., 2003). Although most alkaline ferropicrites have higher contents than low degree partial melts of MIX1G, a significant number of garnet-pyroxenite xenoliths (grey diamonds; GEOROC database) have FeO^{TOT} and MgO contents that would be suitable for production of ferropicrite melts. DW - Fe-rich spinel lherzolite with Mg-number = 0.750 (Dreibus and Wanke, 1985; Bertka and Holloway, 1994); HL5- Chondritic meteorite with Mg-number = 0.766 (Agee and Draper, 2004). **B)** The parental subalkaline ferropicrites are superimposed on the "sail" shaped melting field of the ordinary chondrite HL5 (Milidragovic et al., in preparation), calculated after Langmuir and Hanson (1980). The gently sloping lines are isotherms calculated for P = 5 GPa (Putirka et al., 2007) using the anhydrous composition of the transitional Q-suite parental magma.

event that produced the long-term Re depletion may have also depleted the Al_2O_3 content of the Boston Creek flow source, thus providing a possible explanation for the very low Al_2O_3, content of alkaline ferropicrites. The overall suprachondritic initial ε_{Nd} (2.7 Ga) values of the alkaline ferropicrites from the southern/western Superior and Slave provinces (-2 to +3; (Stone et al., 1995a; Francis et al., 1999; Goldstein and Francis, 2008) suggest that the trace element enrichment of their mantle sources was a short-lived feature originating ≤ 3 Ga. The pyroxenite sources were thus metasomatically enriched in incompatible trace elements a relatively short time before the melting that produced the Neoarchean alkaline ferropicrites. The inferred garnet-pyroxenite sources of the alkaline ferropicrites may have formed by reaction between peridotite and the trace element-enriched metasomatizing melts. Two possible end-member scenarios require either metasomatism of pyrolitic mantle by an Fe-rich component, or metasomatism of an Fe-rich peridotite approaching the composition of the Martian mantle or ordinary chondrites (Milidragovic et al., in preparation; Bertka and Holloway, 1994; Agee and Draper, 2004).

In addition to the low Ni contents, the relatively high Sc/Fe ratios and unfractionated HREE profiles, the Al_2O_3/TiO_2 ratios of the subalkaline ferropicrites are higher than those of the alkaline ferropicrites (Fig. 4-4 and Fig. 4-5) and are consistent with a source in which garnet does not control the partitioning of Al_2O_3 into the melt. The overall Al_2O_3 contents of the subalkaline ferropicrites are low when compared to the rocks of the Archean Fe-poor array, suggesting their peridotite sources were relatively depleted in Al_2O_3. Furthermore, the source peridotites were also depleted in Ni relative to estimates of standard pyrolitic mantle (Herzberg, 2011), and were variably depleted in incompatible trace elements.

The flat to LREE-depleted trace element profiles of the subalkaline ferropicrites suggests that the mantle sources of these magmas did not experience the same metasomatic enrichment inferred for the alkaline ferropicrite source (Stone et al., 1995a), and therefore, that the high-Fe contents of ca. 2.7 Ga subalkaline ferropicrites are not a result of metasomatic enrichment. The array of calculated subalkaline ferropicrite magma compositions suggests either a range in source Fe contents and Al_2O_3/TiO_2 and Nb/Y ratios, or different degrees of melting of compositionally similar source regions under different P-T regimes, or a combination of the two (Milidragovic et al., in preparation).

Volumetrically minor, but widespread emplacement of ca. 2.7 Ga ferropicrites occurred synchronously with the emplacement of ubiquitous komatiites and Mg-tholeiites during the global Neoarchean mantle melting event (Stein and Hofmann, 1994; Condie, 1998, 2000; Rino et al., 2004) that contributed significant volumes of juvenile material to continental crust (Condie et al., 2009; Hawkesworth et al., 2009; Milidragovic and Francis, 2014). Such a scenario is compatible with a model in which domains of Fe-rich peridotite and pyroxenite existed as "plums" (Sun, 1985) in a predominantly pyrolitic peridotite mantle. The compositions of the Fe-rich domains appear to have been as diverse as the present-day upper mantle, yielding magmas that ranged in affinity from modern OIB to MORB. The apparent negatively sloping Al_2O_3/TiO_2 vs. Nb/Y trend (Fig. 4-5) observed among the alkaline ferropicrites projects towards the relatively low Nb/Y and Al_2O_3/TiO_2 ratios of subalkaline ferropicrites, perhaps indicating a spectrum of ferropicrite compositions formed by mixing between two Fe-rich magma end members. If Fe-rich garnet-pyroxenites were formed by metasomatism of Fe-rich peridotite, such mixing would be expected in plums that did not experience complete conversion to

garnet-pyroxenite. The relative scarcity of ferropicrites younger than ca. 2.7 Ga (Hanski and Smolkin, 1995; Gibson et al., 2000; Ichiyama et al., 2006; Heinonen and Luttinen, 2008) may reflect a lower abundance of Fe-rich domains in the post-Archean terrestrial mantle. This observation suggests that most Fe-rich "plums" may have melted out during the Neoarchean melting event.

5. Conclusions

Although ferropicrites are rare in the geological record, there are numerous ca. 2.7 Ga occurrences in the Superior, Slave, Yilgarn, Kaapvaal, West Churchill and Karelia cratons. Ferropicrites form two groups, distinguished by their incompatible trace elements, Ni contents, and Al_2O_3/TiO_2 and Nb/Y ratios. Alkaline ferropicrites are characterized by fractionated REE, an absence of systematic HFSE anomalies, low Al_2O_3/TiO_2 and Sc/Fe ratios and high Ni contents. The subalkaline ferropicrites are characterized by relatively flat to LREE-depleted parental compositions, higher Al_2O_3/TiO_2 and Sc/Fe ratios, and lower concentrations of Ni. The alkaline ferropicrites form an Al_2O_3/TiO_2 vs. Nb/Y array that extends toward subalkaline ferropicrites, suggesting that there may be a spectrum of ferropicrite compositions formed by mixing between two magma end members.

The high Ni contents and low Sc/Fe ratios of the alkaline ferropicrites indicate that they may be derived from olivine-free garnet-pyroxenite sources. The subalkaline ferropicrites, in contrast, appear to have been derived from garnet-free olivine peridotite sources, which buffered the Sc and Ni contents in the melts at relatively high and low concentrations, respectively. Neodymium isotopic data suggests that the garnet-

pyroxenite source of the alkaline ferropicrites was metasomatically enriched shortly before their ca. 2.7 Ga emplacement. The peridotite sources of the subalkaline ferropicrites did not experience such a metasomatic enrichment.

The coeval emplacement of ferropicrite magmas on six separate cratons suggests that they play integral part in the global Neoarchean mantle melting event. The intimate association of ferropicritic magmas with the far more abundant komatiite and Mg-tholeiite magmas is consistent with a "plum" model in which Fe-rich heterogeneities were distributed throughout the Archean mantle. The apparent decrease in ferropicrite abundance since the Neoarchean may indicate that such Fe-rich plums were largely exhausted during the Neoarchean mantle melting.

Acknowledgments

This work was supported by the Natural Science and Research Council of Canada (NSERC) and Polar Continental Shelf grants to D.F. and the Northern Scientific Training Program (NSTP) grant to D.M. We thank Leila Chalati, Greg Dobbelsteyn, Nick Borque, and Ian Carvalho Campos for their assistance in the field.

References

Agee, C.B., Draper, D.S., 2004. Experimental constraints on the origin of Martian meteorites and the composition of the Martian mantle. Earth Planet. Sci. Lett. 224, 415–429.

Armstrong, R.A., Compston, W., Retief, E.A., Williams, I.S., Welke, H.J., 1991. Zircon ion microprobe studies bearing on the age and evolution og the Witwatersrand triad. Precambrian Res. 53, 243–266.

Ayer, J.A., Amelin, Y., Corfu, F., Kamo, S., Ketchum, J., Kwok, K., Trowell, N., 2002. Evolution of the southern Abitibi greenstone belt based on U-Pb geochronology: autochtonous volcanic construction followed by plutonism, regional deformation and sedimentation. Precambrian Res. 115, 63–95.

Bédard, J.H., 1994. A procedure for calculating the equilibrium distribution of trace elements among the minerals of cumulate rocks, and the concentration of trace elements in the coexisting liquids. Chem. Geol. 118, 143–153.

Bédard, J.H., 2003. Metamorphism in the Archaean Minto Block, Northern Superior Province, Canada. J. Geol. 111, 183–205.

Bédard, J.H., 2006. A catalytic delamination-driven model for coupled genesis of Archaean crust and sub-continental lithospheric mantle. Geochim. Cosmochim. Acta 70, 1188–1214.

Bertka, C.M., Holloway, J.R., 1994. Anhydrous partial melting of an iron-rich mantle II: primary melt compositions at 15 kbar. Contrib. to Mineral. Petrol. 115, 323–338.

Bickford, M.E., Wooden, J.L., Bauer, R.L., 2006. SHRIMP study of zircons from Early Archean rocks in the Minnesota River Valley: Implications for the tectonic history of the Superior Province. Geol. Soc. Am. Bull. 118, 94–108.

Bleeker, W., Villeneuve, M.E., 1995. Lithoprobe SNORCLE Rep. 44 8–13.

Böhm, C.O., Heaman, L.M., Creaser, R.A., Corkery, M.T., 2000. Discovery of pre-3.5 Ga exotic crust at the northwestern Superior Province margin, Manitoba. Geology 28, 75–78.

Boily, M., Leclair, A., Maurice, C., Bédard, J.H., David, J., 2009. Paleo- to Mesoarchean basement recycling and terrane definition in the Northeastern Superior Province, Québec, Canada. Precambrian Res. 168, 23–44.

Card, K.D., 1990. A review of the Superior Province of the Canadian Shield, a product of Archean accretion. Precambrian Res. 48, 99–156.

Cates, N.L., Mojzsis, S.J., 2007. Pre-3750 Ma supracrustal rocks from the Nuvvuagittuq supracrustal belt, northern Quebec. Earth Planet. Sci. Lett. 255, 9–21.

Condie, K.C., 1998. Episodic continental growth and supercontinents: a mantle avalanche connection? Earth Planet. Sci. Lett. 163, 97–108.

Condie, K.C., 2000. Episodic continental growth models: afterthoughts and extensions. Tectonophysics 322, 153–162.

Condie, K.C., Belousova, E., Griffin, W.L., Sircombe, K.N., 2009. Granitoid events in space and time: Constraints from igneous and detrital zircon age spectra. Gondwana Res. 15, 228–242.

Corfu, F., Muir, T.L., 1989. The Hemlo-Heron Bay greenstone belt and Hemlo Au-Mo deposit, Superior Province, Ontario, Canada: 1. Sequence of igneous activity determined by zircon U-Pb geochronology. Chem. Geol. 79, 183–200.

Corfu, F., Noble, S.R., 1992. Genesis of the southern Abitibi greenstone belt, Superior Province, Canada: Evidence form zircon Hf-isotope analyses using a single fillament technique. Geochim. Cosmochim. Acta 56, 2527–2531.

Corfu, F., Stott, G.M., 1998. Shebandowan greenstone belt, western Superior Province: U-Pb ages, tectonic implications, and correlations. Geol. Soc. Am. Bull. 110, 1467–1484.

Davis, D.W., Jackson, M.C., 1988. Geochronology of the Lumby Lake greenstone belt: a 3 Ga complex within the wabigoon Subprovince, northwest Ontario. Geol. Soc. Am. Bull. 100, 818–824.

Davis, D.W., Poulsen, K.H., Kamo, S.L., 1989. New insights into Archean crustal development from geochronology in the Rainy Lake area, Superior Province, Canada. J. Geol. 97, 379–398.

De Kock, M.O., Beukes, N.J., Armstrong, R. a., 2012. New SHRIMP U–Pb zircon ages from the Hartswater Group, South Africa: Implications for correlations of the Neoarchean Ventersdorp Supergroup on the Kaapvaal craton and with the Fortescue Group on the Pilbara craton. Precambrian Res. 204-205, 66–74.

Faure, S., Daigneault, R., Godey, S., 2008. Upper mantle architecture of the Archean Superior Province and the implication for the dimension, orientation, metamorphism, and mineralization of the greenstone belts, in: GAC-MAC Joint Annual Meeting, Program with Abstracts.

Francis, D., Ludden, J., Johnstone, R., Davis, W., 1999. Picrite evidence for more Fe in Archean mantle reservoirs. Earth Planet. Sci. Lett. 167, 197–213.

Francis, D., Hynes, A.J., Ludden, J.N., Bédard, J.H., 1981. Crystal fractionation and partial melting in the petrogenesis of a Proterozoic high-MgO volcanic suite , Ungava , Qubéc. Contrib. to Mineral. Petrol. 78, 27–36.

Ghiorso, M.S., Sack, R.O., 1995. Chemical mass transfer in magmatic processes IV. A revised and internally consistent thermodynamic model for the interpolation and extrapolation of liquid-solid equilibria in magmatic systems at elevated temperatures and pressures. Contrib. to Mineral. Petrol. 119, 197–212.

Gibson, S.A., Thompson, R.N., Dickin, A.P., 2000. Ferropicrites : geochemical evidence for Fe-rich streaks in upwelling mantle plumes. Earth Planet. Sci. Lett. 174, 355–374.

Goldstein, S.B., Francis, D., 2008. The Petrogenesis and Mantle Source of Archaean Ferropicrites from the Western Superior Province, Ontario, Canada. J. Petrol. 49, 1729–1753.

Goldstein, S.L., O'Nions, R.K., Hamilton, P.J., 1984. A Sm-Nd isotopic study of atmospheric dusts and particulates from major river systems. Earth Planet. Sci. Lett. 70, 221–236.

Green, J.C., Schulz, K.J., 1977. Iron-rich basaltic komatiites in the early Precambrian Vermillion District, Minnesota. Can. J. Earth Sci. 14, 2181–2192.

Hanski, E.J., Smolkin, V.F., 1995. Iron- and LREE-enriched mantle source for early Proterozoic intraplate magmatism as exemplified by the Pechenga ferropicrites , Kola Peninsula , Russia. Lithos 34, 107–125.

Hawkesworth, C., Cawood, P., Kemp, T., Storey, C., Dhuime, B., 2009. A matter of preservation. Science (80-.). 323, 49–50.

Heinonen, J.S., Luttinen, A. V., 2008. Jurassic dikes of Vestfjella, western Dronning Maud Land, Antarctica: Geochemical tracing of ferropicrite sources. Lithos 105, 347–364.

Herzberg, C., 2011. Identification of Source Lithology in the Hawaiian and Canary Islands: Implications for Origins. J. Petrol. 52, 113–146.

Herzberg, C., Asimow, P.D., 2008. Petrology of some oceanic island basalts: PRIMELT2.XLS software for primary magma calculation. Geochemistry, Geophys. Geosystems 9, 25.

Hirschmann, M.M., Kogiso, T., Baker, M.B., Stolper, E.M., 2003. Alkalic magmas generated by partial melting of garnet pyroxenite. Geology 31, 481–484.

Hollings, P., Wyman, D., 1999. Trace element and Sm-Nd systematics of volcanic and intrusive rocks from the 3 Ga Lumby Lake Greenstone belt, Superior Province: evidence for Archean plume-arc interaction. Lithos 46, 189–213.

Ichiyama, Y., Ishiwatari, A., Hirahara, Y., Shuto, K., 2006. Geochemical and isotopic constraints on the genesis of the Permian ferropicritic rocks from the Mino-Tamba belt, SW Japan. Lithos 89, 47–65.

Jolly, W.T., 1979. Development and degradation of Archean Lavas , Abitibi area , Canada , in light of major element geochemistry. J. Petrol. 21, 323–363.

Kogiso, T., Hirschmann, M.M., Frost, D.J., 2003. High-pressure partial melting of garnet pyroxenite: possible mafic lithologies in the source of ocean island basalts. Earth Planet. Sci. Lett. 216, 603–617.

Labbé, J., Lacoste, P., Leclair, A., Parent, M., Davy, J., 2001. The Qullinaaraaluk Ni-Cu-Co showing: a new type of mineralization in the Archean rocks of the Far North. Géologie Quebéc 1–11.

Langmuir, C.H., Hanson, G.N., 1980. An evaluation of major element heterogeneity in the mantle sources of basalts. Phil. Trans. R. Soc. Lond. A 297, 383–407.

Maurice, C., David, J., Bédard, J.H., Francis, D., 2009. Evidence for a widespread mafic cover sequence and its implications for continental growth in the Northeastern Superior Province. Precambrian Res. 168, 45–65.

McCuaig, T.C., Kerrich, R., Xie, Q., 1994. Phosphorus and high field strength element anomalies of source mineralogy and depth. Earth Planet. Sci. Lett. 124, 221–239.

McIver, J.R., Cawthorn, R.G., Wyatt, B.A., 1982. The Ventersdorp Supergroup - the youngest komatiitic sequence in southern Africa, in: Arndt, N.T., Nisbet, E.G. (Eds.), Komatiites. Allen and Unwin, Boston, pp. 81–90.

Meisel, T., Walker, R.J., Irving, A.J., Lorand, J.-P., 2001. Osmium isotopic composition of mantle xenoliths: A global perspective. Geochim. Cosmochim. Acta 65, 1311–1323.

Milidragovic, D., Francis, D., 2014. Ferropicrite-driven reworking of the Ungava craton and the genesis of Neoarchean pyroxene-granitoids. Earth Planet. Sci. Lett. 386, 138–148.

Mungall, J.E., Harvey, J.D., Balch, S.J., Azar, B., Atkinson, J., Hamilton, M.A., 2010. Eagle's Nest: A magmatic Ni-sulfide deposit in the James Bay Lowlands, Ontario, Canada. Soc. Econ. Geol. Spec. Publ. 15 539–557.

O'Neil, J., Carlson, R.W., Francis, D., Stevenson, R.K., 2008. Neodymium-142 evidence for Hadean mafic crust. Science (80-.). 321, 1828–1831.

Palme, H., Neill, H.S.C.O., 2004. Cosmochemical Estimates of Mantle Composition, in: Holland, H.D., Turrekian, K.K. (Eds.), Treatise on Geochemistry. Elsevier, Amsterdam, The Netherlands, pp. 1–38.

Papunen, H., Halkoaho, T., Luukkonen, E., 2009. Archaean Evolution of the Tipasjärvi-Kuhmo-Suomussalmi Greenstone Complex, Finland. Geol. Surv. Finl. Bulletin 4, 84.

Percival, J.A., Sanborn-Barrie, M., Skulski, T., Stott, G.M., Helmstaedt, H., White, D.J., 2006. Tectonic evolution of the western Superior Province from NATMAP and Lithoprobe studies. Can. J. Earth Sci. 1117, 1085–1117.

Percival, J.A., Stern, R.A., Skulski, T., 2001. Crustal growth through successive arc magmatism : reconnaissance U – Pb SHRIMP data from the Northeastern Superior Province, Canada. Precambrian Res. 109, 203– 238.

Pettigrew, N.T., Hattori, H., 2006. The Quetico Intrusions of Western Superior Province: Neo-Archean examples of Alaskan/Ural-type mafic-ultramafic intrusions. Precambrian Res. 149, 21–42.

Polat, A., 2009. The geochemistry of Neoarchean (ca. 2700 Ma) tholeiitic basalts, transitional to alkaline basalts, and gabbros, Wawa Subprovince, Canada: Implications for petrogenetic and geodynamic processes. Precambrian Res. 168, 83–105.

Polat, A., Kerrich, R., Wyman, D. a, 1999. Geochemical diversity in oceanic komatiites and basalts from the late Archean Wawa greenstone belts, Superior Province, Canada: trace element and Nd isotope evidence for a heterogeneous mantle. Precambrian Res. 94, 139–173.

Rino, S., Komiya, T., Windley, B.F., Katayama, I., Motoki, A., Hirata, T., 2004. Major episodic increases of continental crustal growth determined from zircon ages of river sands; implications for mantle overturns in the Early Precambrian. Phys. Earth Planet. Inter. 146, 369–394.

Roeder, P.L., Emslie, R.F., 1970. Olivine-Liquid Equilibrium. Contrib. to Mineral. Petrol. 29, 275–289.

Russell, J.K., Nicholls, J., 1988. Analysis of petrologic hypotheses with Pearce elemeent ratios. Contrib. to Mineral. Petrol. 99, 25–35.

Said, N., Kerrich, R., 2010. Magnesian dyke suites of the 2.7 Ga Kambalda Sequence, Western Australia: Evidence for coeval melting of plume asthenosphere and metasomatised lithospheric mantle. Precambrian Res. 180, 183–203.

Sandeman, H., Hanmer, S., Davis, W., Ryan, J., Peterson, T., 2004. Neoarchaean volcanic rocks, Central Hearne supracrustal belt, Western Churchill Province, Canada: geochemical and isotopic evidence supporting intra-oceanic, supra-subduction zone extension. Precambrian Res. 134, 113–141.

Schaefer, S.J., Morton, P., 1991. Two komatiitic pyroclastic units, Superior Province, northwestern Ontario: their geology, petrography, and correlation. Can. J. Earth Sci. 28, 1455–1470.

Schulz, K.J., 1982. Magnesian basalts from the Archean terrains of Minnesota, in: Arndt, N.T., Nisbet, E.G. (Eds.), Komatiites. George Allen & Unwin, London, pp. 171–186.

Schweitzer, J., Kröner, A., 1985. Geochemistry and petrogenesis of Early Proterozoic intracrartonic volcanic rocks of the Ventersdorp Supergroup, South Africa. Chem. Geol. 51, 265–288.

Simard, M., 2008. Stratigraphie et géochronologie du nord-est de la Province du Supérieur, in: Simard, M. (Ed.), Synthèse Du Nord-Est de La Province Du Supérieur. Ministère de Ressources Naturelles et de la Faune, Québec, MM2008-2, pp. 23–86.

Smith, P.M., Asimow, P.D., 2005. Adiabat_1ph: A new public front-end to the MELTS, pMELTS, and pHMELTS models. Geochemistry Geophys. Geosystems 6, 1–8.

Sobolev, A. V, Hofmann, A.W., Kuzmin, D.V, Yaxley, G.M., Arndt, N.T., Chung, S.-L., Danyushevsky, L.V., Elliott, T., Frey, F.A., Garcia, M.O., Gurenko, A.A., Kamenetsky, V.S., Kerr, A.C., Krivolutskaya, N. A., Matvienkov, V. V, Nikogosian, I.K., Rocholl, A., Sigurdsson, I.A., Sushchevskaya, N.M., Teklay, M., 2007. The amount of recycled crust in sources of mantle-derived melts. Science 316, 412–7.

Sobolev, A. V, Hofmann, A.W., Sobolev, S. V, Nikogosian, I.K., 2005. An olivine-free mantle source of Hawaiian shield basalts. Nature 434, 590–7.

Stein, M., Hofmann, A.W., 1994. Mantle plumes and episodic crustal growth. Nature 372, 63–68.

Stevenson, R.K., David, J., Parent, M., 2006. Crustal evolution of the western Minto Block, northern Superior Province, Canada. Precambrian Res. 145, 229–242.

Stone, W.E., Crocket, J.H., Dickin, A.P., Fleet, M.E., 1995a. Origin of Archean ferropicrites: geochemical constraints from the Boston Creek Flow, Abitibi greenstone belt, Ontario, Canada. Chem. Geol. 121, 51–71.

Stone, W.E., Crocket, J.H., Fleet, M.E., 1995b. Differentiation processes in an unusual iron-rich alumina-poor Archean ultramafic/mafic igneous body, Ontario. Contrib. to Mineral. Petrol. 119, 287–300.

Stone, W.E., Jensen, L.S., Church, W.R., 1987. Petrography and geochemistry of an unusual Fe-rich basaltic komatiite from Boston Township, northeastern Ontario. Can. J. Earth Sci. 24, 2537–2550.

Stott, G.M., 1999. Precambrian Geology of the Dayohessarah Lake Area, White River, Ontario. Ontario Geol. Surv. Open File Rep. 5984 55.

Sun, S., 1985. Ocean islands - plums or plumes? Nature 316, 103–104.

Sun, S., McDonough, W.F., 1989. Chemical and isotopic systematics of oceanic basalts: implications for mantle composition and processes. Spec. Publ. Vol. Geol. Soc. L. 42, 313–345.

Tomlinson, K.Y., Hughes, D.J., Thurston, P.C., Hall, R.P., 1999. Plume magmatism and crustal growth at 2.9 to 3.0 Ga in the Steep Rock and Lumby Lake area, Western Superior Province. Lithos 46, 103–136.

Tomlinson, K.Y., Stott, G.M., Percival, J.A., Stone, D., 2004. Basement terrane correlations and crustal recycling in the western Superior Province: Nd isotopic character of granitoid and felsic volcanic rocks in the Wabigoon subprovince, N. Ontario, Canada. Precambrian Res. 132, 245–274.

Tuff, J., Takahashi, E., Gibson, S.A., 2005. Experimental constraints on the role of garnet pyroxenite in the genesis of high-Fe mantle plume derived melts. J. Petrol. 46, 2023–2058.

Van der Westhuizen, W.A., de Brutyn, H., Meintjes, P.G., 1991. The Ventersdorp Supergroup: an overview. J. African Earth Sci. 13, 83–105.

Van Kranendonk, M.J., Altermann, W., Beard, B.L., Hoffman, P.F., Johnson, C.M., Kasting, J.F., Melezhik, V.A., Nutman, A.P., Papineau, D., Pirajno, F., 2012. A Chronostratigraphic Division of the Precambrian, in: Gradstein, F.M., Ogg, J.G., Schmitz, M., Ogg, G. (Eds.), The Geologic Time Scale 2012. Elsevier B.V., pp. 299–392.

Walker, R.J., Horan, M.F., Morgan, J.W., Becker, H., Grossman, J.N., Rubin, A.E., 2002. Comparative 187Re-187Os systematics of chondrites: Implications regarding early solar system processes. Geochim. Cosmochim. Acta 66, 4187–4201.

Walker, R.J., Stone, W.E., 2001. Os isotope constraints on the origin of the 2.7 Ga Boston Creek flow, Ontario, Canada. Chem. Geol. 175, 567–579.

Wyman, D.A., 1999. A 2.7 Ga depleted tholeiite suite: evidence of plume-arc interaction in the Abitibi Greenstone Belt, Canada. Precambrian Res. 97, 27–42.

Yaxley, G.M., 2000. Experimental study of the phase and melting relations of homogeneous basalt + peridotite mixtures and implications for the petrogenesis of flood basalts. Contrib. to Mineral. Petrol. 139, 326–338.

CHAPTER 5. Appendices and geological maps

Chapters 2, 3, and 4 describe the character and role of ferropicrite magmas emplaced during the enhanced global growth and stabilization of continental crust ca. 2.7 Ga. Chapter 5 presents the supplementary information collected during the writing of this thesis, including the detailed geological maps of the Q-suite intrusions.

Appendix 5-1: Geology of the Q-suite intrusions

Introduction

Prior to the detailed mapping undertaken during this thesis, study of the Q-suite intrusions (sensu lato) was limited to detailed mapping of the Qullinaaraaluk suite (sensu stricto) type locality in south-central Ungava (Labbé et al., 2001; Baker, 2005), and to reconnaissance mapping at 1:50,000 scale by Ministère des Ressources Naturelles du Québec (Simard, 2008). In order to gain the best possible understanding of the Q-suite plutons, I spent four summers (2008-2011) conducting detailed mapping and sampling in four widely spaced areas of Ungava (Fig. 2-1). The general geology of the studied intrusions is described below.

The Dash dyke

The informally named Dash dyke (Fig. 5-1) is situated in the western Hudson Bay Terrane, ~45 km SE of the town of Inukjuak, and was initially identified during a mapping expedition in 2006, by a team of McGill University geologists. The intrusion has been largely eroded, and its extent was inferred on the basis of isolated outcrops. The central portion of the intrusion, perpendicular to its strike, is well exposed, however. Two sampling transects (in 2006 and 2008) were conducted through the central portion of the Dash dyke. The symmetrically-zoned morphology of the body suggests that the intrusion postdates the surrounding granitoid. The intrusion, however, appears to be brecciated (Fig. 5-2) and re-intruded by dykes of the host granitoids, suggesting near-coeval emplacement. The Dash dyke comprises an inner core of peridotite, an intermediate websterite "shell", and an outer zone of gabbronorite.

Peridotites appear in the field as dense, magnetic, black rocks, composed of largely-

serpentinized olivine crystals, and cm-sized oikocrysts of amphibole ± clinopyroxene. Peridotites collected from the central portion of the transect lack clinopyroxene entirely, and are composed of serpentine pseudomorphs of euhedral olivine (Fig. 5-3), large crystals of orthopyroxene, and optically-continuous mats of amphibole. Relict fresh olivine is present in cores of many serpentine pseudomorphs. Peridotites observed and sampled on either side of clinopyroxene-free harzburgite contain euhedral clinopyroxene, and are characterized by a greenish hue. Websterites of the Dash dyke are weakly magnetic and considerably less fresh than websterites of the Gladel River intrusion (see below). Websterites are greenish to black, and typically have altered, sub-microscopic, interstitial mineralogy. Furthermore, the cumulus pyroxene phases often show patches of microscopic alteration when seen in microscope. Both amphibole and plagioclase are non cumulus, forming irregular shaped small crystals and oikocrysts, and giving the Dash dyke a decisively igneous texture. Replacement of clinopyroxene by amphibole, seen in partial pseudomorps, suggests that amphibole is late product of reaction between pyroxene and hydrous differentiated interstitial melt. Rare websteritic samples are nearly free of amphibole, instead containing an abundance of biotite. Hornblende gabbronorite occurs on the outermost flanks of the Gladel River intrusion and is differentiated from websterite by the presence of equant, modally-abundant (>40 %) feldspar.

The well-preserved cumulate textures, and generally well preserved primary igneous mineralogy (>60 %), indicate that treating the rocks of the Dash dyke as igneous is appropriate. Ubiquitous intrusion by late felsic melts, suggests that alteration of interstitial and cumulus minerals likely reflect late stage metasomatic reactions (see Chapter 2).

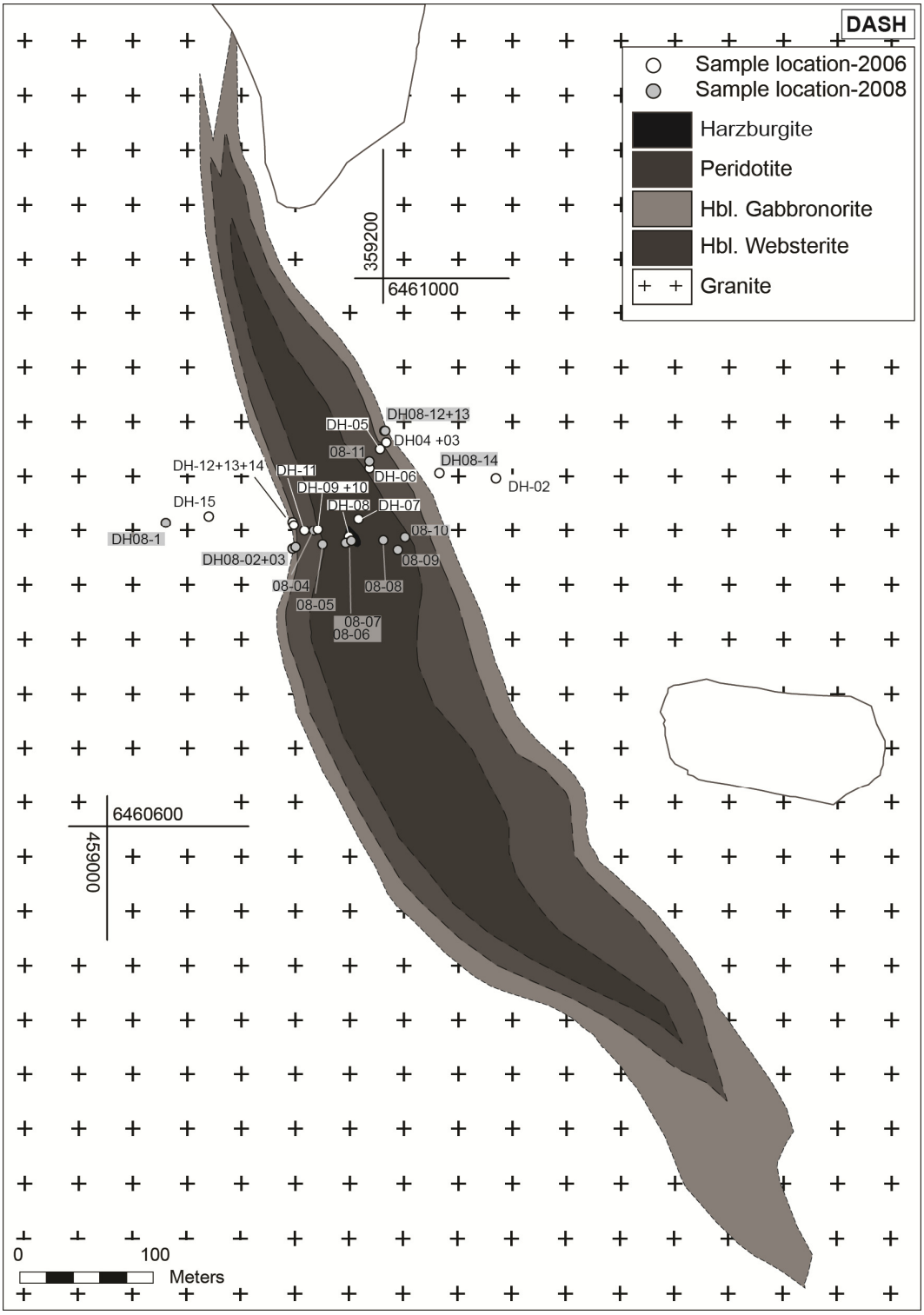

Figure 5-1: Geological map of the DASH intrusion

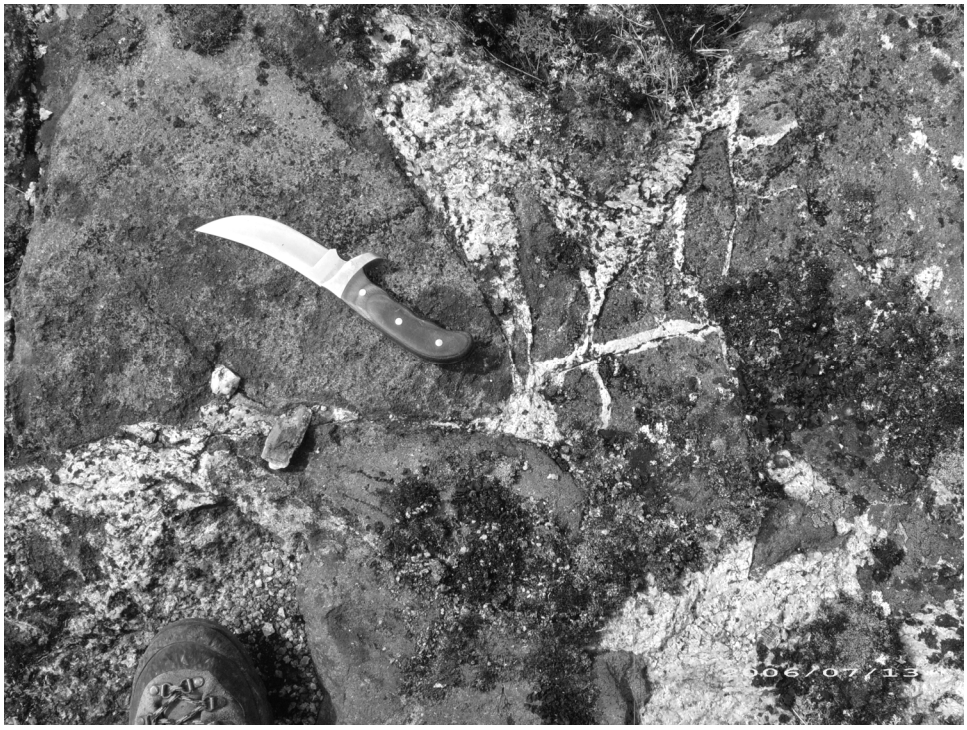

Figure 5-2: Brecciated websterite of the Dash dyke.

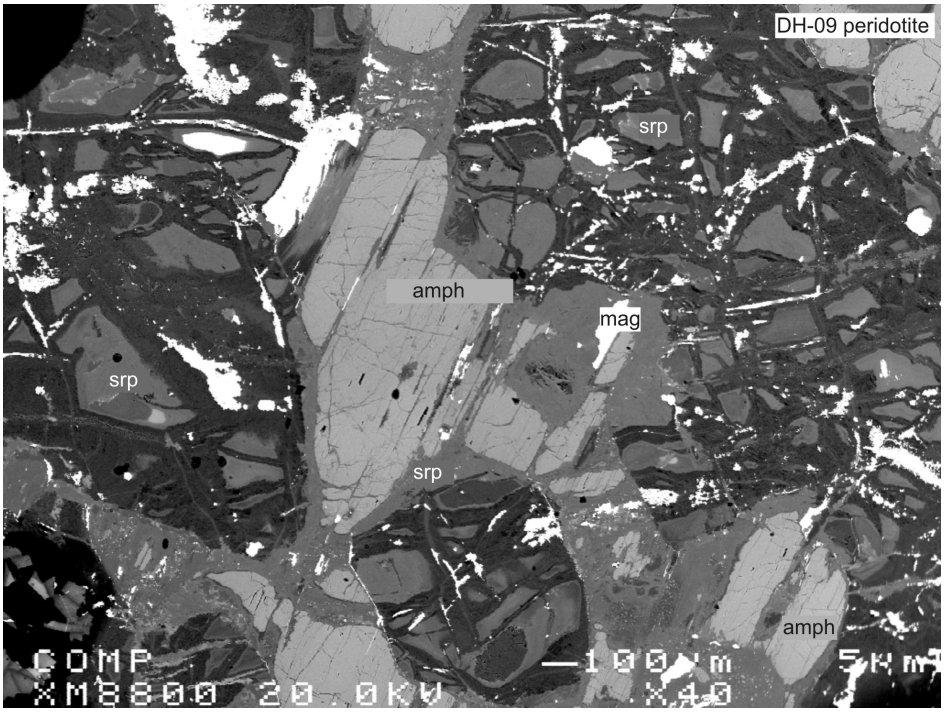

Figure 5-3: BSE image of peridotite from the Dash dyke.
Serpentinized, euhedral olivine cumulus grains, surrounded by amphibole oikocrysts. Serpentinization, was accompanied by fracturing of olivine grains, exsolution of Fe, and development of magnetite micro-veins.

The Gladel River intrusion

The Gladel River intrusion (Fig. 5-4) is situated ~5 km north of the Dash dyke and is accessible via the Gladel River. Previously mapped as 2 separate intrusions, the Gladel River intrusion is an irregularly shaped, zoned body, surrounded by relatively potassic, foliated granite, which postdates the intrusion's emplacement. The intrusion forms a topographic high, over the more easily-weathered, jointed felsic plutonic rocks. The intrusion is ~ 1 km across, and is composed of a websteritic core, a gabbronoritic outer domain, and a discontinuous margin composed of leucocratic gabbronorite to pyroxene-bearing granodiorite. The intrusion is cut by felsic, pegmatitic veins and dykes, with intense brecciation typically seen in the websteritic domain.

Websterite is green-black, coarse grained, weakly magnetic, with large (cm-sized) oikocrysts of amphibole. The central part of the websterite core, parallel to its long axis, is free of plagioclase. Irregular, "wormy"-shaped plagioclase crystals are visible in hand sample towards the outer part of the websterite core. The appearance of equant, subhedral plagioclase crystals marks the transition from websterite to amphibole gabbronorite. Gabbronorite is typically coarse grained, weakly magnetic, black-green and white in colour and is sometimes characterized by very large (few cm), irregular crystals of amphibole. The transition from gabbronorite to granite is sharp along the northeastern side of intrusion. In contrast, the southern margin of the intrusion is characterized by a zone of moderately to strongly magnetic, leucocratic, black and white, medium-grained rock, intermediate in composition between gabbronorite and surrounding granite. Across this zone, and away from the center of the intrusion, the modal abundance of pyroxene and biotite decrease, while the modal abundance of feldspar increases. The leucocratic

rocks of this zone are noticeably free of amphibole.

The rocks of the Gladel River intrusion are characterized by igneous cumulate textures, including poikilitic textures, cuspate interstitial grains. Olivine crystals, observed only in the central part of the websterite core are armoured by orthopyroxene, and interpreted to reflect peritectic reactions. Although it is probable that amphibole may be a primary liquidus phase in the more evolved gabbronorites, textural evidence suggests that amphibole observed in websterites and more primitive gabbronorites crystallized from a more evolved trapped interstitial melt, often replacing pyroxene as a result of hydration (Fig. 5-5).

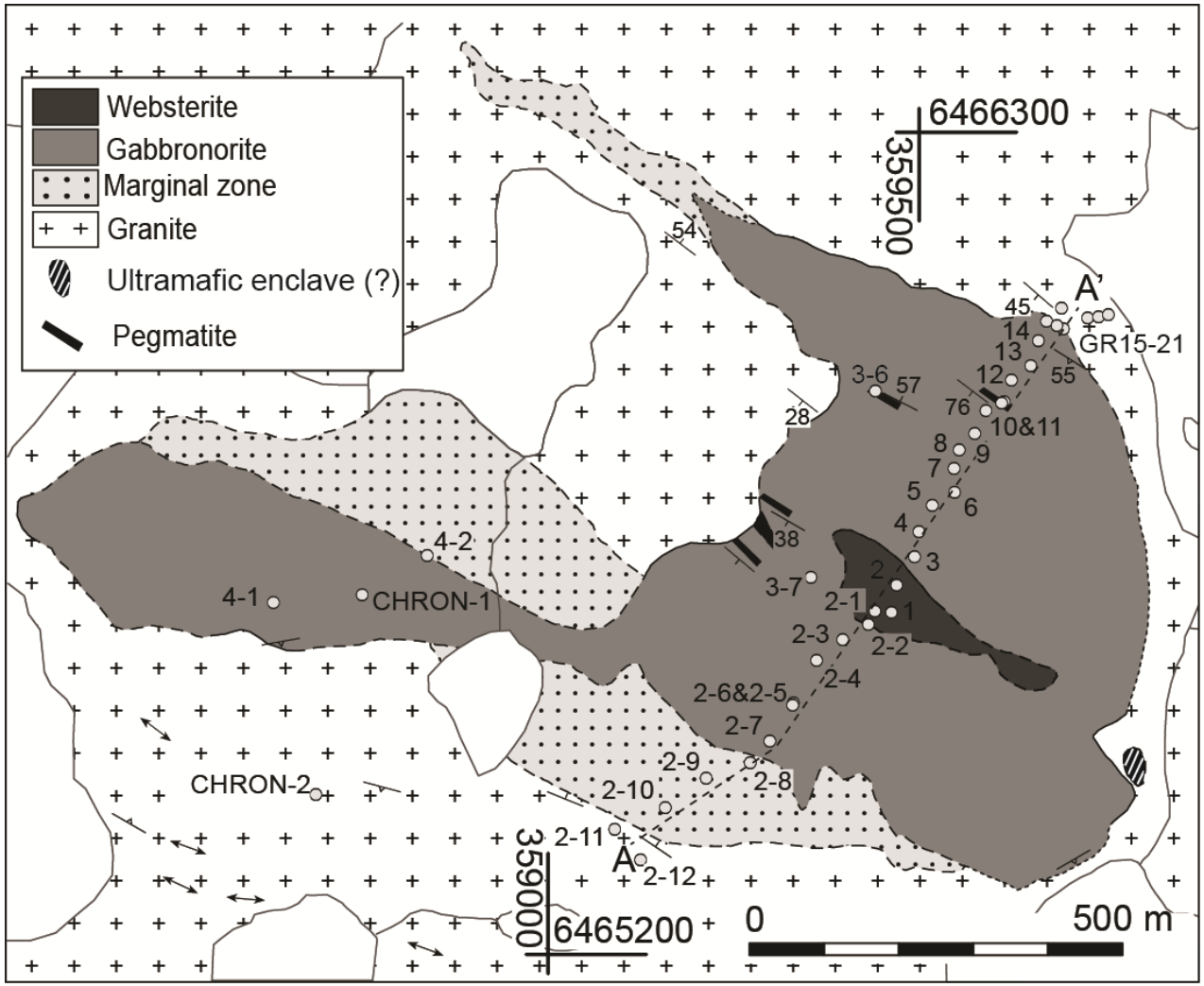

Figure 5-4: Geological Map of the Gladel River intrusion.

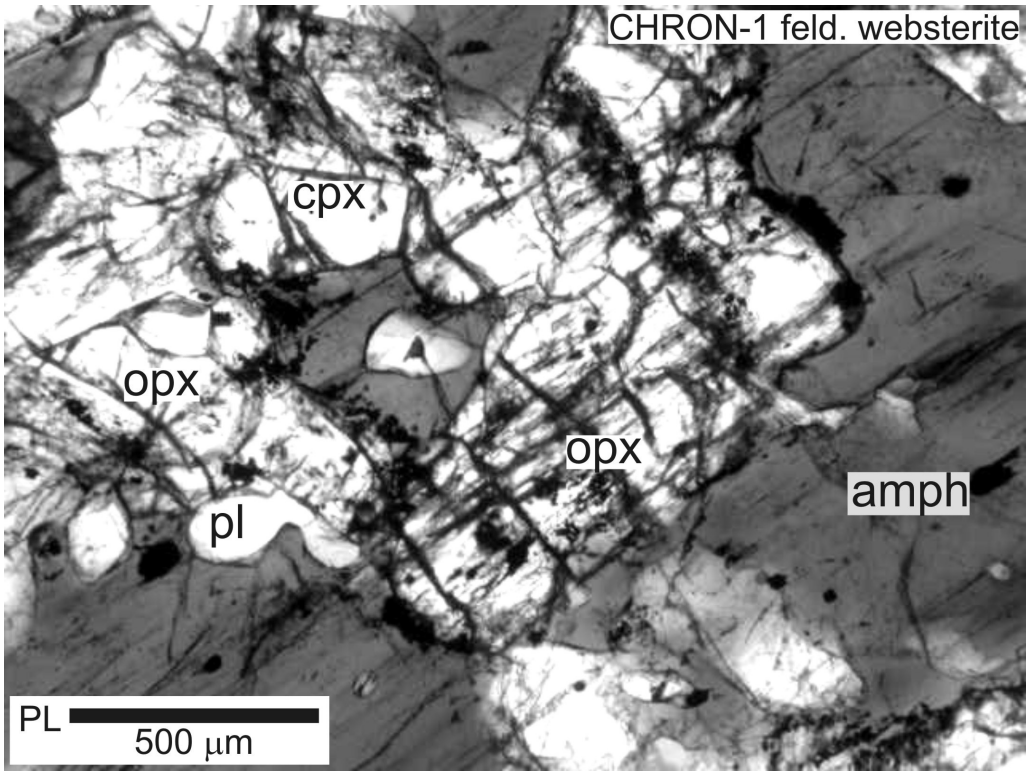

Figure 5-5: Micrograph of a feldspathic websterite from the Gladel River intrusion. Grey-scale transmitted-light micrograph of an amphibole oikocryst partially replacing primary clinopyroxene and orthopyroxene cumulus minerals in feldspathic gabbro.

The Pinguk Hill intrusion

The Pinguk Hill intrusion situated ~7 km NNW of the Gladel River intrusion is the largest Q-suite plutonic body sampled during this project. The intrusion has a shape of a horse shoe and is ~ 3 km long and ~2 km wide. The intrusion is dominated by gabbronorite, similar to that of the Gladel River intrusion, with subordinate websterite. The core of the Pinguk Hill intrusion is composed of a FeO-rich gabbronorite, characterized by strong magnetic susceptibility. Because of its relatively large size, and similar lithological character and proximity to the Gladel River intrusion, a detailed geological map of the Pinguk Hill intrusion was not produced.

Lac Muraalavik intrusions 1-3

Three separate zoned intrusions (Fig. 5-6), located ~120 km ENE of the town of Inukjuak, were mapped during the summer of 2009. The plutonic bodies of the Lac Muraalavik locality comprise lithologies similar to those observed in the Q-suite intrusions of the western Hudson Bay Terrane. Furthermore, the plutons of the Lac Muraalavik region also display locally intense brecciation, similar to that observed in the Q-suite plutons situated further west (Fig. 5-7). Granitic rocks surrounding the Q-suite plutons in the Lac Muraalaavik region are heterogenous, commonly containing foliated/sheared enclaves of mafic rock, although none of the enclaves appear to represent Q-suite lithologies. The country granitoids are commonly foliated in the vicinity of contact with the Q-suite intrusions. Absence of cross-cutting pegmatitic veins in the country granitoids, suggests that their emplacement postdates the emplacement of the Q-suite intrusions.

Peridotite is rare in the Lac Muraalavik region and was only sampled at two

locations. Body # 2 (Fig. 5-6B) contains a long narrow zone of magnetic peridotite, and has an overall zoned morphology that is similar to the Dash dyke. Websterite is very common in all Lac Muraalavik intrusions, and is characterized by green-black colour, visible fresh clinopyroxene and orthopyroxene crystals. The most magnesian websterites contain olivine, armoured by orthopyroxene. Amphibole is the predominant interstitial phase. Incipient pseudomorphism of clinopyroxene by amphibole is a ubiquitous feature of Lac Muraalavik websterites (Fig. 5-8). Hornblende gabbronorite is ubiquitous in the Lac Muraalavik. A number of observed hornblende gabbronorites, display very large (3-4 cm) amphibole oikocrysts. Cumulus amphibole crystals were not observed in any of the Lac Muraalavik intrusions. Gabbronorite at body #2 includes a leucocratic phase that appears similar to the marginal rocks of the Gladel River margin.

The Q-suite intrusions of the Lac Muraalavik intrusion contain relatively fresh, primary igneous mineralogy and are characterized by igneous cumulate textures. Prolonged cooling history has resulted in subsolidus processes, such as serpentinization of olivine and hydration of clinopyroxene to form amphibole.

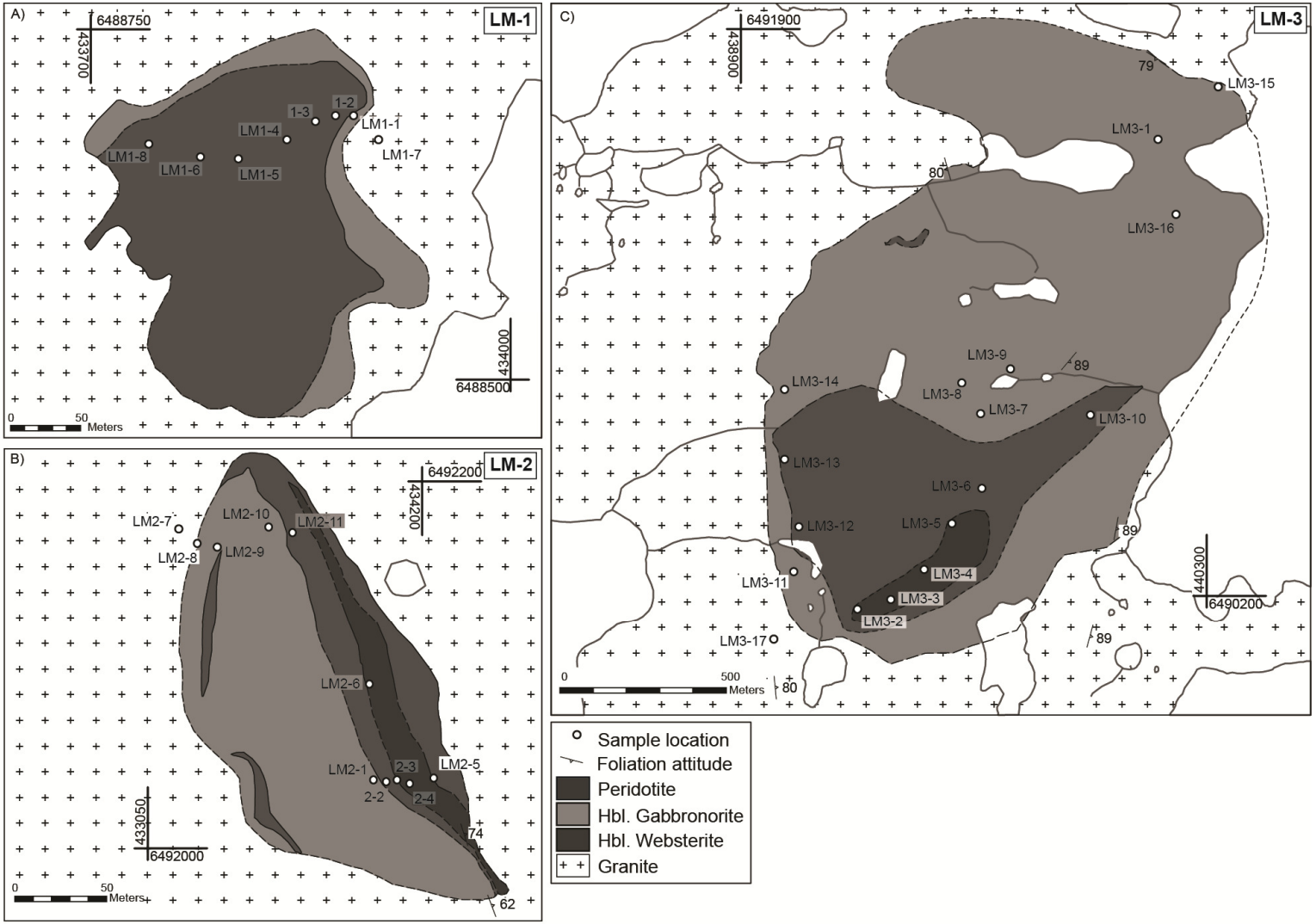

Figure 5-6: Geological maps of the Q-suite intrusions of the Lac Muraalavik region.

Figure 5-7: Brecciated websterite of the Lac Muraalavik (3) region

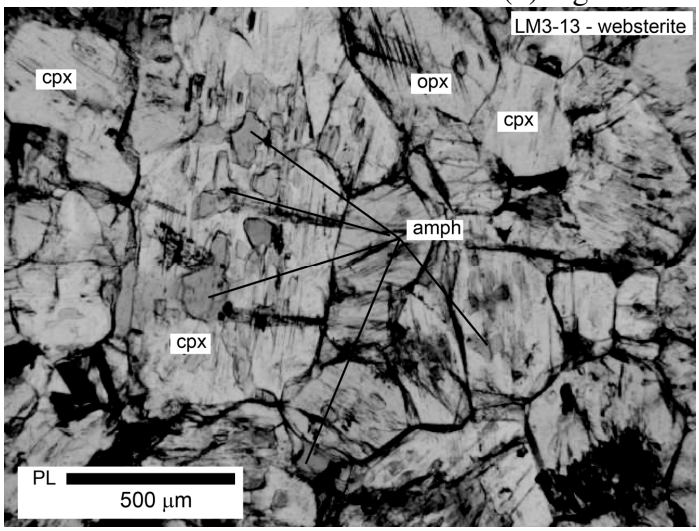

Figure 5-8: Micrograph of websterite from Lac Muraalavik region.
Greyscale transmitted light photomicrograph of a websterite, illustrating the incipient pseudomorphism of clinopyroxene by amphibole.

The Lac Couture intrusion

The Lac Couture intrusion (Fig-5-9A and Fig 5-9B), mapped during the summer of 2010, is situated north of the Lac Couture meteorite impact site in the north-central region of the Ungava Peninsula, within the Rivière Arnaud Terrane. The nearest settlement is Puvurnituq, approximately ~110 km WSW. The Lac Couture intrusion differs from the Q-suite intrusions situated in the western Ungava Peninsula in three main aspects. The rocks of the Lac Couture intrusion: 1) lack orthopyroxene, 2) have experienced significant ductile deformation that followed brecciation (Fig. 5-10), and 3) have experienced extensive late intrusion by late, relatively potassic granitoids. The Lac Couture intrusion was emplaced into foliated tonalite-trondhjemite rocks of the Suite de Rochefort.

As a result of the late ductile deformation, most of the rocks of the Lac Couture intrusion display compositional heterogeneity on a small (metre) scale. In addition to evidence of metasomatism by leucocratic veins, rocks that comprise the ductilly-deformed domains are commonly entirely composed of amphibole and plagioclase, suggesting they have experienced amphibolite-facies metamorphism. Figure 5-9 B is a 1:1000 scale map, which illustrates the compositional heterogeneity and field relationships that are typical of the intrusion. In rare instances, undeformed and unmetamorphosed domains have been preserved. These domains are typically dominated by olivine, and include mesocumulate dunites and wehrlites. Dunites typically weather brown and have smooth surfaces. Dunites have distinctly igneous, cumulate textures and contain fresh to moderately-serpentinized olivine set in oikocrysts of clinopyroxene and amphibole. With the increasing proportion of clinopyroxene, the rocks become more

crumbly, appear coarser grained, and the weathered colour becomes green. Although amphibole is the dominant interstitial mineral in the ultramafic rocks of the Lac Couture intrusion, a number of wehrlites contain biotite as the dominant interstitial mineral. (Meta) Gabbro is a minor component of the Lac Couture body, and when present it is found in the ductilly-deformed domains where it forms globular bodies that frequently contain xenoliths of wehrlite. Gabbro is composed entirely of plagioclase, hornblende, and subordinate titanite, and oxide. All of the observed gabbros are metamorphic, characterized by polygonal grain boundaries, and mineral lineations that are defined by aggregates of hornblende porphyroblasts.

The Lac Couture intrusion has largely been affected by amphibolite-facies metamorphic conditions. However, large (100 m+) "enclaves" of predominatly ultramafic compositions appear to have escaped the metamorphic effects. During sampling, strong emphasis was placed on collecting rocks with a minimal metamorphic/metasomatic overprint.

The Lac Duquet intrusion

The Lac Duquet intrusion (Fig. 5-9C) is situated ~20 km NNE of the Lac Couture intrusion. Although no dunites were identified, the Lac Duquet plutonic body is lithologically similar to the Lac Couture intrusion. The south-western portion of the intrusion was intruded by massive coarse grained granite that contains xenoliths of mafic and ultramafic rock of the Lac Duquet intrusion. The apparent geographical dependence of xenoliths suggests that metamorphism of the Lac Duquet rocks preceded the emplacement of the granite.

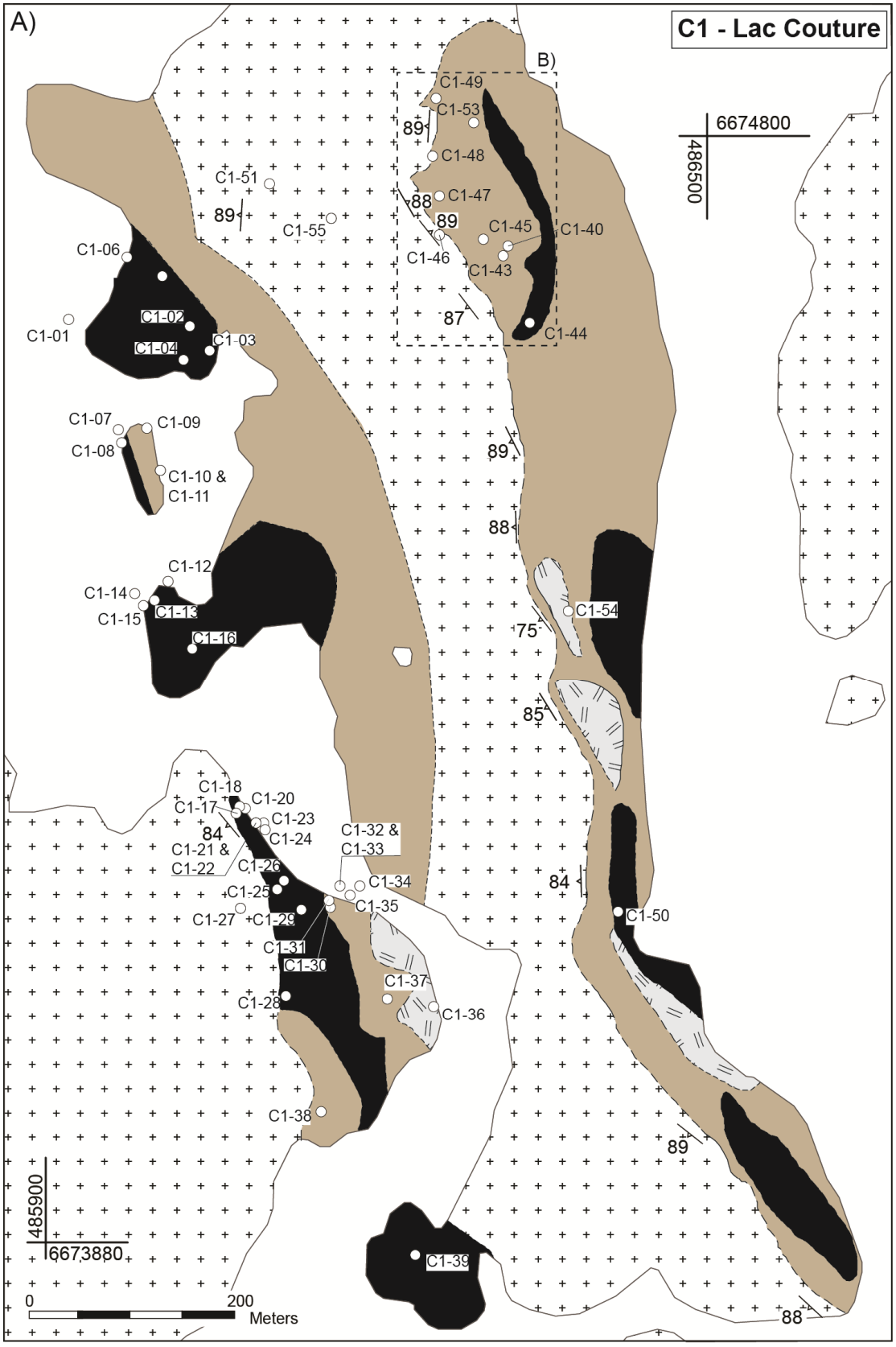
A)
C1 - Lac Couture
B)
6674800
486500
C1-49
C1-53
C1-48
C1-47
C1-45
C1-40
C1-46
C1-43
C1-44
C1-51
C1-55
C1-06
C1-02
C1-01
C1-04
C1-03
C1-07
C1-09
C1-08
C1-10 &
C1-11
C1-12
C1-14
C1-15
C1-13
C1-16
C1-54
C1-18
C1-17
C1-20
C1-23
C1-24
C1-21 &
C1-22
C1-32 &
C1-33
C1-26
C1-34
C1-25
C1-35
C1-27
C1-29
C1-31
C1-30
C1-37
C1-28
C1-36
C1-38
C1-50
C1-39
89
88
87
75
85
84
485900
6673880
0
200
Meters

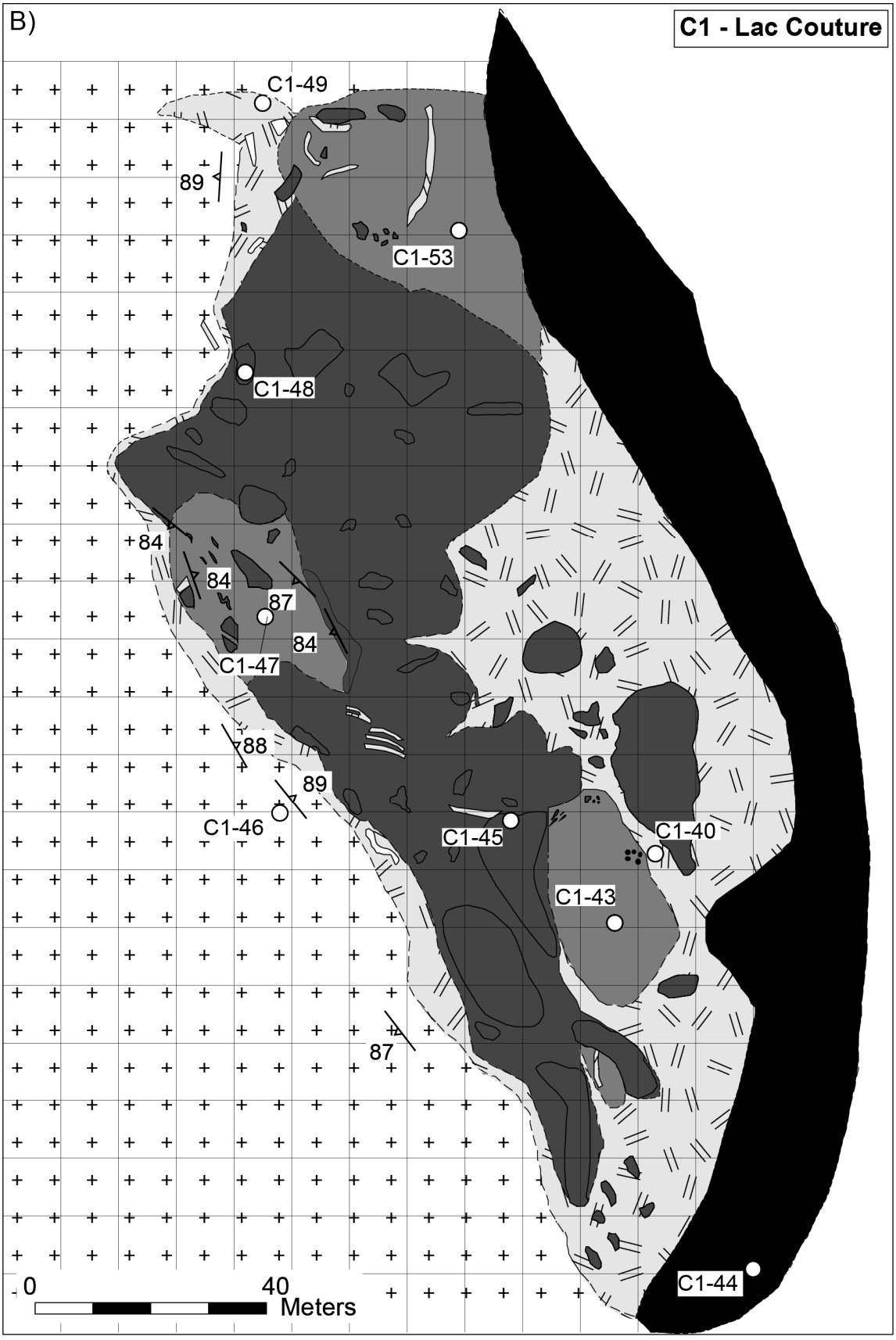
B)
C1 - Lac Couture
C1-49
89
C1-53
C1-48
84
84
87
84
C1-47
88
89
C1-46
C1-45
C1-40
C1-43
87
C1-44
0
40
Meters

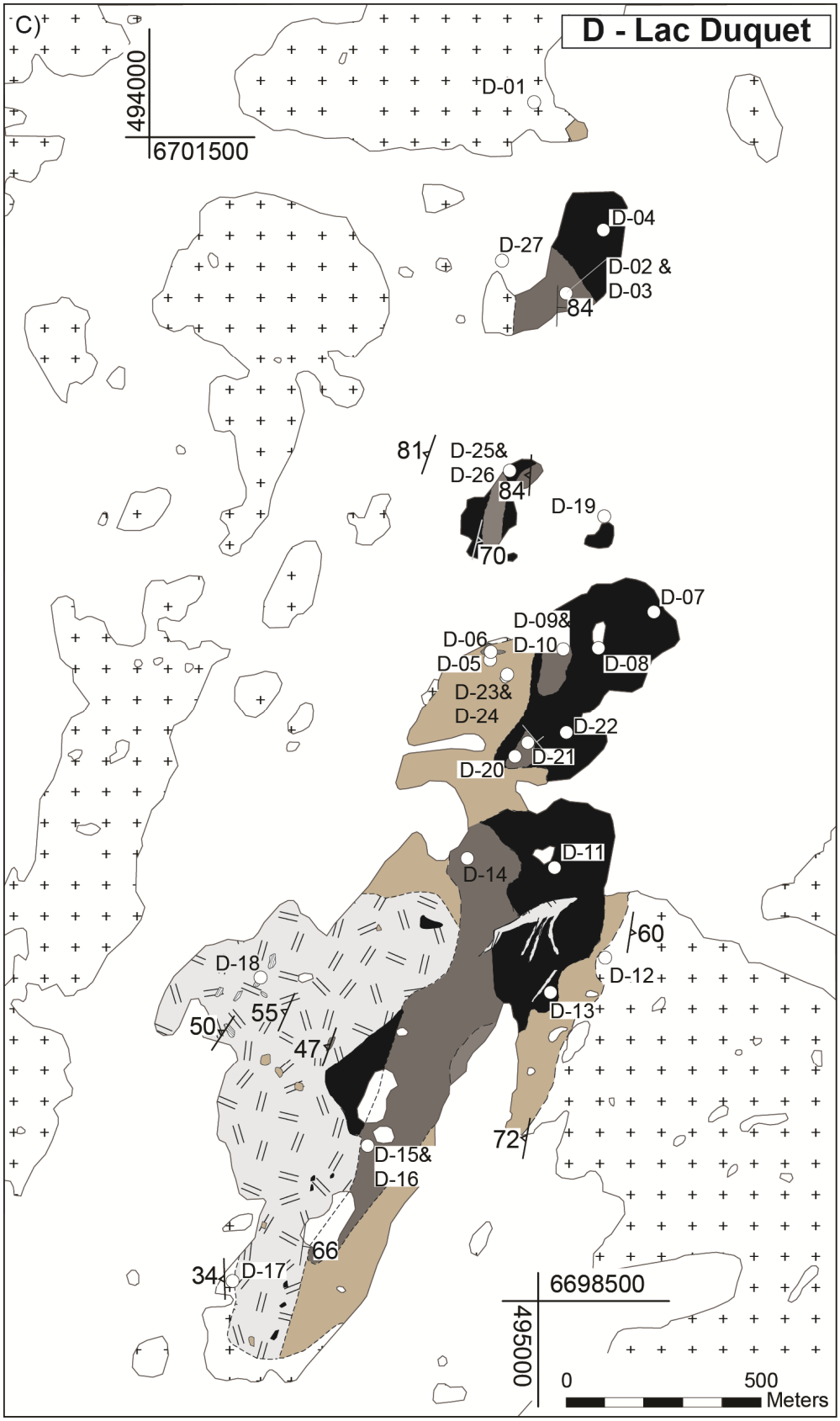
C)
D - Lac Duquet
494000
6701500
D-01
D-04
D-27
D-02 &
D-03
84
81
D-25&
D-26
84
D-19
70
D-07
D-09&
D-10
D-06
D-05
D-08
D-23&
D-24
D-22
D-21
D-20
D-11
D-14
60
D-18
D-12
D-13
55
50
47
72
D-15&
D-16
66
34
D-17
6698500
495000
0
500
Meters

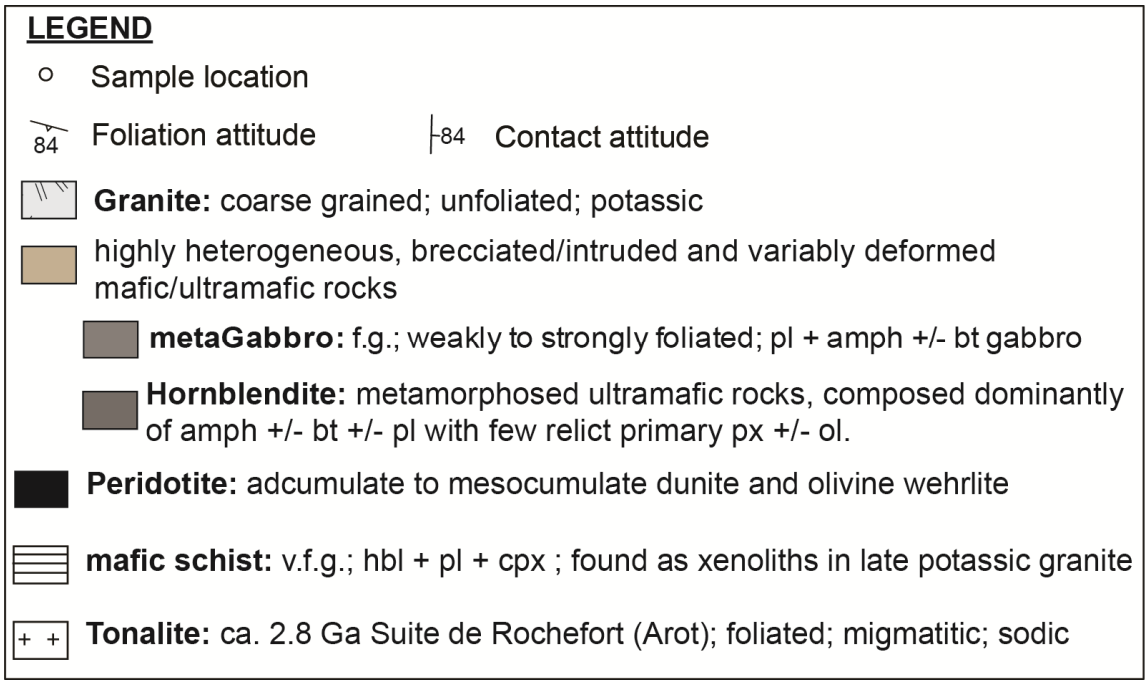

Figure 5-9: Geological maps of the transitional Q-suite intrusions.
Geological map of the Lac Couture intrusion. Dashed rectangle shows the location of the detailed map B), which depicts the complexity of the ductily deformed, brecciated domains. C) Geological map of the Lac Duquet intrusion.

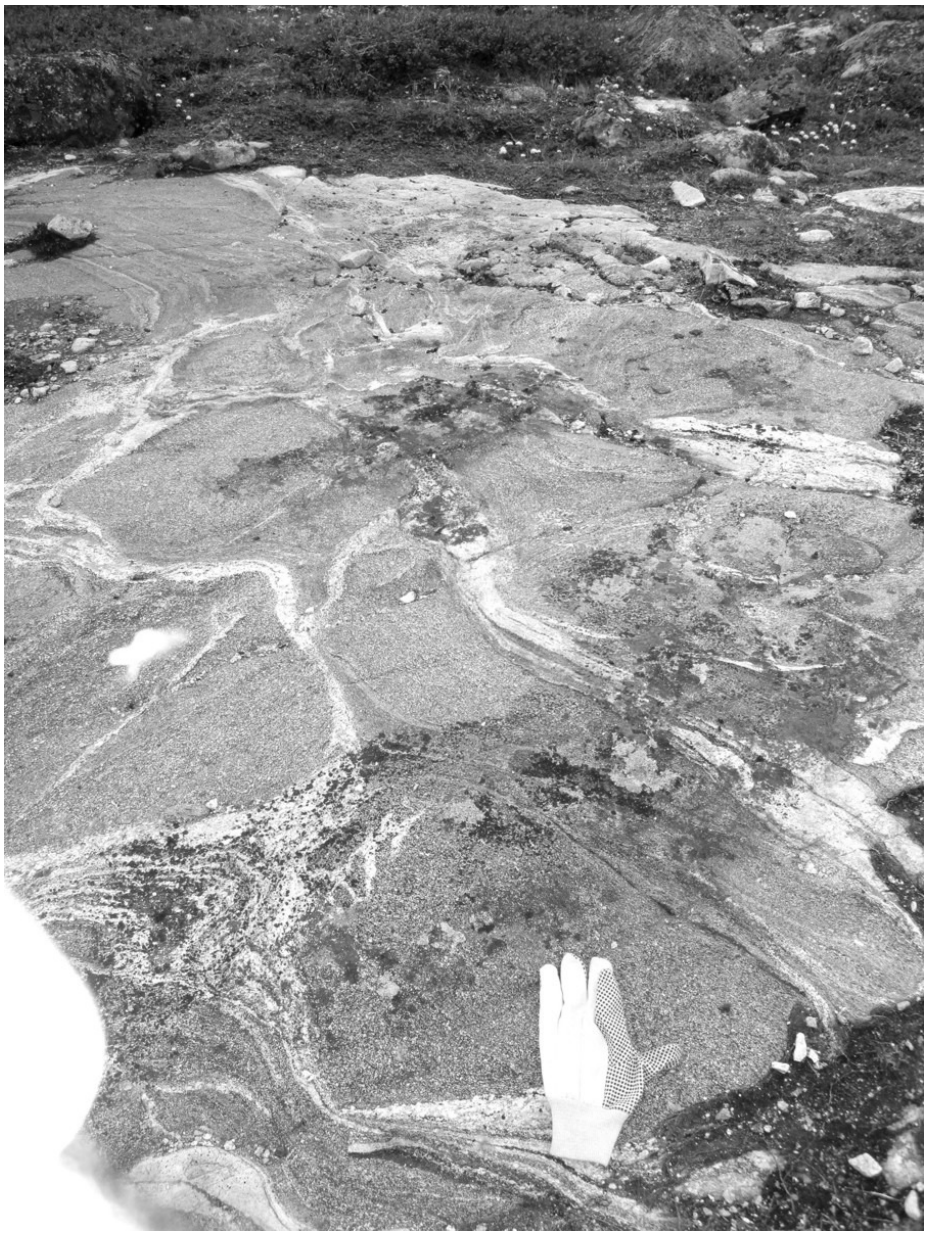

Figure 5-10: Ductilly-deformed rocks of the Lac Couture intrusion.
Prior to ductile deformation, ultramafic rocks of the Lac Couture intrusion experienced an episode of brittle brecciation by felsic dykes and veins (Fig 5-11B). Ductile deformation was accompanied by the development of compositionally heterogeneous domains on metre-scale (heterogeneous unit in Fig 5-9A).

Figure 5-11: Brecciated wehrlite of the Lac Couture intrusion.
Transition from the brittly-brecciated wehrlite of the Lac Couture intrusion (left side of the photograph), to the "wispy", ductilly-deformed and compositionally heterogeneous lithology similar to shown in Fig. 5-10.

Appendix 5-2: The geology of the ≥2.82 Ga Lac Faribault intrusions

Introduction

Mapping of the Québec's Ungava craton by Ministère des Ressources Naturelles (MRN) was performed over a period of 6 years (1998-2003), during which twenty-one geological maps at 1:250,000 scale were produced covering a very large area (>350 000 km^2). The earliest mapping was performed in the east of the craton, starting with the Lac Peters map sheet (24M, Simard and Leclair, 2008; Madore et al., 1999). Mapping in the western portion of the craton did not commence until 2001 (e.g. Madore et al., 2002, Parent et al. 2002), marking the first formal identification of the Couture and Qullinaaraaluk suites. The expedition to the Lac Faribault area in the eastern Ungava craton was motivated by the possibility that the earliest mapping efforts failed to distinguish the intrusive rocks of the Q-suite from other mafic volcanic and intrusive rocks, collectively assigned to the Complexe d'Arnaud (Simard, 2008). The available geochronological data from the rocks of the Complexe d'Arnaud (2818 ± 5 Ma, 2782 ± 7 Ma, 2718 ± 9 Ma, 2725 ± 9 Ma) strongly supports this inference.

The ca 2.82 Ga plutonic rocks of the eastern Ungava craton

The hypersthene-normative mafic to ultramafic plutonic rocks situated along the eastern shore of the Lac Faribault in the Rivière Arnaud Terrane are orthopyroxene-rich and petrographically similar the subalkaline Q-suite intrusions of the western Ungava craton. Their field appearance, including the ubiquitous brecciation of ultramafic lithologies by pegmatitic veins and dykes, and frequent association with pyroxene-bearing granitoid rocks resembles that of the Q-suite plutonic bodies. Four analyzed

zircon grains from a websterite sample (LF-26) have experienced significant lead loss, but indicate a minimum emplacement age of ca. 2.82 Ga ($^{207}Pb/^{206}Pb_{max}$ = 2820.8 ± 1.0 Ma; Milidragovic and Francis, 2013) that is significantly older than the emplacement age of the Q-suite intrusions, however.

The most magnesian collected rocks in the Lac Faribault region are variably serpentinized orthocumulate peridotites. The peridotites are composed of irregularly-shaped olivine inclusions set in orthopyroxene macrocrysts, and cm-sized amphibole oikocrysts (Fig. 5-12A). The olivine inclusions are commonly optically continuous. The peridotites show a range in MgO contents (22-31 wt. %; Table 5-1; Fig. 5-13), but have relatively restricted FeO^{TOT} concentrations (11.2 - 12.2 wt. %) that are typically lower than those of the Q-suite subalkaline peridotites (9.9 - 15.5 wt. %). The moderately high contents of Al_2O_3 (5-8 wt. %) and CaO (5-7 wt. %) are consistent with the relatively high abundances of interstitial amphibole. Nickel (500-1000 ppm) and Cr (600-2500 ppm) contents are variable and poorly correlated. The orthopyroxene-rich peridotites of the Lac Faribault region of the Rivière Arnaud Terrane contain olivine (Table 5-2) that is more magnesian (Fo_{82} – Fo_{85}; Fig. 5-2) than the olivine of the subalkaline Q-suite intrusions from the Hudson Bay Terrane ($Fo_{0.80}$ – $Fo_{0.82}$). Furthermore, the Ni contents (~1190-1230 ppm) of the Lac Faribault peridotites are lower than those of the Q-suite peridotites.

Small (>5 m) amphibole ± biotite-rich feldspathic websterite bodies are ubiquitous in the Lac Faribault region. The websterites are typically fresh and show well developed cumulate textures, including poikilitic textures and cuspate boundaries between interstitial phases (Fig. 5-12B).

Both nepheline and hypersthene-normative, amphibole-rich gabbroic rocks occur in zoned mafic/ultramafic intrusions, as well as in homogenous outcrops of massive gabbro. In contrast to the rocks of the subalkaline Q-suite, orthopyroxene is notably absent from the gabbroic rocks of the Lac Faribault region. Amphibole forms optically continuous inclusions within clinopyroxene, as well as large irregular-shaped crystals that enclose multiple highly altered clinopyroxene grains. Nepheline-normative gabbros are characterized by high normative magnetite (2-5 wt. %) and ilmenite (0.5 – 4 wt. %) contents (Fig. 5-12C).

The trace-element profiles of the ≥ 2.82 Ga mafic and ultramafic rocks from the Lac Faribault region display a "calc-alkaline" character (Fig. 5-14), and are comparable to those of the subalkaline Q-suite intrusions. The Lac Faribault intrusive rocks are characterized by moderate enrichments of LREE over the relatively unfractionated HREE, and pronounced depletions on the HFSE. The Lac Faribault gabbros, in contrast, lack the distinct depletion in Ti, consistent with the high modal abundance of Fe-Ti oxides.

The initial $\varepsilon_{Nd(2.82\ Ga)}$ and $\varepsilon_{Hf(2.82\ Ga)}$ values of the Lac Faribault mafic and ultramafic intrusions range from +1 to -2 and 0 to +3, respectively, overlapping the $\varepsilon_{Nd(2.82\ Ga)}$ values of nearby pyroxene-granitoids and a low-K granodiorite (Milidragovic et al, n.d).

The petrogenesis of the ca 2.82 Ga plutonic rocks

The ≥ 2.82 Ga mafic-ultramafic rocks on the eastern shore of the Lac Faribault crystallized olivine followed by orthopyroxene, clinopyroxene, amphibole/ plagioclase and Fe-Ti oxides, and are thus mineralogically similar to the subalkaline Q-suite plutons. These intrusions were derived from subalkaline parental magmas, with lower Fe-contents

than those of the ca. 2.72-2.70 Ga Q-suite. Their age, geochemistry, and geographical location suggests that they belong to a ca. 2.82 Ga suite of rocks included in the poorly described Complexe d'Arnaud (Simard, 2008) and that they may be the mid-crustal expressions of the ca. 2.82 Ga Mg-tholeiites of the Duquet and Buet greenstone belts of the central and northeastern Ungava craton, respectively (Maurice et al., 2009).

References cited

Madore, L., Bandyayera, D., Bédard, J.H, Brouillette, P., Sharma, K.N.M., Beaumirer, M., and David, J., 1999. Géologie de la région du lac Peters (SNRC 24M). Ministère de Ressources Naturelles et de la Faune, Québec, RG99-07, 41 p.

Madore, L., Larbi, Y., Labbé, J.Y., Sharma, K.N.M., Lacoste, P., and David, J., 2002. Géologie de la région du lac Couture (35B) et des lacs Nuvilik (34G, partie sud). Ministère de Ressources Naturelles et de la Faune, Québec, RG2002-04, 42 p.

Maurice, C., David, J., Bédard, J.H., Francis, D., 2009. Evidence for a widespread mafic cover sequence and its implications for continental growth in the Northeastern Superior Province. Precambrian Research 168, 45–65.

Milidragovic, D. and Francis, D., 2013. Ferropicrite-driven reworking of the Ungava craton and the genesis of the Neoarchean pyroxene-granitoids. Earth and Planetary Science Letters XX, 1-8.

Milidragovic, D., Francis, D., Weis, D., and Constantin, M. Neoarchean (ca. 2.7 Ga) plutons of the Ungava craton, Québec, Canada: reconstructed parental magma compositions and implications for Fe- rich mantle source regions.

Parent, M., Leclair, A., David, J., Sharma, K.N.M., and Lacoste, P., 2002. Géologie de la région du lac Vernon (SNRC 34J). Ministère de Ressources Naturelles et de la Faune, Québec, RG2001-11, 40 p.

Simard, M., 2008. Stratigraphie et géochronologie du nord-est de la Province du Supérieur, *in*: Simard, M. (Ed.), Synthèse Du Nord-est de La Province Du Supérieur. Ministère de Ressources Naturelles et de la Faune, Québec, MM2008-2, 23–86.

Simard, M. and Leclair, A., 2008. Mise en contexte, *in*: Simard, M. (Ed.), Synthèse Du Nord-est de La Province Du Supérieur. Ministère de Ressources Naturelles et de la Faune, Québec, MM2008-2, 9-12.

Table 5-1: Geochemistry of the ca. 2.82 Ga Lac Faribault intrusions

Sample	LF-1	LF-2	LF-4	LF-5	LF-6	LF-7	LF-8	LF-13	LF-14	LF-15	LF-16	LF-17	LF-20
Zone	19	19	19	19	19	19	19	19	19	19	19	19	19
Easting	342207	342228	342305	343235	343232	343243	343242	343224	343199	343232	343191	343229	343241
Northing	6549118	6549211	6549035	6550459	6550471	6550434	6550428	6551091	6551060	6551072	6551061	6551091	6551092
Lithology	*web*	*web*	*gabbro*	*perid*	*perid*	*perid*	*perid*	*perid*	*web*	*perid*	*web*	*gabbro*	*web*
Major elements (wt. %)													
SiO_2	53.1	51.52	52.65	43.43	42.29	44.22	44.05	51.11	51.09	45.95	46.51	50.02	49.27
TiO_2	0.29	0.36	0.51	0.68	0.38	0.52	0.45	0.29	0.5	0.66	1.31	0.35	0.31
Al_2O_3	4.2	7.19	9.05	7.01	4.64	6.91	6.43	5.8	8.26	8.08	10.66	18.97	5.89
MgO	17.54	13.55	8.99	25.49	29.19	26	25.85	21.81	12.83	23.98	11.36	7.19	20.53
FeO	12.65	10.61	9.2	11.74	11.12	11.59	11.78	11.93	7.02	10.95	12.37	6.02	8.13
MnO	0.25	0.23	0.23	0.17	0.17	0.17	0.18	0.21	0.15	0.17	0.21	0.12	0.15
CaO	9.57	12.54	13.57	5.73	5.17	5.18	5.8	5.3	15.21	6.25	10.62	10.26	11.33
Na_2O	0.97	1.67	2.4	1.03	0.61	0.96	1	0.91	1.79	1.19	2.02	3.61	0.95
K_2O	0.47	0.43	1.28	0.53	0.32	0.6	0.48	0.48	1.08	0.43	1.99	1.04	0.46
P_2O_5	0.03	0.05	0.18	0.06	0.06	0.07	0.05	0.03	0.07	0.03	0.17	0.12	0.03
LOI	0.15	0.61	0.83	2.72	4.67	2.31	2.62	0.52	0.93	1.02	1.09	1.35	1.63
Total	99.43	98.83	98.9	98.62	98.71	98.56	98.72	98.76	99.08	99.02	98.34	99.06	98.96
Trace elements (ppm)													
Th	-	-	0.91	0.83	-	-	1.33	1.18	-	0.68	-	1.45	-
U	-	-	0.2	0.25	-	-	0.24	0.23	-	0.14	-	0.21	-
Rb	18.9	6.7	42.7	6.8	5.7	9.1	6.8	9.4	37.8	3.9	68.3	14.1	5.9
Ba	146.6	118.9	476	167.4	139	189	136.5	103.8	322.7	130.1	537.6	308.9	126.2
Pb	1.4	2.4	271.3	1.6	1.4	2.2	3.2	1.2	4.2	1.6	5.3	7.4	1.6
Sr	77.6	125.4	323.3	184.1	123.6	197.9	157.3	78.6	215.5	180.8	220.8	650.9	120.6
Nb	1.9	2.9	2.9	2.5	1.9	2.8	2.7	0.7	1.7	1.1	11.7	2.1	1.3
Ta	-	-	0.07	0.12	-	-	0.14	0.04	-	0.08	-	0.1	-
Zr	46.3	46.4	60.4	35.5	28.5	43.2	37.3	19.6	45	24.8	55.4	39.4	24.2
Hf	-	-	1.9	1.13	-	-	1.0	0.6	-	0.9	-	1.2	-
Y	11.6	12.4	23.1	9.3	5.8	8.4	8.4	4.8	12	9.3	65.4	9.2	6.9
Cr	1411	569.3	78.5	218	590.4	211.9	229.1	2495	947.8	2086	230.1	43.7	1881
Ni	503	273	105	787	966	822	798	506	134	650	148	35	429
La	-	-	28.5	8.20	-	-	9.18	6.88	-	4.96	-	18.8	-
Ce	-	-	77.1	21.31	-	-	22.6	14.6	-	13.9	-	38.2	-
Pr	-	-	10.8	3.04	-	-	3.17	1.76	-	2.17	-	4.54	-
Nd	-	-	45.2	14.26	-	-	14.1	7.14	-	11.1	-	18	-
Sm	-	-	8.71	3.12	-	-	2.93	1.42	-	2.69	-	3.12	-
Eu	-	-	1.51	0.86	-	-	0.77	0.42	-	0.73	-	0.85	-
Gd	-	-	6.1	2.68	-	-	2.33	1.13	-	2.33	-	2.31	-
Tb	-	-	0.85	0.36	-	-	0.31	0.16	-	0.32	-	0.29	-
Dy	-	-	4.43	1.83	-	-	1.63	0.89	-	1.82	-	1.54	-
Ho	-	-	0.81	0.34	-	-	0.3	0.17	-	0.35	-	0.3	-
Er	-	-	2.32	1.07	-	-	0.82	0.54	-	1.02	-	0.84	-
Tm	-	-	0.32	0.13	-	-	0.12	0.085	-	0.14	-	0.12	-
Yb	-	-	2.11	0.82	-	-	0.78	0.58	-	0.93	-	0.84	-
Lu	-	-	0.33	0.11	-	-	0.12	0.094	-	-0.15	-	0.14	-

Table 5-1: Ca. 2.82 Ga Lac Faribault intrusions (cont.)

Sample	LF-23	LF-24	LF-25	LF-26	LF-27	LF-32	LF-33	LF-34	LF-35	LF-37	LF-39	LF2-2	LF3-4
Zone	19	19	19	19	19	19	19	19	19	19	19	19	19
Easting	342245	342138	342158	342152	342182	342299	342319	342712	342697	342621	342689	342790	343270
Northing	6549459	6548954	6549026	6549087	6549512	6548946	6548939	6549944	6549959	6549857	6549935	6549933	6549681
Lithology	*web*	*web*	*web*	*web*	*web*	*web*	*web*	*gabbro*	*web*	*gabbro*	*gabbro*	*perid.*	*gabbro*
Major elements (wt. %)													
SiO_2	51.52	51.94	52.22	52.8	51.73	49.89	49.89	47.45	47.41	45.03	44.05	43.39	52.8
TiO_2	0.37	0.35	0.34	0.42	0.33	0.61	0.6	2.42	1.17	2.73	3.02	0.64	0.97
Al_2O_3	5.77	5.11	5.23	5.1	8.28	8.81	9.14	17.67	9.15	16.85	16.7	7.51	17.32
MgO	14.77	17.78	16.24	14.16	13.09	12.64	12.19	4.13	17.46	4.94	4.79	24.44	5.08
FeO	10.98	13.48	12.78	11	9.93	7.95	7.81	12.46	12.18	14.19	14.92	11.45	8.83
MnO	0.23	0.27	0.27	0.24	0.19	0.16	0.17	0.13	0.2	0.15	0.15	0.18	0.15
CaO	12.07	7.67	9.21	13	11.7	14.66	14.9	8.43	7.1	9.95	9.85	5.87	8.13
Na_2O	1.17	1.1	1.12	1.17	1.72	1.99	2.34	4.01	1.21	3.39	3.31	0.93	4.29
K_2O	0.65	0.5	0.74	0.42	0.7	1.19	0.84	1.01	1.51	0.59	0.71	1.2	0.84
P_2O_5	0.05	0.06	0.06	0.07	0.05	0.15	0.16	0.18	0.07	0.23	0.2	0.11	0.22
LOI	1.38	0.35	0.29	0.59	1.25	1.04	1	0.66	0.89	0.41	0.45	2.42	0.31
Total	99.02	98.83	98.69	99.04	99.04	99.14	99.09	98.55	98.52	98.47	98.16	98.45	98.97
Trace elements (ppm)													
S	-	-	-	-	-	-	-	-	-	-	-	-	-
Th	-	0.53	-	-	-	1.29	-	-	-	0.74	-	-	
U	-	0.14	-	-	-	0.37	-	-	-	0.22	-	-	
Rb	18.5	13	28.7	10.1	17.4	33.1	17	17.7	31.2	4.7	10.8	33.2	10.5
Ba	127.5	144.3	226.1	109.6	151.5	236.3	194.4	387.8	347.4	198.9	218	435.1	443.5
Pb	2.2	3.2	2.6	1.7	3.9	3.7	3.8	12	1.5	5.7	5.7	4.1	7.7
Sr	72.1	90.2	100.9	75.7	143	468.1	506.8	610.9	142.6	710.2	722.5	339.1	515.9
Nb	2.6	2.6	2.7	3.1	2.0	9.7	10.3	5.0	3.6	5.2	5.0	2.5	4.0
Ta	-	0.10	-	-	-	0.37	-	-	-	0.29	-	-	
Zr	52.5	48.4	49	62.4	39.1	56.9	75.1	58.3	39.3	44.9	44.6	49.1	98.2
Hf	-	2.2	-	-	-	1.7	-	-	-	1.6	-	-	
Y	11.3	12.5	12.6	13.4	9.6	11.5	11.7	10.7	16.3	13.2	12.6	10.5	13.8
Cr	502	1517	1314	468.9	544.8	353.4	312.9	11.8	1206	10.3	10.7	2137	193.4
Ni	271	535	469	202	285	179	159-	21	495	7	< 3	925	102
La	-	34.18	-	-	-	55.1	-	-	-	37.8	-	-	
Ce	-	4.27	-	-	-	7.12	-	-	-	4.97	-	-	
Pr	-	17.71	-	-	-	29.8	-	-	-	21.6	-	-	
Nd	-	3.67	-	-	-	5.07	-	-	-	4.41	-	-	
Sm	-	0.69	-	-	-	1.37	-	-	-	1.43	-	-	
Eu	-	3.17	-	-	-	3.62	-	-	-	3.67	-	-	
Gd	-	0.49	-	-	-	0.45	-	-	-	0.5	-	-	
Tb	-	2.70	-	-	-	2.29	-	-	-	2.55	-	-	
Dy	-	12.56	-	-	-	23.3	-	-	-	16	-	-	
Ho	-	0.51	-	-	-	0.42	-	-	-	0.46	-	-	-
Er	-	1.42	-	-	-	1.12	-	-	-	1.3	-	-	-
Tm	-	0.19	-	-	-	0.16	-	-	-	0.18	-	-	-
Yb	-	1.16	-	-	-	0.96	-	-	-	1.14	-	-	-
Lu	-	0.17	-	-	-	0.16	-	-	-	0.17	-	-	-

Table 5-1: Ca. 2.82 Ga Lac Faribault intrusions (cont.)

Sample	LF9-1	LF9-3	LF9-5	LF9-6	LF9-7
Easting	341482	341893	341922	341922	341922
Northing	6553729	6552778	6552675	6552675	6552675
Lithology	*web*	*web*	*perid*	*perid*	*web*
Major elements (wt. %)					
SiO_2	48.11	49.83	42.12	42.81	53.44
TiO_2	0.3	0.3	0.31	0.26	0.33
Al_2O_3	4.41	5.64	4.45	5.46	7.13
MgO	19.93	18.26	26.17	25.16	12.16
FeO	8.38	7.95	10.96	10.85	5.41
MnO	0.16	0.19	0.16	0.19	0.13
CaO	15.04	13.81	6.68	6.26	16.69
Na_2O	0.6	0.92	0.71	0.83	2.19
K_2O	0.3	0.27	0.39	0.62	1.06
P_2O_5	0.05	0.06	0.07	0.1	0.09
LOI	1.50	1.59	6.66	5.73	1.01
Total	99.01	99.17	98.94	98.49	99.67
Trace elements (ppm)					
S	-	-	-	-	-
Th	-	-	-	-	3.16
U	-	-	-	-	0.48
Rb	8.0	3.3	13.1	24.3	52.2
Ba	183.7	63.7	118	161.1	199.7
Pb	3.6	2.0	1.3	<1.0	8.1
Sr	152.1	132.3	120	132.1	251
Nb	0.7	2.4	2.3	2.6	3
Ta	-	-	-	-	0.15
Zr	20.5	23.1	19.6	27.6	38.1
Hf	-	-	-	-	0.9
Y	7.5	6.5	5.5	5.1	8.2
Cr	1631	2405	1843	1604	188.6
Ni	561	393	833	777	191
La	-	-	-	-	31.4
Ce	-	-	-	-	4.07
Pr	-	-	-	-	17.6
Nd	-	-	-	-	3.47
Sm	-	-	-	-	0.885
Eu	-	-	-	-	2.55
Gd	-	-	-	-	0.3
Tb	-	-	-	-	1.7
Dy	-	-	-	-	14.4
Ho	-	-	-	-	0.29
Er	-	-	-	-	0.79
Tm	-	-	-	-	0.11
Yb	-	-	-	-	0.71
Lu	-	-	-	-	0.12

Table 5-2: Average compositions of olivine - Lac Faribault area

Sample:	LF-8	LF-15	LF-20
n	9	5	4
Rock	perid.	perid.	hblite.
WR Mg-	0.80	0.80	0.82
SiO_2	39.4 ± 0.3	39.8± 0.2	39.3± 0.2
TiO_2	<0.04	<0.04	<0.04
Al_2O_3	<0.04	<0.04	<0.05
MgO	44.2 ± 0.4	45.8 ± 0.3	43.6 ± 0.4
FeO	16.3 ± 0.3	14.4 ± 0.7	17.2 ± 0.2
MnO	0.27 ± 0.03	0.21 ± 0.01	0.26 ± 0.01
CaO	<0.01	<0.01	<0.01
Na_2O	-	-	-
NiO	0.16 ± 0.02	0.15 ± 0.01	0.15 ± 0.03
Cr_2O_3	<0.06	<0.06	<0.06
P_2O_5	-	-	-
Total	100.3 ± 0.7	100.4 ± 0.6	100.5 ± 0.5
Fo	82.8 ± 0.3	85.0± 0.7	81.9 ± 0.3
Ni (ppm)	1232 ± 124	1213 ± 92	1187 ± 176
Mg# liq	0.59	0.63	0.58

Olivine compositions were analyzed on a JEOL 8900 instrument at the McGill Electron Microprobe Microanalytical Facility under identical analytical conditions (20.0 kV accelerating voltage, 2.5 nA beam current, 5 μm beam diameter). Errors on individual oxides are ≤ 1% relative (2 s.d.)

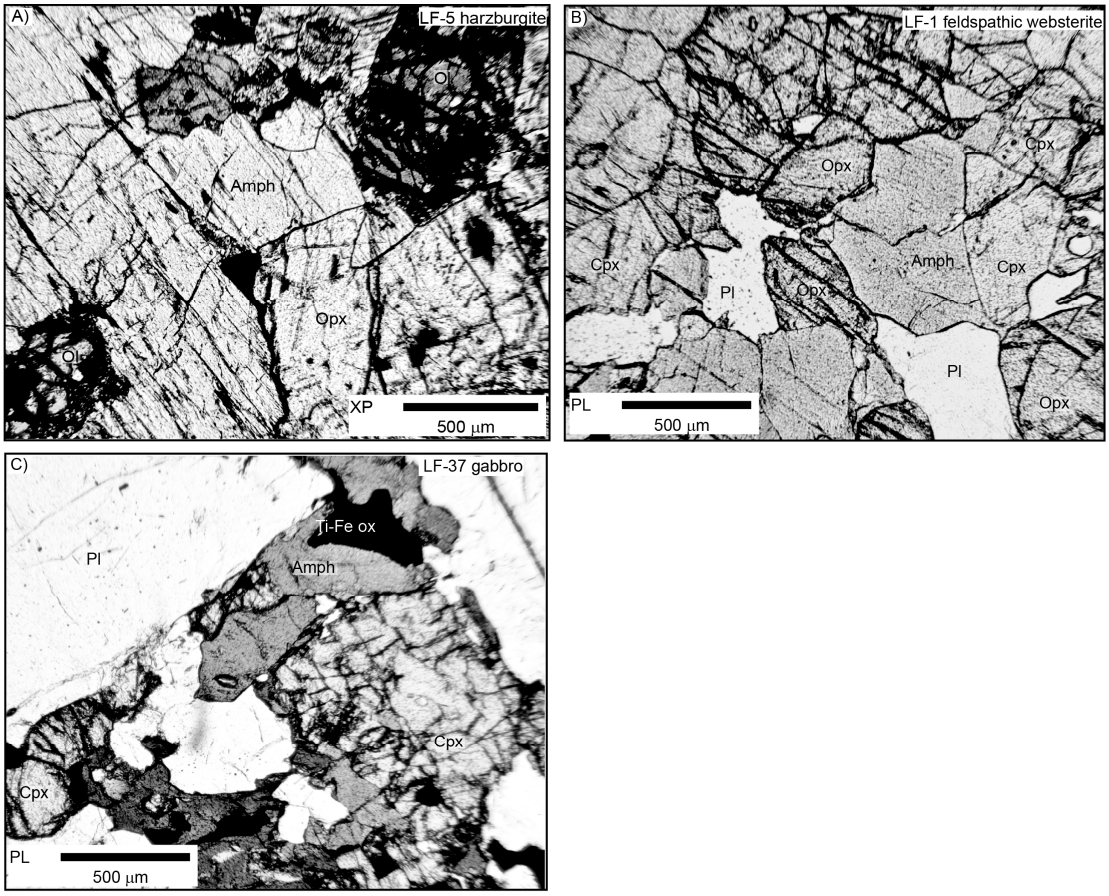

Figure 5-12: Representative petrographic images of Lac Faribault samples.
A) Crossed-polars image of harzburgite LF-5, showing poikilitic growth of amphibole around olivine (lower left) and composite olivine/orthopyroxene macrocrysts (right). **B)** Transmitted-light image of the feldspathic websterite LF-1. C) Transmitted–light image of oxide-rich, nepheline-normative gabbro LF-37.

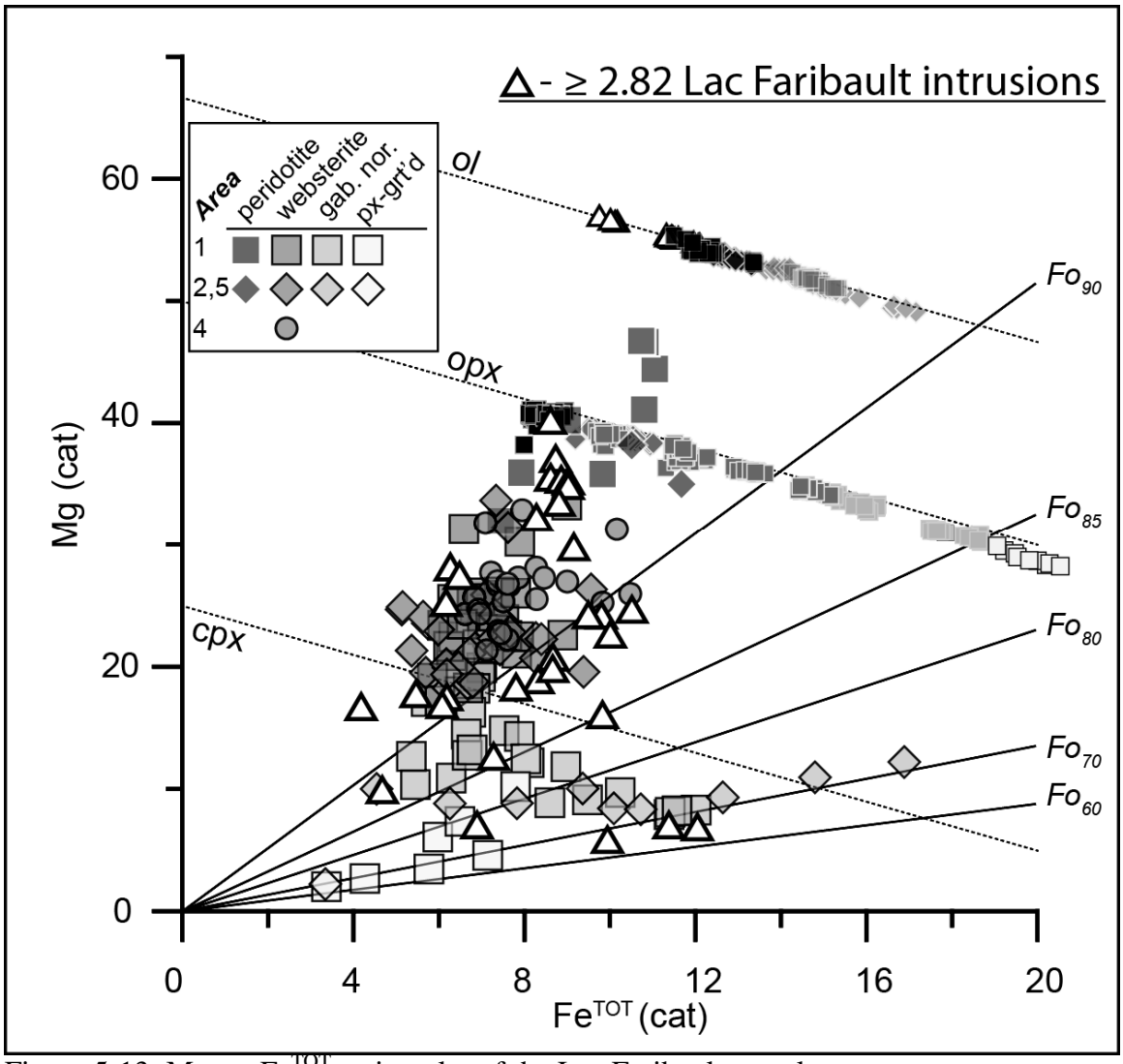

Figure 5-13: Mg vs. Fe^{TOT} cation plot of the Lac Faribault samples
≥2.82 Ga samples are superimposed onto the subalkaline Q-suite intrusions for comparison. Also shown are the olivine compositions of the Lac Faribault peridotites which are notably richer in Fo than those of the Q-suite peridotites. The symbols in the legend refer to the locations discussed in Chapter 2 and shown in Figure 2-1.

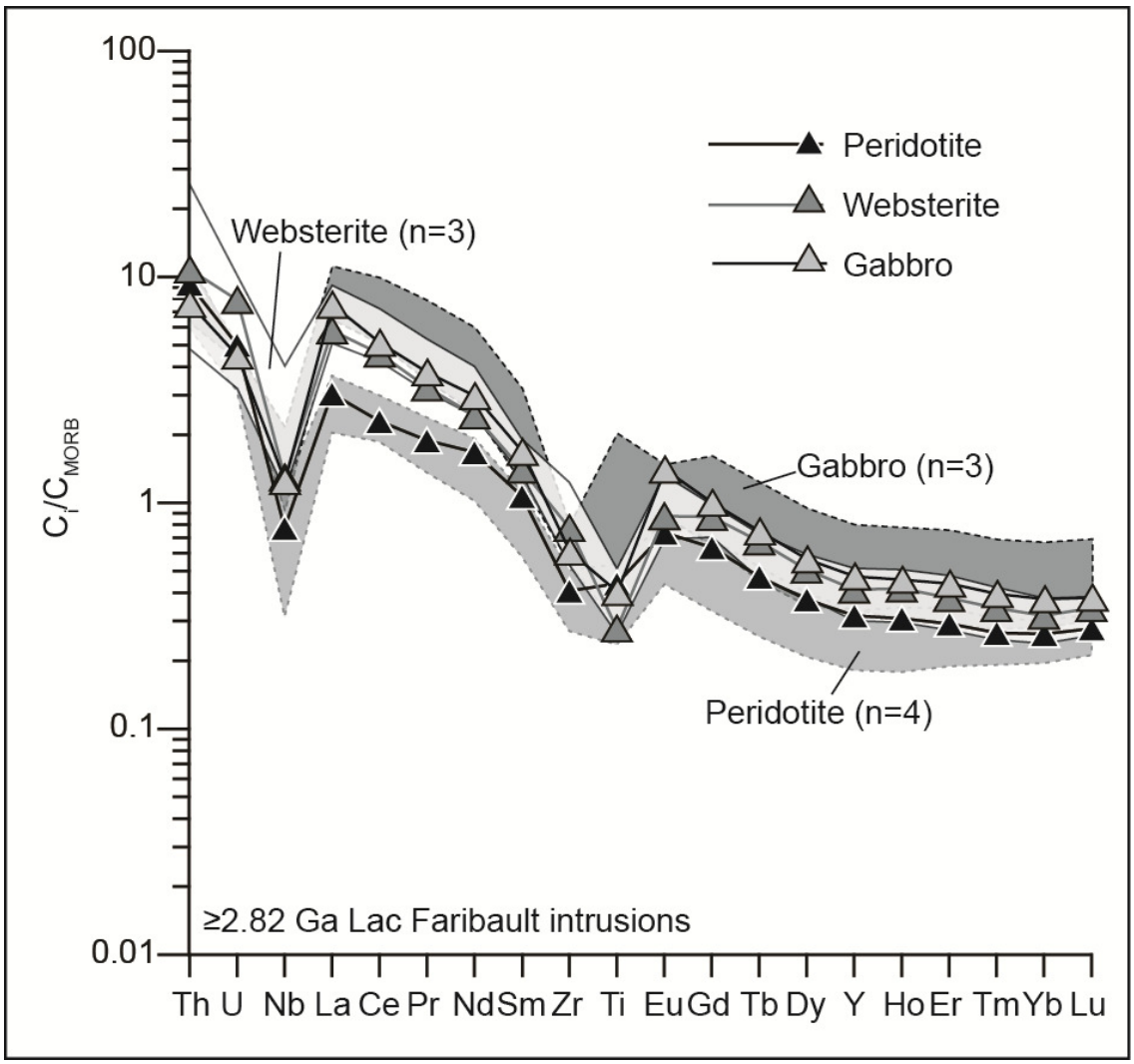

Figure 5-14: Trace element profiles of Lac Faribault intrusions
MORB-normalized trace element abundances of the peridotites, websterites and gabbros sampled near Lac Faribault.

Appendix 5-3: Duplicate geochemical analyses

Table 5-3: Duplicate XRF analyses

Sample	GR2-11					GR2-3				
YEAR	2008	2009	2010	2011	Mean (2 s.d)	2008	2009	2010	2011	Mean (2 s.d)
Major elements (wt. %)										
SiO_2	72.04	72.49	72.68	72.27	72.37 (0.55)	47.68	47.96	47.67	47.74	47.76 (0.27)
TiO_2	0.20	0.18	0.16	0.18	0.18 (0.04)	0.23	0.23	0.23	0.23	0.23 (0.00)
Al_2O_3	14.87	14.78	14.52	14.68	14.71 (0.30)	14.42	14.47	14.44	14.35	14.42 (0.10)
Fe_2O_3	2.09	1.82	1.74	1.82	1.87 (0.30)	7.97	8.13	8.09	8.06	8.06 (0.14)
MnO	0.02	0.02	0.02	0.02	0.02 (0.00)	0.16	0.16	0.15	0.15	0.16 (0.00)
MgO	0.71	0.60	0.62	0.61	0.64 (0.10)	12.12	12.49	12.35	12.33	12.32 (0.31)
CaO	2.13	2.05	2.07	2.03	2.07 (0.09)	13.44	13.22	13.16	13.11	13.23 (0.29)
Na_2O	4.12	4.04	3.95	3.97	4.02 (0.15)	0.83	0.79	0.79	0.78	0.80 (0.05)
K_2O	3.25	3.46	3.40	3.45	3.39 (0.19)	0.35	0.33	0.33	0.34	0.34 (0.02)
P_2O_5	0.07	0.07	0.07	0.07	0.07 (0.00)	0.016	0.02	0.02	0.02	0.02 (0.00)
LOI	0.47	0.45	0.56	0.49	0.49 (0.10)	2.63	2.57	2.89	2.92	2.75 (0.36)
Total	100.11	100.10	99.93	99.71	99.96 (0.37)	100.02	100.54	100.30	100.21	100.27 (0.43)
Trace elements (ppm)										
BaO	1148.0	1225.3	1208.6	1164.6	1186.6 (72.6)	137.6	123.5	115.2	139.2	128.9 (23.1)
Cr_2O_3	27.8	11.5	<10	10.8	12.5 (22.9)	1081.2	1088.5	1079.2	1074	1080.7 (12.0)
Ni	<3.0	<3.0	<3.0	<3.0	-	167.1	168.2	163.1	171.0	167.3 (6.6)
Pb	17.3	17.9	17.8	17.5	17.6 (0.6)	<1.0	<1.0	2.6	1.1	-
Sr	382.2	384.3	377.7	387.3	382.9 (8.1)	553.8	520.2	520.6	510.8	526.4 (37.7)
Rb	77.3	76.4	75.4	75.7	76.2 (1.7)	6.0	6.2	5.9	5.1	5.8 (1.0)
Nb	2.0	1.7	1.8	1.7	1.8 (0.3)	<0.3	<0.3	0.6	<0.3	-
Zr	120.8	104.4	108.5	107.0	110.2 (14.6)	8.5	8.1	9.2	8.0	8.5 (1.1)
Y	3.3	3.3	3.3	3.4	3.3 (0.1)	5.9	6.0	6.2	6.1	6.1 (0.3)

Table 5-3: Duplicate XRF analyses (cont.)

Sample	GR2-7					GR2-9				
YEAR	2008	2009	2010	2011	Mean (2 s.d)	2008	2009	2010	2011	Mean (2 s.d)
Major elements (wt. %)										
SiO_2	50.65	50.75	50.60	50.68	50.67 (0.13)	59.73	59.79	59.32	59.77	59.65 (0.45)
TiO_2	0.36	0.37	0.36	0.36	0.36 (0.01)	0.66	0.65	0.65	0.65	0.65 (0.01)
Al_2O_3	6.34	6.36	6.42	6.35	6.37 (0.07)	16.72	16.94	16.83	16.85	16.84 (0.18)
Fe_2O_3	8.97	9.04	8.92	8.93	8.96 (0.11)	8.09	8.18	8.24	8.09	8.15 (0.15)
MnO	0.18	0.18	0.18	0.18	0.18 (0.00)	0.10	0.10	0.11	0.10	0.10 (0.01)
MgO	15.07	15.12	15.03	15.02	15.06 (0.09)	2.44	2.43	2.53	2.40	2.45 (0.11)
CaO	16.06	16.02	16.02	16.00	16.03 (0.05)	5.99	5.98	6.00	5.93	5.98 (0.06)
Na_2O	1.07	1.09	1.08	1.05	1.07 (0.03)	4.13	4.19	4.14	4.11	4.14 (0.07)
K_2O	0.36	0.36	0.36	0.36	0.36 (0.00)	1.30	1.27	1.26	1.27	1.28 (0.03)
P_2O_5	0.07	0.07	0.07	0.07	0.07 (0.00)	0.19	0.19	0.19	0.19	0.19 (0.01)
LOI	0.98	0.76	0.91	1.07	0.93 (0.26)	0.56	0.49	0.58	0.52	0.54 (0.08)
Total	100.38	100.39	100.21	100.34	100.33 (0.16)	100.05	100.37	99.98	100.02	100.11 (0.35)
Trace elements (ppm)										
BaO	160.9	143.9	145.2	171.1	155.3 (26.2)	1150.3	1130.0	1103.2	1092.2	1118.9 (52.5)
Cr_2O_3	1780.9	1774.7	1775.0	1744.5	1768.8 (32.9)	19.4	16.5	27.2	18.5	20.4 (9.4)
Ni	291.3	301.5	287.4	293.0	293.3 (11.9)	‘3.0	4.9	4.2	3.0	-
Pb	1.8	1.9	2.9	2.5	2.3 (1.0)	8.1	9.1	9.7	10.0	9.2 (1.7)
Sr	160.7	163.4	161.1	158.6	160.9 (3.9)	602.1	610.8	595.1	598.2	601.5 (13.6)
Rb	5.3	5.6	5.2	4.9	5.3 (0.6)	26.3	25.2	25.1	23.8	25.1 (2.0)
Nb	0.9	0.9	0.8	0.6	0.8 (0.3)	3.2	3.2	3.4	3.2	3.3 (0.2)
Zr	30.4	30.1	30.7	30.7	30.5 (0.6)	114.9	106.3	116.6	98.3	109.0 (16.9)
Y	10.0	9.9	10.1	10.2	10.1 (0.3)	11.5	12.2	12.2	12.3	12.1 (0.7)

Table 5-3: Duplicate XRF analyses (cont.)

Sample	GR4-2				
YEAR	2008	2009	2010	2011	Mean (2 s.d)
Major elements (wt. %)					
SiO_2	56.36	56.71	56.61	56.63	56.58 (0.30)
TiO_2	0.55	0.53	0.52	0.53	0.53 (0.02)
Al_2O_3	16.74	16.90	16.63	16.80	16.77 (0.23)
Fe_2O_3	8.40	8.43	8.39	8.35	8.39 (0.07)
MnO	0.12	0.12	0.12	0.12	0.12 (0.00)
MgO	4.31	4.24	4.29	4.19	4.26 (0.10)
CaO	7.70	7.58	7.59	7.54	7.60 (0.14)
Na_2O	3.63	3.66	3.61	3.60	3.63 ((0.06)
K_2O	1.26	1.22	1.19	1.22	1.22 (0.06)
P_2O_5	0.10	0.10	0.09	0.10	0.10 (0.00)
LOI	0.91	0.77	0.92	0.85	0.86 (0.14)
Total	100.18	100.37	100.08	100.03	100.17 (0.30)
Trace elements (ppm)					
BaO	790.9	747.7	733.8	734.0	751.6 (54.0)
Cr_2O_3	34.2	15.9	37.2	19.1	26.6 (21.3)
Ni	14.0	12.9	11.3	11.0	12.3 (2.8)
Pb	9.6	10.0	11.6	10.5	10.4 (1.7)
Sr	544.7	551.7	535	539.8	542.8 (14.3)
Rb	21.7	20.9	20.5	19.7	20.7 (1.7)
Nb	3.0	2.8	2.8	2.6	2.8 (0.3)
Zr	75.9	66.9	78	63.3	71.0 (14.1)
Y	11.5	11.3	11.9	11.7	11.6 (0.5)

Table 5-4: Duplicate ICP-MS analyses

Sample	UM03-2008					GR2-11				
YEAR	2009	2011	2011	Mean (2 s.d. %)	*2012**	2009	2011	2011	Mean (2 s.d. %)	*2012**
Ta	0.21	0.16	0.23	0.20 (36)	*0.18*	0.05	0.02	0.04	0.04 (83)	*0.04*
Hf	0.8	0.6	0.6	0.67 (35)	*0.78*	5.1	4.4	3.0	4.17 (51)	*3.27*
Th	1.59	1.33	1.59	1.50 (20	*1.57*	11.4	10.4	10.2	10.67 (12.1)	*10.84*
U	0.74	0.69	0.82	0.75 (17.5)	*0.84*	0.49	0.40	0.44	0.44 (20.3)	*.0.41*
La	4.71	5.06	4.78	4.85 (7.6)	*4.74*	30.50	34.4	28.60	31.17 (19)	*28.24*
Ce	10.6	9.96	11.00	10.52 (10)	*11.61*	52.50	52.9	48.90	51.43 (8.6)	*53.86*
Pr	1.28	1.33	1.42	1.34 (10.6)	*1.53*	4.93	5.33	4.81	5.02 (10.8)	*5.31*
Nd	5.83	5.95	6.19	5.99 (6.1)	*6.87*	16.7	17.6	15.60	16.63 (12.0)	*17.38*
Sm	1.34	1.34	1.42	1.37 (6.8)	*1.53*	2.32	2.33	2.16	2.27 (8.4)	*2.31*
Eu	0.323	0.325	0.342	0.330 (6.3)	*0.345*	0.829	0.832	0.801	0.821 (4.2)	*0.918*
Gd	1.23	1.23	1.39	1.28 (14.4)	*1.34*	1.44	1.46	1.41	1.44 (3.5)	*1.41*
Tb	0.19	0.19	0.2	0.19 (6.0)	*0.21*	0.16	0.15	0.14	0.15 (13.3)	*0.17*
Dy	1.1	1.08	1.19	1.12 (10.4)	*1.22*	0.72	0.68	0.66	0.69 (8.9)	*0.76*
Ho	0.23	0.22	0.22	0.22 (5.2)	*0.23*	0.13	0.12	0.10	0.12 (26.2)	*0.12*
Er	0.65	0.66	0.68	0.66 (4.6)	*0.71*	0.33	0.35	0.270	0.32 (26.3)	*0.34*
Tm	0.095	0.107	0.102	0.101 (11.9)	*0.112*	0.037	0.048	0.035	0.040 (35)	*0.034*
Yb	0.63	0.69	0.64	0.65 (9.8)	*0.71*	0.29	0.28	0.23	0.27 (24.1)	*0.23*
Lu	0.086	0.113	0.099	0.099 (27)	*0.113*	0.032	0.045	0.039	0.039 (34)	*0.041*

Sample	CHRON-2				DH08-9			
YEAR	2009	2011	2011	Mean (2 s.d. %)	2009	2011	2011	Mean (2 s.d. %)
Ta	0.30	0.21	0.25	0.25 (36)	0.62	<0.01	0.02	-
Hf	8.6	8.2	7.9	8.23 (8.5)	0.5	0.3	0.4	0.4 (50)
Th	13.0	10.4	14.9	12.77 (35)	0.90	0.20	0.24	0.4 (176)
U	0.77	0.71	0.77	0.75 (9.2)	0.13	0.09	.09	0.1 (45)
La	57.0	61.3	61.7	60.0 (8.7)	3.37	3.60	3.28	3.42 (9.7)
Ce	111.	106.0	120.0	112.3 (12.6)	7.52	7.45	7.73	7.57 (3.8)
Pr	11.7	12.1	12.9	12.2 (10.0)	0.92	0.99	1.00	0.97 (9.0)
Nd	43.9	44.6	45.8	44.8 (4.3)	4.17	4.34	4.46	4.32 (6.7)
Sm	7.36	7.31	7.49	7.39 (2.5)	0.89	0.94	0.99	0.94 (10.6)
Eu	1.08	1.10	1.09	1.09 (1.8)	0.236	0.255	0.237	0.243 (8.8)
Gd	5.35	5.13	5.65	5.38 (9.8)	0.78	0.80	0.84	0.81 (7.6)
Tb	0.67	0.64	0.65	0.65 ((4.7)	0.12	0.13	0.13	0.13 (9.1)
Dy	3.24	3.08	3.25	3.19 (6.0)	0.68	0.68	0.67	0.68 (1.7)
Ho	0.58	0.55	0.57	0.57 (5.4)	0.14	0.14	0.14	0.14 (0.00)
Er	1.48	1.53	1.50	1.50 (3.3)	0.38	0.41	0.39	0.39 (7.8)
Tm	0.19	0.208	0.198	0.201 (6.1)	0.051	0.062	0.054	0.056 (20.4)
Yb	1.14	1.22	1.18	1.18 (6.8)	0.37	0.37	0.36	0.37 (3.1)
Lu	0.15	0.186	0.176	0.171 (21)	0.038	0.057	0.060	0.052 (46)

Means calculated from samples analyzed between 2009-2011 at Activation Laboratories. Uncertainty reported as 100 x (2 s.d./ mean). *Denoted in italics are analyses performed at PCIGR in summer 2012.

CHAPTER 6. General conclusions

The study of the mafic and ultramafic intrusions in western half of the Ungava craton establishes a suite of Fe-rich, regionally widespread plutons emplaced during the craton's peak igneous activity (ca. 2.74-2.70 Ga). The intrusions, found across the Ungava croaton, belong to the Qullinaaraaluk, Couture and Chateguay suites, which are collectively referred to as the Q-suite in this thesis. Two new U-Pb zircon ages (2718.0 ± 0.7 Ma and 2710.0 ± 0.5 Ma) are consistent with previously published MRNF data, indicating ca. 2.72-2.70 Ga emplacement of the Q-suite.

The Q-suite comprises a range of cumulate lithologies from olivine-dominated dunite and peridotite, to pyroxene-dominated websterite and wehrlite to plagioclase-rich gabbro and gabbronorite. The most magnesian, olivine-dominated rocks have whole rock and olivine Fe/Mg ratios that suggest derivation from parental magmas significantly more Fe-rich than magmas derived from "pyrolitic" mantle sources. Two distinct types of Q-suite intrusions exist: 1) orthopyroxene-rich, subalkaline intrusions and 2) orthopyroxene-free, transitional intrusions that straddle the plane of critical silica undersaturation.

The magmas parental to the subalkaline Q-suite intrusions were Fe-rich, high-Mg basalts (MgO = 10.8 wt. %, FeO^{TOT} = 14.1 wt. %), with Al_2O_3 (14.8 wt. %) contents similar to most mafic liquids of similar MgO content. The transitional parental magmas differ from the subalkaline magmas both in terms of their higher MgO (14 wt. %) and FeO^{TOT} (16.8 wt. %) contents, and their significantly lower Al_2O_3 contents (6.6 wt. %). The major element composition of the Q-suite parental magmas were estimated using the program alphaMELTS, by modeling isobaric melting of the most magnesian cumulate rocks until non-cumulus phases were melted out and the model liquid Fe/Mg ratio was in equilibrium with the observed olivine compositions.

The Q-suite magmas experienced significant interaction with pre-2.74 Ga TTG crust. The initial $^{143}Nd/^{144}Nd$ ratios of the Q-suite intrusions situated in the isotopically "old" Hudson Bay terrane range from near-chondritic to strongly sub-chondritic ($\varepsilon_{Nd(2.72Ga)}$) = +1 to -10), consistent with contamination by unradiogenic TTG crust with long crustal residence. Second, the intrusions show high Th/Yb ratios (5-200), commonly taken as an index of crustal contamination. Third, some intrusions contain domains of pyroxene-bearing dioritic to granodioritic rocks, characterized by uniform HREE contents, but Zr/Y ratios that rapidly increase with increasing SiO_2 contents. Such geochemical behaviour is consistent with relatively high rates assimilation of TTG crust by Q-suite parental liquids undergoing fractional crystallization (r >1). Thermodynamic modelling, using alphaMELTS suggests that the high assimilation rates require hot ambient mid crustal temperatures of 700-900°C.

The "hybrid" domains of the Q-suite plutons strongly resemble the intermediate (≤ 65 wt. %) members of the pyroxene-granitoid suite, which makes up over 20% of the Ungava craton's exposed surface. Majority of the pyroxene-granitoid plutons were emplaced during the 2.74-2.70 Ga reworking of the Ungava craton, and their strong mineralogical and geochemical similarity to the Q-suite "hybrid"-facies rocks suggests that significant volumes of juvenile, Fe-rich magmas were emplaced into the proto-Ungava crust. Such an interpretation is most consistent with a tectonic model in which Fe-rich picritic to high-Mg basaltic magmas underplated the proto-craton, supplying heat for crustal-scale anatexis and reworking.

The "calc-alkaline" signature of the Q-suite intrusions, typical of modern volcanic arcs, may reflect significant contamination by the strongly LREE-enriched, HFSE-

depleted anatectic melts of the proto-cratonic TTG crust. The cumulate rocks of the Q-suite have trace element profiles characterized by an enrichment of light rare earth elements (LREE) relative to the heavy rare earth elements (HREE), and pronounced depletions in the high field strength elements (HFSE) Nb, Ta, Ti ± Zr ± Hf. Mass balance calculations and the relatively flat to convex upward LREE profiles of the transitional Q-suite dunites suggest that the parental Q-suite magmas may have had flat to LREE-depleted profiles, which were modified by post-accumulation metasomatism by small volumes of TTG anatectic melt. is sufficient to impart the calc-alkaline signature on the cumulate rocks that crystallized from parental magmas with flat (tholeiitic) trace element profiles.

Both the estimated subalkaline and transitional Q-suite magmas are significantly richer in FeO^{TOT} than both modern day and Archean mantle-derived magmas. Comparison with experimental results indicates that the FeO^{TOT} contents of the Q-suite parental magmas are significantly higher than those of "pyrolite"-equilibrated melts. In terms of their FeO^{TOT} content, the Q-suite parental magmas are intermediate between the melts of the Fe-rich fertile peridotite xenoliths from Hawaii and the Fe-rich peridotites representative of the Martian mantle. Furthermore, the exceptionally Ni-poor peridotites and dunites of the Q-suite indicate that Q-suite parental magmas were derived from sources depleted in Ni relative to pyrolitic mantle. Major element considerations prohibit a genetic relationship between the two magma types by fractional crystallization, or differential assimilation of continental crust. The major element compositions of the estimated subalkaline and transitional Q-suite parental magmas reflect derivation from compositionally different Fe-rich mantle sources or derivation from compositionally

similar sources by different degrees of melting at different P-T conditions. The second scenario invokes different degrees of partial melting and pressure control on the olivine-melt partitioning of MgO and FeO, to account for the significant difference in the MgO and FeO^{TOT} contents between the subalkaline and transitional Q-suite magmas. According to this scenario, the transitional magmas equilibrated with harzburgitic residues, and began melting at greater depths (~5GPa), whereas the subalkaline magmas equilibrated with lherzolitic mantle and began melting at shallower mantle levels (~3.5 GPa)

Although rare in the geological record, ferropicritic lavas and pyroclastic deposits of ca. 2.7 Ga age were also erupted as parts of greenstone belts of the southern and western Superior and Western Churchill provinces of the Canadian Shield, and the Karelia Province of the Baltic Shield. Ferropicritic rocks of the same age have also been identified in the Neoarchean sedimentary basins of Slave Province and the Yilgarn and Kaapvaal cratons. The trace element compositions of the Neoarchean ferropicrites suggest the existence of two main Fe-rich magma types. Alkaline ferropicrites have trace element profiles similar to those of modern ocean island basalts (OIBs), high Ni contents and low Sc/Fe ratios. The trace element and isotope geochemistry of alkaline ferropicrites suggests garnet-pyroxenite sources that were metasomatically enriched shortly before ferropicrite genesis. The subalkaline ferropicrites, which also include the transitional Q-suite magmas, are interpreted to have flat to LREE-depleted trace element profiles, low Ni contents and relatively high Sc/Fe ratios typical of modern day MORB. Thus, the subalkaline ferropicrites were produced by melting of unmetasomatized garnet-free mantle. The worldwide distribution of ferropicritic rocks that were emplaced coevally

with the more ubiquitous ca. 2.7 Ga Fe-poor magmas is compatible with the existence of Fe-rich "plums" within the predominantly pyrolitic mantle. The relative scarcity of ferropicrites younger than ca. 2.7 Ga may reflect that Fe-rich "plums" were largely melted out during the Neoarchean melting of the mantle.

A number of outstanding questions regarding ferropicrites remain, requiring future work. The most intriguing question is the process by which the ferropicrite sources acquired their unusual Fe-enrichment. Possible scenarios that invoke secondary processes include metasomatism of pyrolitic mantle by Fe-rich melts, or mixing between pyrolitic mantle and recycled Fe-rich oceanic crust. Alternatively, Fe-rich domains may have survived the early separation of the core, or were added to the mantle as a result of infall of Fe-rich meteorites, such as ordinary chondrites. These questions may perhaps be answered using short-lived isotopic systems (i.e. W-Hf). Relatively unradiogenic $^{182}W/^{184}W$ ratios of ferropicrites would support hypotheses that involve the melting of chondrite-like Fe-rich sources, whose Hf-W system was not fractionated by the segregation of core. In contrast, radiogenic $^{182}W/^{184}W$ ratios would suggest that ferropicrite sources experienced early segregation of siderophile W (and by inference Fe), thus supporting hypotheses in which Fe is added by metasomatism. High resolution (low –level) analyses of the Platinum Group Elements (PGE) may also be used to answer the question of the origin of Fe-enrichment of the source. The second question that needs further resolution is the Fe-content (Mg-number) of the ferropicrite source. There is a dearth of melting experiments on non-pyrolitic mantle compositions, and additional experiments on Martian mantle compositions at variable pressures, and experiments on compositions intermediate between Fe-rich sources of Hawaiian basalts and Martian

mantle may provide important tests for the models presented in Chapter 2. Similarly, melting experiments on pyroxenite sources richer in FeO than MIX1G would test the suggested garnet-pyroxenite origin of alkaline ferropicrites. Finally, Neoarchean ferropicrites occurring outside the Superior and Slave cratons were formally recognized for the first time in this thesis. Many of these occurrences were identified as part of regional-scale projects, or at a time when quality geochemical and isotopic analyses were not universally available. The understanding of ferropicrites would benefit from detailed studies of these occurrences.